Attitude and Orbit Control Techniques for Spacecraft with Electric Propulsion



Mirko Leomanni

PhD Thesis in Information Engineering and Science
University of Siena

UNIVERSITÀ DEGLI STUDI DI SIENA DIPARTIMENTO DI INGEGNERIA DELL'INFORMAZIONE E SCIENZE MATEMATICHE



Attitude and Orbit Control Techniques for Spacecraft with Electric Propulsion

Tesi di Dottorato di

Mirko Leomanni

Advisor: Dr. Antonio Giannitrapani Co-Advisor: Prof. Andrea Garulli

Siena, Febbraio 2015

DOTTORATO DI RICERCA IN INGEGNERIA DELL'INFORMAZIONE E SCIENZE MATEMATICHE

- CICLO XXVII -

Attitude and Orbit Control Techniques for Spacecraft with Electric Propulsion

Mirko Leomanni, © Ph.D. Thesis, University of Siena, February, 2015.



Contents

Ac	knov	vledger	nents	ix
Li	st of	Acrony	ms	xi
In	trodu	ıction		1
	The	sis orga	nization	2
	List	of publ	ications	3
1	Elec	tric Pro	opulsion Challenges	5
	1.1	Electri	ic propulsion applications	6
		1.1.1	Low Earth orbit missions	6
		1.1.2	Formation flying missions	7
		1.1.3	Geostationary missions	7
	1.2	EP-bas	sed spacecraft control techniques	9
		1.2.1	Autonomous station-keeping	9
		1.2.2	Low-thrust rendezvous and docking	10
		1.2.3	Precise attitude control	12
2	Spa	cecraft	Dynamic Model	15
	2.1	Refere	ence frames and notation	15
	2.2	Orbit (dynamics	16
		2.2.1	Aspherical gravity acceleration	19
		2.2.2	Atmospheric drag acceleration	20
		2.2.3	Luni-solar acceleration	22
		2.2.4	Solar radiation pressure acceleration	22
		2.2.5	Thrust acceleration	23
	2.3	Attitud	de dynamics	24
		2.3.1	Gravity gradient torque	26
		2.3.2	Aerodynamic torque	27
		2.3.3	Solar radiation pressure torque	27

		2.3.4	Magnetic torque
		2.3.5	Reaction torque
3	Auto	onomo	us Orbit Control 33
	3.1	Proble	m setting
		3.1.1	Reference trajectory
		3.1.2	Orbit control system
	3.2	Station	n-keeping
		3.2.1	Relative orbital element dynamics
		3.2.2	Orbital element feedback
	3.3	Rende	zvous and docking
		3.3.1	Hill-Clohessy-Wiltshire equations
		3.3.2	Optimal control problem
		3.3.3	Laguerre MPC
		3.3.4	Explicit LMPC
4	Prec	rise Atti	itude Control 51
			m setting
		4.1.1	
		4.1.2	Attitude error dynamics
		4.1.3	Attitude control system
	4.2	Minim	um fuel control
		4.2.1	Unperturbed dynamics
		4.2.2	Minimum impulse bit dynamics
		4.2.3	Perturbed dynamics
	4.3	Minim	um switching oscillations
		4.3.1	Single-input problem
		4.3.2	Multi-input problem
		4.3.3	Numerical examples
	4.4	Minim	um switching control
		4.4.1	Tracking of limit cycle solutions with prescribed period 71
		4.4.2	Tracking of limit cycle solutions with prescribed period and phase 72
		4.4.3	Feasibility with respect to minimum impulse bit
	4.5	MPC-b	pased control scheme
		4.5.1	Problem formulation
		4.5.2	Mixed integer linear program
5	Auto	onomoi	us Navigation 83
	5.1		determination
		5.1.1	Propagation
		5.1.2	Measurement update
	5.2		de determination
		5.2.1	Propagation
		5.2.2	Measurement update
		·-·-	

	5.3	Relativ	ve navigation	,
		5.3.1	Measurement model	,
		5.3.2	Propagation)
		5.3.3	Measurement update)
6	Nun	nerical	Simulations 93	;
	6.1	Autono	omous station-keeping with electric propulsion	;
		6.1.1	Reference mission)
		6.1.2	Spacecraft and power system)
		6.1.3	GNC system analysis)
	6.2	Low-th	nrust rendezvous and docking)
		6.2.1	Reference mission)
		6.2.2	LMPC performance	2
		6.2.3	Rendezvous and docking maneuver analysis	7
	6.3	Precise	e attitude control of all-electric spacecraft	
		6.3.1	Reference mission)
		6.3.2	MPC tuning strategy	ŀ
		6.3.3	Attitude control system analysis	7
	6.4	Perfori	mance evaluation of attitude control laws)
		6.4.1	GEO scenario	
		6.4.2	LEO scenario	3
		6.4.3	Time-varying torques	7
7	Con	clusion	s and Future Work 129)
	7.1	Summ	ary of contributions)
	7.2	Discus	sion of the results)
	7.3	Future	e research directions	L
Α	App	endix	133	,
Bi	bliog	raphy	137	,

Acknowledgments

I am greatly indebted to my advisors Prof. Andrea Garulli and Dr. Antonio Giannitrapani, for their invaluable guide throughout these years. The results achieved in this thesis would not have been possible without their support and motivation.

A special thank goes to Fabrizio Scortecci and his group at Aerospazio Tecnologie, for their long-standing collaboration in the field of space technology.

I wish to extend my gratitude to Profs. Stephen Gabriel and Eric Rogers, and to the people at Mars Space Ltd, with whom I had the pleasure to work during my stay at the University of Southampton.

I also thank Profs. Gianni Bianchini and Francesco Vasca, for agreeing to be in the committee of this thesis.

My deepest gratitude goes to my parents Giuseppe and Milena, for their encouragement and advice in all these years, and to Alessandra, for her patience and support during the time of my studies.

Siena February 16, 2015

List of Acronyms

ACS Attitude Control System
CGT Cold Gas Thruster
ECI Earth Centered Inertial
EKF Extended Kalman Filter
EP Electric Propulsion
ESA European Space Agency

FEEP Field-Effect Electrostatic Propulsion

GEO Geostationary Orbit

GNC Guidance, Navigation and Control

GPS Global Positioning System
HET Hall Effect Thruster

HTET High Temperature Electrothermal Thruster

LEO Low Earth Orbit

LMPC Laguerre Model Predictive Control

LoS Line of Sight

LQR Linear Quadratic Regulator
LVLH Local-Vertical Local-Horizontal
MILP Mixed Integer Linear Program
MPC Model Predictive Control
MS Minimum Switching

NASA National Aeronautics and Space Administration

NSSK North/South Station-Keeping

OL Open-Loop

PCU Power Conditioning Unit
PPT Pulsed Plasma Thruster
PWPF Pulse Width Pulse Frequency

QP Quadratic Program SK Station-Keeping

Introduction

In recent years, all the major spacecraft manufacturers have presented development programs for innovative satellite platforms based on electric propulsion (EP), motivated by the high fuel efficiency of this technology. In particular, it has been demonstrated that the application of EP for orbit raising and station-keeping (SK) operations enables significant propellant mass savings, and therefore reduced satellite launch and servicing costs, compared to traditional chemical propulsion. Electric propulsion technologies have also been proposed for precise attitude control, as an alternative to momentum exchange devices. The potential benefits of EP in this application area are an increased system reliability and a higher pointing stability, as it allows to remove rotating and vibrating parts from the attitude control subsystem.

With respect to chemical propulsion, EP systems can deliver a much smaller thrust. Consequently, they are required to operate steadily for long time periods. Moreover, unlike momentum exchange devices, EP-based reaction control systems must be operated in on/off mode, and restrictions on the duration and number of switching cycles have to be taken into account. One important implication of these aspects is that the conventional approach to spacecraft operation, relying on large delta-v impulses for orbit control, and proportional control torques for attitude stabilization, can no longer be used. Instead, efficient guidance, navigation and control (GNC) techniques, accounting for the peculiarities of the EP technology, have to be devised.

The contribution of the thesis in this context is threefold. First, a control law is derived for autonomous station-keeping of low Earth orbiting spacecraft, by suitably adopting orbital element feedback methods to deal with the presence of atmospheric drag, and the lack of radial thrust. Then, the rendezvous and docking problem is considered. By exploiting a low complexity parametrization of the control sequence, an explicit model predictive control (MPC) scheme is derived, able to enforce the constraints required for safe maneuvering, without incurring an excessive computational cost. Finally, the problem of maintaining the attitude of a spacecraft aligned to a reference orientation, with minimum fuel consumption and minimum switching frequency of the actuators, is studied. Two solutions are presented for this problem. An event-based control law, extending the scalar fuel/switch-optimal solution to the multivariable case, and an MPC scheme, based on the real-time optimization of the actuator switching cycles, as well as the overall fuel consumption.

The application of the proposed control techniques, within an autonomous guidance, navigation and control system, is demonstrated on a realistic simulation environment, including state-of-the-art mathematical models of the attitude and orbital perturbations.

Thesis organization

The thesis is organized as follows.

In **Chapter 1**, several emerging applications of EP technologies are discussed, with particular emphasis on the most common classes of Earth-orbiting spacecraft. An overview of the challenges that need to be faced in the development of efficient control techniques tailored to the considered applications is provided, along with a summary of the way such problems are addressed in the literature and in this thesis.

In **Chapter 2**, some fundamental astrodynamic concepts are recalled, and an accurate mathematical model describing the translational and rotational motion of the spacecraft, as well as the most relevant orbital and attitude perturbations, is presented. This model provides a testbed for validating all the techniques proposed in the thesis.

In **Chapter 3**, the problem of maintaining a desired low altitude orbit, and that of performing autonomous rendezvous and docking, are addressed for spacecraft with low-thrust propulsion. A hybrid continuous/impulsive control law, able to keep the spacecraft close to the reference orbit, without the need for radial thrust, is derived for the first problem. An explicit MPC scheme, based on a polynomial approximation of the control sequence, is developed for the second one.

In **Chapter 4**, the problem of maintaining the attitude of a spacecraft aligned to a given orientation, while minimizing both the propellant consumption and the on/off switching frequency of the actuators, in the presence of persisting disturbances, is studied. The classical single-axis solution is extended to the coupled multivariable case, and an event-based feedback control law is derived to steer the attitude of the spacecraft towards the provided multivariable solution. An MPC scheme, based on real-time optimization of the fuel and switching costs, is also presented, which can be applied to more general system dynamics.

In **Chapter 5**, an orbit determination filter, an attitude determination filter and a relative navigation filter, based on extended Kalman filtering (EKF) techniques, are developed, in order to assess the performance of the proposed control techniques within a closed-loop GNC system.

In **Chapter 6**, the results of numerical simulations are reported and analyzed to evaluate the performance of the proposed control techniques, and the applicability of the considered EP technologies to different types of space missions.

In **Chapter 7**, the main contributions of this thesis are summarized and discussed, and future directions of research are outlined.

List of publications

Most of the material in this thesis is based on published or submitted articles. The contribution on orbit control is inspired by the following papers:

- [O1] M. Leomanni, E. Rogers, S.B. Gabriel, "Explicit Model Predictive Control Approach for Low-Thrust Spacecraft Proximity Operations" *Journal of Guidance, Control and Dynamics*, Vol. 37, No. 6, 2014, pp. 1780–1790.
- [O2] S. Gabriel, E. Rogers, M. Leomanni, "The Applicability of Pulsed Plasma Thrusters to Rendezvous and Docking of Cubesats", 33rd International Electric Propulsion Conference, 2013.
- [O3] A. Garulli, A. Giannitrapani, M. Leomanni, F. Scortecci, "Autonomous Low Earth Orbit Station-Keeping with Electric Propulsion", *AIAA Journal of Guidance, Control and Dynamics*, Vol. 34, No. 6, 2011, pp. 1683-1693.
- [O4] A. Garulli, A. Giannitrapani, M. Leomanni, F. Scortecci, "Autonomous LEO Station-Keeping with a Hybrid Continuous/Impulsive Electric Propulsion System", *32nd International Electric Propulsion Conference*, 2011.
- [O5] N. Ceccarelli, A. Garulli, A. Giannitrapani, M. Leomanni, F. Scortecci, "Spacecraft Localization via Angle Measurements for Autonomous Navigation in Deep Space Missions", 17th Symposium on Automatic Control in Aerospace, 2007.

The attitude control techniques are presented in the following papers:

- [A1] A. Garulli , A. Giannitrapani, M. Leomanni, "Minimum Switching Control for Systems of Coupled Double Integrators", submitted to *Automatica*.
- [A2] M. Leomanni, A. Garulli, A. Giannitrapani, F. Scortecci, "All-Electric Spacecraft Precision Pointing using Model Predictive Control", *Journal of Guidance, Control and Dynamics*, Vol. 38, No. 1, 2015, pp. 161–168.
- [A3] A. Garulli , A. Giannitrapani, M. Leomanni, "Minimum Switching Limit Cycle Oscillations for Systems of Coupled Double Integrators", 53rd IEEE Conference on Decision and Control, 2014.
- [A4] M. Leomanni, A. Garulli, A. Giannitrapani, F. Scortecci, "An MPC-based Attitude Control System for All-Electric Spacecraft with On/Off Actuators", *52nd IEEE Conference on Decision and Control*, 2013.
- [A5] M. Leomanni, A. Garulli, A. Giannitrapani, F. Scortecci, "Precise Attitude Control of All-Electric GEO Spacecraft using Xenon Microthrusters", *33rd International Electric Propulsion Conference*, 2013.

Electric Propulsion Challenges

Electric propulsion represents nowadays a solid established technology which can provide benefits over a large number of spacecraft missions and enable new challenging applications. An EP system is a set of devices arranged so as to convert electrical power from the spacecraft power system into kinetic energy of a propellant jet engine exhaust. This can be accomplished by using different types of engine architectures. Operation can be steady or pulsed; the propellant can be a noble gas or even a solid; gas acceleration can be electrothermal, electrostatic or electromagnetic. Of the many proposed architectures, the one having reached a considerable level of maturity can be classified as: resistojets, arcjets, Hall thrusters (HET), ion engines, pulsed plasma thrusters (PPT), field-effect electrostatic propulsion (FEEP), colloidal ion thrusters, and magnetoplasmadynamic thrusters, see e.g. [93]. The common paradigm of all these architectures is to provide a higher specific impulse, i.e. a higher exhaust speed and therefore an increased fuel efficiency, when compared to conventional chemical engines. This is especially relevant because, for a given amount of propellant, the fuel efficiency ultimately dictates the lifetime and the capability of a space mission. On the other hand, the thrust generated by EP systems is usually much weaker than that of chemical engines, due to the limited power level that can be supplied to accelerate the propellant. Consequently, EP systems are required to operate continuously for a significant period of the overall mission time.

The design of guidance, navigation and control schemes for spacecraft driven by low-thrust EP systems is complicated by the fact that the relatively simple impulsive control schemes available for high-thrust chemical systems can no longer be applied. Instead, a continuous thrusting strategy, accounting for the peculiarities of the actuators, is required, which often poses a difficult design challenge. In fact, analytical or approximate solutions to low-thrust problems exist only for some special applications, but the general continuous-thrust problem requires full numerical integration of each initial condition and thrust profile, as well as the consideration of input amplitude constraints. For this reason, during the last few years a considerable research effort has been directed towards the development of low-thrust GNC techniques, with particular focus on two fundamental aspects: the open-loop optimization of low-thrust trajectories, see e.g. [10, 26], and the derivation of closed-loop control laws, see e.g. [75, 85, 87]. In this thesis, the interest lies mainly on the second aspect. More specifically, the attitude and orbit control problems will be addressed for some representative classes of Earth orbit missions that could greatly benefit from the application of an EP system, within an autonomous GNC scheme.

1.1 Electric propulsion applications

In this section, several emerging applications the EP technology are discussed, with particular emphasis on the most common classes of space missions, i.e. low Earth orbit, formation flying and geostationary missions.

1.1.1 Low Earth orbit missions

While the use of EP technologies for station-keeping and orbit transfer of commercial geostationary satellites and deep space missions is widely discussed in the literature (e.g. [90, 91, 103, 105, 114]), relatively few studies have been proposed for low Earth orbit (LEO) missions. Nevertheless, the capability of EP to compensate for atmospheric drag effects over several thousands of hours, together with the reduced propellant mass consumption, allows for accurate LEO station-keeping operations over sufficiently long duration missions, as opposed to traditional chemical technologies. In this regard, the GOCE mission represents a breakthrough in space technology [21, 100]. Some recent studies have been focused on drag free spacecraft operations [12, 44]. Besides these challenging scientific missions, there are other classes of LEO missions that have a potential commercial interest, like Earth observation by means of small and cheap satellites. In [42], for instance, it is shown that high resolution Earth imaging can be achieved, by using small optical instruments, from altitudes of about 300 km and below. Moreover, recent ESA studies on remote sensing applications have clearly demonstrated that operating an EP system on a LEO orbit can give a net advantage in terms of both reduced launch mass and enhanced payload performance [25].

Miniaturized HET thrusters are particularly well-suited for LEO station-keeping when compared to other classes of EP devices, thanks to the lower input power required. For a given amount of available power, the thrust produced is nearly two times the one of gridded ion thrusters and about four times the one provided by FEEP thrusters [116]. For this reason, HET technologies enable a reduced orbit altitude for the benefit of low-budget Earth observation missions, which could find a mass-market e.g. in cartographic applications. In addition to HET, different types of low-power EP technologies, such as resistojet thrusters, can be considered as a secondary propulsion system to counteract LEO perturbations other than drag, in order to trade-off the thrust efficiency with the limitations imposed by the spacecraft mass and available power [51, 102].

Besides the choice of a specific thruster architecture, it is worth remarking that maintaining a given low Earth orbit traditionally requires frequent, ground-based control actions, in order to compensate for atmospheric drag and other disturbing forces. For small, low cost satellites, ground-in-the-loop control can be a dominant element of both cost and risk [73]. The combined use of EP technologies and autonomous GNC techniques provides an effective way to address this issue. In particular, the application of a suitable EP system allows for significant savings of propellant mass and a consequent increase of the spacecraft lifetime. On the other hand, autonomous station-keeping provides reduced operational costs, as demonstrated by the UoSat-12 [45], Demeter [78] and PRISMA [31] missions.

1.1.2 Formation flying missions

Spacecraft formation flying is an enabling technology for many present and future space missions. Examples include technology demonstrators like PRISMA [54] and PROBA-3 [127], the space interferometer DARWIN [46], the Mars sample return scientific mission [95], and on-orbit servicing projects such as the Automated Transfer Vehicle [106] or the orbital life extension vehicle SMART-OLEV [68]. In most current applications, active control of the formation is achieved by using cold-gas thrusters, which represent the simplest type of chemical propulsion. This type of thruster technology, however, is affected by a very low specific impulse and by constraints on the minimum impulse capability, which limit both the number of formation keeping/reconfiguration maneuvers that can be performed and the achievable control accuracy.

Another application of recent interest is represented by formation flying of picosatellite class spacecraft that follow the cubesat standard [48, 92]. This standard limits single-unit (1U) cubesats to 1.5 kg and a 10 cm cube, and three-unit (3U) cubesats to 4 kg and a 30 cm x 10 cm x 10 cm envelope. Despite their limited size, the increasing capabilities of cubesats, together with the relatively inexpensive development and flight costs, create the opportunity for these spacecraft to serve as a low-cost and reliable access to space for companies and universities. Cubesat specifications does not currently allow for integration of high-pressure tanks onboard the spacecraft due to the risk of rupture or misfire. Therefore, propulsion technologies other than cold-gas thrusters may be required for orbit control of future cubesat formations.

Motivated by the problems outlined above, EP technologies, such as FEEP and PPT thrusters, have been considered as a possible alternative to cold-gas systems for spacecraft formation flying [39, 110]. In terms of flight readiness, however, few EP systems are currently available. This is especially true for cubesat spacecraft, due to the severe volume, power and mass constraints imposed to these platforms. This thesis addresses the suitability of a miniaturized PPT called PPTCUP, which is very close to being flight qualified, having recently completed one million shots in a life testing campaign [24]. Using a set of typical requirements for rendezvous and docking operations, the applicability of a cluster of these thrusters is investigated from a control perspective, i.e. whether the thrusters can meet the control requirements, given the constraints on controllability, mass, number of engines and their location. Notice that the very low thrust level delivered by PPT engines leads to severe limitations in the performance achievable by the control system. Therefore, a constrained control design is required, where both input and state constraints have to be enforced.

1.1.3 Geostationary missions

Spacecraft systems using geostationary orbit (GEO) have a high commercial and strategic value, thanks to the ability to provide continuous coverage over a wide geographical area. The vast majority of communication satellites and an increasing number of Earth observa-

tion missions are in fact designed to operate in GEO, see e.g. [32, 74]. The recent growth of satellite communication services has imposed severe restrictions on the size and the number of free GEO locations. At the same time, many scientific organizations have suffered from budget limitations. As a consequence, commercial platforms with shared communications and observation payloads have received considerable interest, providing a consistent, dependable and affordable access to space [3, 125]. In order to meet the mission requirements imposed by multiple payloads, satellite operators are demanded to constantly upgrade the performance of their systems.

All-electric spacecraft seems to be one of the most promising concepts to enable high performance GEO missions at a substantially decreased cost compared to conventional platforms. This is achieved through the considerable reduction of spacecraft mass and size allowed by the use of high efficiency electric propulsion systems for orbit raising and SK operations [43, 55]. Several solutions, however, are still under investigation to provide precise attitude control of all-electric spacecraft, as required for operation of advanced communications and Earth observation payloads. Momentum exchange devices, such as ball-bearing reaction wheels and control moment gyros, are by far the most commonly used actuators. Their main advantage is that a minimum amount of fuel is needed to counteract attitude perturbations, in particular when momentum dumping is conveniently performed during SK maneuvers, using EP thrusters [9]. Nevertheless, micro-vibrations associated with wheel unbalance, zero-rate crossing and friction instabilities represent serious drawbacks of these systems, especially for applications that require high pointing accuracy. In addition, momentum exchange devices tend to be costly, massive, and require a large amount of power. As an attempt to solve some of these issues, a wheel-less EP-based attitude control system (ACS) has been proposed in [77] for the Geo-Oculus mission. A solar pressure attitude control concept has been successfully experimented on a class of GEO satellites, but there exist several practical implementation problems to be solved prior to a large-scale application of this advanced technique [138]. The potential application of teflon PPT has been investigated in [70], and later demonstrated in space by the NASA mission EO-1 [143].

Reaction control systems based on xenon thrusters, sharing a common propellant bus with the primary EP system, represent another viable solution, that could be beneficial to reduce development complexity and costs of all-electric spacecraft [102]. Cold-gas and electrothermal microthrusters, with thrust levels scaled down to the millinewton range, are particularly well suited for precise attitude control, providing very small impulse bits and a minimal excitation of the spacecraft flexible modes. While the poor fuel efficiency of cold-gas systems restricts their use to operational environment where the delta-v budget is considerably low, the foreseen availability of very high temperature resistojet and hollow cathode technologies, providing a substantial increase of the thruster specific impulse, raises the possibility of replacing existing momentum exchange devices with simple, reliable and relatively inexpensive electrothermal microtrusters [23, 53, 80]. However, these thrusters are typically operated in on/off mode, and restrictions on the duration and number of thruster firings have to be accounted for in the design of the attitude control scheme.

1.2 EP-based spacecraft control techniques

Having discussed the benefit of EP technologies for some representative classes of space missions, this section gives an overview of the challenges that need to be faced in order to develop efficient control techniques tailored to these applications, and briefly describes the contribution of this thesis.

1.2.1 Autonomous station-keeping

Station-keeping refers to the process of controlling a spacecraft so as to maintain the nominal orbit. In general, SK can be either ground-based, which means that a sequence of control commands is transmitted from the ground segment to the spacecraft, or autonomous, which indicates that the command is evaluated onboard the spacecraft. For high-performance spacecraft, ground-in-the-loop orbit control can be the dominant factor of both mission cost and risk, requiring frequent ground commands to be uplinked to the spacecraft. Conversely, autonomous SK can provide reduced mission costs as well as increased reliability, thanks to the possibility of executing the corrective actions in real time. In particular, the orbit becomes fully predictable so that the position of the spacecraft at all future times is known in advance within the accuracy of the control system.

Motivated by these advantages, autonomous SK systems have been developed since the early 90's [30, 73], and their potential application to spacecraft constellations has been investigated in terms of absolute orbit control of each vehicle in the formation [136]. However, these systems are based on traditional impulsive control schemes, which are not directly applicable to low-thrust problems, mainly because in such problems the magnitude of the orbital perturbations can approach the thrust level delivered by the propulsion system, as in the case of small EP-based LEO missions.

Up to now, relatively few studies have been focused on developing autonomous SK strategies for low-thrust spacecraft. Nevertheless, the theoretical framework for solving such type of problems is already well-established in the formation flying literature. More specifically, continuous control laws based on orbital element feedback [58, 120] provide an effective way to evaluate the thrust command to EP-based orbit maintenance systems. In fact, the SK problem can be recast as the problem of tracking the orbital elements of a virtual spacecraft [29, 50], and therefore it is not conceptually different from the rendezvous problem, for which the above-mentioned orbital element control laws have been originally developed. The orbit of the virtual spacecraft, however, is affected only by the Earth's gravitational field, so that non-conservative perturbations have to be considered in the design. In particular, atmospheric drag can have a significant impact on the achievable control performance for LEO missions. In such applications, the design of a real-time control scheme can be quite challenging, due to the difficulty in obtaining a reliable estimate of the atmospheric density.

Another important requirement for autonomous SK is the availability of an autonomous navigation system, providing absolute position and velocity information. For autonomous navigation in LEO, a GPS receiver, coupled with an orbit determination filter, represents a viable solution [73].

In this thesis, a GNC system is proposed for autonomous SK of LEO spacecraft driven by low-thrust propulsion. A simple control law is derived in Section 3.2, by suitably adopting orbital element feedback methods to account for the large amount of atmospheric drag acting on the spacecraft. The navigation solution is based on an EKF that estimates the position and velocity of the spacecraft from GPS measurements, as described in Section 5.1. The simulation of a LEO mission is discussed in Section 6.1, to validate the proposed GNC solution and evaluate the performance of a propulsion system consisting of HET and resistojet thrusters.

1.2.2 Low-thrust rendezvous and docking

The development of guidance and control techniques for spacecraft formation flying is the subject of significant research efforts, due to the key role of such problems in many present and future space missions. Of particular interest in this field is the optimization of low-thrust rendezvous and docking trajectories, motivated by the application of miniaturized or high-efficiency propulsion technologies [57, 97]. When two or more spacecraft in a formation are required to operate in close proximity, these trajectories must be safe with respect to collisions and other possible anomalies [17]. This generally leads to complex trajectory optimization problems, subject to both thrust magnitude and path constraints. Due to the increasing level of autonomy of future space applications, it is critical to efficiently compute the solution to these problems and to design a control system tracking the resulting trajectories [135, 140]. To this purpose, efficient guidance and control algorithms have to be devised.

Two approaches can be considered for the rendezvous and docking trajectory tracking problem. The first method separates the vehicle guidance and control problems into an outer guidance loop and an inner control loop. The inner loop computes the control command required to follow the trajectories generated by the outer loop. A wide variety of optimization techniques, based on either direct or indirect methods, have been proposed in the literature for the guidance loop, see e.g. [40, 59, 61, 112, 115], whereas robust feedback techniques are typically used in the control loop [49, 109, 126]. The second method uses an integrated approach wherein both the guidance and control problems are solved simultaneously. In this case, modern control design techniques, such as receding horizon control [16, 33, 62, 83, 111], can be applied.

Cascade control architectures can be advantageous over integrated approaches because much of the complexity of the tracking problem is transferred into the guidance problem, which is usually solved at a slower sampling rate compared to that of the control loop. For the same reason, however, cascade control may be less indicated for applications with a high degree of autonomy, for which the guidance and control problem should ideally be solved in real-time. In order to tackle this issue, a number of different approaches have been investigated, see e.g. [11, 79, 83].

In particular, model predictive control, based on computing the optimal control sequence over a finite number of future sampling instances, under a receding horizon strategy, is becoming increasingly attractive, thanks to the possibility of systematically handling thrust magnitude and path constraints in the design. An effective MPC design requires the control horizon to be comparable with the settling time of the controlled process. Therefore, a long control horizon is needed to guarantee adequate performance in low-thrust problems. During close proximity operations, this is coupled with the requirement to use a small discretization step, to avoid the violation of path constraints between discrete time samples. In such cases, the main drawback of MPC is the need to solve a trajectory optimization problem with a large number of decision variables at each time sample, which may make this method too computationally intensive to be implemented on-line on low-power spacecraft processors [118]. A possible way to overcome this last difficulty is to parameterize the control sequence with a set of Laguerre functions, where the poles of these functions are used to reflect the time scale of the control system, see e.g. [133]. In this setting, which belongs to the family of direct optimization methods, the number of decision variables can be made significantly smaller than the length of the control horizon, while path constraints can still be enforced over a sufficiently fine discretization grid.

Another important factor, which may prevent the implementation of the MPC design methods discussed so far, is the requirement to embed a control solver with guaranteed runtime on board the spacecraft. This requirement can be avoided by solving the control problem explicitly, i.e. by finding off-line a feedback control law defined on a partition of the state space [8]. However, this is generally feasible only for low-dimensional problems, due to the worst-case exponential growth of the number of regions in the partition with the length of the control sequence [134]. An alternative approach, based on the explicit solution of a quadratically constrained linear quadratic regulator (LQR) problem, has been recently developed in [79] for a rendezvous problem with thrust constraints, which confirms the need for computationally efficient feedback control methods specifically tailored to the considered application area.

The contribution of the thesis in this context is twofold. First, a low-complexity MPC scheme is developed for the low-thrust rendezvous and docking problem. In the derivation of the control algorithm, the trajectory optimization problem is reformulated by parameterizing the control sequence by a set of Laguerre functions, which allows a long control horizon to be considered without using a large number of decision variables. Then, an explicit solution is derived by exploiting this new algorithm in combination with multiparametric programming techniques, to enable a trade-off between feasibility and performance of the guidance and control system. Since the proposed approach does not require online optimization, it is especially suitable for implementation on board small spacecraft with limited computational capabilities. The derivation of the control scheme is discussed in Section 3.3. A navigation scheme based on the EKF, which can be used in combination with the proposed control law, within an autonomous GNC scheme, is presented in Section 5.3. A detailed simulation-based assessment of the performance achievable under the considered design is given in Section 6.2 for a cubesat mission with electric propulsion, in comparison to standard MPC and linear quadratic regulator (LQR) techniques.

1.2.3 Precise attitude control

Pointing accuracy is a key requirement in communication satellites and Earth observation missions. Attitude control systems must guarantee tracking of the reference attitude, while accounting for mission performance indexes such as fuel consumption and actuator wear. Electric propulsion systems, with thrust levels scaled down to the millinewton range, are particularly well suited for precise attitude control. Because these systems work by expelling propellant mass, the minimization of the fuel consumption is the primary requirement in the design of an EP-based attitude control system. Moreover, thrusters are commonly operated in on/off mode, so that restrictions on the minimum duration of their firings (the so-called minimum impulse bit) and the number of on/off cycles which can be delivered have to be taken into account. In particular, the number of switching cycles has an impact on both the lifetime of the thrusters, due to valve wear, and on the specific impulse performance, which is affected by transient effects on the actuator dynamics. Thus, in order to maximize the performance and the reliability of a thruster control system, attitude control maneuvers should ideally be made by few long firings rather than several short firings [19, 28]. Such considerations typically lead to oscillating behaviors of the closed-loop system [104]. Since the amplitude of these oscillations is inversely proportional to the thruster switching frequency, achieving precise attitude control while retaining an acceptable number of on/off cycles is a challenging problem.

A wide variety of control techniques have been proposed in the literature for three-axis attitude stabilization with on on/off actuators, including phase plane methods [35], LQR with pulse-width pulse-frequency modulators (PWPF) [1, 76], mixed-integer linear programming (MILP) control allocation [36], and MPC [63, 132]. While many of these techniques do explicitly account for fuel minimization and impulse duration constraints, they do not address the problem of minimizing the actuator switching frequency, which has a key impact on the performance of the thrusters and hence of the mission itself.

A suitable approach consists in the formulation of an optimal control problem, in which both the number of input transitions and the control accuracy requirements are explicitly taken into account, so that to minimize the average switching frequency of the actuators, while guaranteeing adequate pointing performance. For the single-axis attitude stabilization problem, with the error dynamics approximated by a perturbed double integrator [35], the limit cycle corresponding to the fuel/switch-optimal solution has been fully characterised since long time [38, 60, 69]. However, for multivariable systems, the minimum switching control problem with state constraints becomes very challenging even for simple dynamics, such as the case of coupled double integrators. In fact, the optimization methods available for generic switching systems [14, 113, 123, 141] turn out to be of limited help, due to the combinatorial explosion of the number of state-space modes with the dimension of the system, and the presence of a nonconvex objective function. This has motivated a thorough theoretical analysis of the minimum switching problem for systems of coupled integrators of arbitrary dimension, subject to a constant disturbance term and controlled by on/off actuators.

In this thesis, the minimum switching control problem is addressed from a novel perspective, based on the extension to the multivariable case of the classical fuel/switch-optimal limit cycle solution [52]. The first contribution is a suboptimal solution providing an analytic upper bound to the minimum switching frequency required to satisfy given (polytopic) state constraints. By exploiting the further degrees of freedom provided by the relative phases of the periodic trajectories of each state variable along the limit cycle, a less conservative upper bound is found, through the numerical solution of a static optimization problem. Moreover, a feedback control law is derived, in order to track the trajectories corresponding to the solutions previously obtained. The last contribution is an MPC scheme based on the real-time optimization of the number of thruster firings and the fuel consumption [81, 82], which can be applied, to a certain extent, to a more general class of dynamical systems.

The derivation of the attitude control laws is described in Chapter 4. A relative navigation EKF, which provides the attitude, angular rate, and disturbance torque estimates required by these control laws, is presented in Section 5.2. The applicability of the MPC scheme, in combination with a reaction control system based on electrothermal microthrusters, is demonstrated through numerical simulations of an all-electric GEO mission in Section 6.3. The performance of the proposed MPC and minimum switching control laws is compared in Section 6.4.

Spacecraft Dynamic Model

In this chapter, some fundamental astrodynamic concepts are recalled and an accurate model describing the translational and rotational motion of the spacecraft is presented. The material of this chapter is mainly based on [131] and [137].

2.1 Reference frames and notation

Three reference frames are used in this thesis. The first one is the Earth Centered Inertial (ECI) frame. The other two coordinate systems are moving frames centered at the spacecraft center of mass. The so called Local-Vertical/Local-Horizontal (LVLH) frame is oriented so that its Z axis is aligned with the nadir vector, the Y axis is normal to the orbital plane and the X axis completes an orthogonal right handed frame. The X, Y and Z directions of the LVLH frame are referred to as the along-track, cross-track and radial directions respectively, and the motion along the XY or XZ planes is referred as the horizonal-plane or in-plane motion, respectively. The spacecraft body frame is aligned with the the principal axes of inertia of the spacecraft. The three reference frames are illustrated in Fig. 2.1

Vector and matrices are denoted by boldface symbols, where 1 denotes a vector whose components are all equal to 1, the identity matrix is denoted by I and the symbol 0 denotes the null matrix or vector of compatible dimensions. Diag and blockdiag denote the diagonal and block-diagonal matrices, the symbol $\oplus^n \mathbf{A}$ denotes a block-diagonal matrix with n diagonal blocks, each equal to \mathbf{A} and $\|\mathbf{x}\|_1$, $\|\mathbf{x}\|$ and $\|\mathbf{x}\|_{\infty}$ indicate the 1-norm, 2-norm and ∞ -norm of a vector $\mathbf{x} \in \mathbb{R}^n$, respectively. The orientation of reference frame B with respect to a reference frame A is represented by the rotation matrix \mathbf{R}_{AB} or, equivalently, by the quaternion $\mathbf{q}_{AB} = [q_{AB}, \vec{\mathbf{q}}_{AB}^T]^T$, where q_{AB} and $\vec{\mathbf{q}}_{AB}$ are termed the scalar part and the vector part of the quaternion. The cross-product operation is denoted by the symbol \times , and the quaternion multiplication operation \circ is defined by

$$\mathbf{q}_{AC} = \mathbf{q}_{BC} \circ \mathbf{q}_{AB} = \begin{bmatrix} q_{BC}q_{AB} - \vec{\mathbf{q}}_{BC}^T \vec{\mathbf{q}}_{AB} \\ q_{BC}\vec{\mathbf{q}}_{AB} + q_{AB}\vec{\mathbf{q}}_{BC} - \vec{\mathbf{q}}_{BC} \times \vec{\mathbf{q}}_{AB} \end{bmatrix},$$

which corresponds to the sequence of rotations $\mathbf{R}_{AC} = \mathbf{R}_{BC} \mathbf{R}_{AB}$. Small rotations are represented in quaternion form as $\mathbf{q}(\delta \boldsymbol{\theta}) = [1\,,\,\,\delta \boldsymbol{\theta}^T\!/2]^T$, where $\delta \boldsymbol{\theta}$ is a three-dimensional rotation vector, and the skew-symmetric matrix constructed from a vector $\boldsymbol{\omega}$ is denoted by $\boldsymbol{\omega}^{\times}$.

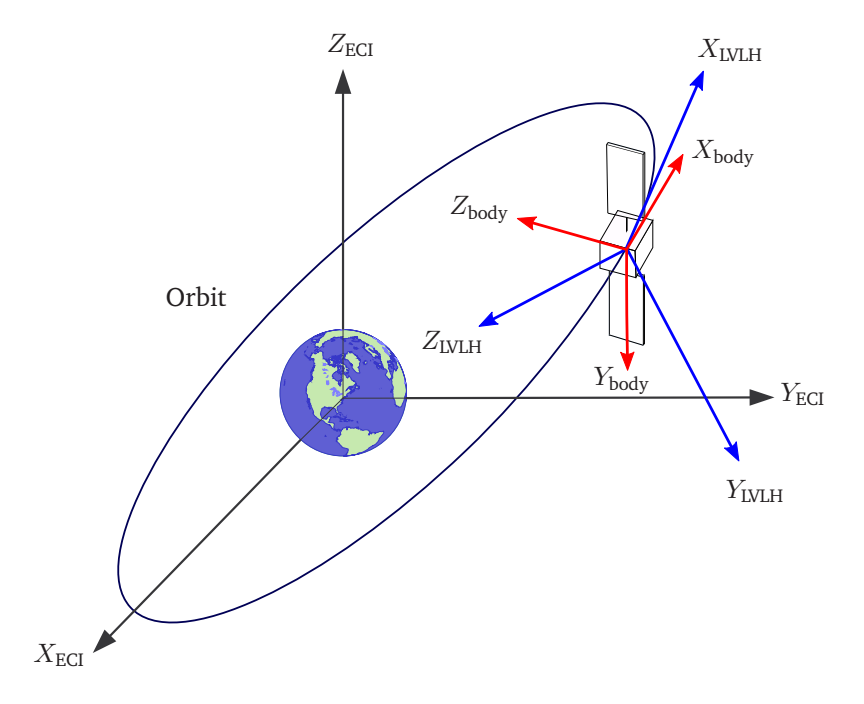


Figure 2.1: Reference frames.

2.2 Orbit dynamics

In the ECI frame, the force g exerted by a spherical central body with uniform density on a spacecraft of mass m located at position ${\bf r}$ relative to the central body is given by the Newton's law of universal gravitation

$$\mathbf{g} = -\frac{\mu \, m}{r^3} \, \mathbf{r},\tag{2.1}$$

where $\mathbf{r} = [r_x, r_y, r_z]^T$ indicates the spacecraft position vector, $r = ||\mathbf{r}||$, and μ is the gravitational parameter of the central body. Ideally, \mathbf{g} is the only force acting on the spacecraft and the point-mass dynamics are easily obtained from (2.1) as

$$\ddot{\mathbf{r}} = -\frac{\mu}{r^3} \,\mathbf{r}.\tag{2.2}$$

The solution to (2.2) is the so-called Keplerian orbit, which takes the form of an ellipse or a conic section, depending on the initial condition $\mathbf{r}(t_0)$, $\dot{\mathbf{r}}(t_0)$. In this thesis, the focus is on Earth orbiting spacecraft, i.e. spacecraft moving along elliptic orbits. The trajectory of a spacecraft in an elliptic Keplerian orbit can be parameterized by a vector of six orbital

elements $\mathbf{o} = [a, e, i, \Omega, \omega, \nu]^T$ through the following mapping

$$a = \mu r / (2\mu - r \|\dot{\mathbf{r}}\|^{2})$$

$$e = \|\epsilon\|$$

$$i = \arccos(h_{z}/\|\mathbf{h}\|)$$

$$\Omega = \kappa_{1} \arccos(n_{x}/\|\mathbf{n}\|) + (1 - \kappa_{1})\pi$$

$$\omega = \kappa_{2} \arccos\left(\frac{\mathbf{n}^{T} \epsilon}{\|\mathbf{n}\|\|\epsilon\|}\right) + (1 - \kappa_{2})\pi$$

$$\nu = \kappa_{3} \arccos\left(\frac{\epsilon^{T} \mathbf{r}}{\|\epsilon\|r}\right) + (1 - \kappa_{3})\pi,$$
(2.3)

where

$$\mathbf{h} = [h_x, h_y, h_z]^T = \mathbf{r} \times \dot{\mathbf{r}}$$

$$\mathbf{n} = [n_x, n_y, n_z]^T = [0, 0, 1]^T \times \mathbf{h}$$

$$\boldsymbol{\epsilon} = [\epsilon_x, \epsilon_y, \epsilon_z]^T = (\dot{\mathbf{r}} \times \mathbf{h})/\mu - \mathbf{r}/r$$

and $\kappa_1 = \operatorname{sgn}(n_y)$, $\kappa_2 = \operatorname{sgn}(e_z)$, $\kappa_3 = \operatorname{sgn}(\mathbf{r}^T\dot{\mathbf{r}})$ ensure that the corresponding angles are expressed in the correct quadrant. The inverse mapping is given by

$$\mathbf{r} = \mathbf{R}_{OI} \begin{bmatrix} \frac{p \cos(\nu)}{1 + e \cos(\nu)} \\ \frac{p \sin(\nu)}{1 + e \cos(\nu)} \\ 0 \end{bmatrix}$$

$$\dot{\mathbf{r}} = \mathbf{R}_{OI} \begin{bmatrix} -\sin(\nu)\sqrt{\mu/p} \\ (e + \cos(\nu))\sqrt{\mu/p} \\ 0 \end{bmatrix},$$
(2.4)

where $p=a(1-e^2)$ and the matrix ${\bf R}_{OI}$ represents the orientation of the orbital plane in the inertial frame, given by

$$\mathbf{R}_{OI} = \begin{pmatrix} c(\Omega)c(\omega) - s(\Omega)c(i)s(\omega) & -c(\Omega)s(\omega) - s(\Omega)c(i)c(\omega) & s(\Omega)s(i) \\ s(\Omega)c(\omega) + c(\Omega)c(i)s(\omega) & -s(\Omega)s(\omega) + c(\Omega)c(i)c(\omega) & -c(\Omega)s(i) \\ s(i)s(\omega) & s(i)c(\omega) & c(i) \end{pmatrix},$$

where c and s denote the cosine and sine functions, respectively.

Orbital elements are particularly useful because they provide a clear physical insight of the orbital motion. The semi-major axis a and eccentricity e define the shape of the orbit. The inclination i, longitude of the ascending node Ω and argument of perigee ω define the orientation of the orbital plane with respect to the inertial frame. The true anomaly ν defines the instantaneous angle at which the spacecraft is located relative to the ascending node position, as illustrated in Fig. 2.2. Notice that the mapping (2.3) is singular for circular (e=0) and equatorial (i=0) orbits. These singularities, however, can be avoided by adopting an alternative parametrization. For near-circular, inclined orbits, the eccentricity and argument of perigee are commonly replaced by the eccentricity vector $\mathbf{e} = [e\cos(\omega), e\sin(\omega)]^T$.

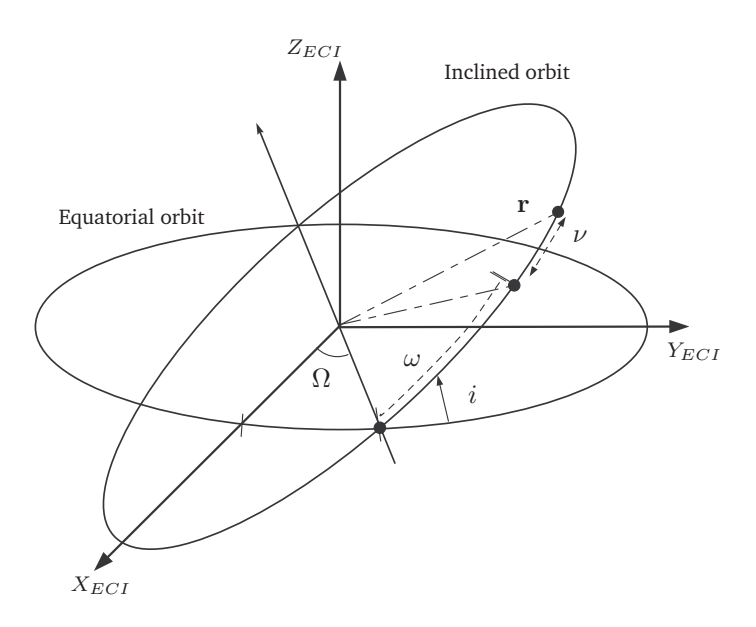


Figure 2.2: Classical orbital elements.

Moreover the true anomaly ν is replaced by the true argument of latitude

$$\nu_l = \omega + \nu = \operatorname{sgn}(r_z) \operatorname{arccos}\left(\frac{\mathbf{n}^T \mathbf{r}}{\|\mathbf{n}\|r}\right) + (1 - \operatorname{sgn}(r_z))\pi, \tag{2.5}$$

resulting in the nonsingular representation $\mathbf{o} = [a, \mathbf{e}^T, i, \Omega, \nu_l]^T$. For equatorial orbits, the globally nonsingular representation provided by the equinoctial elements $\mathbf{o} = [a, \mathbf{e}^T, \mathbf{i}^T, \lambda_t]^T$ is commonly used. In this parametrization, the quantity $\mathbf{i} = [\tan(i/2)\sin(\Omega), \tan(i/2)\cos(\Omega)]^T$ is termed the inclination vector, the eccentricity vector is defined as $\mathbf{e} = [e\cos(\varpi), e\sin(\varpi)]^T$, where

$$\varpi = \omega + \Omega = \operatorname{sgn}(\epsilon_y)\operatorname{arccos}(\epsilon_x/\|\epsilon\|) + (1 - \operatorname{sgn}(\epsilon_y))\pi,$$

and the true longitude λ_t is given by

$$\lambda_t = \omega + \Omega + \nu = \operatorname{sgn}(r_y)\operatorname{arccos}(r_x/r) + (1 - \operatorname{sgn}(r_y))\pi. \tag{2.6}$$

Notice that ν in (2.3), ν_l in (2.5) and λ_t in (2.6) are time-varying parameters (360 deg per orbit), whereas the other elements are constants for Keplerian orbits.

Keplerian orbits represent a fairly simple approximation of the real motion of a spacecraft, due to the presence of a number of perturbations which are not modeled by (2.2). In order to produce a more accurate description of the spacecraft motion, one possibility is to use the so-called Cowell's formulation, which consists of directly adding the perturbing accelerations to (2.2). Then,

$$\ddot{\mathbf{r}} = -\frac{\mu}{r^3}\,\mathbf{r} + \mathbf{a}_p,\tag{2.7}$$

where \mathbf{a}_p denotes the perturbing acceleration. In this thesis, the acceleration vector \mathbf{a}_p accounts for the most significant environmental disturbances \mathbf{a}_e and the acceleration due to

the thrust \mathbf{a}_t produced by the spacecraft propulsion system. The environmental disturbances include the aspherical gravity acceleration \mathbf{a}_g , the atmospheric drag acceleration \mathbf{a}_d , the luni-solar gravity acceleration \mathbf{a}_l , and the solar radiation pressure acceleration \mathbf{a}_r . The perturbing term is therefore given by

$$\mathbf{a}_{p} = \mathbf{a}_{e} + \mathbf{a}_{t} = \mathbf{a}_{q} + \mathbf{a}_{d} + \mathbf{a}_{l} + \mathbf{a}_{r} + \mathbf{a}_{t}.$$
 (2.8)

It is worth remarking that the mapping (2.3) (and the ones presented thereafter) can still be applied to the trajectories resulting from the solution of (2.7), but in this case all the orbital elements are time-varying. More precisely, the variation of the orbital elements with respect to their ideal counterpart is related to the type and the size of the perturbation. As an example, the qualitative impact of the environmental disturbance on the orbital elements is reported in Table 2.1 for spacecraft in low Earth orbits (LEO) [72]. In this table, secular means "which progressively increases with time", whereas periodic perturbations have periods that range from days to years. The effects of the perturbations are referred as "small" if their magnitude is below 1-2 km per month, "moderate" if their magnitude is in the order of 10 km per month and "big" if their magnitude is above few kilometers per day. The mathematical model of the perturbing accelerations is described next.

	Secul	ar	Periodic	
	Big	Small	Moderate	Small
Aspherical Earth	Ω , ω	-	e	i, Ω, ω
Atmosperic drag	a, e	i	-	Ω , ω
Luni-solar effects	-	-	-	a, e, i, Ω, ω

Table 2.1: Impact of environmental disturbances on orbit elements in LEO.

2.2.1 Aspherical gravity acceleration

The gravitational field of the Earth can be decomposed into the ideal contribution (2.1) and an additional contribution due to the asphericity of the central body, which is typically the dominant source of perturbation in LEO. According to the joint gravity model (JGM) developed by NASA, OT, OSU, CNES [41], the disturbance acceleration due to the asphericity of the Earth can be expressed as the gradient of the following spherical potential function

$$U(r,\varphi,\lambda) = \frac{\mu}{r} \left(1 + \sum_{n=2}^{n_{\text{max}}} \sum_{m=0}^{n} \left(\frac{R}{r} \right)^n P_{nm}(\sin(\varphi)) \left(C_{nm} \cos(m\lambda) + S_{nm} \sin(m\lambda) \right) \right),$$

where R is the Earth radius, φ and λ are the spacecraft geocentric latitude and its East longitude, n_{\max} is the maximum degree of the expansion, C_{nm} and S_{nm} are spherical harmonic coefficients, and $P_{nm}(\sin\varphi)$ indicates the associated Legendre function of degree n and order m. The spacecraft geocentric latitude and its longitude are given by

$$\varphi = \operatorname{atan2}(r_z, \sqrt{r_x^2 + r_y^2})$$

$$\lambda = \alpha - \alpha_q = \operatorname{atan2}(r_y, r_x) - \alpha_q,$$
(2.9)

where α is the spacecraft right ascension and α_g is the right ascension of the Greenwich meridian. The associated Legendre functions are given by

$$P_{nm}(\sin(\varphi)) = \frac{(\cos(\varphi))^m}{2^n n!} \frac{\partial^{n+m}}{\partial (\sin(\varphi))^{n+m}} (\sin^2(\varphi) - 1)^n.$$

The coefficients of the harmonics are referred as zonal if m=0, sectorial if m=n or tesseral if $n>m\neq 0$. They are commonly disclosed in the normalized form \bar{C}_{nm} , \bar{S}_{nm} , given by

$$\bar{C}_{nm} = \left[\frac{(n+m)!}{(2n+1)k(n-m)!}\right]^{\frac{1}{2}} C_{nm}$$

$$\bar{S}_{nm} = \left[\frac{(n+m)!}{(2n+1)k(n-m)!} \right]^{\frac{1}{2}} S_{nm},$$

where k = 1 if m = 0 and k = 2 otherwise.

The cartesian components of the disturbance acceleration can be expressed in the ECI frame as

$$a_{x} = \left(\frac{1}{r}\frac{\partial U}{\partial r} - \frac{r_{z}}{r^{2}\sqrt{r_{x}^{2} + r_{y}^{2}}}\frac{\partial U}{\partial \varphi}\right)r_{x} - \left(\frac{1}{r_{x}^{2} + r_{y}^{2}}\frac{\partial U}{\partial \lambda}\right)r_{y}$$

$$a_{y} = \left(\frac{1}{r}\frac{\partial U}{\partial r} - \frac{r_{z}}{r^{2}\sqrt{r_{x}^{2} + r_{y}^{2}}}\frac{\partial U}{\partial \varphi}\right)r_{y} + \left(\frac{1}{r_{x}^{2} + r_{y}^{2}}\frac{\partial U}{\partial \lambda}\right)r_{x}$$

$$a_{z} = \left(\frac{1}{r}\frac{\partial U}{\partial r}\right)r_{z} - \left(\frac{\sqrt{r_{x}^{2} + r_{y}^{2}}}{r^{2}}\frac{\partial U}{\partial \varphi}\right),$$

$$(2.10)$$

resulting in the disturbance vector $\mathbf{a}_g = [a_x, a_y, a_z]^T$. The partial derivatives of the potential U with respect to r, φ and λ are given by

$$\frac{\partial U}{\partial r} = -\frac{\mu}{r^2} \sum_{n=2}^{n_{\text{max}}} \sum_{m=0}^{n} \left(\frac{R}{r}\right)^n (n+1) P_{nm}(\sin\varphi) \left(C_{nm}\cos(m\lambda) + S_{nm}\sin(m\lambda)\right)
\frac{\partial U}{\partial \lambda} = \frac{\mu}{r} \sum_{n=2}^{n_{\text{max}}} \sum_{m=0}^{n} \left(\frac{R}{r}\right)^n \left(P_{n,m+1}(\sin\varphi) - m\tan(\varphi)P_{nm}(\sin\varphi)\right)
(C_{nm}\cos(m\lambda) + S_{nm}\sin(m\lambda))
\frac{\partial U}{\partial \varphi} = \frac{\mu}{r} \sum_{n=2}^{n_{\text{max}}} \sum_{m=0}^{n} \left(\frac{R}{r}\right)^n m P_{nm}(\sin\varphi) \left(S_{nm}\cos(m\lambda) - C_{nm}\sin(m\lambda)\right).$$

2.2.2 Atmospheric drag acceleration

For spacecraft orbiting at low altitudes, atmospheric drag can be a significant perturbation, causing a spiraling motion towards the Earth that shortens the orbital lifetime. Atmospheric drag at orbital altitudes is caused by the collisions of gas molecules with the satellite. Since energy is lost in this process due to friction, drag represents a nonconservative perturbation.

2.2. Orbit dynamics 21

In most space applications, it is reasonable to neglect the aerodynamic lift and consider the cross-sectional area of the spacecraft for the calculation of the atmospheric drag disturbance. In this case, the disturbance acceleration can be modeled as

$$\mathbf{a}_d = -\frac{1}{2} C_D \, \rho_a \, \frac{A}{m} \, \mathbf{v} \| \mathbf{v} \|, \tag{2.11}$$

where ρ_a expresses the atmospheric density, C_D is the drag coefficient, A denotes the cross-sectional area and \mathbf{v} indicates the velocity of the spacecraft relative to the atmosphere. The vector \mathbf{v} is given by

$$\mathbf{v} = \dot{\mathbf{r}} - \boldsymbol{\omega}_{\ominus} \times \mathbf{r},$$

where $\omega_{\ominus} = [0, 0, \omega_{\ominus}]^T$ is the vector constructed from the Earth's rotation rate ω_{\ominus} about the Z axis of the ECI frame.

An accurate atmospheric model is essential for the calculation of the disturbance acceleration due to drag. In this thesis, the atmospheric density value is obtained from the *Jacchia-71* model [67], which accounts for several factors including solar and geomagnetic activity, seasonal variations, and orbit altitude. The model relies on a polynomial approximation of the density profile based on numeric tables obtained from empirical observations, and complies with the ECSS standard for space environment [41]. A typical atmospheric density profile is reported as a function of the orbit altitude in Fig. 2.3.

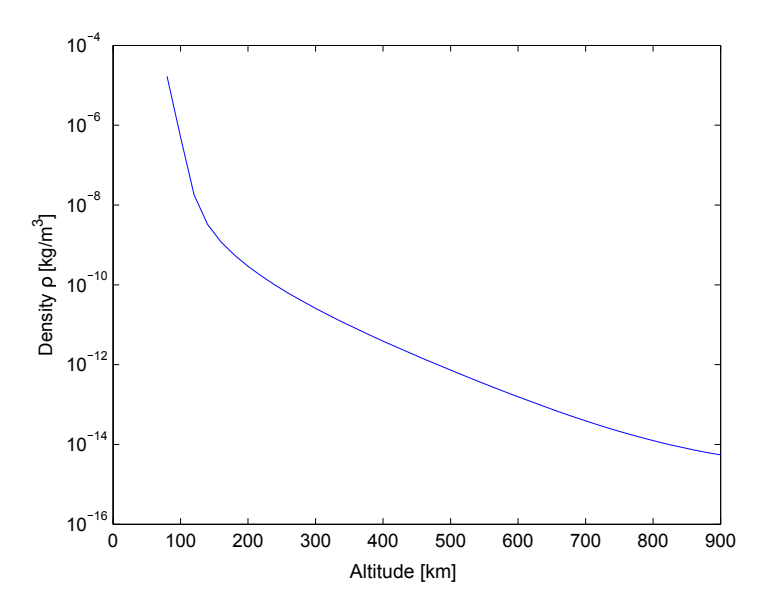


Figure 2.3: Typical atmospheric density profile.

2.2.3 Luni-solar acceleration

The perturbation effects due to the gravity of the Sun and the Moon, which are commonly referred as third-body perturbations, become noticeable when the effect of atmospheric drag begins to diminish (say above 800 km). Because the cause of third-body perturbations is the gravitational attraction, the resulting forces are conservative. In order to evaluate the luni-solar disturbance acceleration, one needs to know the position of the the Sun and the Moon in the ECI frame. In this thesis, the Moon position vector $\mathbf{r}_{\circlearrowleft}$ and the Sun position vector $\mathbf{r}_{\circlearrowleft}$ are obtained through precise ephemerides. Modeling the Sun and the Moon as point-masses, the luni-disturbance acceleration turns out to be [2]

$$\mathbf{a}_{l} = \mu_{\mathfrak{P}} \left(\frac{\mathbf{r}_{\diamond \mathfrak{P}}}{\|\mathbf{r}_{\diamond \mathfrak{P}}\|^{3}} - \frac{\mathbf{r}_{\mathfrak{P}}}{\|\mathbf{r}_{\diamond \mathfrak{P}}\|^{3}} \right) + \mu_{\mathfrak{C}} \left(\frac{\mathbf{r}_{\diamond \mathfrak{C}}}{\|\mathbf{r}_{\diamond \mathfrak{C}}\|^{3}} - \frac{\mathbf{r}_{\mathfrak{C}}}{\|\mathbf{r}_{\mathfrak{C}}\|^{3}} \right), \tag{2.12}$$

where $\mu_{\stackrel{\leftrightarrow}{\mathcal{L}}}$ and $\mu_{\mathbb{C}}$ are the gravitational parameters of the Sun and the Moon, respectively, and the vectors from the spacecraft to the Sun $\mathbf{r}_{\diamond\stackrel{\leftrightarrow}{\mathcal{L}}}$ and to the Moon $\mathbf{r}_{\diamond\mathbb{C}}$ are given by

$$\mathbf{r}_{\diamond \circlearrowleft} = \mathbf{r}_{\circlearrowleft} - \mathbf{r}$$
 $\mathbf{r}_{\diamond \circlearrowleft} = \mathbf{r}_{\circlearrowleft} - \mathbf{r}$.

The geometry of the problem is illustrated in Fig. 2.4.

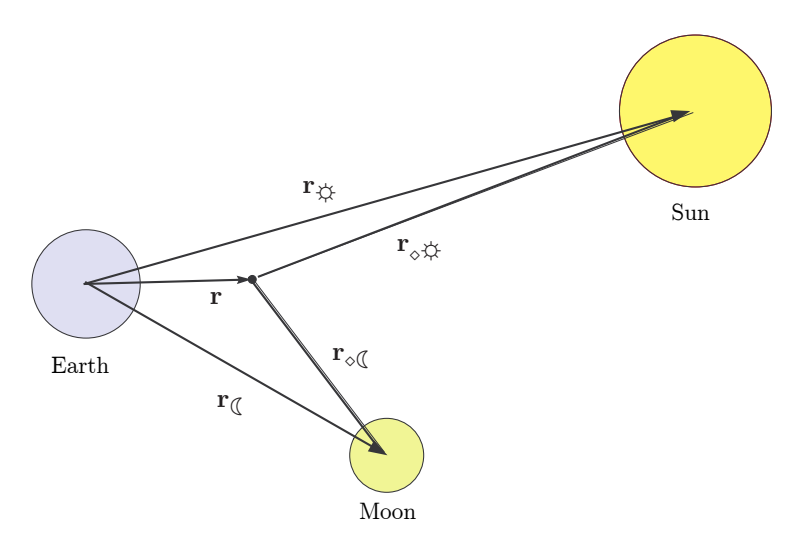


Figure 2.4: Geometry of third-body perturbations.

2.2.4 Solar radiation pressure acceleration

The solar radiation pressure is caused by the absorption or the reflection of photons emitted by the Sun on the spacecraft surface. Like drag, solar radiation pressure is a nonconservative

perturbation, but becomes pronounced at high orbit altitudes. The average value of the pressure generated on a perfectly absorbing planar surface is approximately given by [56]

$$P_r = 4.56 \cdot 10^{-6} \,\text{N/m}^2. \tag{2.13}$$

As long as a point-mass model of the spacecraft is concerned, it is usually reasonable to adopt the so-called *Cannonball model*, where the shape of the satellite is assumed to be a sphere. Under this assumption, the solar radiation disturbance acceleration, which depends on the mass and the properties of the surface exposed to the radiation, is given by

$$\mathbf{a}_r = -s_r P_r C_R \frac{A}{m} \frac{\mathbf{r}_{\diamond \mathfrak{D}}}{\|\mathbf{r}_{\diamond \mathfrak{D}}\|},\tag{2.14}$$

where C_R is the solar radiation pressure coefficient of the spacecraft and s_r is the shadow function, which accounts for the eclipse effects that occur when the Earth passes between the spacecraft and the Sun. The shadow function is defined as follows

$$\begin{cases} s_r = 0 & \text{Satellite in umbra} \\ s_r \in (0,1) & \text{Satellite in penumbra} \\ s_r = 1 & \text{Satellite exposed to radiation.} \end{cases} \tag{2.15}$$

For a detailed derivation of this function, see e.g. [99].

2.2.5 Thrust acceleration

The thrust generated by the spacecraft propulsion system can be considered as a perturbation which may quickly produce a significant effect on the orbit. In general, this perturbation may include disturbance accelerations \mathbf{a}_a due to firing of the attitude control thrusters and control accelerations \mathbf{a}_I generated by the orbit control subsystem. For a spacecraft with multiple engines $i=1,\ldots,n$, the acceleration due to thrust is given by

$$\mathbf{a}_t = \mathbf{a}_a + \mathbf{a}_I = \sum_{i=1}^n \frac{\mathbf{p}_i}{m},\tag{2.16}$$

where \mathbf{p}_i indicates the thrust vector of the *i*-th engine, expressed in the ECI frame, and the contribution \mathbf{a}_a is in general much smaller than \mathbf{a}_I .

According to the Newton's third law of motion, thrust is produced by expelling stored propellant mass. The relation between the magnitude of the thrust vector and the rate of change of the propellant mass for a single thruster is given by

$$\|\mathbf{p}_i\| = -g_0 \, I_{sp_i} \, \dot{m}_i \,, \tag{2.17}$$

where I_{sp_i} and \dot{m}_i denote the specific impulse and the mass flow rate of engine i, respectively, and g_0 indicates the standard gravity. Considering the contributions of all engines, the rate of change of the spacecraft mass is obtained from (2.17) as

$$\dot{m} = -\sum_{i=1}^{n} \frac{\|\mathbf{p}_i\|}{g_0 I_{sp_i}}.$$
(2.18)

The control acceleration a_I is sometimes approximated by the impulsive velocity change

$$\Delta \mathbf{v}_I = \Delta \dot{\mathbf{r}} = \sum_{i=1}^n \Delta \dot{\mathbf{r}}_i, \tag{2.19}$$

where $\Delta \dot{\mathbf{r}}_i$ denotes the velocity change produced by the *i*-th engine. For short impulse durations (say less than few minutes), this approach introduces a small error in the solution to (2.8). When an impulsive maneuver occur, the orbit dynamics (2.7) are updated as follows

$$\mathbf{v}^{\uparrow} = \mathbf{v}^{\downarrow} + \Delta \mathbf{v}_{I},\tag{2.20}$$

where the superscripts \downarrow and \uparrow indicate the time instants immediately preceding and following the maneuver, respectively, and $\mathbf{v}=\dot{\mathbf{r}}$. Moreover, (2.18) is updated according to the well-know Tsiolkovsky rocket equation

$$m^{\uparrow} = m^{\downarrow} \exp\left(-\sum_{i=1}^{n} \frac{\|\Delta \dot{\mathbf{r}}_{i}\|}{g_{0} I_{sp_{i}}}\right). \tag{2.21}$$

2.3 Attitude dynamics

In this thesis, the orientation of the spacecraft body frame with respect to the ECI frame is represented by the attitude quaternion \mathbf{q}_{IB} or, equivalently, by the rotation matrix \mathbf{R}_{IB} , while the angular rate of the body frame with respect to ECI frame, expressed in the body frame, is denoted by $\boldsymbol{\omega}$.

In order to describe the evolution of the spacecraft attitude, the time derivatives of both the quaternion and the angular velocity of the spacecraft are required. The time derivative of the quaternion \mathbf{q}_{IB} is defined as

$$\dot{\mathbf{q}}_{IB} = \lim_{\Delta t \to 0} \frac{\mathbf{q}_{IB}(t + \Delta t) - \mathbf{q}_{IB}(t)}{\Delta t},\tag{2.22}$$

where Δt is a vanishing time interval. From the definition of the quaternion product operation, one has that

$$\mathbf{q}_{IB}(\Delta t + t) = \mathbf{q}(\delta \boldsymbol{\theta}) \circ \mathbf{q}_{IB}(t), \tag{2.23}$$

where $\delta \theta = \delta \theta(\Delta t)$ and the small rotation $\mathbf{q}(\delta \theta)$ is given by

$$\mathbf{q}(\delta\boldsymbol{\theta}) = \begin{bmatrix} 1\\0 \end{bmatrix} + \begin{bmatrix} 0\\\delta\boldsymbol{\theta}/2 \end{bmatrix}. \tag{2.24}$$

Substituting (2.24) into (2.23), one obtains

$$\mathbf{q}(\delta\boldsymbol{\theta}) \circ \mathbf{q}_{IB} = \mathbf{q}_{IB} + \frac{1}{2} \begin{bmatrix} 0 \\ \delta\boldsymbol{\theta} \end{bmatrix} \circ \mathbf{q}_{IB}.$$
 (2.25)

Using (2.23) and (2.25) in (2.22), and observing that

$$\lim_{\Delta t \to 0} \frac{\delta \boldsymbol{\theta}}{\Delta t} = \boldsymbol{\omega},$$

one gets the final expression for the quaternion kinematic equation

$$\dot{\mathbf{q}}_{IB} = \lim_{\Delta t \to 0} \frac{1}{\Delta t} \begin{pmatrix} \frac{1}{2} \begin{bmatrix} 0 \\ \delta \boldsymbol{\theta} \end{bmatrix} \circ \mathbf{q}_{IB} \end{pmatrix} = \frac{1}{2} \begin{bmatrix} 0 \\ \omega \end{bmatrix} \circ \mathbf{q}_{IB}. \tag{2.26}$$

The angular rate dynamics are derived under the following assumptions: (i) the space-craft can be modeled as rigid body and (ii) the spacecraft does not contain rotating parts, such as momentum exchange devices. Whereas the first one is rather common in the attitude control literature, the second one follows from the electric propulsion design considered in this thesis, in which torques are generated by using thrust. Under these assumptions, the time derivative of the spacecraft angular momentum corresponds to the external torque acting on the spacecraft, according to the Euler's second law

$$\dot{\boldsymbol{v}}_I = \boldsymbol{\tau}_I, \tag{2.27}$$

where v_I and τ_I denote the angular momentum and the external torque, respectively, in the ECI frame. Equation (2.27) can be expressed in the spacecraft body frame as

$$\dot{\boldsymbol{v}} = \boldsymbol{\tau} - \boldsymbol{\omega} \times \boldsymbol{v},\tag{2.28}$$

where $v = \mathbf{R}_{IB} \ v_I$, $\tau = \mathbf{R}_{IB} \boldsymbol{\tau}_I$. The relation between the angular momentum and the spacecraft angular rate is simply given by

$$v = \mathbf{I}_M \, \boldsymbol{\omega},\tag{2.29}$$

where I_M indicates the spacecraft inertia matrix, expressed in the body frame. For a rigid body with variable mass, the time derivative of (2.29) is

$$\dot{\boldsymbol{v}} = \mathbf{I}_M \, \dot{\boldsymbol{\omega}} + \dot{\mathbf{I}}_M \, \boldsymbol{\omega}. \tag{2.30}$$

Combining (2.28)-(2.30) and rearranging terms, the angular rate dynamics can be expressed as

$$\dot{\omega} = \mathbf{I}_{M}^{-1} \left(\tau - \omega \times \mathbf{I}_{M} \ \omega - \dot{\mathbf{I}}_{M} \ \omega \right). \tag{2.31}$$

In this thesis, the external torque vector τ accounts for the most significative environmental disturbances, as well as the torque generated by the spacecraft propulsion system. The environmental disturbances include the gravity gradient torque τ_g , the aerodynamic torque τ_d , the solar radiation pressure torque τ_r and the magnetic torque τ_m . The torque produced by the propulsion system is denoted by τ_t . Therefore, the vector τ is given by

$$\tau = \tau_g + \tau_d + \tau_r + \tau_m + \tau_t, \tag{2.32}$$

where all contributions are expressed in the spacecraft body frame. Some qualitative aspects of the environmental disturbance components are reported in Table 2.2. Their mathematical model is reported next, along with the one of the reaction torque from propulsive maneuvers.

Source	Dependence on orbit radius	Dominant
Aerodynamic	e^{-kr}	Below $\sim 500~\mathrm{km}$
Gravity gradient	$1/r^3$	$\sim 500-35000~\mathrm{km}$
Magnetic	$1/r^3$	$\sim 500-35000~\mathrm{km}$
Solar radiation	Independent	Above 36000 km

Table 2.2: Effects of environmental torques

2.3.1 Gravity gradient torque

Every nonsymmetric object of finite dimension orbiting the Earth is subject to a gravity gradient torque caused by the variation of the gravitational force along the object; there would be no gravity gradient in a uniform gravity field. A number of mathematical models are available in the literature to describe this phenomenon, ranging from simple models where the Earth is assumed to be spherical to more complex models taking into account the oblateness of the planet. For most applications, it is sufficient to consider a spherical Earth approximation.

The gravitational force $d \mathbf{g}_i$ acting on an infinitesimal element of mass $d m_i$, located at position \mathbf{r}_i with respect to the Earth's center, is given by

$$\mathbf{dg}_i = -\frac{\mu \, \mathbf{d}m_i}{\|\mathbf{r}_i\|^3} \mathbf{r}_i,$$

where μ is the gravitational parameter of the Earth. The torque due to the force dg_i , located at position \mathbf{r}'_i with respect to the spacecraft center of mass, is obtained as

$$d\tau_i = \mathbf{r}_i' \times d\mathbf{g}_i. \tag{2.33}$$

By integrating (2.33) over the entire spacecraft body and expressing the resulting torque in the body frame, after some manipulations, one obtains the total gravity gradient contribution

$$\boldsymbol{\tau}_g = \frac{3\mu}{r^5} \left[\mathbf{r}_B \times \mathbf{I}_M \, \mathbf{r}_B \right], \tag{2.34}$$

where $\mathbf{r}_B = \mathbf{R}_{IB}\mathbf{r}$. The gravity gradient torque has the following properties:

- The torque is always orthogonal to the the gravity force;
- The torque is inversely proportional to the cubic distance between the spacecraft and Earth;
- The torque vanishes for spherically symmetric objects, for which the inertia matrix is a diagonal matrix with equal entries.

To make an example, the gravity gradient torque acting on a small spacecraft at an orbit altitude of about 400 km is in the order of 10^{-5} Nm.

2.3.2 Aerodynamic torque

The aerodynamic torque is often the dominant source of attitude perturbations at orbit altitudes below 400 km. The force producing this torque arises from the interaction of the atmospheric particles with the spacecraft surfaces, where the interaction can be modeled as a purely elastic collision. Under the assumption that surface the spacecraft can be decomposed into a set of planar surfaces, the aerodynamic torque contribution τ_i of a surface element A_i , with outward unit normal \vec{n}_i and a lever arm \mathbf{r}_i , is well approximated by

$$\boldsymbol{\tau}_{i} = \mathbf{r}_{i} \times -\frac{1}{2} C_{D} \rho_{a} \left(\vec{\mathbf{n}_{i}}^{T} \mathbf{v}_{B}\right) \mathbf{v}_{B} A_{i}, \tag{2.35}$$

where $\mathbf{v}_B = \mathbf{R}_{IB}\mathbf{v}$ indicates the velocity of the spacecraft relative to the atmosphere, expressed in the body frame, and the remaining quantities are defined in Section 2.2.2. The lever arm \mathbf{r}_i in (2.35) corresponds to the position of the center of pressure of the *i*-th surface with respect to the spacecraft center of mass, as illustrated in Fig. 2.5. For planar surfaces with no shadowing effects, the center of pressure is located at the geometric center of the surface.

Notice that a contribution τ_i is produced only when the unit normal of the *i*-th surface element satisfies $\vec{\mathbf{n}}_i^T \mathbf{v}_B > 0$, because the second term in (2.35), denoting the aerodynamic force, must point in the opposite direction of the velocity vector \mathbf{v}_B by definition. Hence, the total aerodynamic torque on the spacecraft can be expressed as

$$\boldsymbol{\tau}_d = \sum_{V} \boldsymbol{\tau}_i,\tag{2.36}$$

where $V=\{i: \vec{\mathbf{n}}_i^T\mathbf{v}_B>0\}$. Moreover, one can define the center of pressure of the spacecraft as the vector \mathbf{r}_{cp} satisfying

$$\mathbf{r}_{cn} \times m \, \mathbf{R}_{IB} \, \mathbf{a}_d = \boldsymbol{\tau}_d,$$

where a_d is given by (2.11). In practice, the magnitude of the aerodynamic torque at an altitude of about 400 km can be in the order of 10^{-4} Nm.

2.3.3 Solar radiation pressure torque

The solar radiation pressure torque is largely independent from the orbit altitude and hence becomes dominant in high-altitude orbits and interplanetary spaces. The *Cannonball model* described in Section 2.2.4 provides a reasonable approximation of the force acting on the spacecraft center of mass due to the solar radiation. However, it is in general not suitable for the evaluation of the corresponding torque, because the forces from the interaction of the solar radiation with the individual surface elements of the spacecraft are not modeled. A more accurate model is presented next, which can be used for the evaluation of both the solar radiation force and the resulting torque in most applications.

The force on a surface element can be adequately modeled by considering that the incident radiation can be in part absorbed, in part specularly reflected and in part diffusely

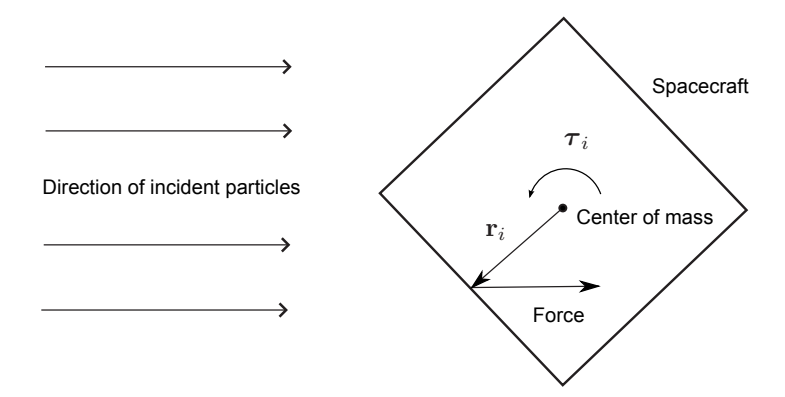


Figure 2.5: Geometric model for the calculation of the aerodynamic torque.

reflected, depending on the physical properties of the surface. Under the assumption that the surface of the spacecraft can be decomposed into a set of planar surfaces, the force \mathbf{f}_i^{abs} due to the portion of radiation which is absorbed on a surface element A_i , with outward unit normal $\vec{\mathbf{n}}_i$, is given by

$$\mathbf{f}_i^{abs} = -P_r C_a \cos(\gamma_i) \,\vec{\mathbf{s}} \, A_i, \tag{2.37}$$

where P_r is given by (2.13), $\vec{\mathbf{s}} = \mathbf{R}_{IB}(\mathbf{r}_{\diamond \stackrel{\sim}{\mathcal{N}}}/\|\mathbf{r}_{\diamond \stackrel{\sim}{\mathcal{N}}}\|)$ is the unit vector from the spacecraft to the Sun, $\gamma_i = \arccos(\vec{\mathbf{n}}_i \cdot \vec{\mathbf{s}})$ is the angle between this vector and the surface unit normal $\vec{\mathbf{n}}_i$, and C_a is the absorption coefficient of the surface. Moreover, the force \mathbf{f}_i^{ref} due to specular reflection is given by

$$\mathbf{f}_{i}^{ref} = -2P_{r} C_{s} \cos^{2}(\gamma_{i}) \, \vec{\mathbf{n}} A_{i},$$
 (2.38)

where C_s is the specular reflection coefficient of the surface. Finally, the contribution \mathbf{f}_i^{dif} from diffuse reflection can be expressed as

$$\mathbf{f}_{i}^{dif} = -P_{r} C_{d} \left(\frac{2}{3} \cos(\gamma_{i}) \, \vec{\mathbf{n}} + \cos(\gamma_{i}) \, \vec{\mathbf{s}} \right) A_{i}, \tag{2.39}$$

where C_d is the diffuse reflection coefficient of the surface. Notice that the absorption, specular reflection and specular diffusion coefficients must satisfy the physical constraint $C_a + C_s + C_d = 1$. The graphical interpretation of these components is reported in Fig. 2.6.

When $\cos(\gamma_i)$ is negative in (2.37), (2.38) and (2.39), the surface element A_i is not illuminated and therefore it is not subject to solar radiation forces. Moreover, the shadow function s_r in (2.15), modeling the solar eclipse effects, has to be taken into account. Considering these factors, the total force acting on the spacecraft can be expressed as

$$\mathbf{f}_r = s_r \sum_{S} \mathbf{f}_i^{abs} + \mathbf{f}_i^{ref} + \mathbf{f}_i^{dif}, \qquad (2.40)$$

where $S = \{i : \cos(\gamma_i) > 0\}$. The corresponding torque is given by

$$\boldsymbol{\tau}_r = s_r \sum_{S} \mathbf{r}_i \times \left(\mathbf{f}_i^{abs} + \mathbf{f}_i^{ref} + \mathbf{f}_i^{dif} \right), \tag{2.41}$$

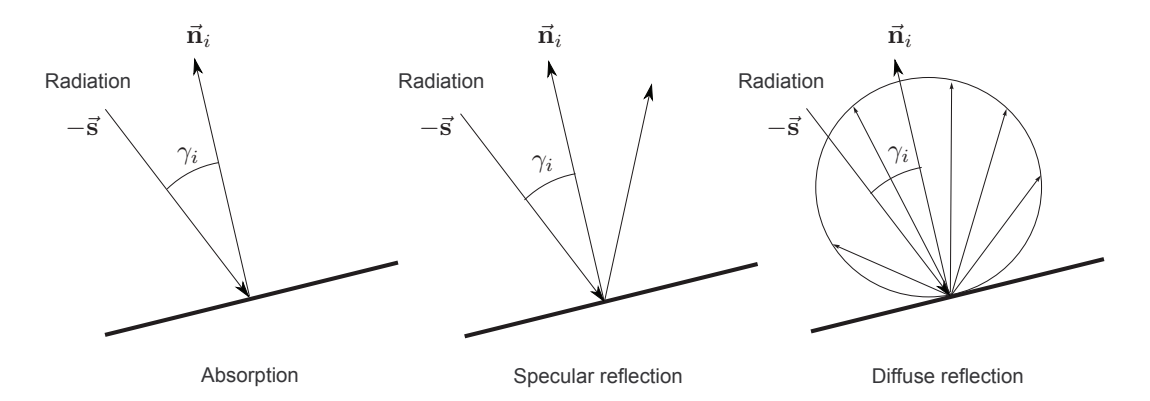


Figure 2.6: Absorption, specular reflection and diffuse reflection of solar radiation.

where the centre of pressure \mathbf{r}_i of the *i*-th surface element is defined in Section 2.3.2. From (2.40)-(2.41), one can define the center of solar pressure of the spacecraft as the vector \mathbf{r}_{csp} satisfying

$$\mathbf{r}_{csp} \times \mathbf{f}_r = \boldsymbol{\tau}_r.$$

The torque generated by the solar radiation pressure on a medium-size spacecraft is typically in the order of 10^{-6} Nm.

2.3.4 Magnetic torque

The magnetic disturbance torque, arising from the interaction of the residual magnetic dipole of the spacecraft with the Earth's magnetic field, can be the dominant attitude perturbation for spacecraft in low Earth orbits. The instantaneous value of the magnetic torque is given by

$$\tau_m = \mathbf{m} \times \mathbf{b},\tag{2.42}$$

where m denotes the total magnetic dipole of the spacecraft and b indicates the geomagnetic field. According to the international geomagnetic reference field (IGRF) model [6], the geomagnetic field can be expressed as the gradient of the following spherical potential function

$$V(r,\vartheta,\lambda) = R \sum_{n=1}^{n_{\text{max}}} \sum_{m=0}^{n} \left(\frac{R}{r}\right)^{(n+1)} (\bar{G}_{nm}\cos(m\lambda) + \bar{H}_{nm}\sin(m\lambda)) \bar{P}_{nm}(\cos(\vartheta)),$$

where \bar{G}_{nm} and \bar{H}_{nm} are the normalized Gauss coefficients of the spherical harmonics, $\vartheta=\pi/2-\varphi$, $\bar{P}_{nm}(\cos\varphi)$ denotes the Schmidt semi-normalized associated Legendre function of degree n and order m, and the remaining symbols are defined in Section 2.2.1. Because the coefficients \bar{G}_{nm} and \bar{H}_{nm} are time varying, they are periodically updated based on data from space observations.

The components of the geomagnetic field in the spherical coordinate frame are given by

$$b_{r} = -\frac{\partial V}{\partial r} = \sum_{n=1}^{n_{\text{max}}} \sum_{m=0}^{n} \left(\frac{R}{r}\right)^{(n+2)} (n+1) \left(\bar{G}_{nm}\cos(m\lambda) + \bar{H}_{nm}\sin(m\lambda)\right) \bar{P}_{nm}\left(\cos(\vartheta)\right)$$

$$b_{\vartheta} = -\frac{1}{r} \frac{\partial V}{\partial \vartheta} = -\sum_{n=1}^{n_{\text{max}}} \sum_{m=0}^{n} \left(\frac{R}{r}\right)^{(n+2)} \left(\bar{G}_{nm}\cos(m\lambda) + \bar{H}_{nm}\sin(m\lambda)\right) \frac{\partial \bar{P}_{nm}\left(\cos(\vartheta)\right)}{\partial \vartheta}$$

$$b_{\lambda} = \frac{-1}{\sin\vartheta} \frac{\partial V}{\partial \lambda} = \frac{-1}{\sin\vartheta} \sum_{n=1}^{n_{\text{max}}} \sum_{m=0}^{n} \left(\frac{R}{r}\right)^{(n+2)} m \left(\bar{H}_{nm}\sin(m\lambda) - \bar{G}_{nm}\cos(m\lambda)\right) \bar{P}_{nm}\left(\cos(\vartheta)\right).$$

By using simple coordinate transformations, the geomagnetic field vector can be expressed in the ECI frame as

$$\mathbf{b}_{I} = \begin{bmatrix} (b_{r}\cos(\varphi) + b_{\vartheta}\sin(\varphi))\cos(\alpha) - b_{\lambda}\sin(\alpha) \\ (b_{r}\cos(\varphi) + b_{\vartheta}\sin(\varphi))\sin(\alpha) + b_{\lambda}\cos(\alpha) \\ (b_{r}\sin(\varphi) - b_{\vartheta}\cos(\varphi)) \end{bmatrix}, \tag{2.43}$$

where α and φ are given by (2.9). The magnetic vector field at an altitude of 300 km is depicted in Figure 2.7. In order to evaluate the disturbance torque (2.42), the geomagnetic field vector (2.43) is expressed in the body frame as

$$\mathbf{b} = \mathbf{R}_{IB}\mathbf{b}_{I}.$$

For a spacecraft in LEO with magnetic moment of 0.1 At·m², the magnetic torque is in the order of 10^{-5} Nm.

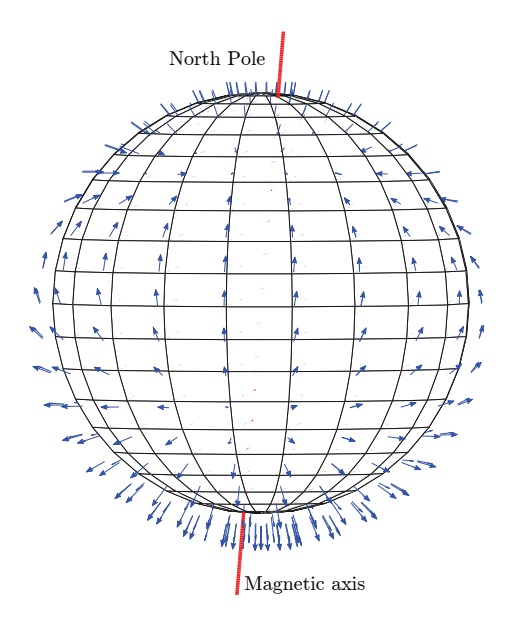


Figure 2.7: Magnetic vector field.

2.3.5 Reaction torque

Reaction torques are produced by the spacecraft propulsion system whenever the thrust vector of the engines is not aligned with the spacecraft center of mass. In general, reaction torques may include disturbance torques $\boldsymbol{\tau}_o$ due to misalignment of the orbit control thrusters and attitude control torques $\boldsymbol{\tau}_u$ provided by the reaction control subsystem to orientate the spacecraft. For a spacecraft with multiple engines $i=1,\ldots,n$, the reaction torque is given by

$$\boldsymbol{\tau}_t = \boldsymbol{\tau}_o + \boldsymbol{\tau}_u = \sum_{i=1}^n \mathbf{r}_i' \times \mathbf{t}_i, \tag{2.44}$$

where \mathbf{r}'_i indicates the position of the *i*-th engine relative to the spacecraft center of mass and \mathbf{t}_i is the corresponding thrust vector.

Because reaction torques are generated by mass-expulsion devices, the rate of change of the spacecraft mass (2.18) must be taken into account. Moreover, a variable mass implies a time-varying inertia-matrix. In general, the rate of change of the inertia matrix $\dot{\mathbf{I}}_M$ is difficult to model and represents a minor contribution in (2.30). Therefore, it can be treated as a small perturbation to be rejected by the attitude control system. Finally, notice that the reaction torque (2.44) and the thrust acceleration (2.16) are coupled by the following relationship

$$\mathbf{p}_i = \mathbf{R}_{IB}^T \mathbf{t}_i.$$

In most practical applications, a different set of actuators is employed for orbit and attitude control, so that the coupling effects are weak and can't be exploited for control purposes. Instead, torques due to operation of the orbit control system are treated as perturbations to be rejected by the attitude control system, and vice versa. For this reason, the attitude and orbit control problems are addressed separately in the following chapters.

Autonomous Orbit Control

In this chapter, two orbit control problems are addressed for spacecraft in near-circular orbits. The first is that of maintaining a desired orbit in the presence of a large amount of atmospheric drag, as required for autonomous station-keeping of LEO satellites with electric propulsion. A Lyapunov-based control law, able to keep the spacecraft close to the reference orbit, without the need for thrust along the radial axis of the LVLH frame, is derived for this problem.

The second problem is that of autonomous rendezvous and docking between two space-craft with low-thrust propulsion. In this case, an important requirement is to enforce a given set of constraints on the input and the state, without incurring an excessive computational cost. An explicit MPC scheme, based on a polynomial parametrization of the control sequence, is developed to this purpose.

The material in this chapter is mainly based on [50] and [83].

3.1 Problem setting

Autonomous orbit control techniques aim at controlling the spacecraft position relative to a given reference trajectory, without ground operator intervention. The orbit control problem can be cast in terms of relative orbital elements or relative cartesian coordinates, where the relationship between these two parameterizations has been discussed in Section 2.2. The former approach is advantageous because the controlled quantities have a clear physical interpretation. The latter is particularly useful for applications in which constraints on the relative states between two or more spacecraft are specified in a cartesian reference frame, see e.g. [30, 144].

3.1.1 Reference trajectory

For orbit control purposes, the reference trajectory can be modeled as the evolution of the position $\bar{\bf r}$ and the velocity $\dot{\bar{\bf r}}$ of a reference point mass, which is denoted as the target spacecraft. In the case of Earth orbiting spacecraft, the reference dynamics must be in the form (2.7), hence

$$\ddot{\mathbf{r}} = -\frac{\mu}{\|\bar{\mathbf{r}}\|^3} \bar{\mathbf{r}} + \bar{\mathbf{a}}_p, \tag{3.1}$$

where the reference acceleration $\bar{\mathbf{a}}_p$ depends on the specific application in exam. In station-keeping problems, the reference trajectory can be modeled as the steady state motion of a

virtual target spacecraft which is affected by the gravitational effect (2.10) only, so that

$$\bar{\mathbf{a}}_p = \bar{\mathbf{a}}_q \tag{3.2}$$

in (3.1), where $\bar{\mathbf{a}}_g = \mathbf{a}_g(\bar{\mathbf{r}})$. In fact, for a specific set of initial conditions, the solution to (3.1)-(3.2) defines a class of orbits which are of practical interest in several missions, including sun-synchronous, repeating ground-track, and frozen orbits. Because (3.2) is required to track these orbits, it is not treated as a disturbance to be rejected by the orbit control system.

In formation flying applications, the target spacecraft is a real spacecraft and hence it is affected by all environmental disturbances. In particular, for autonomous rendezvous and docking, it is typically assumed that the target spacecraft is passive, so that

$$\bar{\mathbf{a}}_p = \bar{\mathbf{a}}_e \tag{3.3}$$

in (3.1), where $\bar{\mathbf{a}}_e = \mathbf{a}_e(\bar{\mathbf{r}})$. In this case, the reference trajectory is defined by the solution to (3.1),(3.3).

The mapping (2.3), possibly combined with (2.5)-(2.6), can be used to parameterize the reference trajectory in terms of orbital elements. Moreover, the initial condition for the integration of (3.1) is related to the parameters defining the initial orbit by the transformation (2.4).

3.1.2 Orbit control system

The considered orbit control system can generate thrust only in the along-track and cross-track directions of the LVLH frame, so that no thrust is available in the radial direction. This is a desirable configuration for many space applications, because the orbit dynamics can be controlled by using only along-track and cross-track maneuvers, whereas the use of radial maneuvers is generally less fuel efficient. Moreover, radial thrust may not be available in small satellite missions due to mass and power restrictions.

In station-keeping applications, the control system is required to maintain the spacecraft sufficiently close to the desired orbit, by means of an efficient rejection of the orbital disturbances. In rendezvous and docking applications, the objective of the control system is to provide a trade-off between the propellant consumption and the maneuver time, while guaranteeing safe proximity operations.

Hereafter, the acceleration provided by the control system is denoted by a when expressed in the LVLH frame and by \mathbf{a}_I in the ECI frame. Similarly, $\Delta \mathbf{v}$ expresses an impulsive velocity change in the LVLH frame and $\Delta \mathbf{v}_I$ the corresponding quantity in the ECI frame. The matrix \mathbf{R}_{IL} which expresses the rotation from the ECI to the LVLH frame (see Fig. 2.1) is defined in (4.1).

3.2 Station-keeping

In this section, the problem of maintaining a given orbit is addressed for a single LEO space-craft. It is assumed that continuous thrust is available in the along-track direction and that

the thrust in the cross-track direction can be modeled as an impulsive velocity change of the form (2.19), resulting in a hybrid continuous/impulsive control scheme. This kind of design allows a trade-off between the thrust efficiency and the limitations imposed by the satellite mass and available power. In fact, one can take advantage of high specific impulse, low-thrust technologies to reduce the propellant consumption required by drag compensation, which is typically the dominant factor in the LEO delta-v budget, while using high-thrust, low-power technologies to counteract smaller cross-track perturbations, at the price of a reduced specific impulse.

Let o and \bar{o} denote the orbital elements corresponding to the solution of (2.7) and (3.1)-(3.2), respectively, through the mapping (2.3). Moreover, let the tracking error be expressed as

$$\delta \mathbf{o} = \mathbf{o} - \bar{\mathbf{o}}.\tag{3.4}$$

Then, the station-keeping control problem can be formalized as follows.

Problem 3.2.1. Find a continuous/impulsive feedback control law

$$\mathbf{a} = \begin{bmatrix} u(\delta \mathbf{o}), 0, 0 \end{bmatrix}^{T}$$

$$\Delta \mathbf{v} = \begin{bmatrix} 0, \Delta v(\delta \mathbf{o}), 0 \end{bmatrix}^{T},$$
(3.5)

which guarantees that

$$\lim_{t \to \infty} \delta \mathbf{o}(t) = \mathbf{0}. \tag{3.6}$$

The control signals \mathbf{a} and $\Delta \mathbf{v}$ are related to the inputs \mathbf{a}_I and $\Delta \mathbf{v}_I$ in (2.16) and (2.20), respectively, by the relationships $\mathbf{a}_I = \mathbf{R}_{IL}^T \mathbf{a}$ and $\Delta \mathbf{v}_I = \mathbf{R}_{IL}^T \Delta \mathbf{v}$.

In the following, an autonomous control law, based on the orbital element parametrization, is derived for Problem 3.2.1.

3.2.1 Relative orbital element dynamics

The vast majority of LEO spacecraft operate in near-circular, near-polar orbits and hence the mapping (2.3), with e and ω replaced by the eccentricity vector $\mathbf{e} = [e\cos(\omega), e\sin(\omega)]^T$, and ν replaced by (2.5), provides a suitable means of expressing the trajectories of the controlled and the (virtual) target spacecraft, given by the solution of (2.7) and (3.1)-(3.2), in terms of orbital elements. Then, $\mathbf{o} = [a, \mathbf{e}^T, i, \Omega, \nu_l]^T$, $\bar{\mathbf{o}} = [\bar{a}, \bar{\mathbf{e}}^T, \bar{i}, \bar{\Omega}, \bar{\nu}_l]^T$ and

$$\delta \mathbf{o} = [\delta a, \, \delta \mathbf{e}^T, \delta i, \, \delta \Omega, \, \delta \nu_l]^T.$$

Recall from Section 2.2 that all the components of δo can be time-varying, due to the presence of the perturbation terms \mathbf{a}_p in (2.7) and $\bar{\mathbf{a}}_q$ in (3.1)-(3.2).

Based on Gauss' variational equations of motion, adapted for near-circular, near-polar orbits [98], the relative orbital element dynamics can be approximated as

$$\delta \dot{\mathbf{o}} = [0, 0, 0, 0, \delta n]^T + \mathbf{B}(\mathbf{a} + \mathbf{d}),$$
 (3.7)

where δn is the relative mean motion, a is the control acceleration, expressed in the LVLH frame (see Fig. 2.1), and d accounts for nonconservative perturbations acting on the system. The relative mean motion δn can be expressed as

$$\delta n = \sqrt{\frac{\mu}{a^3}} - \sqrt{\frac{\mu}{\bar{a}^3}}. (3.8)$$

The input matrix **B** is given by

$$\mathbf{B} = \sqrt{\frac{a}{\mu}} \begin{bmatrix} 2a & 0 & 0 \\ 2\cos(\nu_l) & 0 & -\sin(\nu_l) \\ 2\sin(\nu_l) & 0 & \cos(\nu_l) \\ 0 & -\cos(\nu_l) & 0 \\ 0 & -\sin(\nu_l) & 0 \\ 0 & 0 & 0 \end{bmatrix}.$$
(3.9)

In the considered problem, the term d in (3.7) mainly depends on atmospheric drag, i.e $d \approx \mathbf{R}_{IL}\mathbf{a}_d$, with \mathbf{a}_d given by (2.11), while the other environmental disturbances have a minor impact. Due to the difficulty in obtaining a reliable estimate of the atmospheric density, drag can be treated as an unknown disturbance to be compensated. If the tracking error is kept reasonably small, the disturbance due to drag can be approximated by a constant acceleration in the along-track direction of the form

$$\mathbf{d} = [d, 0, 0]^T, \tag{3.10}$$

where $d \leq 0$.

Finally, note that mean orbital elements can be used in place of the classical orbital elements in (3.4) and (3.7), so that differential oscillations (with respect to the virtual spacecraft on the reference orbit) due to short periodic gravitational perturbations are not perceived as tracking errors. The classical elements can be converted to the corresponding mean elements by using the Brouwer's analytical transformation [18]. For additional details, the reader is referred to [120].

3.2.2 Orbital element feedback

Orbital element feedback is a well established topic in the orbit control literature see e.g. [58, 120]. Most of the proposed solutions, however, demand full actuation, while the orbit control system considered in Section 3.1.2 can provide thrust only in the along-track and cross-track directions. Moreover, the effect of atmospheric drag is often neglected. In the following, an hybrid continuous/impulsive control scheme is derived, by taking into account the structure of the matrix ${\bf B}$ and the specific features of the considered problem.

The matrix B in (3.9) can be partitioned as follows

$$\mathbf{B} = \begin{bmatrix} \mathbf{b}_1 & \mathbf{0} & \mathbf{c} \\ \mathbf{0} & \mathbf{b}_2 & \mathbf{0} \\ 0 & 0 & 0 \end{bmatrix}, \tag{3.11}$$

and the equations of motions (3.7) are decomposed into three subsystems. The first subsystem consists of the dynamics of the the relative orbital elements $\delta \mathbf{o}_1 = [\delta a, \ \delta \mathbf{e}^T]^T$, with along-track acceleration u, given by

$$\delta \dot{\mathbf{o}}_1 = \mathbf{b}_1 \ (u+d) \,. \tag{3.12}$$

The second subsystem describes the variation of the orbital elements $\delta \mathbf{o}_2 = [\delta i, \ \delta \Omega]$, due to a sequence of impulsive velocity changes Δv in the cross-track direction, as follows

$$\delta \mathbf{o}_2(t_{k+1}) = \delta \mathbf{o}_2(t_k) + \mathbf{b}_2(t_k) \, \Delta v(t_k), \tag{3.13}$$

where $k \in \mathbb{N}$ is the index of the elements of the sequences and t_k is the corresponding time. The third subsystem is obtained from (3.7)-(3.9) as

$$\delta \dot{\nu}_l = \delta n = \sqrt{\frac{\mu}{a^3}} - \sqrt{\frac{\mu}{\bar{a}^3}}.$$
 (3.14)

The following proposition addresses the stabilization of system (3.12) in the absence of disturbances (d = 0).

Proposition 3.2.1. *The system*

$$\delta \dot{\mathbf{o}}_1 = \mathbf{b}_1 u,\tag{3.15}$$

together with the control law

$$u(\delta \mathbf{o}) = -\mathbf{b}_1^T \mathbf{K}_1 \delta \mathbf{o}_1, \tag{3.16}$$

where

$$\mathbf{b}_1 = 2\mu^{-\frac{1}{2}} \left[a^{\frac{3}{2}}, \ a^{\frac{1}{2}} \cos(\nu_l), \ a^{\frac{1}{2}} \sin(\nu_l) \right]^T, \tag{3.17}$$

a > 0, and $\mathbf{K}_1 = diag(K_a, K_{ex}, K_{ey})$ is a positive definite diagonal matrix, is asymptotically stable.

Proof. The proof, reported in Appendix A, follows from conventional arguments in Lyapunov stability theory. □

Remark 3.2.1. Notice that \mathbf{b}_1 in (3.11) expresses the effectiveness of the input u in controlling the relative orbital element \mathbf{o}_1 . Hence, \mathbf{b}_1^T in (3.16) provides a suitable means of scaling the magnitude of the input with its effectiveness. Because the magnitude of the input is proportional to the fuel consumption, the control law (3.16) is known to yield a good fuel efficiency.

The control law (3.16) has to be modified in order to compensate for the steady state tracking error of the semi-major axis, arising from the disturbance d in (3.12), due to drag. One possibility is to estimate d by using a suitable filtering scheme and then subtract the estimate from the control input u. Another option is to introduce an integral term in the control law, as shown by the following result.

Proposition 3.2.2. *Let*

$$u(\delta \mathbf{o}) = -\mathbf{b}_1^T \mathbf{K}_1 \delta \mathbf{o}_1 + K_I z$$

$$\dot{z} = -K_I \mathbf{b}_1^T \delta \mathbf{o}_1,$$
(3.18)

where K_I is a positive gain and z(0) = 0. Then system (3.12), with the control law (3.18), is asymptotically stable.

Proof. The proof, reported in Appendix A, is similar to that of Theorem 3.2.1.

Remark 3.2.2. Observe that the equilibrium of system (3.12),(3.18) is attained for $u = K_I z = -d$, i.e drag is compensated by the control acceleration, at steady state.

The benefits of this approach over the solution provided by Theorem 3.2.1 are demonstrated in the following numerical example.

Example 3.2.1. Let $\bar{a}=6.6\cdot 10^6$ m, $d=-4\cdot 10^{-5}$ m/s² in (3.12), $K_a=10^{-10}$ in (3.16),(3.18), and $K_I=10^{-7}$ in (3.18). The semi-major axis tracking errors, resulting from the application of the two control laws to (3.12), are reported in Fig. 3.1, for an initial δa of 100 m. It can be clearly seen that the control law (3.18) drives the tracking error to zero, whereas a steady-state error of approximately -235 m is obtained with the control law (3.16). The evolution of the parameter z in (3.18) is reported in Fig. 3.2. As expected, this parameter converges to the value $\bar{z}=-d/K_I$.

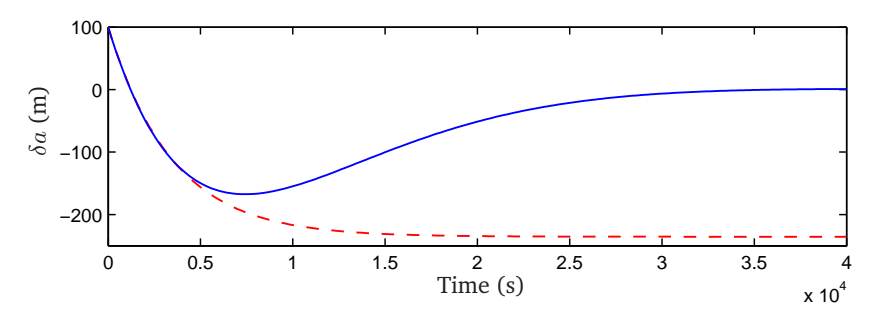


Figure 3.1: Semi-major axis tracking error from the application of (3.16) (dashed) and (3.18) (solid).

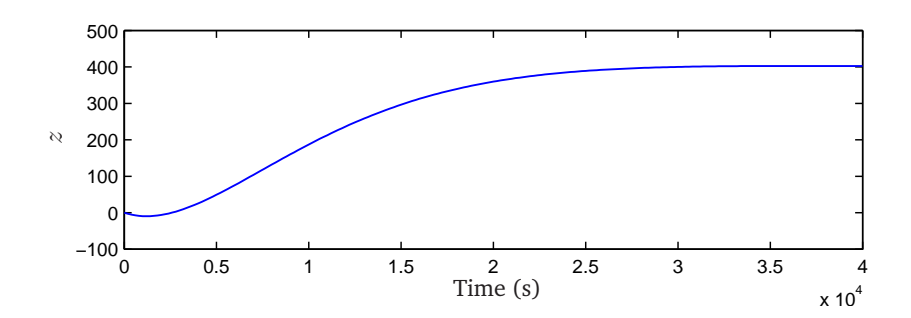


Figure 3.2: Parameter z in (3.18).

An impulsive control scheme is derived for the cross-track dynamics (3.13), by taking advantage of the fact that these are decoupled from the along-track dynamics (3.12).

Proposition 3.2.3. *The control law*

$$\begin{cases} \Delta v(\delta \mathbf{o}) = \frac{\sqrt{\mu}}{\sqrt{a}\cos(\nu_l)} \delta i & \text{for } \nu_l = m\pi \\ \Delta v(\delta \mathbf{o}) = \frac{\sqrt{\mu}}{\sqrt{a}\sin(\nu_l)} \delta \Omega & \text{for } \nu_l = m\pi + \pi/2, \end{cases}$$
(3.19)

where $m \in \mathbb{Z}$, drives the trajectory of system (3.13) to the origin in finite-time.

Proof. By letting ν_l vary in the interval $(-\pi, \pi]$ and applying (3.19) to (3.13), it follows that (3.13) is steered to the origin in finite-time, by using only two impulses at $\nu_l(t_1) = -\pi/2$ and $\nu_l(t_2) = 0$.

Remark 3.2.3. From (3.9), it is evident that the efficiency of an cross-track maneuver for δi and $\delta \Omega$ adjustments is maximized at $\nu_l = m\pi$ and $\nu_l = m\pi + \pi/2$, respectively. Therefore, the control law (3.19) guarantees a good fuel efficiency.

In some applications, small secular perturbations, which are not modeled by (3.7), may affect the evolution of system (3.13). Moreover, the impulsive velocity changes (3.19) may not be compatible with the thrust level generated by the propulsion system. In such cases, an effective approach consists in applying a sequence of impulsive burns of fixed magnitude Δv_n at $\nu_l = m\pi$ or $\nu_l = m\pi + \pi/2$, whenever the tracking errors δi or $\delta \Omega$ exceed a predefined control window [119, 131]. The sequence of burns is stopped when the corresponding tracking error reaches the opposite side of the control window. Formally, let the control windows be defined as $i_L \leq \delta i \leq i_U$ and $\Omega_L \leq \delta \Omega \leq \Omega_U$, where the subscripts L and U denote predefined lower and upper bounds for the tracking errors. Moreover, let the direction of the perturbations be such that d/dt $\delta i < 0$ and d/dt $\delta \Omega < 0$, (the reasoning is the same for d/dt $\delta i > 0$ or d/dt $\delta \Omega > 0$). Then, if Δv_n is sufficiently small, (3.19) can be replaced by

$$\begin{cases} \Delta v(\delta \mathbf{o}) = -\frac{\Delta v_n}{\cos(\nu_l)} & \text{for } \nu_l = m\pi & \text{once } \delta i \leq i_L, \text{ until } \delta i \geq i_U \\ \Delta v(\delta \mathbf{o}) = -\frac{\Delta v_n}{\sin(\nu_l)} & \text{for } \nu_l = m\pi + \pi/2 & \text{once } \delta \Omega \leq \Omega_L, \text{ until } \delta \Omega \geq \Omega_U. \end{cases}$$
(3.20)

Finally, an effective method for correcting the argument of latitude error $\delta \dot{\nu}_l$ is to treat a as an input to system (3.14) [101]. In particular, the following proposition holds.

Proposition 3.2.4. *Let*

$$a = \left(-K_{\nu} \,\delta\nu_l + \frac{1}{\bar{a}^{3/2}}\right)^{-2/3}.\tag{3.21}$$

in (3.14). Then, $\lim_{t \to \infty} \delta \nu_l = 0$, for $0 < K_{\nu} \le \frac{1}{\pi \bar{a}^{\frac{3}{2}}}$.

Proof. The proof is reported in Appendix A.

Remark 3.2.4. In order to steer a to the to the solution prescribed by (3.21), one possibility is to set

$$\delta \mathbf{o}_1 = [\delta a', \, \delta \mathbf{e}^T]^T \tag{3.22}$$

in (3.18), where $\delta a' = a - a'$ and

$$a' = \left(-K_{\nu} \,\delta\nu_l + \frac{1}{\bar{a}^{3/2}}\right)^{-2/3}.\tag{3.23}$$

Notice that the time constant of system (3.12), with the control law (3.18), (3.22), can be made much smaller than the time constant of system (3.14), by suitably choosing the gains \mathbf{K}_1 , K_I and K_{ν} . This leads to $a \to a'$ thanks to the application of (3.18),(3.22), and consequently to $\delta \nu_l \to 0$ by Proposition 3.2.4. Moreover, when $\delta \nu_l$ vanishes in (3.23), the parameter a' matches the reference value \bar{a} . Consequently, one has that $a' \to \bar{a}$ and $\delta \mathbf{o}_1 \to \mathbf{0}$, as desired.

Summing up the application of the control laws (3.18)-(3.20), together with (3.22)-(3.23) provides a solution to Problem 3.2.1 for spacecraft in near circular orbits, for which the error dynamics can be approximated by (3.7). The considered solution requires the absolute position and velocity of the spacecraft to be estimated in real-time. To this aim, a suitable EKF scheme is presented in Section 5.1. In addition, the reference trajectory must be available on-board the spacecraft. A formal proof of the stability of the overall system goes beyond the scope of this thesis. The effectiveness of the proposed design is demonstrated through numerical simulations in Section 6.1.

3.3 Rendezvous and docking

The problem of performing autonomous rendezvous and docking between two spacecraft in formation is conceptually similar to that of tracking a virtual spacecraft, treated in the previous section. In both cases, the objective is to drive to zero the relative position and velocity of the spacecraft. However, the control accuracies required by these applications have different orders of magnitude. Moreover, a number of safety requirements have to be taken into account for spacecraft operating in close proximity. Consider a target-chaser spacecraft formation, in which the chaser is required to maintain visual contact and to safely approach the target, based on relative position and velocity data.

Let the target trajectory tracking error be expressed in the LVLH frame centered at the target, according to

$$\mathbf{x} = \begin{bmatrix} \bar{\mathbf{R}}_{IL}(\mathbf{r} - \bar{\mathbf{r}}) + \mathbf{r}_d \\ \bar{\mathbf{R}}_{IL}(\dot{\mathbf{r}} - \dot{\bar{\mathbf{r}}}) - \bar{\boldsymbol{\omega}}_L^{\times} \bar{\mathbf{R}}_{IL}(\mathbf{r} - \bar{\mathbf{r}}) \end{bmatrix}, \tag{3.24}$$

where \mathbf{r} , $\dot{\mathbf{r}}$ and $\bar{\mathbf{r}}$, $\dot{\bar{\mathbf{r}}}$ correspond to the solution of (2.7) and (3.1),(3.3), respectively, $\bar{\mathbf{R}}_{IL}$ expresses the rotation between the inertial frame and the LVLH frame (the overbar denotes that $\bar{\mathbf{R}}_{IL}$ refers to the target trajectory), $\bar{\omega}_L$ denotes the target LVLH rate vector and $\mathbf{r}_d = [r_d, 0, 0]$, with $r_d \geq 0$, represents the desired docking position (assuming that the docking port is located behind the target).

Let X be an admissible subset of the state space defined by the following requirements [17].

- Collision avoidance: the spacecraft must not collide with each other.
- Line-of-Sight (LoS): the relative motion must be confined within a certain region of the state space (the so-called docking cone) to maintain visual contact.

These can be represented by the path constraints $x \in X$, where

$$\mathbb{X} = \left\{ \mathbf{x} : x_1 \le 0, \sqrt{x_2^2 + x_3^2} \le (x_d - x_1) \tan(\theta/2) \right\}, \tag{3.25}$$

the angle θ specifies the size of the docking cone, and $x_d \ge 0$ is a predefined constant offset.

The admissible input set \mathbb{U} is bounded by the maximum thrust u_M that can be delivered by the propulsion system, as

$$\mathbb{U} = \{ \mathbf{u} : \|\mathbf{u}\|_{\infty} \le u_M \}. \tag{3.26}$$

Since radial thrust is not available, $\mathbf{u} = [u_1, u_2]^T$ in (3.26), where u_1 and u_2 denote the along-track and cross-track thrust components provided by the orbit control system.

The control objective is to minimize a combination of the fuel consumption and the maneuver time $t_m = t_f - t_0$. Moreover, it is desired to reduce as much as possible the magnitude and/or the amount of thruster firings directed towards the target during the final phase of the approach. Then, a relevant cost function is [88]

$$J(\mathbf{x}, \mathbf{u}) = \alpha \int_{t_0}^{t_f} ||\mathbf{u}(t)||_1 dt + (1 - \alpha) \int_{t_0}^{t_f} 1 dt + \beta \int_{t_0}^{t_f} \epsilon(t) dt,$$
 (3.27)

where $\alpha \in [0, 1]$ is a relative weight on the fuel consumption (first term) and the maneuver time (second term), and $\beta \ge 0$ is a weight on the function ϵ , which accounts for plume impingement requirements. Due to the particular form of (3.25), the thruster plume impingement function can be taken as [112]

$$\epsilon(t) = \begin{cases} u_1^-(t) & \text{if } |x_1(t)| \le x_{\epsilon 1} \\ 0 & \text{otherwise,} \end{cases}$$
 (3.28)

where $x_{\epsilon 1} > 0$ is a predefined tolerance and $u_1^-(t)$ is the negative part of the along-track thrust, defined by

$$u_1^-(t) = \begin{cases} |u(t)| & \text{if } u(t) < 0\\ 0 & \text{otherwise.} \end{cases}$$

Notice that (3.28) accounts for thruster firings directed towards the target (i.e. in order to produce a force in the negative along-track direction, the thruster which points in the positive along-track direction, towards the target, must be fired) when the two spacecraft are close to each other.

Then, the considered control problem takes the following form.

Problem 3.3.1. Find a control law

$$\mathbf{u} = [u_1(\mathbf{x}), u_2(\mathbf{x})]^T \tag{3.29}$$

which solves the optimal control problem

$$\min_{\mathbf{u}} \quad J(\mathbf{x}, \mathbf{u})$$
s.t. $(2.7), (2.16)$

$$\mathbf{a}_{I} = \mathbf{R}_{IL}^{T} [\mathbf{u}^{T}/m, 0]^{T}$$

$$(3.1), (3.3), (3.24)$$

$$\mathbf{x} \in \mathbb{X}, \ \mathbf{u} \in \mathbb{U}$$

$$\mathbf{x}(t_{f}) = \mathbf{0},$$
(3.30)

where the final time t_f is free and m is the mass of the spacecraft.

In order to solve Problem 3.3.1, a feedback guidance and control scheme, with the ability to handle thrust magnitude and path constraints, can be considered. In particular, model predictive control has been recognized as an attractive solution. Nevertheless, the capability of spacecraft onboard processors to handle the real-time computational load that this technique can generate still needs to be fully validated, especially for low-thrust problems, where a long control horizon is required.

Motivated by this issue, a low-complexity MPC design is proposed in the following for the low-thrust rendezvous and docking problem. First, the trajectory optimization problem is reformulated by parameterizing the control sequence by a set of Laguerre functions, which allows a long control horizon to be considered without using a large number of decision variables. Then, an explicit MPC scheme is derived by exploiting the Laguerre parametrization, in combination with multi-parametric programming techniques. Because the proposed design does not require on-line optimization, it is especially suitable for implementation on simple hardware.

3.3.1 Hill-Clohessy-Wiltshire equations

In order to design a low-complexity control scheme, the use of a linearized model is preferable over the full nonlinear model (2.7),(3.1),(3.3). For many applications, the following assumptions hold: (i) the orbit is nearly circular (ii) the distance between the chaser and the target is small compared to the orbit radius and (iii) the two spacecraft have similar physical properties.

Differentiating (3.24) and linearizing the resulting expression, under the above assumptions, yields the celebrated Hill-Clohessy-Wiltshire (HCW) equations [22]

$$\ddot{x}_{1} = 2\bar{\omega}_{L}\dot{x}_{3} + u_{1}/m
\ddot{x}_{2} = -\bar{\omega}_{L}^{2}x_{2} + u_{2}/m
\ddot{x}_{3} = 3\bar{\omega}_{L}^{2}x_{3} - 2\bar{\omega}_{L}\dot{x}_{1},$$
(3.31)

where $\mathbf{x} = [x_1, x_2, x_3, \dot{x}_1, \dot{x}_2, \dot{x}_3]^T$ contains the along-track, cross-track and radial components of the relative position and velocity vectors, $\mathbf{u} = [u_1, u_2]^T$ is the control thrust of the

form (3.29), expressed in the LVLH frame (see Fig. 2.1) and $\bar{\omega}_L = [0, -\bar{\omega}_L, 0]$. Using (3.31), the tracking error dynamics can be represented in the state space form

$$\dot{\mathbf{x}} = \mathbf{A}_c \, \mathbf{x} + \mathbf{B}_c \, \mathbf{u} \,, \tag{3.32}$$

with

$$\mathbf{A}_{c} = \begin{bmatrix} 0 & 0 & 0 & 1 & 0 & 0 \\ 0 & 0 & 0 & 0 & 1 & 0 \\ 0 & 0 & 0 & 0 & 0 & 1 \\ 0 & 0 & 0 & 0 & 0 & 2\bar{\omega}_{L} \\ 0 & -\bar{\omega}_{L}^{2} & 0 & 0 & 0 & 0 \\ 0 & 0 & 3\bar{\omega}_{L}^{2} & -2\bar{\omega}_{L} & 0 & 0 \end{bmatrix}$$

$$(3.33)$$

and

$$\mathbf{B}_c = \begin{bmatrix} 0 & 0 & 0 & 1/m & 0 & 0 \\ 0 & 0 & 0 & 0 & 1/m & 0 \end{bmatrix}^T. \tag{3.34}$$

For the considered problem, the variation of the spacecraft mass m is negligible and therefore one can assume that ${\bf B}$ is constant. Finally, notice that the controllability matrix

$$\mathbf{C}_{M} = \left[\mathbf{B}_{c}, \mathbf{A}_{c} \mathbf{B}_{c}, \dots, \mathbf{A}_{c}^{5} \mathbf{B}_{c} \right]$$
 (3.35)

has full rank and therefore system (3.32) is controllable with the input u.

3.3.2 Optimal control problem

Problem 3.3.1 does not admit an analytic solution and must be solved numerically. Due to the limited processing power of spacecraft onboard computers, the implementation of a feedback control scheme based on the on-line solution to (3.30) may not be feasible. Therefore, (3.30) is relaxed by making use of the linearized model (3.32) in place of the nonlinear model (2.7),(3.1),(3.3), and approximating (3.27) with a quadratic cost function of the form

$$J_c(\mathbf{x}, \mathbf{u}) = \|\mathbf{W}_f \mathbf{x}(t_f)\|^2 + \int_{t_0}^{t_f} (\|\mathbf{Q}_c \mathbf{x}(t)\|^2 + \|\mathbf{R}_c \mathbf{u}(t)\|^2) dt,$$
 (3.36)

where \mathbf{W}_f , \mathbf{Q}_c and \mathbf{R}_c are square weighting matrices and \mathbf{R}_c is nonsingular. In the above equation, t_f is fixed and the weight \mathbf{W}_f on the terminal state relaxes the terminal constraint $\mathbf{x}(t_f) = \mathbf{0}$ in (3.30). Notice that the non-convex plume impingement function (3.28) is not included in (3.36). Nevertheless, the choice of a quadratic performance index ensures that $\|\mathbf{u}(t)\|$ is kept small close to the steady state, so that the plume impingement effect is limited.

Moreover, the set (3.25) is approximated by a polyhedral set $\bar{\mathbb{X}}$ of the form

$$\bar{\mathbb{X}} = \left\{ \mathbf{x} : \mathbf{C} \,\mathbf{x} \le \mathbf{d} \right\},\tag{3.37}$$

where

$$\mathbf{C} = \begin{bmatrix} 1 & 0 & 0 & 0 & 0 & 0 \\ k_1 & 1 & 0 & 0 & 0 & 0 \\ k_1 & -1 & 0 & 0 & 0 & 0 \\ k_1 & 0 & 1 & 0 & 0 & 0 \\ k_1 & 0 & -1 & 0 & 0 & 0 \end{bmatrix}, \quad \mathbf{d} = \begin{bmatrix} 0 \\ 1 \\ 1 \\ 1 \\ 1 \end{bmatrix} k_1 x_d, \tag{3.38}$$

and $k_1 = \tan(\theta/2)/\sqrt{2}$. The set (3.37)-(3.38) describes the interior of a pyramid inscribed within the LoS cone, as illustrated in Fig. 3.3.

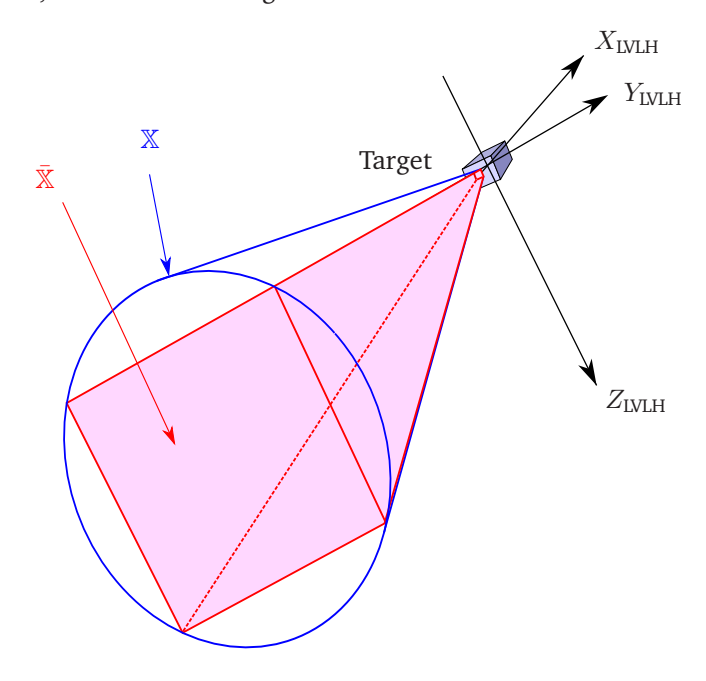


Figure 3.3: LoS cone approximation.

By using (3.36)-(3.38), Problem 3.3.1 is reformulated as follows.

Problem 3.3.2. Find a control law

$$\mathbf{u} = [u_1(\mathbf{x}), u_2(\mathbf{x})]^T \tag{3.39}$$

which solves the optimal control problem

$$\min_{\mathbf{u}} \quad J_c(\mathbf{x}, \mathbf{u})$$
s.t. (3.31)
$$\mathbf{x} \in \bar{\mathbb{X}}$$

$$\mathbf{u} \in \mathbb{U}.$$
(3.40)

Model predictive control is a potential design method for Problem 3.3.2, as it allows to derive a feedback control law under the receding horizon strategy [94]. According to this approach, the solution to (3.40) is computed over a finite number of future sampling instances, and the first element of the optimal control sequence is applied to the plant, at each time step. To avoid numerically solving the optimal control problem, at each time step, an explicit MPC law can be derived, by solving off-line a suitable multi-parametric quadratic program. However, it is known that the complexity of an explicit solution can grow exponentially with length of the control sequence [134]. This problem could well

arise in the considered application, because the control problem must be defined over a long horizon, to account for the limited control authority, and discretized with a relatively small step, to avoid the violation of path constraints between discrete time samples. A possible workaround consist in parameterizing the input sequence with a set of Laguerre functions (see e.g. [130, 133]), as described next.

Remark 3.3.1. Notice that a control law solving Problem 3.3.1 ensures finite-time convergence to the desired docking position, whereas one solving Problem 3.3.2, under the receding horizon principle, can only guarantee asymptotic tracking. In the considered application, this is a minor issue, because a dedicated docking mechanism is activated as soon as the two spacecraft get sufficiently close.

3.3.3 Laguerre MPC

For digital implementation of the control law, system (3.32) is discretized with a sampling period T_s using a zero-order hold, resulting in the discrete state space model

$$\mathbf{x}(k+1) = \mathbf{A}\,\mathbf{x}(k) + \mathbf{B}\,\mathbf{u}(k),\tag{3.41}$$

where

$$\mathbf{A} = e^{\mathbf{A}_c T_s}, \quad \mathbf{B} = \left(\int_0^{T_s} e^{\mathbf{A}_c \tau} d\tau \right) \mathbf{B}_c. \tag{3.42}$$

The MPC design requires the predicted future states generated from the state space model (3.41) at the current sampling instant, based on the current state and the computed input sequence. Let $\mathbf{u}(k+i)$ denote the input to be computed i sampling steps ahead from the current sampling instant k. The basic idea underpinning Laguerre MPC (LMPC) is to parameterize $\mathbf{u}(k+i)$ using a set of discrete Laguerre polynomials, according to

$$\mathbf{u}(k+i) = \begin{bmatrix} u_1(k+i) \\ u_2(k+i) \end{bmatrix} = \begin{bmatrix} \mathbf{l}_1^T(i) & \mathbf{0} \\ \mathbf{0} & \mathbf{l}_2^T(i) \end{bmatrix} \begin{bmatrix} \boldsymbol{\eta}_1 \\ \boldsymbol{\eta}_2 \end{bmatrix} = \mathbf{L}(i)\,\boldsymbol{\eta},\tag{3.43}$$

where $\mathbf{l}_j(i)$ is the Laguerre function vector and η , which represents the new decision vector, is termed the coefficient vector. The Laguerre function vector satisfies the difference equation

$$\mathbf{l}_{j}(i+1) = \begin{bmatrix} a_{j} & 0 & \dots & 0 \\ b_{j} & a_{j} & \ddots & \vdots & 0 \\ -a_{j}b_{j} & b_{j} & \ddots & 0 & 0 \\ \vdots & \vdots & \ddots & \ddots & 0 \\ -a_{j}^{N_{j}-2} & -a_{j}^{N_{j}-3}b_{j} & \dots & b_{j} & a_{j} \end{bmatrix} \mathbf{l}_{j}(i)$$
(3.44)

with

$$\mathbf{l}_{j}(0) = \sqrt{b_{j}} \begin{bmatrix} 1 & -a_{j} & a_{j}^{2} & -a_{j}^{3} & \dots & (-1)^{N_{j}-1} a_{j}^{N_{j}-1} \end{bmatrix}^{T},$$
 (3.45)

where $b_j = (1 - a_j^2)$, N_j is the number of terms in the expansion and $a_j \in [0, 1]$ is the scaling factor of the Laguerre network for input u_j . Both a_j and N_j are fixed design parameters.

For $a_j = 0$ in (3.44)-(3.45), the input sequence (3.43) takes the form

$$\begin{cases}
[u_j(k), \dots, u_j(k+N_j)]^T = \boldsymbol{\eta}_j \\
u_j(k+i) = \mathbf{l}_j^T(i) \, \boldsymbol{\eta}_j = 0, \quad i > N_j.
\end{cases}$$
(3.46)

Notice from (3.46) that, when $a_j=0$, optimizing with respect to η_j corresponds to optimize with respect to the input sequence $u_j(k),\ldots,u_j(k+N_j)$, as it is done in the standard MPC design with control horizon N_j . Choosing $a_j>0$ allows a trade-off between the time scale of the input sequence, i.e. $\mathbf{1}_j^T(i)\,\eta_j$ exponentially decays to zero instead of being identically zero for $i>N_j$, and the accuracy of its pointwise approximation. This is particularly relevant when the number of decision variables N_j is selected to be small to keep the computation feasible and then the truncated parametrization given by (3.46) cannot adequately describe the future input trajectory.

By substituting (3.43) into (3.41), the state dynamics N_p sampling instants ahead of k can be expressed as

$$\begin{cases}
\mathbf{x}(k+1|k) = \mathbf{A} \mathbf{x}(k) + \mathbf{BL}(0) \boldsymbol{\eta} \\
\mathbf{x}(k+2|k) = \mathbf{A}^{2} \mathbf{x}(k) + (\mathbf{A}\mathbf{BL}(0) + \mathbf{BL}(1)) \boldsymbol{\eta} \\
\vdots \\
\mathbf{x}(k+N_{p}|k) = \mathbf{A}^{N_{p}} \mathbf{x}(k) + (\mathbf{A}^{N_{p}-1}\mathbf{BL}(0) + \dots + \mathbf{BL}(N_{p}-1)) \boldsymbol{\eta}.
\end{cases} (3.47)$$

where the prediction horizon N_p is unrelated to the number of entries in η , which is equal to $(N_1 + N_2)$. The prediction model can be written in the compact form

$$\chi = \mathbf{F} \,\mathbf{x}(k) + \mathbf{\Phi} \,\boldsymbol{\eta} \,, \tag{3.48}$$

where

$$\chi = \begin{bmatrix} \mathbf{x}^{T}(k+1|k) & \mathbf{x}^{T}(k+2|k) & \dots & \mathbf{x}^{T}(k+N_{p}|k) \end{bmatrix}^{T}
\mathbf{F} = \begin{bmatrix} (\mathbf{A})^{T} & (\mathbf{A}^{2})^{T} & \dots & (\mathbf{A}^{N_{p}})^{T} \end{bmatrix}^{T}
\Phi = \begin{bmatrix} \mathbf{BL}(0) & \mathbf{0} & \dots & \mathbf{0} \\ \mathbf{ABL}(0) & \mathbf{BL}(1) & \dots & \mathbf{0} \\ \vdots & \vdots & \ddots & \mathbf{0} \\ \mathbf{A}^{N_{p}-1}\mathbf{BL}(0) & \mathbf{A}^{N_{p}-2}\mathbf{BL}(1) & \dots & \mathbf{BL}(N_{p}-1) \end{bmatrix}.$$
(3.49)

Moreover, the cost function (3.36) is discretized to give

$$J_d = \chi^T \mathbf{Q} \chi + \eta^T \mathbf{R} \eta, \qquad (3.50)$$

where $\mathbf{Q} = \operatorname{blockdiag}(\oplus^{N_p-1}T_s\mathbf{Q}_c^T\mathbf{Q}_c, \mathbf{Q}_f)$ is a $6N_p \times 6N_p$ matrix, $\mathbf{Q}_f = T_s\mathbf{W}_f^T\mathbf{W}_f$ and $\mathbf{R} = T_s\mathbf{M}_u^T(\oplus^{N_p}\mathbf{R}_c^T\mathbf{R}_c)\mathbf{M}_u$ is a $(N_1+N_2)\times(N_1+N_2)$ matrix, with

$$\mathbf{M}_{u} = \begin{bmatrix} \mathbf{L}^{T}(0) & \mathbf{L}^{T}(1) & \dots & \mathbf{L}^{T}(N_{p} - 1) \end{bmatrix}^{T}.$$
 (3.51)

Hence, by substituting (3.48) into (3.50), the MPC problem can be equivalently rewritten as

$$\min_{\boldsymbol{\eta}} \quad \boldsymbol{\eta}^{T} \boldsymbol{\Omega} \, \boldsymbol{\eta} + 2 \, \mathbf{x}^{T}(k) \boldsymbol{\Psi}^{T} \boldsymbol{\eta} + \, \mathbf{x}^{T}(k) \mathbf{F}^{T} \mathbf{Q} \mathbf{F} \mathbf{x}(k), \tag{3.52}$$

where $\Omega = (\Phi^T \mathbf{Q} \Phi + \mathbf{R})$ and $\Psi = \Phi \mathbf{Q} \mathbf{F}$. In the absence of constraints, the global minimum of problem (3.52) is attained (assuming the required matrix inverse exists) at

$$\boldsymbol{\eta}^*(k) = -\boldsymbol{\Omega}^{-1} \, \boldsymbol{\Psi} \, \mathbf{x}(k) \,. \tag{3.53}$$

Under the receding horizon principle, only the first element of the optimal input sequence is applied to the plant and hence

$$\mathbf{u}(k) = \mathbf{L}(0)\,\boldsymbol{\eta}^*(k). \tag{3.54}$$

Proposition 3.3.1. *System* (3.41), *with the control law* (3.53)-(3.54), *is asymptotically stable provided that the eigenvalues of*

$$\mathbf{A} - \mathbf{B}(\mathbf{L}(0)\mathbf{\Omega}^{-1}\mathbf{\Psi})$$

lie inside the unit circle.

Input and state constraints are included in the MPC design to account for the operating range of the actuators and to ensure safe proximity operations. Unlike the unconstrained case, the constrained MPC problem does not admit an analytic solution and must be solved numerically. The input amplitude constraints $\mathbf{u} \in \mathbb{U}$ in (3.26) can be rewritten as

$$-u_M \mathbb{1} \le \mathbf{L}(i) \, \boldsymbol{\eta} \le \mathbb{1} u_M \qquad i = 1, \dots, N_p.$$
 (3.55)

To reduce the sensitivity of the control system to output noise, one possibility is to introduce a slack variable $s_1 \geq 0$, which bounds the variation of $\mathbf{u}(k)$ with respect to $\mathbf{u}(k-1)$, and penalize it in the cost function. The value of s_1 is obtained from the linear inequality

$$-s_1 \mathbb{1} \le \mathbf{L}(0) \boldsymbol{\eta} - \mathbf{u}(k-1) \le \mathbb{1}s_1, \tag{3.56}$$

where $\mathbf{u}(k-1)$ is treated as an additional input to the optimization problem.

The path constraints $x \in \bar{\mathbb{X}}$, with $\bar{\mathbb{X}}$ given by (3.37), are softened according to

$$C \mathbf{x}(k+i|k) \le 1 s_2 + \mathbf{d}$$
 $i = 1, ..., N_p,$ (3.57)

where $s_2 \ge 0$ is a slack variable which relaxes (3.37) in the ∞ -norm sense, to ensure feasibility in the presence of observation noise. Notice that (3.55) and (3.57) can be enforced on predefined subsets of samples $\mathbb{M}_u \subseteq \{1, \ldots, N_p - 1\}$ and $\mathbb{M}_x \subseteq \{1, \ldots, N_p\}$, respectively, rather than on all samples, in order to trade-off the performance and the complexity of control algorithm.

Let $\eta_C = [\eta^T \ s_1 \ s_2]^T = [\eta^T \ s^T]^T$ be the augmented decision vector and $\mathbf{x}_C(k) = [\mathbf{x}^T(k) \ \mathbf{u}^T(k-1)]^T$ the augmented initial condition for the constrained optimization problem. Then, the constraints (3.55)-(3.57) can be written in the compact form

$$\begin{bmatrix} \mathbf{M}_{u} & \mathbf{0} & \mathbf{0} \\ -\mathbf{M}_{u} & \mathbf{0} & \mathbf{0} \\ \mathbf{L}(0) & -\mathbb{1} & \mathbf{0} \\ -\mathbf{L}(0) & -\mathbb{1} & \mathbf{0} \\ \mathbf{C}_{N} \mathbf{\Phi} & \mathbf{0} & -\mathbb{1} \end{bmatrix} \begin{bmatrix} \boldsymbol{\eta} \\ s_{1} \\ s_{2} \end{bmatrix} \leq \begin{bmatrix} \mathbb{1}u_{M} \\ \mathbb{1}u_{M} \\ \mathbf{0} \\ \mathbf{0} \\ \mathbf{d}_{N} \end{bmatrix} - \begin{bmatrix} \mathbf{0} & \mathbf{0} \\ \mathbf{0} & \mathbf{0} \\ \mathbf{0} & -\mathbf{I} \\ \mathbf{0} & \mathbf{I} \\ \mathbf{C}_{N} \mathbf{F} & \mathbf{0} \end{bmatrix} \begin{bmatrix} \mathbf{x}(k) \\ \mathbf{u}(k-1) \end{bmatrix},$$
(3.58)

where **F** and Φ are given by (3.49), $\mathbf{C}_N = \bigoplus^{N_p} \mathbf{C}$, and $\mathbf{d}_N = [\mathbf{d}^T \dots \mathbf{d}^T]^T$. The constrained LMPC problem of the form (3.52) to be solved is

$$\min_{\boldsymbol{\eta}_{C}} \quad \boldsymbol{\eta}_{C}^{T} \begin{bmatrix} \boldsymbol{\Omega} & \mathbf{0} \\ \mathbf{0} & \mathbf{R}_{s} \end{bmatrix} \boldsymbol{\eta}_{C} + 2 \mathbf{x}_{C}^{T}(k) \begin{bmatrix} \boldsymbol{\Psi} & \mathbf{0} \\ \mathbf{0} & \mathbf{0} \end{bmatrix} \boldsymbol{\eta}_{C}$$
s.t. (3.58),

where $\mathbf{R}_s = \operatorname{diag}(R_1, R_2)$, with $R_1, R_2 \geq 0$, is a 2×2 matrix which penalizes the slack vector \mathbf{s} , and the term $\mathbf{x}^T(k)\mathbf{F}^T\mathbf{QFx}(k)$ in (3.52), which is constant, has been dropped. Problem (3.59) is a quadratic program (QP) with linear constraints, which can be efficiently solved using convex optimization algorithms. By applying the solution to (3.59) to the plant via (3.54), at each sampling instant, a feedback control scheme is obtained. The following proposition provides a condition that guarantees the stability of the design.

Proposition 3.3.2. Let $\mathbf{x}(k+N_p|k)=0$ be an additional constraint, $\mathbf{R}_s=\mathrm{diag}(0,0)$ and $s_2=0$ in (3.58)-(3.59). Moreover, assume that problem (3.59) is feasible at each time sample. Then, the control law (3.54),(3.59) guarantees that, for system (3.41),

$$\lim_{k \to \infty} \mathbf{x}(k) = \mathbf{0}. \tag{3.60}$$

Proof. The proof is reported in Appendix A.

Remark 3.3.2. The stabilizing terminal constraint $\mathbf{x}(k+N_p|k)=0$ is rarely used in practice, as it limits the domain of attraction of the controller. Instead, the combination of a suitable terminal weight \mathbf{Q}_f and a terminal set \mathbb{X}_f , such that $\mathbf{x}(k+N_p|k) \in \mathbb{X}_f$, can be considered [96]. For sufficiently long prediction and control horizons, the constraint $\mathbf{x}(k+N_p|k) \in \mathbb{X}_f$ does not need to be included explicitly in the optimal control problem, being automatically satisfied for every initial state $\mathbf{x}(k)$ in a given compact set. In addition, state constraints are often softened $(s_2>0, R_2>0)$ in practical implementations, to guarantee global feasibility.

Finally, observe that the proposed MPC design can be readily extended to satellites in elliptic orbits and formations with large inter-spacecraft separations, by simply adopting a different set of linearized equations in place of the HCW equations (3.31). For elliptic orbits, the Tschauner-Hempel equations can be used [129]. For spacecraft which are far from each other, and therefore subject to differential gravitational perturbations, a suitable model is provided by the Schweighart-Sedwick equations [122].

3.3.4 Explicit LMPC

Even if the optimization problem (3.59) can be solved efficiently using existing QP algorithms, the required computations may not be feasible onboard small spacecraft. Moreover, the running time of QP solvers is in general not guaranteed, whereas the reliability of the control system is a primary concern for space applications. In this respect, one possibility is to use explicit MPC.

Before proceeding, it is useful to rewrite the constrained LMPC problem in terms of the simplified notation

$$\begin{aligned} & \min_{\boldsymbol{\eta}_{C}} & & \boldsymbol{\eta}_{C}^{T} \mathbf{H} \, \boldsymbol{\eta}_{C} + 2 \, \mathbf{x}_{C}^{T} \, \mathbf{G} \, \boldsymbol{\eta}_{C} \\ & \text{s.t.} & & \mathbf{M} \, \boldsymbol{\eta}_{C} \leq \mathbf{D} + \mathbf{E} \, \mathbf{x}_{C}, \end{aligned} \tag{3.61}$$

where the matrices H, G, M, D and E are obtained from (3.58) and (3.59). By defining the new variable

$$\mathbf{z} = \boldsymbol{\eta}_C + \mathbf{H}^{-1} \mathbf{G}^T \mathbf{x}_C, \tag{3.62}$$

(3.61) can be transformed by completing squares into the equivalent multi-parametric quadratic program

$$\min_{\mathbf{z}} \quad \mathbf{z} \mathbf{H} \mathbf{z}
\text{s.t.} \quad \mathbf{M} \mathbf{z} \leq \mathbf{D} + (\mathbf{E} + \mathbf{M} \mathbf{H}^{-1} \mathbf{G}^{T}) \mathbf{x}_{C}, \tag{3.63}$$

where \mathbf{x}_C , which appears only in the right hand side of this equation, is treated as a parameter vector.

Problem (3.63) can be solved explicitly for all the parameters \mathbf{x}_C inside a given polyhedral set $\bar{\mathbb{X}}_C$, as described, for example, in [8]. Hence, the explicit LMPC problem to be solved is

Problem 3.3.3.

$$\min_{\mathbf{z}} \quad \mathbf{z} \, \mathbf{H} \, \mathbf{z}
\text{s.t.} \quad \mathbf{M} \, \mathbf{z} \leq \mathbf{D} + (\mathbf{E} + \mathbf{M} \, \mathbf{H}^{-1} \mathbf{G}^{T}) \, \mathbf{x}_{C}
\quad \mathbf{x}_{C} \in \bar{\mathbb{X}}_{C}.$$
(3.64)

For the proposed MPC design, it is beneficial to consider a region of additional size $\mathbf{d}_s \geq \mathbf{0}$ with respect to the set defined by (3.37), together with the maximum excursion of the control. The resulting set \mathbb{P} is given by

$$\mathbb{P} = \{ \mathbf{x}_C : \mathbf{C} \, \mathbf{x} \le \mathbf{d} + \mathbf{d}_s, \, \gamma \in \mathbb{U} \}, \tag{3.65}$$

where $\mathbf{x}_C = [\mathbf{x}^T, \ \boldsymbol{\gamma}^T]^T$. Since the set \mathbb{P} is not closed, auxiliary bounds are specified for the along-track position and the velocity parameters using

$$-x_1 \le x_M \tag{3.66}$$

$$|x_4| < -k_2 x_1 + \varepsilon$$
, $|x_5| < -k_2 x_1 + \varepsilon$, $|x_6| < -k_2 x_1 + \varepsilon$, (3.67)

where x_M is the maximum feasible along-track separation between the two spacecraft, $\varepsilon \geq 0$ is a specified tolerance and k_2 is a positive slope. The linear dependence of the velocity bounds (3.67) on x_1 is justified by collision avoidance requirements and by the linear dependence of the LoS constraints on x_1 . The inequalities (3.66)-(3.67) define the set

$$\mathbb{P}_a = \left\{ \mathbf{x} : \mathbf{C}_a \, \mathbf{x} \le \mathbf{d}_a \right\},\tag{3.68}$$

where

$$\mathbf{C}_{a} = \begin{bmatrix} -1 & 0 & 0 & 0 & 0 & 0 \\ k_{2} & 0 & 0 & 1 & 0 & 0 \\ k_{2} & 0 & 0 - 1 & 0 & 0 \\ k_{2} & 0 & 0 & 0 & 1 & 0 \\ k_{2} & 0 & 0 & 0 & -1 & 0 \\ k_{2} & 0 & 0 & 0 & 0 & 1 \\ k_{2} & 0 & 0 & 0 & 0 -1 \end{bmatrix}, \quad \mathbf{d}_{a} = \begin{bmatrix} x_{M} \\ \varepsilon \end{bmatrix}.$$

$$(3.69)$$

Combining (3.65)-(3.68), the parameter space takes the final form

$$\bar{\mathbb{X}}_C = \left\{ \mathbf{x}_C : \mathbf{x}_C \in \mathbb{P} \cap \mathbb{P}_a \right\}. \tag{3.70}$$

The solution $\mathbf{z}^*(\mathbf{x}_C)$ to Problem 3.3.3 is a piece-wise affine linear function defined over a polyhedral partition of $\bar{\mathbb{X}}_C$. Hence, the control law

$$\mathbf{u}(\mathbf{x}_C) = \begin{bmatrix} \mathbf{L}(\mathbf{0}) & \mathbf{0} \end{bmatrix} (\mathbf{z}^*(\mathbf{x}_C) - \mathbf{H}^{-1} \mathbf{G}^T \mathbf{x}_C), \qquad (3.71)$$

which is obtained from (3.54) and (3.62), observing that $\eta_C = [\eta^T \mathbf{s}^T]^T$, is piece-wise affine and can be stored in the following look-up table form

$$\mathbf{u}(\mathbf{x}_C) = \mathbf{K}_m \, \mathbf{x}_C + \mathbf{g}_m \quad \text{if} \quad \mathbf{H}_m \, \mathbf{x}_C \le \mathbf{b}_m, \ m = 1, \dots, N_{\text{mpc}}, \tag{3.72}$$

where the polyhedral sets $\{\mathbf{H}_m\mathbf{x}_C \leq \mathbf{b}_m\}$, $m=1,\ldots,N_{\mathrm{mpc}}$ are the partition of $\bar{\mathbb{X}}_C$, N_{mpc} indicates the number of regions in the partition, and \mathbf{K}_m , \mathbf{H}_m , \mathbf{g}_m , \mathbf{b}_m are found from the solution to (3.64). In this thesis, the Multi-Parametric Toolbox [64] is employed to solve Problem 3.3.3.

The on-line evaluation of $\mathbf{u}(\mathbf{x}_C(k))$ consist of locating the state space region and hence the look-up table entry that contains the pre-computed control law for a given $\mathbf{x}_C(k) = [\mathbf{x}^T(k), \mathbf{u}^T(k-1)]^T$, through the solution of a set-membership problem. Hence, the on-line computational load is limited to a piece-wise affine function evaluation.

Remark 3.3.3. The asymptotic stability of an explicit control law can be checked a posteriori, see e.g. [117], for cases in which the a priori stability of the design is not guaranteed.

It can be concluded that the control law (3.72) provides an approximate solution to Problem 3.3.2 (and hence to Problem 3.3.1) for a suitable tuning of the parameters \mathbf{Q}_c , \mathbf{Q}_f , \mathbf{R}_c in (3.36), a_j , N_j in (3.44)-(3.45) and \mathbf{R}_s in (3.59). To enable the implementation of the control law, within an autonomous GNC scheme, the position and velocity of the chaser with respect to the target must be known. To this aim, a relative navigation EKF is presented in Section 5.3, which provides an estimate of the vector $\mathbf{x}(k)$. A detailed simulation-based assessment of the performance achievable under this design is given in Section 6.2, in comparison to standard MPC (i.e., without Laguerre parametrization of the input signal, see (3.46)) and LQR techniques.

Precise Attitude Control

Motivated by the potential application of EP-based reaction control systems to Earth observation and communication satellites, this chapter studies the problem of maintaining the attitude of a spacecraft precisely aligned to a given orientation, using on/off actuators. Due to the presence of on/off restrictions and of persisting disturbances, affecting the attitude dynamics, the problem does not admit a constant steady state solution. Instead, an oscillating motion about the set-point must be accepted. In establishing such type of motion, the minimization of both the propellant consumption and the on/off switching frequency of the actuators is a key requirement.

The first contribution of this chapter is an analytical upper bound on the minimum switching frequency required to guarantee fuel-optimal oscillations with prescribed amplitude about the set-point, based on the extension to the coupled multivariable case of the classical single-axis solution. The provided upper bound does not depend on the relative phases of the oscillations of each state variable. On the basis of this observation, a less conservative solution is found, by exploiting phase synchronization. In order to track the periodic trajectories corresponding to the provided solutions, a minimum switching control law is derived. Finally, an MPC scheme, based on the real-time optimization of the fuel consumption, as well as the number of actuator switching cycles, is proposed. This last approach is general enough to be applied for spacecraft with nonsymmetric thruster configurations (e.g. overactuated ACS), and in the presence of angular rate constraints.

The material in this chapter is mainly based on [52] and [81].

4.1 Problem setting

In this section, the model describing the attitude error dynamics is introduced, and the main features of the attitude control problem are presented.

4.1.1 Reference attitude

It is fairly common in the attitude control literature to describe the orientation of a spacecraft in terms of the tracking error of a reference LVLH attitude. This is typically the attitude regime the vehicle is designed for (e.g. to keep the observation window towards Earth, radiators out of the sun, and solar arrays exposed to the sun). Moreover, the accelerations required for orbit control are best expressed in the LVLH frame, as seen in Chapter 3.

The matrix \mathbf{R}_{IL} which describes the orientation of the LVLH frame with respect to the ECI frame (see Fig. 2.1), for a spacecraft at position \mathbf{r} with respect to the Earth's center of mass, is given by

$$\mathbf{R}_{IL} = \left[\frac{\mathbf{h}}{h} \times \frac{\mathbf{r}}{r}, -\frac{\mathbf{h}}{h}, -\frac{\mathbf{r}}{r} \right]^{T}. \tag{4.1}$$

where $\mathbf{h} = \mathbf{r} \times \dot{\mathbf{r}}$ denotes the spacecraft specific angular momentum and $h = \|\mathbf{h}\|$. For control design purposes, the rotation (4.1) is parameterized by the quaternion \mathbf{q}_{IL} . From (2.2) and (4.1), it follows that the LVLH frame rotates 360 deg per orbital period about its Y_{LVLH} axis, with an instantaneous angular velocity given by

$$\boldsymbol{\omega}_L = \begin{bmatrix} 0, & -\omega_L, & 0 \end{bmatrix}^T. \tag{4.2}$$

where $\omega_L = h/r^2$. For circular orbits, $\omega_L = n = \sqrt{\mu/r^3}$ is constant.

4.1.2 Attitude error dynamics

Let \mathbf{q}_{LI} denote the inverse rotation of (4.1) in quaternion form. Using quaternion algebra, the attitude error \mathbf{q}_{LB} , corresponding to the orientation of the spacecraft body frame relative to the LVLH frame, can be expressed as

$$\mathbf{q}_{LB}=\mathbf{q}_{IB}\circ\mathbf{q}_{LI},$$

where \mathbf{q}_{IB} is the solution to (2.26). If the attitude error is small, it can be approximated by the three-dimensional rotation vector $\delta \boldsymbol{\theta}$, which is obtained from the vector part $\vec{\mathbf{q}}_{LB}$ of the attitude error quaternion as

$$\delta \theta = 2\vec{\mathbf{q}}_{LB}.\tag{4.3}$$

The angular rate error is given by the difference between the body frame rotation rate ω and the LVLH frame rotation rate, expressed in the body frame

$$\delta \omega = \omega - \widetilde{\omega},\tag{4.4}$$

where ω is the solution to (2.31) and $\tilde{\omega} = \mathbf{R}_{IB}\mathbf{R}_{IL}^T \omega_L$.

For small deviations about the setpoint, the tracking error dynamics can be linearized with negligible loss in accuracy. Because the setpoint is given by the LVLH frame orientation and angular rate, the attitude error dynamics are obtained by differentiating (4.3)-(4.4) and linearizing the resulting expression. The time derivative of $\delta\theta$ is simply¹

$$\delta \dot{\boldsymbol{\theta}} = \delta \boldsymbol{\omega}. \tag{4.5}$$

For linearization purposes, one can assume that the inertia matrix $\mathbf{I}_M = \operatorname{diag}(I_x, I_y, I_z)$ is constant in (4.4) [84]. In this case, substituting (2.31) into (4.4) and differentiating (4.4) with respect to time yields

$$\delta \dot{\boldsymbol{\omega}} = \mathbf{I}_{M}^{-1} \boldsymbol{\tau} - \mathbf{I}_{M}^{-1} (\widetilde{\boldsymbol{\omega}} + \delta \boldsymbol{\omega})^{\times} \mathbf{I}_{M} (\widetilde{\boldsymbol{\omega}} + \delta \boldsymbol{\omega}) - \dot{\widetilde{\boldsymbol{\omega}}}. \tag{4.6}$$

¹Alternatively, one can set $\delta \omega = \omega - \omega_L$ in (4.4). Then $\delta \dot{\theta} = \delta \omega - \omega_L^{\times} \delta \theta$.

4.1. Problem setting 53

Observing that $\widetilde{\boldsymbol{\omega}} \approx (\mathbf{I} - \delta \boldsymbol{\theta}^{\times}) \boldsymbol{\omega}_L$ and $\dot{\widetilde{\boldsymbol{\omega}}} \approx -\delta \boldsymbol{\omega}^{\times} (\mathbf{I} - \delta \boldsymbol{\theta}^{\times}) \boldsymbol{\omega}_L$ for small rotations, and linearizing (4.6) about $(\delta \boldsymbol{\theta}, \delta \boldsymbol{\omega}) = (\mathbf{0}, \mathbf{0})$ gives

$$\delta \dot{\omega} = \mathbf{A}_1 \delta \boldsymbol{\theta} + \mathbf{A}_2 \delta \boldsymbol{\omega} + \mathbf{I}_M^{-1} \boldsymbol{\tau}, \tag{4.7}$$

where the torque τ is treated as an exogenous input and the matrices A_1 , A_2 turn out to be

$$\mathbf{A}_{1} = \begin{bmatrix} \frac{I_{z} - I_{y}}{I_{x}} \omega_{L}^{2} & 0 & 0 \\ 0 & 0 & 0 & 0 \\ 0 & 0 & \frac{I_{x} - I_{y}}{I_{z}} \omega_{L} \end{bmatrix}, \quad \mathbf{A}_{2} = \begin{bmatrix} 0 & 0 & \frac{I_{x} - I_{y} + I_{z}}{I_{x}} \omega_{L} \\ 0 & 0 & 0 & 0 \\ \frac{I_{y} - I_{x} - I_{z}}{I_{z}} \omega_{L} & 0 & 0 \end{bmatrix}.$$

$$(4.8)$$

Notice the cross coupling terms in (4.8) due to the rotation of the LVLH frame.

As long as precise attitude control on nearly circular orbits (e.g. GEO) is concerned, the dynamic coupling in (4.7)-(4.8) is tipically negligible because $|\mathbf{A}_1\delta\theta+\mathbf{A}_2\delta\omega|\ll |\mathbf{I}_M^{-1}\tau|$, see e.g. [34]. In this case, the error dynamics can be approximated by the double integrator system

$$\delta \ddot{\boldsymbol{\theta}} = \mathbf{I}_{M}^{-1} \boldsymbol{\tau},\tag{4.9}$$

where au is given by

$$\tau = \tau_e + \tau_u,\tag{4.10}$$

and $\tau_e = \tau_g + \tau_d + \tau_r + \tau_m + \tau_o$ denotes the disturbance torque vector (see (2.32) and (2.44)).

4.1.3 Attitude control system

A typical design for attitude control systems based on electric propulsion consists of on-off reaction thrusters mounted at a fixed orientation with respect to the spacecraft body frame. For this design, the control torque τ_u in (4.10) can be expressed as

$$\tau_u = \mathbf{G}\,\boldsymbol{\mu},\tag{4.11}$$

where $\mu \in \{0,1\}^m$ indicates the on-off activation commands of the m thrusters (or thruster pairs) and the matrix \mathbf{G} expresses the linear mapping from this command to the control torque. Notice that, for the common case of symmetric thruster configurations $\mathbf{G} = [\widetilde{\mathbf{G}}, -\widetilde{\mathbf{G}}]$, equation (4.11) can be rewritten as

$$\boldsymbol{\tau}_u = \widetilde{\mathbf{G}} \, \widetilde{\boldsymbol{\mu}},\tag{4.12}$$

where $\widetilde{\boldsymbol{\mu}} \in \{-1,0,1\}^{\frac{m}{2}}$.

Attitude control torques are produced by expelling propellant mass. Because spacecraft only contain a finite amount of propellant and refill operations are costly and impractical, the amount of propellant mass being expended ultimately dictates the lifetime of a space mission. Consequently, the minimization of the fuel consumption is the primary requirement for the considered problem. Besides the fuel consumption, restrictions on the duration and number of thruster firings have to be accounted for. In particular, the number of firing cycles

has an impact on both the lifetime and the specific impulse of the thrusters, due to valve wear and transient effects on the actuator dynamics.

An efficient attitude control scheme must then focus on simultaneously minimizing the fuel consumption and the thruster switching frequency, while at the same time enforcing the attitude control accuracy requirements. The minimum fuel and minimum switching control problems are addressed next.

4.2 Minimum fuel control

This section tackles the problem of minimizing the fuel consumption of the attitude control system, under the assumptions that the attitude dynamics can be approximated by the system (4.9), and that the thruster configuration is symmetric. Combining (4.9)-(4.10) and (4.12), the tracking error dynamics can be expressed as

$$\delta \ddot{\boldsymbol{\theta}}(t) = \mathbf{B} \, \widetilde{\boldsymbol{\mu}}(t) + \mathbf{d},\tag{4.13}$$

where $\theta(t) \in \mathbb{R}^n$, $\mathbf{B} = \mathbf{I}_M^{-1} \widetilde{\mathbf{G}}$ and $\mathbf{d} = \mathbf{I}_M^{-1} \boldsymbol{\tau}_e$. Notice that, although in the considered application n=3, in the following the minimum fuel and minimum switching problems will be studied for the more general case in which n is arbitrary. The assumption is made that \mathbf{B} is square and nonsingular, and that $\|\mathbf{B}^{-1}\mathbf{d}\|_{\infty} < 1$, to ensure the controllability of the system. In this case, (4.13) describe a system of n double integrators, controlled by $\frac{m}{2} = n$ switching inputs $\widetilde{\boldsymbol{\mu}}$, which are coupled through the $n \times n$ matrix \mathbf{B} .

The control accuracy requirements are typically dictated by the spacecraft payload, and specified as the maximum allowed deviation from the set-point. Hence, the objective of the control system is to guarantee that

$$\|\mathbf{W}_{\theta} \,\delta\boldsymbol{\theta}(t)\|_{\infty} \le 1, \quad \forall t \ge \bar{t}$$
 (4.14)

for some $\bar{t} \geq 0$, where \mathbf{W}_{θ} can be taken as a diagonal weighting matrix. By applying the fuel consumption expression (2.18) to the thruster configuration specified by (4.12), under the assumption that the thruster specific impulse is fixed and equal for all thrusters, a cost function proportional to the average amount of expended fuel is defined as

$$J_f(\widetilde{\boldsymbol{\mu}}) = \lim_{T \to \infty} \frac{1}{T} \int_0^T \|\widetilde{\boldsymbol{\mu}}(t)\|_1 dt.$$
 (4.15)

Let us now introduce the new state variables $\mathbf{x}(t) = \mathbf{T}^{-1} \delta \boldsymbol{\theta}(t)$, where

$$T = BD, (4.16)$$

$$\mathbf{D} = \operatorname{diag}(\operatorname{sgn}(\rho_1), \dots, \operatorname{sgn}(\rho_n)), \tag{4.17}$$

with sgn(0) = 1, and $\varrho = \mathbf{B}^{-1}\mathbf{d}$. Then, system (4.13) can be rewritten as

$$\ddot{\mathbf{x}}(t) = \mathbf{u}(t) + \mathbf{k}\,,\tag{4.18}$$

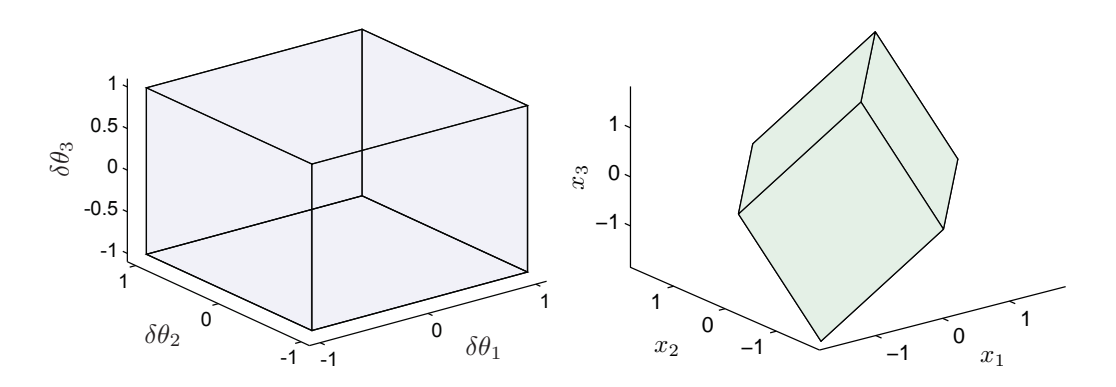


Figure 4.1: Feasible set defined by (4.14).

Figure 4.2: Feasible set defined by (4.20).

where $\mathbf{k} = \mathbf{T}^{-1}\mathbf{d}$ and $\mathbf{u} = \mathbf{D}^{-1}\widetilde{\boldsymbol{\mu}}$, with

$$\mathbf{u} \in \{-1, 0, 1\}^n. \tag{4.19}$$

In the following, the j-th entries of the vectors \mathbf{x} and \mathbf{u} are denoted by x_j and u_j , respectively. By definition of \mathbf{T} and \mathbf{D} , it turns out that $\mathbf{k} \geq 0$ in (4.18). Moreover, the constraint (4.14) takes the form

$$\|\mathbf{C}\mathbf{x}(t)\|_{\infty} \le 1, \quad \forall t \ge \bar{t},$$
 (4.20)

where $C = W_{\theta}T$. Notice that, for $t \geq \bar{t}$, (4.20) is equivalent to

$$\max_{i} \max_{t} |w_i(t)| \le 1, \tag{4.21}$$

where

$$w_i(t) = \sum_{j=1}^{n} c_{ij} x_j(t), \tag{4.22}$$

and the coefficients c_{ij} are the entries of C.

In the formulation (4.18)-(4.20), the n double integrators have been decoupled, but the state constraints (4.20) are now coupled. In fact, while the feasible set for $\delta \theta(t)$ in (4.13) is a box, that of $\mathbf{x}(t)$ in (4.18) is a parallelotope, as illustrated in Figs. 4.1-4.2. Moreover, observe that

$$J_f(\boldsymbol{\mu}) = J_f(\widetilde{\boldsymbol{\mu}}) = J_f(\mathbf{u}). \tag{4.23}$$

Then, the minimum fuel control problem can be formulated as follows.

Problem 4.2.1. Find a feedback control law $\mathbf{u}(\mathbf{x},\dot{\mathbf{x}})$, which solves the optimal control problem

$$\min_{\mathbf{u}} J_f(\mathbf{u})
\text{s.t.} (4.18), (4.19), (4.20).$$

The solution to Problem 4.2.1, for the ideal case in which ${\bf k}={\bf 0}$ and the more realistic case in which ${\bf k}>{\bf 0}$ in (4.18), is presented hereafter.

4.2.1 Unperturbed dynamics

Consider the system (4.18) in the absence of perturbations, so that $\mathbf{k}=\mathbf{0}$. Moreover, replace (4.20) by

$$\mathbf{x}(t) = \mathbf{0}, \quad \forall t \ge \bar{t}. \tag{4.25}$$

In this case, both the system (4.18) and the state constraints (4.25) are decoupled, and problem (4.24) reduces to a set of n scalar problems of the form

$$\min_{u} \quad J_{f}(u)$$
s.t. $\ddot{x} = u$

$$x(t) = 0 \quad \forall t \ge \bar{t}$$

$$u \in \{-1, 0, 1\}.$$

$$(4.26)$$

Observe that any control law able to steer the system $\ddot{x} = u$ to the origin in finite time, from any initial condition, solves problem (4.26) with the optimal cost $J_f^*(u) = 0$, because for such control law the steady state fuel consumption is zero. One example is represented by the well-know time-optimal control law (see e.g. [4])

$$u(x, \dot{x}) = \begin{cases} -1 & \text{if} \quad s_t(x, \dot{x}) > 0 \quad \text{or} \quad s_t(x, \dot{x}) = 0 \text{ and } \dot{x} > 0 \\ 1 & \text{if} \quad s_t(x, \dot{x}) < 0 \quad \text{or} \quad s_t(x, \dot{x}) = 0 \text{ and } \dot{x} < 0, \end{cases}$$
(4.27)

where switching function $s_t(x, \dot{x})$ is given by

$$s_t(x, \dot{x}) = x + \frac{1}{2}\dot{x}|\dot{x}|.$$
 (4.28)

Two state trajectories resulting from the application of this control law to the system $\ddot{x} = u$ are reported in the phase plane shown in Fig. 4.3.

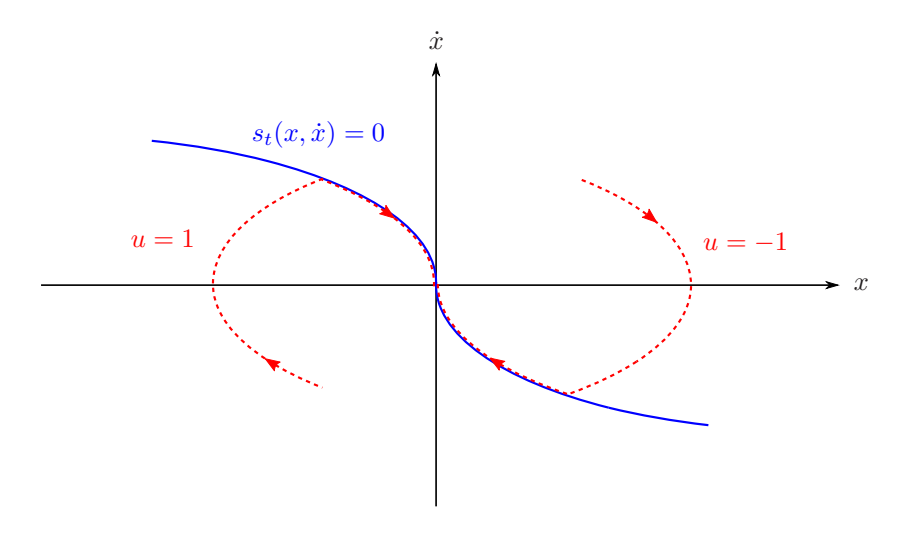


Figure 4.3: Time-optimal trajectories (dashed) from the application of (4.27)-(4.28).

Hence, it is straightforward to verify that the control law (4.27)-(4.28), or equivalently any control law satisfying (4.25), provides a solution to Problem 4.2.1 when applied for every input channel of the unperturbed system (4.18), independently from the choice of the constraint matrix C in (4.20).

Unfortunately, such a trivial result holds only if the duration of the thruster firings can be made arbitrarily small, which is often not the case in practical applications. When the impulse provided by the control system has a fixed lower bound, the so-called minimum impulse bit, the attitude control accuracy requirements can have a significant impact on the fuel consumption, as explained next.

4.2.2 Minimum impulse bit dynamics

In the absence of disturbance torques, it would theoretically be possible place the satellite into a perfect LVLH attitude, rotating about the $Y_{\rm LVLH}$ axis 360 deg per orbit to remain pointed towards the Earth's surface. In practical applications, however, constraints on the minimum duration of thruster firings and hence on the minimum impulse bit provided by the attitude control system usually prevent the angular rate of the spacecraft from being driven exactly to zero. In such cases, the solution to the minimum fuel control problem generally takes the form of a limit-cycle oscillation.

An example of a limit cycle due to the minimum impulse bit and hence the minimum rate change Δv_{min} provided by the control system is reported in the phase plane shown in Fig. 4.4, for the single-input system $\ddot{x}=u$. In this figure, u=-1 and u=1 are applied for the minimum possible firing time to reverse the sign of the angular velocity before exceeding the bound defined by $|x(t)| \leq b$. Notice that b also represents the amplitude of the resulting limit cycle. Because pulses of minimum duration are considered, the angular rate dynamics

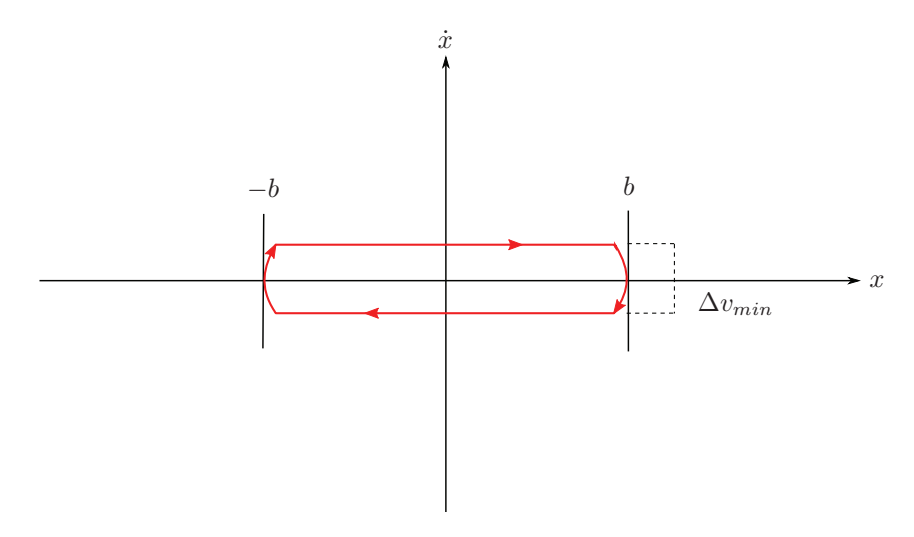


Figure 4.4: Minimum impulse bit limit cycle.

can be approximated by a sequence of impulsive velocity changes, from which it follows that

the average fuel consumption is inversely proportional to the time between two consecutive pulses and hence to b, according to

$$J_f(u) = \frac{\Delta v_{min}}{b}. (4.29)$$

This explains why the desire of a high pointing accuracy (i.e. a small *b*) can be in conflict with the requirement to minimize the fuel consumption of a reaction control system.

Let us assume that the desired long-term behaviour for the multi-input system (4.18), with $\mathbf{k} = \mathbf{0}$, consists in limit cycles of the form depicted in Fig. 4.4 with amplitudes b_j , for all axes $j = 1, \ldots, n$, and that the minimum impulse bit is fixed and equal for all thrusters. Then, a cost function that accounts for the fuel consumption of system (4.18) is obtained from (4.29) as

$$J_f(\mathbf{u}) = \sum_{j=1}^n \frac{\Delta v_{min}}{b_j}.$$
 (4.30)

By using (4.21)-(4.22), under the assumption that $|x_i(t)| \le b_i$, one has that

$$\max_{t} |w_i(t)| \le \max_{t} \sum_{j=1}^{n} |c_{ij}| |x_j(t)| \le \sum_{j=1}^{n} |c_{ij}| |b_j,$$
(4.31)

and hence (4.20) can be enforced by imposing

$$\|\overline{\mathbf{C}}\,\mathbf{b}\|_{\infty} \le 1,\tag{4.32}$$

where $\overline{\mathbf{C}}$ is the matrix whose entries are $|c_{ij}|$ and $\mathbf{b} = [b_1, \dots, b_n]$. By replacing (4.20) with (4.32) and enforcing (4.30), problem (4.24) boils down to

$$\min_{\mathbf{b}} \quad \Delta v_{min} \sum_{j=1}^{n} \frac{1}{b_{j}}$$
s.t. $\|\overline{\mathbf{C}} \mathbf{b}\|_{\infty} \le 1$

$$b_{j} > 0, \quad j = 1, \dots, n.$$
(4.33)

Problem (4.33) can be solved numerically for a given constraint matrix $\overline{\mathbb{C}}$, yielding a vector \mathbf{b}^* of optimal limit cycle amplitudes. In order to steer the state of the system (4.18) to the periodic trajectories corresponding to the solution to (4.33), the control law (4.27) can be modified by adding a symmetric deadband of amplitude b_i^* for all axes, as follows

$$u_{j}(x_{j}, \dot{x}_{j}) = \begin{cases} -1 & \text{if} \quad s_{t}(x_{j}, \dot{x}_{j}) \ge b_{j}^{*} \\ 1 & \text{if} \quad s_{t}(x_{j}, \dot{x}_{j}) \le -b_{j}^{*} \\ 0 & \text{else}, \end{cases}$$
(4.34)

where $j = 1, \ldots, n$.

Proposition 4.2.1. The control law (4.34) provides a suboptimal solution to Problem 4.2.1 for the case k = 0, in the presence of minimum impulse bit restrictions.

Proof. Considering input quantization, the control law (4.34) drives the solution of (4.18) to limit cycles of amplitudes b_j^* , $j=1,\ldots,n$, in finite time, from any initial condition. The suboptimality follows from the fact that the optimal cost of problem (4.33) is an upper bound on the optimal cost of problem (4.24), due to the particular class of periodic trajectories considered in (4.33).

4.2.3 Perturbed dynamics

In many practical applications, the attitude error dynamics (4.18) are perturbed by a disturbance term $\mathbf{k}>\mathbf{0}$ that is approximately constant with respect to the error dynamics timescale. Examples include disturbance torques arising from atmospheric drag at low orbital altitudes and torques generated during station-keeping operations, due to misalignment of the orbit control system (see Section 2.3). A disturbance estimator is often capable of identifying such contributions. Therefore, in the following it is assumed that \mathbf{k} is constant and known.

Let us analyze first the fuel-optimal control problem for the single-input system

$$\ddot{x}(t) = u(t) + k,$$
 (4.35)

where k > 0 is a fixed scalar parameter and

$$u(t) \in \{-1, 0, 1\}.$$
 (4.36)

In this case, the constraint (4.20) takes the form

$$|x(t)| \le b, \quad \forall t \ge \bar{t},\tag{4.37}$$

where b is a scalar bound, and problem (4.24) becomes

$$\min_{u} J_f(u)
s.t. (4.35), (4.36), (4.37).$$
(4.38)

The following proposition is a standard result from optimal control theory.

Proposition 4.2.2. A minimizer of problem (4.38) satisfies

$$u(t) \in \{-1, 0\}. \tag{4.39}$$

Moreover,

$$J_f^*(u) = k. (4.40)$$

Proof. Let u(t) be an input signal guaranteeing that (4.37) holds. Then, $\dot{x}(t)$ is bounded and therefore

$$\lim_{T \to \infty} \frac{1}{T} \left(\dot{x}(0) + \int_0^T \left(u(t) + k \right) dt \right) = 0,$$

which gives

$$\lim_{T \to \infty} \frac{1}{T} \int_0^T u(t) \, dt = -k. \tag{4.41}$$

Hence, the solution to (4.38) is also a minimizer of problem

$$\min_{u} J_f(u)
s.t. (4.36), (4.41).$$
(4.42)

It is straightforward to check that a minimizer of (4.42) satisfies $u(t) \in \{-1, 0\}$. By enforcing this condition in (4.41), it follows that $J_f(u) = k$.

Remark 4.2.1. *Notice that any input sequence satisfying* (4.39) *and guaranteeing that* (4.37) *holds, satisfies also* (4.40) *and therefore it is a fuel-optimal solution.*

It is well-known (see e.g. [4]) that a fuel-optimal control law for system (4.35) is

$$u(t) = \begin{cases} -1 & \text{if} \quad s(x, \dot{x}) > 0 \quad \text{or} \quad s(x, \dot{x}) = 0 \text{ and } \dot{x} > 0 \\ 0 & \text{if} \quad s(x, \dot{x}) < 0 \quad \text{or} \quad s(x, \dot{x}) = 0 \text{ and } \dot{x} < 0, \end{cases}$$
(4.43)

where the switching function $s(x, \dot{x})$ is given by

$$s(x, \dot{x}) = \begin{cases} x - \frac{1}{2(k-1)} \dot{x}^2 & \text{if} \quad \dot{x} \ge 0\\ x - \frac{1}{2k} \dot{x}^2 & \text{if} \quad \dot{x} < 0. \end{cases}$$
(4.44)

Such a control law guarantees that the trajectory of the closed-loop system converges to the origin in finite time, from any initial condition, as illustrated in Fig. 4.5. Hence, it also enforces (4.37) indefinitely and therefore it solves problem (4.38).

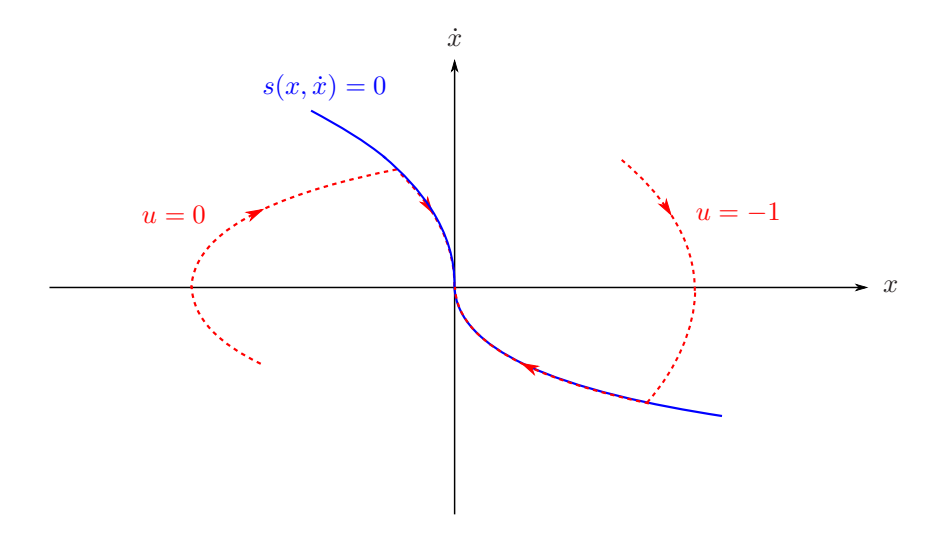


Figure 4.5: Fuel-optimal trajectories (dashed) from the application of (4.43)-(4.44).

For the multivariable system (4.18), the minimum-fuel problem amounts to minimising (4.23). In this case, the following proposition holds.

Proposition 4.2.3. A minimizer of problem (4.24) satisfies

$$\mathbf{u} \in \{-1, 0\}^n. \tag{4.45}$$

Moreover

$$J_f^*(\mathbf{u}) = \|\mathbf{k}\|_1. \tag{4.46}$$

Proof. Thanks to the decoupling provided by (4.16), the optimality condition (4.39) can be applied for each input channel of (4.18), leading to (4.45)-(4.46).

Consequently, it can be easily verified that the application of the control law (4.43)-(4.44) to each input channel of (4.18) provides a solution to Problem 4.2.1, for $\mathbf{k}>\mathbf{0}$. However, notice that an infinite switching frequency is required to keep the trajectory of system (4.13) exactly at the origin with an input of the form (4.45), which translates into undesirable chattering of the actuators in practical implementations. This motivates the problem of minimizing both the fuel consumption and the switching frequency of the control system, while keeping the attitude error within the bound specified by (4.20), as described in the next section.

4.3 Minimum switching oscillations

A well-established application of attitude control systems based on electric propulsion is represented by the compensation of persisting disturbance torques [70]. In this case, problem (4.24) admits multiple fuel-optimal solutions, as discussed in Section 4.2.3. The aim of this section is to find, among all these solutions, the one which minimises the actuator switching frequency, in order to maximise the lifetime and the performance of the ACS.

Notice that the switching frequency of a single actuator corresponds to the average number of input transitions per time unit commanded by the control system. Therefore, a cost function that accounts for the average number of input transitions of system (4.18) (and hence of system (4.13)) is given by

$$J_t(\mathbf{u}) = \lim_{T \to \infty} \frac{1}{T} \int_0^T \|\dot{\mathbf{u}}(t)\|_1 dt.$$
 (4.47)

Another possibility is represented by the upper bound of the switching frequency per actuator

$$J_s(\mathbf{u}) = \max_j \lim_{T \to \infty} \frac{1}{T} \int_0^T |\dot{u}_j(t)| dt.$$
 (4.48)

Because (4.48) is an useful indicator of the propulsion system lifetime, it will be adopted throughout this section. Hence, the minimum switching problem can be formulated as

Problem 4.3.1.

$$\min_{\mathbf{u}} J_s(\mathbf{u})
s.t. (4.18), (4.20), (4.45),$$
(4.49)

with k > 0 in (4.18).

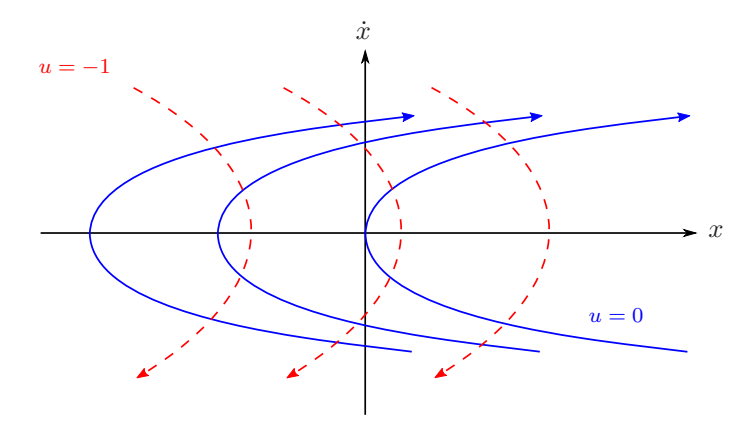


Figure 4.6: Trajectories of system (4.35) for u = 0 (solid) and u = -1 (dashed).

In the following, the minimum switching problem is reviewed for a single-input double integrator, and the trajectory parameterizations necessary to solve problem (4.49) is introduced. Then, two different suboptimal solutions to Problem 4.3.1 are derived.

4.3.1 Single-input problem

For the perturbed double integrator system (4.35), the minimum switching problem (4.49) takes the form

$$\min_{u} J_{s}(u) = \lim_{T \to \infty} \frac{1}{T} \int_{0}^{T} |\dot{u}(t)| dt$$
s.t. (4.35), (4.37), (4.39).

The solution to (4.50) can be found by using phase plane arguments. The trajectories obtained for u(t)=0 and u(t)=-1 in (4.35) are reported in the phase plane in Fig. 4.6. From (4.37) and (4.39), it follows that fuel-optimal state trajectories are bounded paths switching between the curves in Fig. 4.6.

Let

$$\psi^{L} = \{(x, \dot{x}) : x - \frac{1}{2k} \dot{x}^{2} = -b, \quad -b \leq x < \bar{x}\},$$

$$\psi^{U} = \{(x, \dot{x}) : x - \frac{1}{2(k-1)} \dot{x}^{2} = b, \quad \bar{x} \leq x \leq b\},$$
(4.51)

where $\bar{x} = b(1-2k)$. Then, the following result characterizes the solution to problem (4.50) [60, 69].

Proposition 4.3.1. Every optimal solution $u^*(t)$ of problem (4.50) is such that the resulting trajectory satisfies $(x, \dot{x}) \in \psi^U \cup \psi^L$ and

$$u^*(t) = \begin{cases} -1 & \text{if } (x(t), \dot{x}(t)) \in \psi^U \\ 0 & \text{if } (x(t), \dot{x}(t)) \in \psi^L, \end{cases}$$
(4.52)

for all $t \geq \tilde{t}$, for some $\tilde{t} \geq 0$. Moreover, the resulting minimum switching frequency is

$$J_s^*(u) = 2\sqrt{\gamma/b},\tag{4.53}$$

where

$$\gamma = k(1 - k)/16. \tag{4.54}$$

Proof. By integrating system (4.35) with either u=0 or u=-1, one gets the trajectories $x-\frac{1}{2(k-1)}\dot{x}^2=\beta_1$ and $x-\frac{1}{2k}\dot{x}^2=\beta_2$, respectively, with $\beta_1,\ \beta_2\in\mathbb{R}$ (see Fig. 4.6). Problem (4.50) requires to maximize the average time between consecutive input transitions, while satisfying constraint (4.37). This can be done by choosing the trajectory ψ^U when u=-1 ($\beta_1=b$) and ψ^L when u=0 ($\beta_2=-b$) i.e. (4.52). By intersecting ψ^U and ψ^L , straightforward calculations allow one to compute the times spent over each trajectory, which amount to

$$t^U = 4\sqrt{\frac{bk}{1-k}} \qquad \text{if} \quad u = -1,$$

$$t^L = 4\sqrt{\frac{b(1-k)}{k}} \qquad \text{if} \quad u = 0.$$

Hence, the period of the resulting trajectory is $p=t^U+t^L=\sqrt{b/\gamma}$, with γ given by (4.54). Since two input switchings per period are required, $J_s^*(u)=2/p=2\sqrt{\gamma/b}$. Finally, it can be observed that the limit cycle defined by ψ^U and ψ^L can be reached in finite time from any initial condition x(0), $\dot{x}(0)$, with only one input switching, which clearly does not affect the optimal cost $J_s^*(u)$

Proposition 4.3.1 provides a minimum switching and fuel-optimal solution for system (4.35), under the constraint (4.36) and (4.37), in terms of a limit cycle in the phase plane. Fig. 4.7 shows the resulting trajectory. Through straightforward manipulations, the periodic trajectory of system (4.35) along the limit cycle $\psi^U \cup \psi^L$ can be expressed as

$$x(t) = a f(\lambda),$$

$$a = p^2 \gamma,$$

$$\lambda = \text{mod}(t/p + \phi, 1),$$

$$(4.55)$$

where a=b is the amplitude, p is the period, $\phi \in [0,1]$ is the phase, γ is given by (4.54), and $f(\lambda) \in [-1,1]$ is defined as

$$f(\lambda) = \begin{cases} 1 - \frac{8}{k} (\lambda - \frac{k}{2})^2 & \text{if } 0 \le \lambda \le k \\ -1 - \frac{8}{k - 1} (\lambda - \frac{k + 1}{2})^2 & \text{if } k < \lambda < 1. \end{cases}$$
(4.56)

Then, the optimal input signal $u^*(t)$ in (4.52) can be rewritten as

$$u^{*}(t) = \begin{cases} -1 & \text{if } 0 \le \lambda \le k \\ 0 & \text{if } k < \lambda < 1. \end{cases}$$
 (4.57)

From (4.55)-(4.57), it follows that the optimal input signal $u^*(t)$ is pulse-width modulated with period $p^* = \sqrt{b/\gamma}$ and duty cycle k. The periodic solution (4.55)-(4.56) will be exploited in the next section, to parameterize the solutions of Problem 4.3.1.

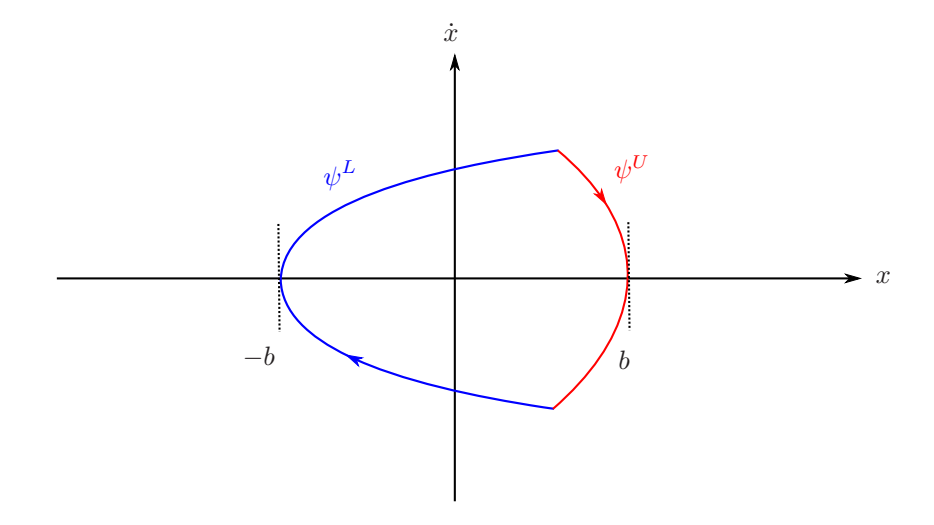


Figure 4.7: Fuel/switch-optimal solution to problem (4.50).

4.3.2 Multi-input problem

Problem 4.3.1 is hard to solve if all feasible solutions to (4.18) are considered. Therefore, taking inspiration from the optimal solution (4.55)-(4.57) of the single-input problem, we restrict our attention to solutions of the form

$$x_{j}(t) = a_{j} f(\lambda_{j}),$$

$$\lambda_{j} = \text{mod}(t/p_{j} + \phi_{j}, 1),$$

$$a_{j} = p_{j}^{2} \gamma_{j},$$

$$\gamma_{j} = k_{j} (1 - k_{j})/16,$$
(4.58)

where a_j and ϕ_j are free parameters, $f(\lambda_j) \in [-1, 1]$ is given by (4.56), and the input signals turn out to be

$$u_j(t) = \begin{cases} -1 & \text{if } 0 \le \lambda_j \le k_j \\ 0 & \text{if } k_j < \lambda_j < 1, \end{cases}$$
 (4.59)

for $j=1,\ldots,n$. The input signals $\mathbf{u}(t)=[u_1(t),\ldots,u_n(t)]^T$ in (4.59) satisfy (4.45) and $J_f(\mathbf{u})=\|\mathbf{k}\|_1$. Hence, according to Proposition 4.2.3, they are fuel-optimal. Being these signals double-switch periodic, one has

$$J_s(u_j) = \frac{2}{p_j}. (4.60)$$

By enforcing (4.58) (which satisfies (4.18), (4.45), by definition), problem (4.49) becomes

$$\min_{\mathbf{p}, \phi} \max_{j} \frac{2}{p_{j}}
\text{s.t.} \quad (4.20), (4.58)
0 \le \phi_{j} < 1
p_{j} > 0, \quad j = 1, \dots, n.$$
(4.61)

where $\mathbf{p} = [p_1, \dots, p_n]^T$ and $\boldsymbol{\phi} = [\phi_1, \dots, \phi_n]^T$. Notice that the solution of problem (4.61) does not change if all phases ϕ_j are shifted by the same quantity. Hence, without loss of generality, in the sequel we will enforce $\phi_1 = 0$.

So far, the dynamic optimization problem (4.49) has been converted into a static optimization problem, where the decision variables are \mathbf{p} and ϕ . Note, however, that the problem is still difficult, being non-convex in these decision variables. Consequently, some simplifying assumptions will be made in order to derive an upper bound to the solution of problem (4.61). Let us observe that by (4.21)-(4.22) and (4.58)

$$\max_{t} |w_i(t)| \le \max_{t} \sum_{j=1}^{n} |c_{ij}| |x_j(t)| \le \sum_{j=1}^{n} |c_{ij}| a_j,$$
(4.62)

and hence (4.20) can be enforced by imposing (similarly to the derivation in (4.32))

$$\|\overline{\mathbf{C}}\,\mathbf{a}\|_{\infty} \le 1,\tag{4.63}$$

where $\mathbf{a} = [a_1, \dots, a_n]^T$. From (4.58), it follows that

$$p_j = \sqrt{a_j/\gamma_j}. (4.64)$$

By replacing (4.20) with (4.63) and substituting (4.64) in (4.60), problem (4.61) boils down to

$$\min_{\mathbf{a}} \max_{j} 2 \sqrt{\frac{\gamma_{j}}{a_{j}}}$$
s.t. $\|\overline{\mathbf{C}}\mathbf{a}\|_{\infty} \le 1$

$$a_{j} > 0, \quad j = 1, \dots, n.$$

$$(4.65)$$

By (4.62), the solution of (4.65) is an upper bound to that of (4.61). It turns out that problem (4.65) can be solved analytically, as stated by the following theorem.

Theorem 4.3.1. A global minimum of problem (4.65) is attained at

$$\mathbf{a}^* = \frac{1}{\|\mathbf{Q}\|_{\infty}} \Gamma \mathbb{1},\tag{4.66}$$

where $\Gamma = diag(\gamma_1, \dots, \gamma_n)$, $\mathbf{Q} = \overline{\mathbf{C}}\Gamma$, $\|\cdot\|_{\infty}$ denotes the matrix infinity norm and $\mathbb{1} = [1, \dots, 1]^T$.

Proof. Let $\mathbf{r} = \mathbf{\Gamma}^{-1}\mathbf{a}$. Then, problem (4.65) can be rewritten as

$$\min_{\beta, \mathbf{r}} \quad \beta \\
\text{s.t.} \quad \frac{2}{\sqrt{r_j}} \le \beta \\
\|\mathbf{Q}\mathbf{r}\|_{\infty} \le 1 \\
r_j > 0, \quad j = 1, \dots, n.$$
(4.67)

The statement of the theorem is proven if $\mathbf{r}^* = \frac{1}{\|\mathbf{Q}\|_{\infty}} \mathbb{1}$, $\beta^* = 2\sqrt{\|\mathbf{Q}\|_{\infty}}$ is a global minimum for problem (4.67). Let $\hat{\mathbf{r}}$, $\hat{\beta}$ be a feasible solution of (4.67). From feasibility, we get

$$\hat{r}_j \ge \frac{4}{\hat{\beta}^2}, \quad \forall j = 1, \dots, n,$$

and, being $q_{ij} \geq 0$, $\forall i, j$, where q_{ij} denotes the entries of **Q**, one has

$$1 \ge \sum_{j=1}^{n} q_{ij} \hat{r}_j \ge \frac{4}{\hat{\beta}^2} \sum_{j=1}^{n} q_{ij}, \quad \forall i = 1, \dots n.$$

Hence,

$$\hat{\beta} \ge 2\sqrt{\max_{i=1,...,n} \sum_{j=1}^{n} q_{ij}} = \beta^*,$$

which concludes the proof.

Remark 4.3.1. Since by (4.66) all the entries of $\Gamma^{-1}\mathbf{a}^*$ are equal, it follows from (4.64) that the periods of the closed trajectories resulting from the solution of problem (4.65) are

$$p_1^* = p_2^* = \dots = p_n^* = \frac{1}{\sqrt{\|\mathbf{Q}\|_{\infty}}}.$$
 (4.68)

Remark 4.3.2. A geometric interpretation of the relaxation (4.65) of problem (4.61) is as follows. Consider the box $\mathcal{B} = \{\mathbf{x} \in \mathbb{R}^n : |x_i| \leq a_i, i = 1,n\}$ and the parallelotope $\mathcal{P} = \{\mathbf{x} \in \mathbb{R}^n : \|\mathbf{C}\mathbf{x}\|_{\infty} \leq 1\}$. Then, a necessary and sufficient condition for $\mathcal{B} \subseteq \mathcal{P}$ is given by (4.63). In other words, condition (4.63) forces the trajectory of the system to lie within a box inscribed in the parallelotope describing the state constraints; then, problem (4.65) optimizes the sides of the box, in order to maximize the period of the trajectories, thus minimizing the switching frequency.

In the relaxation (4.65) of problem (4.61), the additional degrees of freedom provided by the phases ϕ_j have not been exploited. In order to find a less conservative relaxation, we enforce directly the property (4.68) into the original problem (4.61). This leads to the new relaxed problem

$$\max_{\mathbf{p}, \phi} \frac{p_1}{2}$$
s.t. (4.20), (4.58)
$$0 \le \phi_j < 1, \quad j = 1, \dots, n$$

$$p_1 = p_2 = \dots = p_n > 0,$$
(4.69)

where $\phi_1 = 0$. The following theorem provides the solution to problem (4.69).

Theorem 4.3.2. The global maximum of problem (4.69) is attained at

$$p_1^* = \frac{1}{\sqrt{\sigma(\phi^*)}},\tag{4.70}$$

where

$$\sigma(\phi^*) = \min_{\phi} \ \sigma(\phi), \tag{4.71}$$

and

$$\sigma(\phi) = \max_{i} \max_{0 \le t \le p_1} \Big| \sum_{i=1}^{n} c_{ij} \, \gamma_j f(t/p_1 + \phi_j) \Big|. \tag{4.72}$$

Proof. By exploiting (4.58), in combination with (4.21)-(4.22), one can rewrite the constraints (4.20),(4.58) as

$$p_1^2 \sigma(\boldsymbol{\phi}) \le 1.$$

Then, problem (4.69) boils down to

$$\max_{\mathbf{p}, \phi} \frac{p_1}{2}$$
s.t. $p_1^2 \sigma(\phi) \le 1$ (4.73)
$$0 \le \phi_j < 1, \quad j = 1, \dots, n$$

$$p_1 = p_2 = \dots = p_n > 0,$$

where $\phi_1 = 0$. Notice that $\sigma(\phi)$ in (4.72) does not depend on the actual value of the period p_1 , because the peak values of the sums of the p_1 -periodic functions $f(t/p_1 + \phi_j)$, evaluated over the period, are independent from the period itself. Consequently, the solution to (4.73) is that specified by (4.70)-(4.71), which concludes the proof.

Remark 4.3.3. Due to (4.68) and the fact that (4.20) is less restrictive than (4.63), the solution of problem (4.69) is a lower bound to that of (4.65), while still being an upper bound to that of (4.61).

Remark 4.3.4. According to (4.59), the input signals u_j^* corresponding to the solution provided by Theorem 4.3.2 are pulse-width modulated with period $p_j^* = p_1^*$ and phases $\phi_1^* = 0$ and ϕ_j^* for j = 2, ..., n.

The unconstrained problem (4.71) is essentially a crest factor minimization problem, which is known to be a hard optimization problem, being $\sigma(\phi)$ a non convex function (see [15] for a study of the crest factor problem in the sinusoidal case). Nevertheless, for low dimensional cases, such as n=3, which are of practical interest in the considered application, a global minimizer of (4.71) can be found by numeric search over the free phases ϕ_j . The benefits of this approach over the solution provided by Theorem 4.3.1 are demonstrated on two numerical examples, in the following.

4.3.3 Numerical examples

Example 4.3.1. Let n = 2, $\mathbf{k} = [0.7, 0.1]^T$ in (4.18), and

$$\mathbf{C} = \begin{bmatrix} \cos(\pi/3) & \sin(\pi/3) \\ -\sin(\pi/3) & \cos(\pi/3) \end{bmatrix},$$

in (4.20). The solutions provided by Theorem 4.3.1 and Theorem 4.3.2 are compared next.

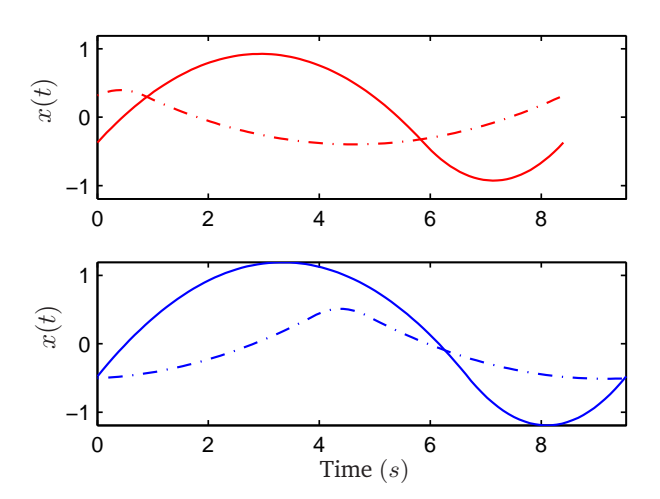


Figure 4.8: Trajectories $x_1(t)$ (solid) and $x_2(t)$ (dash-dotted) from the solution to (4.65) (top) and (4.69) (bottom).

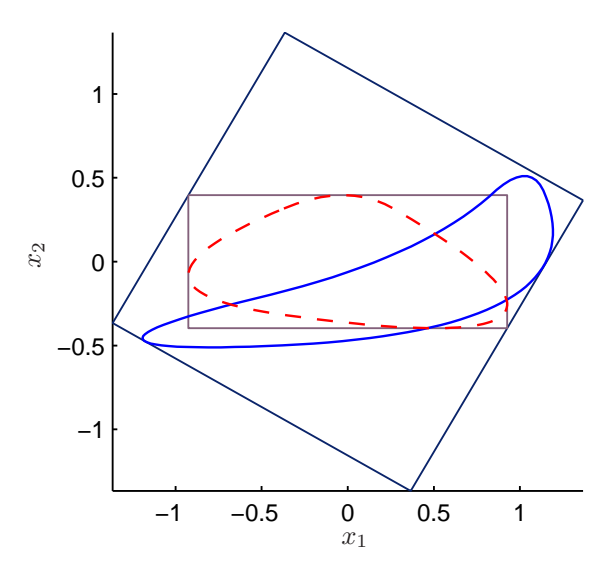


Figure 4.9: Trajectories in the x_1, x_2 plane from the solutions to (4.65) (dashed) and (4.69) (solid), with constraints (4.20) (outer parallelogram) and $|x_i| \le a_i^*$ (inner box).

According to Theorem 4.3.1, the solution to (4.65) is given by $\mathbf{a}^* = [0.9257, 0.3967]^T$. From (4.68), it follows that $p_1^* = p_2^* = 8.4$ and hence the resulting average switching frequency is $J_s^* = 2/p_1^* = 0.238$. In order to exploit the additional degrees of freedom provided by ϕ , problem (4.69) is solved using Theorem 4.3.2. The solution of (4.71) is found numerically through a one-dimensional search over ϕ_2 , with $\phi_1 = 0$. One gets $\phi_2^* = 0.59$ and $p_1^* = p_2^* = 9.53$, which give $J_s^* = 2/p_1^* = 0.21$. Hence, the optimal cost of (4.69) is lower than the optimal cost of (4.65) by approximately 12%.

The trajectories $x_1(t)$, $x_2(t)$ of system (4.18) are obtained by substituting the solutions

 p^* and ϕ^* in (4.58), for both approaches. Since the solution of (4.65) holds for any ϕ , without loss of generality one can set $\phi_1^* = \phi_2^* = 0$ in the first approach. The resulting trajectories are shown in Fig. 4.8 over a single period. The same trajectories are reported in the x_1 x_2 plane in Fig. 4.9, together with the set defined by (4.20) and the box $|x_j| \leq a_j^*$. It can be clearly seen that the control requirements (4.20) are met in both cases. However, the trajectories satisfying (4.66) are constrained to lie inside a smaller region. Being the period proportional to the square root of the oscillation amplitude, this yields a higher switching frequency of the actuators.

Example 4.3.2. *Let* n = 3,

$$\mathbf{T} = \begin{bmatrix} 0.05 & 0.25 & 1 \\ -1 & 1 & -0.2 \\ 0.65 & 1.2 & -1.2 \end{bmatrix},$$

and $\mathbf{k} = [0.4, 0.1, 0.7]^T$ in the transformed system (4.18). Moreover, let $\mathbf{W}_{\theta} = \mathbf{I}$ in (4.14) and hence $\mathbf{C} = \mathbf{T}$ in (4.20). The solutions provided by Theorem 4.3.1 and Theorem 4.3.2 are compared next.

The solution provided by Theorem 4.3.1 is $\mathbf{a}^* = [0.465\,,0.174,\,0.407]^T$, which corresponds to the period $p_1^* = p_2^* = p_3^* = 5.57$ and the optimal cost $J_s^* = 0.36$. In order to apply Theorem 4.3.2, one has to search the 2-dimensional parameter space ϕ_2,ϕ_3 for a global minimizer of (4.71). Notice that $\sigma(\phi)$ in (4.70) is a non-convex function of the decision variables ϕ with multiple local minima, as shown in Fig. 4.10.

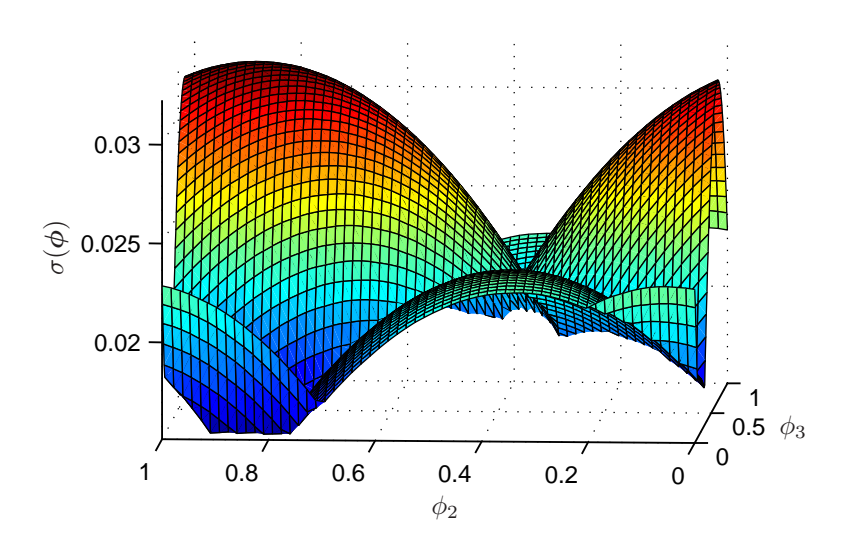


Figure 4.10: Plot of function $\sigma(\phi)$ for the three-dimensional example.

The solution to (4.69) is $\phi_2^* = 0.91$, $\phi_3^* = 0.1$ and $p_1^* = p_2^* = p_3^* = 8.14$, corresponding to the optimal cost $J_s^* = 0.246$. As expected, when ϕ is optimized, the on-off control law requires a lower switching frequency, while the average fuel consumption $J_f^* = \|\mathbf{k}\|_1 = 1.2$

is the same for both solutions, by construction. The optimal cost resulting from the application of Theorem 4.3.2 is lower than that corresponding to the solution provided by Theorem 4.3.1 by approximately 32%, which translates into a significant reduction of the actuator switching cycles. The three-dimensional plot of the trajectories $x_1(t)$, $x_2(t)$ and $x_3(t)$ is reported in Fig. 4.11, where it can be seen that the control accuracy requirements (represented by the 3-dimensional parallelotope) are satisfied.

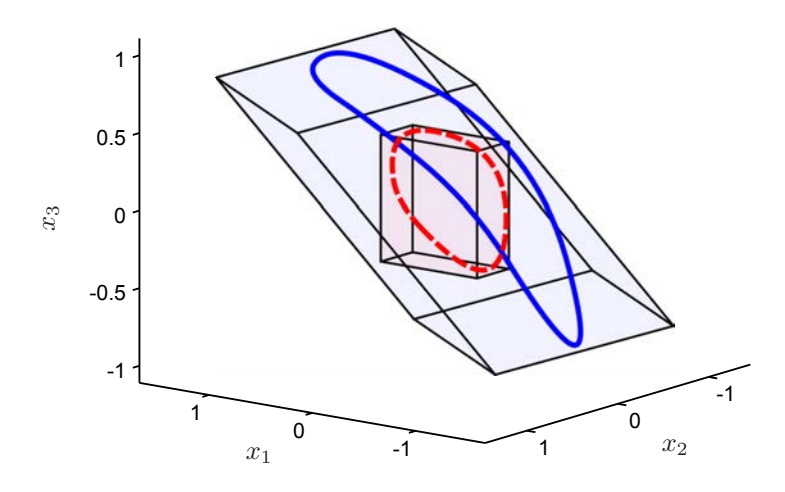


Figure 4.11: Trajectories resulting from the solution to (4.65) (dashed) and (4.69) (solid), together with state constraints (4.20) (outer parallelotope) and $|x_i| \le a_i^*$ (inner box).

It can be concluded that Theorem 4.3.1 and Theorem 4.3.2 provide two suboptimal solutions to Problem 4.3.1. A control law tracking the periodic trajectories corresponding to these solutions is presented next.

4.4 Minimum switching control

In the previous section, the problem of finding the fuel/switch-optimal periodic trajectories satisfying given state constraints has been addressed for the multivariable double integrator system (4.18), and two suboptimal (in terms of switching frequency) solutions have been provided. In this section, it is shown how to steer the system to these solutions from any given initial condition. Since in (4.18) the n double integrators have been decoupled, this problem can be tackled by using n single-input feedback control laws based on system (4.35). For the solution provided by Theorem 4.3.1, this amounts to design a control law tracking a limit cycle with prescribed period. For the solution specified by Theorem 4.3.2, the control law must also track a given phase along the limit cycle.

4.4.1 Tracking of limit cycle solutions with prescribed period

In order to steer the state of the system (4.35) to a limit cycle with prescribed period p from any initial condition, the fuel-optimal control law (4.43) is modified as follows

$$u(t) = \begin{cases} -1 & \text{if } s(x, \dot{x}) \ge a \\ 0 & \text{if } s(x, \dot{x}) \le -a \\ u_p & \text{otherwise,} \end{cases}$$
 (4.74)

where $u_p = -1$ if $s(x, \dot{x}) \ge a$ occurred more recently than $s(x, \dot{x}) \le -a$, and $u_p = 0$ otherwise. The resulting closed-loop system consists of the nonlinear system (4.35), (4.44) under the relay feedback (4.74), with hysteresis defined by a.

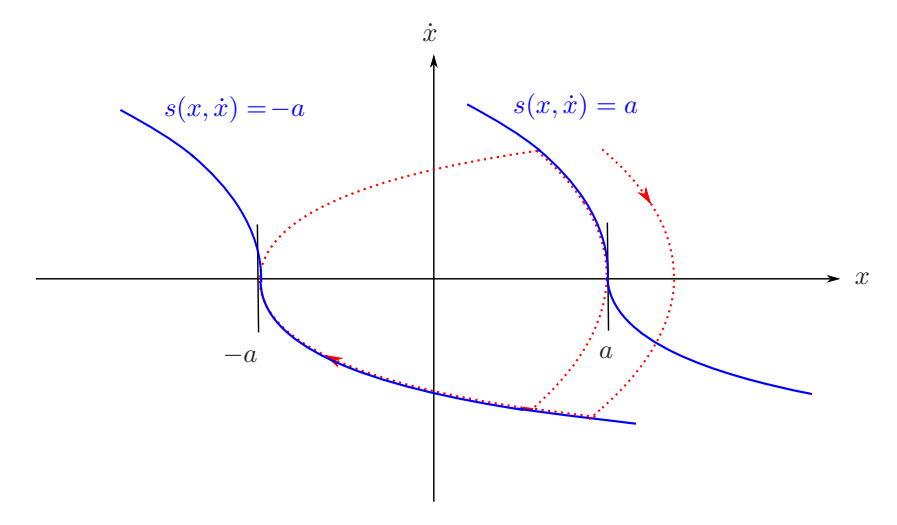


Figure 4.12: *Switching curves (solid) and example of a state trajectory (dotted).*

The switching curves $s(x,\dot{x})=a$ and $s(x,\dot{x})=-a$ are reported in the phase plane in Fig. 4.12, together with an example of a state trajectory (dotted). By analysing the phase portrait in Fig. 4.12, it is evident that, by switching the control input at most once, a limit cycle is reached from any initial condition. Combining this observation with the parametrization (4.55), one has the following result.

Proposition 4.4.1. The perturbed double integrator (4.35) with the control law (4.74) converges in finite time to a periodic trajectory of the form (4.55)-(4.56), with period

$$p = \sqrt{a/\gamma}. (4.75)$$

Moreover, only one switching of the control input is required to reach this trajectory from any initial condition.

Corollary 4.4.1. By applying for each input signal $u_j(t)$ of system (4.18) the control law (4.74) with $a = a_j^*$ given by (4.66), the periodic trajectories (4.58) with period p_j^* in (4.68) are reached in finite time with one switching per input, from any initial condition.

4.4.2 Tracking of limit cycle solutions with prescribed period and phase

Assume now that the aim is to design a control law tracking a periodic solution in the form (4.55)-(4.56), with prescribed period and phase. Besides the relation between the hysteresis of the relay element and the period of the limit cycle provided by (4.75), a relation between a variation of the hysteresis width and a corresponding phase shift does indeed exist. Therefore, the approach proposed hereafter is to steer both the period and the phase of the closed-loop trajectory to the prescribed values, by using a time-varying hysteresis defined by two parameters $a^U(t)$ and $a^L(t)$. More specifically, the following procedure is proposed: upon reaching of a switching curve, the parameter defining the offset of the opposite switching curve is updated, to enforce a cycle whose duration is designed to steer both the phase and the period to the prescribed values. To this purpose, the control law (4.74) is modified as

$$u(t) = \begin{cases} -1 & \text{if} \quad s(x, \dot{x}) \ge a^U(t) \\ 0 & \text{if} \quad s(x, \dot{x}) \le -a^L(t) \\ u_p & \text{otherwise,} \end{cases}$$
 (4.76)

where $u_p=-1$ if $s(x,\dot{x})\geq a^U(t)$ occurred more recently than $s(x,\dot{x})\leq -a^L(t)$, and $u_p=0$ otherwise, with $a^L(t)+a^U(t)>0$. The time-varying parameters are designed as explained next.

Let $\{z_i^L\}$, $\{z_i^U\}$ denote two sequences of increasing time instants at which the state trajectory reaches the switching curves of the control law (4.76). Formally

$$\begin{split} z_i^L : \left\{ \begin{array}{l} s(x(z_i^L), \dot{x}(z_i^L)) = -a^L(z_i^L) \\ \exists b : \forall t \in (z_i^L - b, z_i^L) \ s(x(t), \dot{x}(t)) \neq -a^L(t), \end{array} \right. \\ z_i^U : \left\{ \begin{array}{l} s(x(z_i^U), \dot{x}(z_i^U)) = a^U(z_i^U) \\ \exists b : \forall t \in (z_i^U - b, z_i^U) \ s(x(t), \dot{x}(t)) \neq a^U(t). \end{array} \right. \end{split} \tag{4.77} \end{split}$$

Without loss of generality, let us consider $u(t_0)=0$ (the case $u(t_0)=-1$ being analogous) and construct a sequence $\{z_l\}$ of increasing time instants as follows

$$\{z_l\} = \{z_1^U, z_1^L, z_2^U, z_2^L, \ldots\}.$$
 (4.78)

The proposed approach is to update $a^U(t)$ and $a^L(t)$ in (4.76) at times z^L_i and z^U_i , respectively. To this aim, we define a sequence $\{a_l\}$ such that

$$a^{L}(t) = a_{2m-1}$$
 for $t \in [z_{2m-1}, z_{2m+1}),$
 $a^{U}(t) = a_{2m}$ for $t \in [z_{2m}, z_{2m+2}).$ (4.79)

Notice that the offset of a switching curve is updated when the trajectory is not lying on the same curve.

The sequence $\{z_l\}$ in (4.78) depends on the application of the control law (4.76) to system (4.35) and hence on the particular choice of the update sequence $\{a_l\}$ in (4.79). The controlled evolution of the system is illustrated in Fig. 4.13, where the state trajectory (dotted) reaches the time-varying switching curves (solid) at times z_l , z_{l+1} and z_{l+2} . The

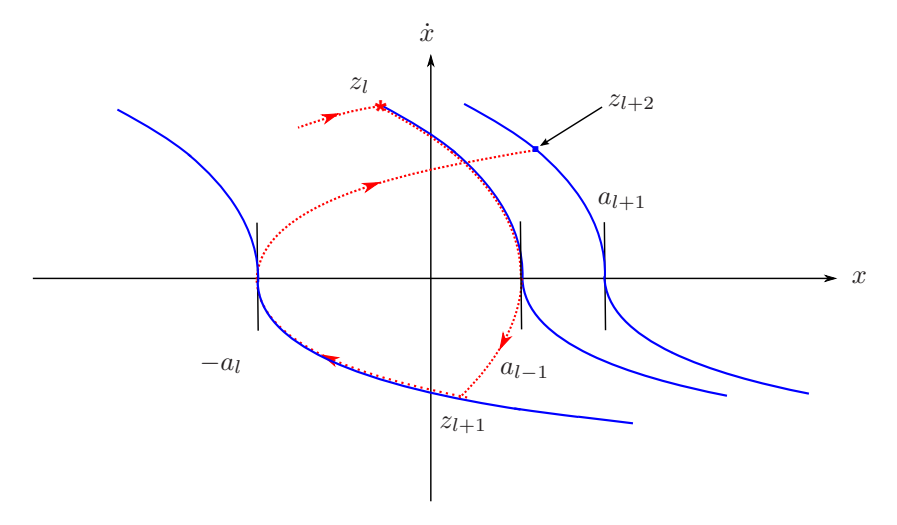


Figure 4.13: Scheme for the computation of the event times: switching curves (solid) and example of a closed-loop trajectory (dotted).

event times can be computed iteratively according to

$$z_{l+1} = z_l + \frac{|\dot{x}(z_{l+1})| + |\dot{x}(z_l)|}{q(z_l)},$$
(4.80)

where $q(z_l) = |k + u(z_l)|$ and the velocity $|\dot{x}(z_{l+1})|$ is given by

$$|\dot{x}(z_{l+1})| = 4\sqrt{2\gamma(a_l + a_{l-1})}.$$
 (4.81)

From the previous observations, it follows that the objective of driving the system to a steady state periodic solution in the form (4.55)-(4.56), with prescribed period p and phase ϕ , can be recast in terms of the design of the sequence $\{a_l\}$.

Theorem 4.4.1. Let $a=p^2\gamma$ and define

$$a_0 = a, (4.82)$$

$$a_l = a \left(1 + 4\widetilde{\phi}_l + 2\widetilde{\phi}_l^2 \right), \quad l = 1, \dots, n,$$
 (4.83)

where

$$\widetilde{\phi}_{l} = mod\left(\frac{\overline{z}_{l+2} - \hat{z}_{l+2}}{p} + \frac{1}{2}, 1\right) - \frac{1}{2},$$
(4.84)

$$\hat{z}_{l+2} = z_l + \frac{|\dot{x}(z_l)|}{q(z_l)} + \frac{q(z_l)}{2}p + \frac{\sqrt{2}}{4}\sqrt{p^2 + \frac{a_{l-1}}{\gamma}},\tag{4.85}$$

and the sequence $\{\bar{z}_l\}$ is defined according to

$$\bar{z}_{2m-1} = -\phi p,
\bar{z}_{2m} = (k - \phi) p,$$
(4.86)

for $m \in \mathbb{N}$. Then, the solution of system (4.35) with the control law (4.76)-(4.79) converges in finite time to the periodic trajectory (4.55)-(4.56) with period p and phase ϕ . Moreover, only three switchings of the control input are required to reach this trajectory from any initial condition.

Proof. Under the assumption that $u(t_0)=0$ (the reasoning is the same if $u(t_0)=-1$), the closed-loop system trajectory will reach the curve $s(x,\dot{x})=a_0=a$ at a certain time z_1 , at which the input switches to $u(z_1)=-1$. Without loss of generality, let $z_1=0$. Since $q(z_1)=1-k$, (4.82) and (4.85) give

$$\hat{z}_3 = \frac{\dot{x}(z_1)}{1-k} + \left(1 - \frac{k}{2}\right)p.$$

By using (4.80)-(4.81), it is possible to check that \hat{z}_3 represents the time at which the trajectory of the closed-loop system would reach again the curve $s(x, \dot{x}) = a$ if one enforced $a_1 = a_2 = a$ in (4.76)-(4.79). Being $\bar{z}_3 = -\phi p$,

$$\widetilde{\phi}_1 = h - \phi - \frac{|\dot{x}(z_1)|}{p(1-k)} + \frac{k}{2},$$
(4.87)

for some $h \in \mathbb{Z}$. By using a_1 from (4.83), with $\widetilde{\phi}_1$ given by (4.87), the procedure is repeated at time z_2 . After simple manipulations, one obtains

$$\hat{z}_4 = \frac{|\dot{x}(z_1)|}{1-k} + p(1+\tilde{\phi}_1) + \frac{k}{2}p,
\bar{z}_4 = (k-\phi)p,
\tilde{\phi}_2 = \mod\left(-\frac{1}{2} - h, 1\right) - \frac{1}{2} = 0,$$

and hence $a_2=a$. By induction, it can be easily verified that $\widetilde{\phi}_l=0$ and $a_l=a \ \forall \ l\geq 2$, for any $\dot{x}(z_1)$. Hence, by (4.79), $a^U(t)=a^L(t)=a$, for all $t\geq z_3$. From Proposition 4.4.1, one has that the closed-loop trajectory converges to a solution of the form (4.55)-(4.56) with period p. Moreover, from (4.80)-(4.81) it follows that the sequence of switching times z_l satisfies

$$\mod\left(\frac{\bar{z}_l - z_l}{p} + \frac{1}{2}, 1\right) - \frac{1}{2} = 0, \quad \forall l \ge 4.$$
 (4.88)

On the other hand, the switching times of the periodic solution (4.55)-(4.56) with given phase ϕ occur at time instants \tilde{t} such that either $\operatorname{mod}(\tilde{t}/p+\phi,1)=0$ or $\operatorname{mod}(\tilde{t}/p+\phi,1)=k$. These equations lead to to $\tilde{t}=z_{2m-1}$ and $\tilde{t}=z_{2m}$ in (4.86), respectively. Therefore, (4.88) guarantees that, for all $t\geq z_4$, the switching times of the closed-loop trajectory coincide with those of the periodic solution (4.55)-(4.56), with desired period p and phase p. Finally, since by (4.84) $-1/2\leq \tilde{\phi}_1<1/2$, which implies $a_1\geq -1/2$ p by (4.83), one has that $a^L(t)+a^U(t)>0$ $\forall t$, as it is required for the control law (4.76) to be well defined. This concludes the proof.

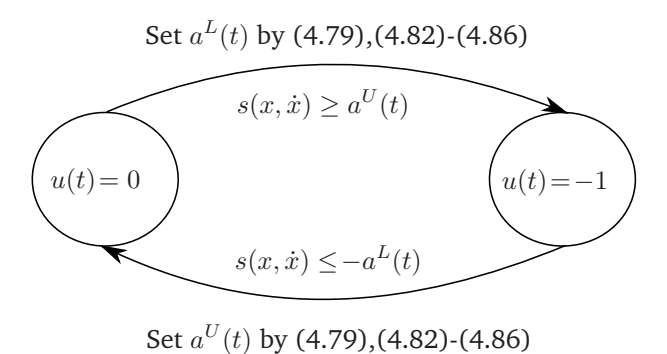


Figure 4.14: Event-based switching logic.

Corollary 4.4.2. By applying for each input signal $u_j(t)$ of system (4.18) the control law (4.76)-(4.79), with the input sequence $\{a_l\}$ chosen as in (4.82)-(4.86) and $p=p_j^*$, $\phi=\phi_j^*$ given by (4.70)-(4.71), the periodic trajectories (4.58) with period p_j^* and phase ϕ_j^* are reached in finite time with three switchings per input, from any initial condition.

Notice that $a_0=a$ is not strictly necessary to prove Theorem 4.4.1. The same conclusions can be drawn for any a_0 such that $a_0+a_1>0$. Also notice that one has just to shift by 1 the indices of the sequences $\{z_l\}$, $\{a_l\}$ and $\{\bar{z}_l\}$ when $u(t_0)=-1$. For practical implementation of the control law, the event-based switching logic depicted in Fig. 4.14 can be used. Finally, observe that the thruster on/off command $\mu \in \{0,1\}^{m=2n}$ in (4.11) is obtained from $\tilde{\mu} = \mathbf{D}\mathbf{u}$, where \mathbf{D} is given by (4.17), as follows

$$\begin{cases}
\mu_j = \widetilde{\mu}_j, & \mu_{j+n} = 0 & \text{if } \widetilde{\mu}_j \ge 0 \\
\mu_j = 0, & \mu_{j+n} = -\widetilde{\mu}_j & \text{if } \widetilde{\mu}_j < 0,
\end{cases}$$
(4.89)

for $j = 1, \ldots, n$.

Example 4.4.1. Consider the problem defined by Example 4.3.2. For any given initial condition, the periodic trajectories corresponding to the solution specified by Theorem 4.3.2 can be tracked by applying the control law (4.76) for each input channel. For simulation purpose, system (4.18) is discretized with sampling time $\Delta t_s = 0.005$ s. The control law is implemented using the switching logic depicted in Fig. 4.14, for each input channel, and the initial conditions for the simulation are set to $\mathbf{x}(t_0) = [-3, 1, -2]^T$ and $\dot{\mathbf{x}}(t_0) = [0.2, 0.4, -0.3]^T$.

The trajectory of the closed-loop system is reported in Fig. 4.15. It can be clearly seen that, after a finite transient, the system trajectory converges to the reference limit cycle (marked). The control inputs are reported in Fig. 4.16. Notice that, as stated by Corollary 4.4.2, the desired duty cycle is attained from the fourth input transition onwards, for each input channel.

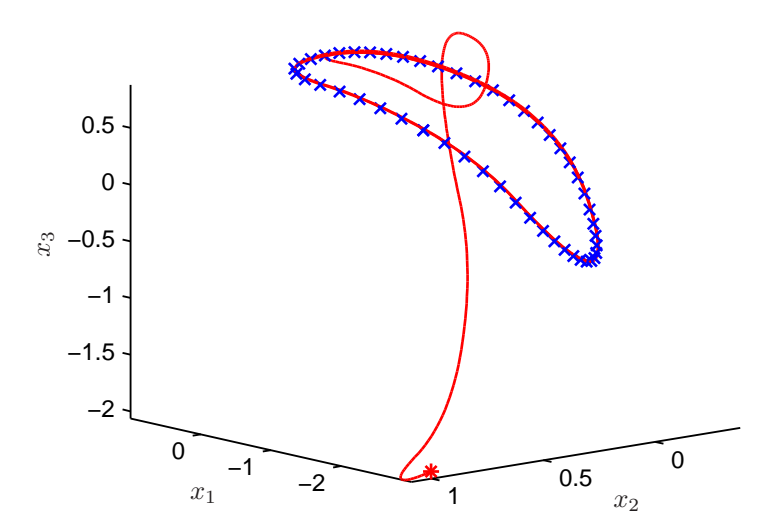


Figure 4.15: Closed-loop trajectory (solid) and reference limit cycle (marked).

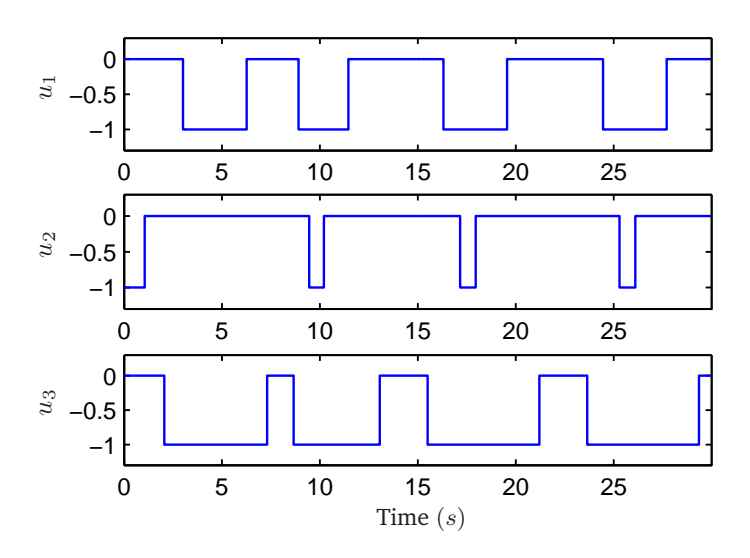


Figure 4.16: Control inputs.

4.4.3 Feasibility with respect to minimum impulse bit

There are particular cases in which one or more elements of the the disturbance vector ${\bf k}$ in (4.18) can be very small. In such cases, the thruster firing time required by the minimum switching control law may not be compatible with the minimum impulse bit of the thrusters. Because the minimum impulse bit of attitude control systems based on electric propulsion is typically very small, this is a rare scenario. Nonetheless, it must be taken into account for

a reliable implementation of the control scheme. The thruster firing duration required to track a limit cycle of period given by (4.68), or equivalently the trajectory from the solution to (4.70)-(4.71), on channel j, is simply $k_j p_j^*$, because the j-th input is modulated with duty cycle k_j and period p_j^* . Then, an effective way to detect if the commanded impulse is below the minimum firing time Δt_{min} to check whether

$$k_j p_j^* \le \Delta t_{min}. \tag{4.90}$$

If (4.90) holds at least for one j, a suboptimal approach, which guarantees that (4.20) is satisfied, is to fix $\mathbf{a} = \mathbf{b}^*$, where \mathbf{b}^* is the minimizer to (4.33). Then, the control law (4.34) can be used for all axes for which

$$k_j \sqrt{b_j^*/\gamma_j} \le \Delta t_{min},$$

while the control law (4.74), with $a = b_j^*$, can be employed for the remaining axes.

4.5 MPC-based control scheme

So far, the minimum switching control problem has been tackled under the assumptions that the attitude dynamic model can be approximated by a system of coupled double integrators and that the thruster configuration is symmetric. These assumptions, however, may not apply to certain scenarios. In such cases, the solution to the minimum switching problem can be approached via numerical optimization techniques.

In this section, a model predictive control scheme based on the linearized model (4.5)-(4.7) is derived, as an alternative to the minimum switching control law previously developed. A finite horizon cost functional including both the fuel consumption and the number of firing cycles of the control system is minimized at each time step within a receding horizon scheme, yielding a closed-loop control law. Due to the presence of linear performance indexes and on/off actuators, the problem requires the solution of a mixed integer linear program.

4.5.1 Problem formulation

A discrete-time linear approximation of the attitude error dynamics is derived for control purposes. Using the linearized equations (4.5)-(4.7), together with (4.10)-(4.11), the tracking error dynamics are represented by the state space model

$$\dot{\mathbf{y}} = \mathbf{A}_m \, \mathbf{y} + \mathbf{B}_m \, \boldsymbol{\mu} + \mathbf{B}_e \, \boldsymbol{\tau}_e, \tag{4.91}$$

where $\mathbf{y} = \begin{bmatrix} \delta \boldsymbol{\theta}^T, \ \delta \boldsymbol{\omega}^T \end{bmatrix}^T \in \mathbb{R}^{2n}$ and $\boldsymbol{\mu} \in \{0,1\}^m$. Notice that, in this formulation, (4.12) does not have to be satisfied with m=2n, as in the previous derivations. Instead, it is sufficient that (4.11) is such that system (4.91) is controllable. The state matrix in (4.91) is obtained from (4.5)-(4.7) as

$$\mathbf{A}_m = \begin{bmatrix} \mathbf{0} & \mathbf{I} \\ \mathbf{A}_1 & \mathbf{A}_2 \end{bmatrix},\tag{4.92}$$

where the A_1 and A_2 are given by (4.8). The input matrices are given by

$$\mathbf{B}_{m} = \begin{bmatrix} \mathbf{0} \\ \mathbf{I}_{M}^{-1} \mathbf{G} \end{bmatrix}, \qquad \mathbf{B}_{e} = \begin{bmatrix} \mathbf{0} \\ \mathbf{I}_{M}^{-1} \end{bmatrix}, \tag{4.93}$$

where the matrix G does not need to be invertible. The continuous time model is discretized with a sampling time Δt_s compatible with the minimum firing time of the attitude control thrusters, thus obtaining

$$\mathbf{y}(t+1) = \mathbf{F}\,\mathbf{y}(t) + \mathbf{H}\,\boldsymbol{\mu}(t) + \mathbf{H}_e\,\boldsymbol{\tau}_e(t),\tag{4.94}$$

with
$$\mathbf{F} = e^{\mathbf{A}_m \Delta t_s}$$
, $\mathbf{H} = \left(\int_0^{\Delta t_s} e^{\mathbf{A}_m \rho} d\rho \right) \mathbf{B}_m$ and $\mathbf{H}_e = \left(\int_0^{\Delta t_s} e^{\mathbf{A}_m \rho} d\rho \right) \mathbf{B}_e$.

The attitude control system developed in this section is based on an MPC approach, which explicitly incorporates the limitations on pointing and pointing rate accuracy, as well as a performance criterion accounting for the fuel consumption and the number of firing cycles of the control system. The control accuracy requirements can be formulated in terms of the following constraint

$$\|\mathbf{W}\mathbf{y}\|_{\infty} \leq 1, \tag{4.95}$$

where $\mathbf{W} = \operatorname{blockdiag}(\mathbf{W}_{\theta}, \mathbf{W}_{\omega})$ and the weighting matrices \mathbf{W}_{θ} and \mathbf{W}_{ω} account for proper scaling of the attitude and angular rate errors. Notice that angular rate constraints are included in the formulation (4.95), in addition to the attitude error constraints in (4.14). These may be required for applications demanding a high pointing stability, e.g. high-accuracy Earth observation missions.

In order to obtain a tractable MPC design problem, the minimum fuel and minimum switching cost functions have to be reformulated over a finite horizon. According to (4.15), a cost function proportional to the amount of expended fuel from time t to time $t + N_u$ is given by

$$J_1(\mathbf{U}) = \sum_{i=0}^{N_u} \| \boldsymbol{\mu}(t+i) \|_1, \qquad (4.96)$$

where $\mathbf{U} = \{ \boldsymbol{\mu}(t), \dots, \boldsymbol{\mu}(t+N_u) \}$ is the input sequence on the considered control horizon, of length N_u . Moreover, being $\boldsymbol{\mu} \in \{0,1\}^m$, the number of input transitions is obtained from (4.47) as

$$J_2(\mathbf{U}) = \sum_{i=0}^{N_u} \| \boldsymbol{\mu}(t+i) - \boldsymbol{\mu}(t+i-1) \|_1.$$
 (4.97)

The cost function for the control problem is defined as a trade-off between the fuel consumption and the number of actuator switching cycles, by introducing a relative weight $\alpha \in [0, 1]$ of the terms J_1 and J_2 from (4.96) and (4.97), respectively. Given a state vector $\mathbf{y}(t)$, the computation of the control input sequence U at time t can be formulated as an optimization problem of the following form.

Problem 4.5.1.

$$\min_{\mathbf{U}} \quad (1-\alpha) J_1(\mathbf{U}) + \alpha J_2(\mathbf{U})$$
s.t.
$$\mathbf{y}(t+i+1) = \mathbf{F} \mathbf{y}(t+i) + \mathbf{H} \boldsymbol{\mu}(t+i) + \mathbf{H}_e \boldsymbol{\tau}_e(t+i)$$

$$\|\mathbf{W} \mathbf{y}(t+i)\|_{\infty} \le 1$$

$$\mathbf{M} \boldsymbol{\mu}(t+i) \le \mathbb{1}$$

$$\boldsymbol{\mu}(t+i) \in \{0,1\}^m \quad \forall i = 0, \dots, N_u.$$
(4.98)

The matrix M in (4.98) is defined to account for control allocation constraints, such as preventing firing of opposite thrusters. In a receding horizon control strategy (see, e.g., [89]), one has to solve problem (4.98) at each time t and then apply the first element of the computed input sequence, which hereafter will be denoted by $\mathbf{U}_{t+N_u|t} = \{\boldsymbol{\mu}(t|t), \dots, \boldsymbol{\mu}(t+N_u|t)\}$. Hence, the instantaneous thruster activation command is given by $\boldsymbol{\mu}(t) = \boldsymbol{\mu}(t|t)$.

In order to ensure feasibility in the presence of estimation errors and model uncertainties, the state constraints in problem (4.98) are relaxed by introducing slack variables $\mathbf{S} = \{\mathbf{s}(t+1), ..., \mathbf{s}(t+N)\}$ and penalizing them in the cost function. Such relaxation is motivated by the fact that small violations of the constraints can be tolerated for short time periods, provided that slightly conservative bounds on the pointing and pointing rate accuracy are used. Hence, problem (4.98) can be reformulated as

$$\min_{\mathbf{U}_{t}, \mathbf{S}} \quad (1-\alpha) J_{1}(\mathbf{U}_{t+N_{u}|t}) + \alpha J_{2}(\mathbf{U}_{t+N_{u}|t}) + \sum_{i=1}^{N} \| \mathbf{s}(t+i) \|_{1}$$
s.t.
$$\mathbf{y}(t|t) = \mathbf{y}(t)$$

$$\mathbf{y}(t+i+1|t) = \mathbf{F} \mathbf{y}(t+i|t) + \mathbf{H} \boldsymbol{\mu}(t+i|t) + \mathbf{H}_{e} \boldsymbol{\tau}_{e}(t+i)$$

$$-\mathbf{s}(t+i) - \mathbf{K}_{s} \mathbb{1} \leq \mathbf{K}_{s} \mathbf{W} \mathbf{y}(t+i|t) \leq \mathbf{K}_{s} \mathbb{1} + \mathbf{s}(t+i)$$

$$-\mathbf{s}(t+i) \leq \mathbf{K}_{s} \mathbf{y}(t+N|t) \leq \mathbf{s}(t+N)$$

$$\mathbf{s}(t+i) \geq \mathbf{0}$$

$$\mathbf{M} \boldsymbol{\mu}(t+i|t) \leq \mathbb{1}$$

$$\boldsymbol{\mu}(t+i|t) \in \{0,1\}^{m} \quad \forall i=0,\ldots,N-1$$

$$\boldsymbol{\mu}(t+N_{u}+1|t) = \ldots = \boldsymbol{\mu}(t+N-1|t) = \mathbf{0}.$$
(4.99)

The weight on the terminal state \mathbf{K}_y is a standard tool in MPC, which favours stability of the receding horizon control strategy [96], while matrix \mathbf{K}_s is introduced to penalize the weighted 1-norm of the the slack variables on constraint violations. In order to solve problem (4.99), the initial state $\mathbf{y}(t|t)$ and of the disturbance term $\boldsymbol{\tau}_e(t+i)$, $i=0,\ldots,N_u-1$ should be available. Since these quantities are not known in advance, one has to resort to a navigation algorithm to estimate them. To this aim, a suitable EKF algorithm can be adopted (see Chapter 5).

It is worth noticing that in problem (4.99), the control horizon N_u is different from the prediction horizon N, on which the state constraints are enforced ($N_u \leq N-1$). After the first N_u samples, the control variables are set to zero while the state constraints must

be satisfied also in the subsequent $N-N_u-1$ samples. This allows one to trade-off the number of optimization variables and the performance of the attitude control system. In fact, problem (4.99) is a MILP problem, which is known to be computationally intractable in the general case. Nevertheless, if the control horizon is kept short enough, state-of-the-art MILP algorithms can provide an approximate solution in a reasonable amount of time. The effectiveness of this approach is demonstrated through numerical simulations in Section 6.3.

4.5.2 Mixed integer linear program

For practical implementation, the MPC problem can be rewritten as a mixed-integer linear program. The derivation of the MPC matrices is similar to the one described in Section 3.3.3. In the present design, however, the optimization variables are simply the elements of the control sequence, which allows for integer input values. The mixed-integer linear program corresponding to (4.99) takes the following form

$$\min_{\mathbf{z}_{\mu} \in \{0,1\}^{mN_{u}}} \begin{bmatrix} (1-\alpha)\mathbb{1} \\ \alpha \mathbb{1} \\ \mathbb{1} \end{bmatrix}^{T} \begin{bmatrix} \mathbf{z}_{\mu} \\ \mathbf{z}_{\Delta} \\ \mathbf{z}_{s} \end{bmatrix}
\text{s.t.} \begin{bmatrix} \mathbf{\Phi} & \mathbf{0} & -\mathbf{I} \\ -\mathbf{\Phi} & \mathbf{0} & -\mathbf{I} \\ \mathbf{\Psi} & -\mathbf{I} & \mathbf{0} \\ -\mathbf{\Psi} & -\mathbf{I} & \mathbf{0} \\ \mathbf{\bar{M}} & \mathbf{0} & \mathbf{0} \end{bmatrix} \begin{bmatrix} \mathbf{z}_{\mu} \\ \mathbf{z}_{\Delta} \\ \mathbf{z}_{s} \end{bmatrix} \leq \begin{bmatrix} \mathbf{m} - \mathbf{f} - \boldsymbol{\vartheta} \\ \mathbf{m} + \mathbf{f} + \boldsymbol{\vartheta} \\ [\mu(t-1)^{T}, \mathbf{0}]^{T} \\ -[\mu(t-1)^{T}, \mathbf{0}]^{T} \end{bmatrix}, \tag{4.100}$$

where

$$\mathbf{z}_{\mu} = \left[\boldsymbol{\mu}^{T}(t), \dots, \boldsymbol{\mu}^{T}(t+N_{u})\right]^{T}$$

$$\mathbf{z}_{\Delta} = \left[|\boldsymbol{\mu}^{T}(t) - \boldsymbol{\mu}^{T}(t-1)|, \dots, |\boldsymbol{\mu}^{T}(t+N_{u}) - \boldsymbol{\mu}^{T}(t+N_{u}-1)|\right]^{T},$$

$$\mathbf{z}_{s} = \left[\mathbf{s}^{T}(t+1), \dots, \mathbf{s}^{T}(t+N)\right]^{T}$$

 $\bar{\mathbf{M}} = \oplus^{N_u} \mathbf{M}$, and $\mathbf{\Phi}$, $\boldsymbol{\vartheta}$, \mathbf{f} , $\mathbf{\Psi}$, \mathbf{m} are given by

$$oldsymbol{\Phi} = \left[egin{array}{cccc} \mathbf{K}_s \mathbf{W} \mathbf{H} & \dots & \mathbf{0} \\ drain & \ddots & drain \\ \mathbf{K}_s \mathbf{W} \mathbf{F}^{N_u} \mathbf{H} & \dots & \mathbf{K}_s \mathbf{W} \mathbf{H} \\ drain & drain & drain \\ \mathbf{K}_y \mathbf{F}^{(N_x-1)} \mathbf{H} & \dots & \mathbf{K}_y \mathbf{F}^{(N_x-N_u)} \mathbf{H} \end{array}
ight],$$

$$\boldsymbol{\vartheta} = \left[\begin{array}{ccc} \mathbf{K}_s \mathbf{W} \mathbf{H}_e & \dots & \mathbf{0} \\ \vdots & \ddots & \vdots \\ \mathbf{K}_y \mathbf{F}^{(N_x-1)} \mathbf{H}_e & \dots & \mathbf{K}_y \mathbf{H}_e \end{array} \right] \left[\begin{array}{c} \boldsymbol{\tau}_e(t) \\ \vdots \\ \boldsymbol{\tau}_e(t) \end{array} \right],$$

$$oldsymbol{\Psi} = \left[egin{array}{cccc} \mathbf{I} & \mathbf{0} & \dots & \mathbf{0} \ -\mathbf{I} & \mathbf{I} & \dots & \mathbf{0} \ dots & \ddots & \ddots & dots \ \mathbf{0} & \dots & -\mathbf{I} & \mathbf{I} \end{array}
ight], \quad \mathbf{f} = \left[egin{array}{c} \mathbf{K}_s \mathbf{WF} \ dots \ dots \ \mathbf{K}_{s} \ \mathbf{K}_{n} \mathbf{F}^{N_x} \end{array}
ight] \mathbf{y}(t), \quad \mathbf{m} = \left[egin{array}{c} \mathbf{K}_s \ dots \ \mathbf{K}_s \ \mathbf{0} \end{array}
ight] \mathbb{1}.$$

In this thesis, the IBM ILOG CPLEX mixed-integer programming solver [66], based on a branch and bound algorithm, is employed to solve problem (4.100).

Autonomous Navigation

One critical aspect for the successful implementation of the feedback control techniques developed so far is the capability of autonomously estimating the position, velocity and orientation of the spacecraft, as well as a number of additional parameters, such as the disturbance torque acting on the spacecraft. Therefore, nonlinear estimation techniques play a key role in the development of an autonomous GNC system. Among these techniques, the extended Kalman filter (EKF) is widely used, and found to provide adequate performance, in most space applications.

In this chapter, three different navigation schemes based on the continuous-discrete EKF design [27] are developed for application within a closed-loop control system. First, an orbit determination filter is presented, which can be used in combination with the control scheme developed in Section 3.2, for autonomous station-keeping of LEO spacecraft. Then, an attitude determination filter is derived, to enable the implementation of the control laws presented in Chapter 4. The last contribution is a navigation filter estimating the relative state between two spacecraft, as required for the application of the rendezvous and docking control scheme developed in Section 3.3. The important topic of accurate sensor modeling is not addressed in this chapter. Instead, a number of simplifying assumptions about the measurement process are made in order to asses the performance of the proposed control techniques, within a closed-loop GNC system.

5.1 Orbit determination

In this section, an orbit determination filter is presented, which can be used in combination with the control scheme developed in Section 3.2. The filter processes GPS measurements to estimate the absolute position and velocity of the spacecraft. The output of the GPS is modeled as the true absolute position from the solution to (2.7) plus sensor noise \mathbf{w}_r , according to

$$\check{\mathbf{r}} = \mathbf{r} + \mathbf{w}_r. \tag{5.1}$$

5.1.1 Propagation

The navigation state is a six-dimensional vector $\hat{\mathbf{y}} = [\hat{\mathbf{r}}^T, \hat{\mathbf{v}}^T]^T$, including the inertial position $\hat{\mathbf{r}}$ and the inertial velocity $\hat{\mathbf{v}} = \hat{\dot{\mathbf{r}}}$ of the spacecraft. The dynamic model used to propagate

the navigation state is derived from (2.7) as

$$\dot{\hat{\mathbf{r}}} = \hat{\mathbf{v}} \tag{5.2}$$

$$\dot{\hat{\mathbf{v}}} = \mathbf{v} \tag{5.2}$$

$$\dot{\hat{\mathbf{v}}} = -\frac{\mu}{\|\hat{\mathbf{r}}\|^3} \hat{\mathbf{r}} + \mathbf{a}_{J2}(\hat{\mathbf{r}}), \tag{5.3}$$

where $\mathbf{a}_{J2}(\hat{\mathbf{r}})$ is the estimate of the gravitational disturbance \mathbf{a}_g in (2.10), based on the J2 harmonic of the gravity field. The expression for $\mathbf{a}_{J2}(\hat{\mathbf{r}})$ is given by [131]

$$\mathbf{a}_{J2}(\hat{\mathbf{r}}) = -\frac{3}{2} \frac{\mu C_{20} R^2}{\hat{r}^7} \begin{bmatrix} (\hat{r}^2 - 5\,\hat{r}_z^2)\hat{r}_x \\ (\hat{r}^2 - 5\,\hat{r}_z^2)\hat{r}_y \\ (3\,\hat{r}^2 - 5\hat{r}_z^2)\hat{r}_z \end{bmatrix},\tag{5.4}$$

where C_{20} denote the second harmonic coefficient, $\hat{\mathbf{r}} = [\hat{r}_x, \hat{r}_y, \hat{r}_z]^T$ and $\hat{r} = \|\hat{\mathbf{r}}\|$.

It should be noticed that no thrust and drag accelerations are considered in equation (5.3), because for the considered application $\mathbf{a}_t \approx -\mathbf{a}_d$ in (2.8). The effects of minor orbital perturbations is also neglected. The uncertainty introduced by these assumptions is modeled as white process noise \mathbf{w}_a , with covariance given by

$$E\left[\mathbf{w}_{a}(t)\,\mathbf{w}_{a}(t')^{T}\right] = \mathbf{Q}_{a}\delta(t - t'),\tag{5.5}$$

where \mathbf{Q}_a is the noise spectral density and $\delta(t-t')$ denote the Dirac delta function. The covariance matrix $\mathbf{P} = E\left[\hat{\mathbf{y}}\,\hat{\mathbf{y}}^T\right]$ of the filter is propagated according to

$$\dot{\mathbf{P}} = \mathbf{F}\mathbf{P} + \mathbf{P} \ \mathbf{F}^T + \mathbf{Q} \,. \tag{5.6}$$

Making use of the model equations (5.2)-(5.3), the Jacobian matrix of the system, computed at the current estimate, can be expressed as

$$\mathbf{F} = \begin{bmatrix} \mathbf{0} & \mathbf{I} \\ \dot{\partial} \hat{\mathbf{v}} / \partial \hat{\mathbf{r}} & \mathbf{0} \end{bmatrix} . \tag{5.7}$$

The process noise covariance is a block diagonal matrix Q defined by

$$\mathbf{Q} = \text{blockdiag} \left(\mathbf{0}_{3 \times 3}, \mathbf{Q}_a \right), \tag{5.8}$$

where Q_a is given by (5.5). When an impulsive maneuver occurs, the filter state vector and covariance matrix must be updated according to

$$\hat{\mathbf{v}}^{\uparrow} = \hat{\mathbf{v}}^{\downarrow} + \Delta \mathbf{v}_{I} \tag{5.9}$$

$$\mathbf{P}^{\uparrow} = \mathbf{P}^{\downarrow} + \mathbf{Q}_{D}. \tag{5.10}$$

The correction term \mathbf{Q}_D is given by

$$\mathbf{Q}_D = \text{blockdiag} \left(\mathbf{0}, \mathbf{Q}_v \right), \tag{5.11}$$

where \mathbf{Q}_v is the covariance associated to the impulsive maneuver uncertainty.

5.1.2 Measurement update

When measurements are available, the state of the filter is updated by using the classical update equations

$$\begin{bmatrix} \hat{\mathbf{r}}^+ \\ \hat{\mathbf{v}}^+ \end{bmatrix} = \begin{bmatrix} \hat{\mathbf{r}}^- + \delta \hat{\mathbf{r}} \\ \hat{\mathbf{v}}^- + \delta \hat{\mathbf{v}} \end{bmatrix}, \tag{5.12}$$

where

$$\begin{bmatrix} \delta \hat{\mathbf{r}}^+ \\ \delta \hat{\mathbf{v}}^+ \end{bmatrix} = \mathbf{K} (\check{\mathbf{r}} - \hat{\mathbf{r}}^-). \tag{5.13}$$

and the superscripts - and + denote the state before and after the update, respectively. The Kalman filter gain is given by

$$\mathbf{K} = \mathbf{P}^{-}\mathbf{S}^{T}(\mathbf{S}\mathbf{P}^{-}\mathbf{S}^{T} + \mathbf{N})^{-1},\tag{5.14}$$

where the S is the Jacobian of the observation model and N indicates the measurement noise covariance matrix. The matrices S and N for the considered problem are obtained from (5.1) as $S = \begin{bmatrix} I & 0 \end{bmatrix}$ and

$$E\left[\mathbf{w}_{r}(t_{k})\ \mathbf{w}_{r}(t_{k'})^{T}\right] = \mathbf{N}\delta_{kk'},\tag{5.15}$$

where $\delta_{kk'}$ is the Kronecker delta function. The filter covariance is updated according to

$$\mathbf{P}^{+} = (\mathbf{I} - \mathbf{K} \mathbf{S}) \mathbf{P}^{-}. \tag{5.16}$$

5.2 Attitude determination

In this section, an attitude determination filter is presented which can be used in combination with the control laws presented in Chapter 4. The attitude determination filter processes data from a star tracker and a set of three orthogonal gyros to estimate the attitude and angular rate of the spacecraft, and the resultant of the disturbance torques. The output of the star-tracker is a quaternion of the form

$$\dot{\mathbf{q}}_{IB} = \mathbf{q}(\delta \mathbf{w}_{\theta}) \circ \mathbf{q}_{IB},\tag{5.17}$$

where \mathbf{w}_{θ} indicates the measurement noise. Gyro measurements are modeled as

$$\dot{\omega} = \omega + \mathbf{b}_{\omega} + \mathbf{w}_{\omega},\tag{5.18}$$

where ω is the true angular rate, \mathbf{w}_{ω} is the measurement noise and \mathbf{b}_{ω} is the gyro bias. The gyro bias can be modeled as a random walk process, as

$$\dot{\mathbf{b}}_{\omega} = \mathbf{w}_b,\tag{5.19}$$

where \mathbf{w}_b is the rate random walk noise.

5.2.1 Propagation

The dynamic model of attitude determination filters typically include the quaternion $\hat{\mathbf{q}}_{IB}$, defining the orientation of the spacecraft with respect to the inertial frame, and the gyro bias $\hat{\mathbf{b}}_{\omega}$, while the angular rate dynamics can either be included or replaced by the estimate provided by the difference between the gyro output and the estimated gyro bias [107]

$$\hat{\boldsymbol{\omega}} = \check{\boldsymbol{\omega}} - \hat{\mathbf{b}}_{\boldsymbol{\omega}}.\tag{5.20}$$

In the following derivation, the filter state does include the angular rate dynamics, to provide an estimate $\hat{\tau}_e$ of the disturbance torques acting on the spacecraft. In fact, the most significant disturbance torques τ_e are slowly varying, and can be treated as constant parameters to be estimated by the EKF. A design based on (5.20) is presented in Section 5.3.

Using a constant approximation of the inertia matrix of the form $I_M = \text{diag}(I_x, I_y, I_z)$, the filter state propagation model is obtained from eqs. (2.26), (2.31) and (5.19) as

$$\dot{\hat{\mathbf{q}}}_{IB} = \frac{1}{2} \begin{bmatrix} 0 \\ \hat{\boldsymbol{\omega}} \end{bmatrix}^T \circ \hat{\mathbf{q}}_{IB}$$
 (5.21)

$$\dot{\hat{\omega}} = \mathbf{I}_{M}^{-1} \left(\hat{\boldsymbol{\tau}}_{e} + \boldsymbol{\tau}_{u} - \hat{\boldsymbol{\omega}} \times \mathbf{I}_{M} \, \hat{\boldsymbol{\omega}} \right) \tag{5.22}$$

$$\dot{\hat{\mathbf{b}}}_{\omega} = \mathbf{0} \tag{5.23}$$

$$\dot{\hat{\tau}}_e = 0, \tag{5.24}$$

where τ_u is the commanded control torque from (4.11). To avoid covariance singularities, due to the quaternion unit-norm constraint, a modified estimation error vector $\delta \mathbf{m}$ is adopted to propagate the covariance matrix and to update both the state and the covariance matrix of the filter. In the modified error vector, the attitude error is parameterized by using the three-dimensional rotation vector $\delta \boldsymbol{\theta}$, instead of being expressed in quaternion form. Hence,

$$\delta \mathbf{m} = \begin{bmatrix} \delta \boldsymbol{\theta}^T & \delta \boldsymbol{\omega}^T & \delta \mathbf{b}_{\omega}^T & \delta \boldsymbol{\tau}_e^T \end{bmatrix}^T.$$
 (5.25)

Making use of the model equations (5.22)-(5.24), and the linearized Bortz equation [107]

$$\delta \dot{\boldsymbol{\theta}} = -\hat{\boldsymbol{\omega}}^{\times} \delta \boldsymbol{\theta} + \delta \boldsymbol{\omega}, \tag{5.26}$$

the Jacobian matrix of the system, computed at the current estimate, can be expressed as

$$\mathbf{J} = \begin{bmatrix} -\hat{\boldsymbol{\omega}}^{\times} & \mathbf{I} & \mathbf{0} & \mathbf{0} \\ \mathbf{0} & \mathbf{J}' & \mathbf{0} & \mathbf{I}_{M}^{-1} \\ \mathbf{0} & \mathbf{0} & \mathbf{0} & \mathbf{0} \\ \mathbf{0} & \mathbf{0} & \mathbf{0} & \mathbf{0} \end{bmatrix}, \tag{5.27}$$

where

$$\mathbf{J}' = \begin{bmatrix} 0 & \frac{I_y - I_z}{I_x} \hat{\omega}_z & \frac{I_y - I_z}{I_x} \hat{\omega}_y \\ \frac{I_z - I_x}{I_y} \hat{\omega}_z & 0 & \frac{I_z - I_x}{I_y} \hat{\omega}_x \\ \frac{I_x - I_y}{I_z} \hat{\omega}_y & \frac{I_x - I_y}{I_z} \hat{\omega}_x & 0 \end{bmatrix}$$
(5.28)

and $\hat{\boldsymbol{\omega}} = [\hat{\omega}_x, \ \hat{\omega}_y, \ \hat{\omega}_z]^T$. The covariance matrix $\mathbf{P} = E[\hat{\mathbf{m}} \ \hat{\mathbf{m}}^T]$ of the filter is propagated according to (5.6), where the process noise covariance is given by the block diagonal matrix

$$\mathbf{Q} = \text{blockdiag } (\mathbf{0}_3, \mathbf{Q}_{\omega}, \mathbf{Q}_b, \mathbf{Q}_{\tau}). \tag{5.29}$$

In (5.29), \mathbf{Q}_{ω} accounts for inertia, thruster noise and alignment uncertainties, \mathbf{Q}_{b} is obtained from (5.19) as $E\left[\mathbf{w}_{b}(t)\ \mathbf{w}_{b}(t')^{T}\right] = \mathbf{Q}_{b}\delta(t-t')$, and \mathbf{Q}_{τ} is set to a value depending on the expected level of uncertainty of the disturbance torque model.

5.2.2 Measurement update

When measurements are available, the attitude estimate is updated by using a multiplicative approach, while the classical update equations are adopted for the other states. Then

$$\begin{bmatrix} \hat{\mathbf{q}}_{IB}^{+} \\ \hat{\omega}^{+} \\ \hat{\mathbf{b}}_{\omega}^{+} \\ \hat{\tau}_{e}^{+} \end{bmatrix} = \begin{bmatrix} \mathbf{q}(\delta\boldsymbol{\theta}) \circ \hat{\mathbf{q}}_{IB}^{-} \\ \hat{\omega}^{-} + \delta\boldsymbol{\omega} \\ \hat{\mathbf{b}}_{\omega}^{-} + \delta\mathbf{b}_{\omega} \\ \hat{\tau}_{e}^{-} + \delta\boldsymbol{\tau}_{e} \end{bmatrix}, \tag{5.30}$$

where

$$\delta \mathbf{m} = \begin{bmatrix} \delta \boldsymbol{\theta}^T & \delta \boldsymbol{\omega}^T & \delta \mathbf{b}_{\omega}^T & \delta \mathbf{r}_{e}^T \end{bmatrix}^T = \mathbf{K} \begin{bmatrix} 2 \, \vec{\mathbf{q}}_{\hat{B} \check{B}}^T \\ \check{\boldsymbol{\omega}} - \hat{\boldsymbol{\omega}}^T - \hat{\mathbf{b}}_{\omega}^T \end{bmatrix}, \tag{5.31}$$

 $\mathbf{q}_{BB}^- = \check{\mathbf{q}}_{IB} \circ \hat{\mathbf{q}}_{BI}^-$ and the Kalman gain \mathbf{K} is given by (5.14). The filter covariance is updated as in (5.16). The observation matrix \mathbf{S} and measurement noise covariance matrix \mathbf{N} for the considered problem are obtained from (5.17)-(5.18) as

$$\mathbf{S} = \begin{bmatrix} \mathbf{I} & \mathbf{0} & \mathbf{0} & \mathbf{0} \\ \mathbf{0} & \mathbf{I} & \mathbf{I} & \mathbf{0} \end{bmatrix} \tag{5.32}$$

$$\mathbf{N} = \text{blockdiag}(\mathbf{N}_{\theta}, \, \mathbf{N}_{\omega}), \tag{5.33}$$

where

$$E\left[\mathbf{w}_{\theta}(t_{k})\ \mathbf{w}_{\theta}(t_{k'})^{T}\right] = \mathbf{N}_{\theta}\delta_{kk'} \tag{5.34}$$

and

$$E\left[\mathbf{w}_{\omega}(t_{k})\ \mathbf{w}_{\omega}(t_{k'})^{T}\right] = \mathbf{N}_{\omega}\delta_{kk'}.$$
(5.35)

5.3 Relative navigation

In this section, a relative navigation filter is developed, which can be used in combination with the control technique presented in Section 3.3 for autonomous rendezvous and docking of a target-chaser spacecraft formation. In particular it is shown how the state of the target spacecraft, including position, velocity, attitude and angular rate, can be estimated on-board the chaser, based on optical measurements of known target features. Notice that

this approach is only feasible for close proximity operations, because the accuracy of optical observations rapidly decreases as the distance between the two spacecraft grows. To circumvent this issue, a different navigation solution, based for instance on differential GPS measurements, can be considered during the initial phase of the rendezvous maneuver.

This section is organized as follows. First, the measurement model is presented. Then, an EKF design based on the attitude and orbit determination filters previously discussed is derived. For the sake of a clear exposition, in this section the target trajectory, from the solution to (3.1),(3.3), will be denoted by $\mathbf{r}_T = \bar{\mathbf{r}}$, $\mathbf{v}_T = \dot{\mathbf{r}}$.

5.3.1 Measurement model

The observation model used include GPS, gyro, star-tracker, and optical camera measurements. The GPS, gyro and star-tracker models are described in the previous two sections. The optical camera provides line-of-sight information, i.e. azimuth and elevation angles, by measuring the location of known features of the target spacecraft in the camera focal plane. Notice that the considered sensors are installed on the chaser spacecraft, so that the target may be passive.

The measured azimuth and elevation angles $\check{\alpha}_i$ and $\check{\psi}_i$ of a feature i of the target are modeled as

$$\check{\alpha}_i = \tan^{-1} \left(\frac{l_y}{l_x} \right) + w_\alpha \tag{5.36}$$

$$\check{\psi}_i = \sin^{-1}(l_z) + w_\psi$$
(5.37)

where $l_x \ l_y \ l_z$ denote the individual components of the relative line-of-sight unit vector \mathbf{l}_i , and w_{α} , w_{ψ} model the sensor noise. The line-of-sight vector can be written in terms of the noise-free angle measurements α_i and ψ_i , according to

$$\mathbf{l}_{i} = \begin{bmatrix} \cos(\psi_{i})\cos(\alpha_{i}) \\ \cos(\psi_{i})\sin(\alpha_{i}) \\ \sin(\psi_{i}) \end{bmatrix}. \tag{5.38}$$

Alternatively, it can be expressed as a function of the inertial state, as follows

$$l_i = \rho_i / \|\rho_i\| \tag{5.39}$$

$$\rho_i = \mathbf{R}_{IB} \left[\mathbf{r}_T + \mathbf{R}_{IT}^T \mathbf{r}_i - (\mathbf{r} + \mathbf{R}_{IB}^T \mathbf{r}_c) \right], \tag{5.40}$$

where ρ_i denote the relative range vector, \mathbf{r}_i denote the position of the *i*-th feature in the target frame, \mathbf{r}_c indicates the camera position in the chaser frame, and \mathbf{R}_{TI} expresses the rotation from the target frame to the ECI frame. The geometry of the problem is illustrated in Fig. 5.1.

Notice that the target must lie within the field of view of the optical camera to enable the estimation of the relative position and velocity. Moreover, the observation of at least three features of the target spacecraft is required to determine its attitude.

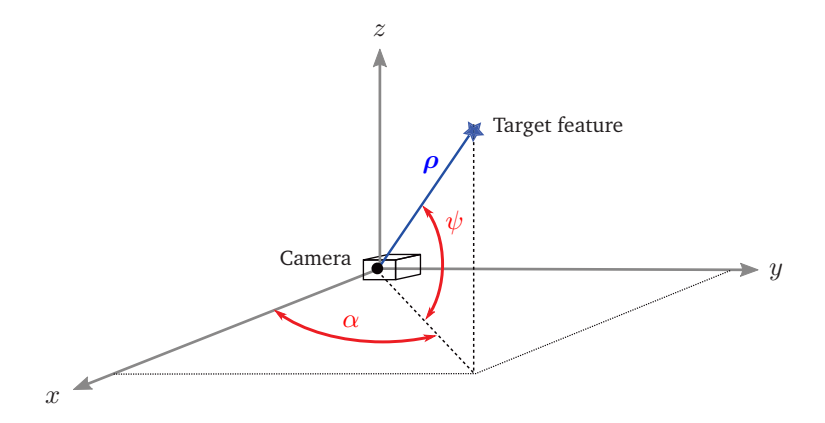


Figure 5.1: Optical measurement model.

5.3.2 Propagation

For relative navigation and pose estimation, it is debatable whether to use relative states to limit the size of the navigation filter versus the absolute states to maximize the available information [139]. The design presented hereafter is based on the absolute states of the two spacecraft, according to the orbit and attitude determination approaches presented so far. The dynamic model of the filter is given by

$$\dot{\hat{\mathbf{r}}}_T = \hat{\mathbf{v}}_T \tag{5.41}$$

$$\dot{\hat{\mathbf{v}}}_T = -\frac{\mu}{\|\hat{\mathbf{r}}_T\|^3} \,\hat{\mathbf{r}}_T + \mathbf{a}_{J2}(\hat{\mathbf{r}}_T) \tag{5.42}$$

$$\dot{\hat{\mathbf{q}}}_{IT} = \frac{1}{2} \begin{bmatrix} 0 \\ \hat{\boldsymbol{\omega}}_T \end{bmatrix} \circ \hat{\mathbf{q}}_{IT} \tag{5.43}$$

$$\dot{\hat{\omega}}_T = \mathbf{I}_L^{-1} \left(\hat{\omega}_T \times \mathbf{I}_T \ \hat{\omega}_T \right) \tag{5.44}$$

$$\dot{\hat{\mathbf{r}}} = \hat{\mathbf{v}} \tag{5.45}$$

$$\dot{\hat{\mathbf{v}}} = -\frac{\mu}{\|\hat{\mathbf{r}}\|^3} \,\hat{\mathbf{r}} + \mathbf{a}_{J2}(\hat{\mathbf{r}}) + \hat{\mathbf{a}}_I \tag{5.46}$$

$$\dot{\hat{\mathbf{q}}}_{IB} = \frac{1}{2} \begin{bmatrix} 0 \\ \hat{\boldsymbol{\omega}} \end{bmatrix} \circ \hat{\mathbf{q}}_{IB} \tag{5.47}$$

$$\dot{\hat{\mathbf{b}}}_{\omega} = \mathbf{0} \tag{5.48}$$

where \mathbf{q}_{IT} , $\boldsymbol{\omega}_{T}$, \mathbf{I}_{T} and $\boldsymbol{\tau}_{T}$ denote the attitude, angular rate and inertia matrix of the target spacecraft, $\hat{\mathbf{a}}_{I}$ is the control acceleration, and the angular rate dynamics of the chaser

are replaced by the difference between the gyro output and the estimated gyro bias, by using (5.20) in (5.47). Notice that, in the considered application, the attitude of the chaser spacecraft is nominally aligned to the LVHL frame, so that

$$\hat{\mathbf{a}}_I = \hat{\mathbf{R}}_{IB}^T [\mathbf{u}^T, 0]^T / m, \tag{5.49}$$

where u is given by (3.29). Equation (5.49) is consistent with the fact that the orbit control thrusters are mounted at fixed orientation with respect to the spacecraft body frame.

Similarly to the design presented in Section 5.2, the attitude estimation error is parameterized by using a three-dimensional rotation vector to propagate the covariance matrix and to update both the state and the covariance matrix of the filter. Hence, the Jacobian matrix of the system, computed at the current estimate, can be expressed as

where \mathbf{J}' is given by (5.28) and $\mathbf{a} = [\mathbf{u}^T, 0]^T/m$. Moreover, the process noise covariance matrix is given by

$$\mathbf{Q} = \text{blockdiag} \left(\mathbf{0}, \mathbf{T}_a, \mathbf{0}, \mathbf{T}_{\omega}, \mathbf{0}, \mathbf{Q}_a, \mathbf{0}, \mathbf{Q}_{\omega} + \mathbf{N}_{\omega}, \mathbf{Q}_b \right), \tag{5.51}$$

where the covariance matrices T_a and T_{ω} account for uncertainties due to unmodeled dynamics in (5.42) and (5.44), respectively. The covariance matrix of the filter is propagated according to (5.6).

5.3.3 Measurement update

When measurements are available, the state of the filter is updated according to the procedure described in Section 5.1.2 and 5.2.2. In this case, the update takes the form

$$\begin{bmatrix} \hat{\mathbf{r}}_{T}^{+} \\ \hat{\mathbf{v}}_{T}^{+} \\ \hat{\mathbf{q}}_{IT}^{+} \\ \hat{\mathbf{q}}_{IT}^{+} \\ \hat{\boldsymbol{\omega}}_{T}^{+} \\ \hat{\mathbf{r}}^{+} \\ \hat{\mathbf{r}}^{+} \\ \hat{\mathbf{q}}_{IB}^{+} \\ \hat{\mathbf{b}}_{\omega}^{+} \end{bmatrix} = \begin{bmatrix} \hat{\mathbf{r}}_{T}^{-} + \delta \mathbf{r}_{T} \\ \hat{\mathbf{v}}_{T}^{-} + \delta \mathbf{v}_{T} \\ \mathbf{q}(\delta \boldsymbol{\theta}_{T}) \circ \hat{\mathbf{q}}_{IB}^{-} \\ \hat{\boldsymbol{\omega}}_{T}^{-} + \delta \mathbf{w}_{T} \\ \hat{\mathbf{r}}^{-} + \delta \mathbf{r} \\ \hat{\mathbf{v}}^{-} + \delta \mathbf{v} \\ \mathbf{q}(\delta \boldsymbol{\theta}) \circ \hat{\mathbf{q}}_{IB}^{-} \\ \hat{\mathbf{b}}_{\omega}^{-} + \delta \mathbf{b}_{\omega} \end{bmatrix},$$
(5.52)

where

$$\begin{bmatrix} \delta \mathbf{r}_{T}^{T} & \delta \mathbf{v}_{T}^{T} & \delta \boldsymbol{\theta}_{T}^{T} & \delta \mathbf{w}_{T}^{T} & \delta \mathbf{r}^{T} & \delta \mathbf{v}^{T} & \delta \mathbf{e}^{T} & \delta \mathbf{b}_{\omega}^{T} \end{bmatrix}^{T} = \mathbf{K} \begin{bmatrix} \dot{\mathbf{r}} - \hat{\mathbf{r}}^{-} \\ 2 \dot{\mathbf{q}}_{\hat{B}\dot{B}}^{-} \\ \tilde{\mathbf{z}}_{o}^{-} \end{bmatrix}, \quad (5.53)$$

and $\tilde{\mathbf{z}}_o^-$ denotes the measurement residual from optical observations (before the update). The observation matrix \mathbf{S} and measurement noise covariance matrix \mathbf{N} , for the considered problem, are given by

$$\mathbf{S} = \begin{bmatrix} 0 & 0 & 0 & \mathbf{I} & 0 & 0 & 0 \\ 0 & 0 & 0 & 0 & 0 & \mathbf{I} & 0 \\ \hline & \mathbf{S}_o & & & & & \\ \end{bmatrix}$$
 (5.54)

$$\mathbf{N} = \text{blockdiag}(\mathbf{N}_r, \mathbf{N}_{\theta}, \mathbf{N}_{o}). \tag{5.55}$$

The filter covariance is updated as in (5.16). The residual $\tilde{\mathbf{z}}_o$ and the matrices \mathbf{S}_o , \mathbf{N}_o are obtained as explained next.

The residual $\tilde{\mathbf{z}}_i$ for the optical measurement of the *i*-th target feature is given by

$$\tilde{\mathbf{z}}_i = \check{\mathbf{z}}_i - \hat{\mathbf{z}}_i = \begin{bmatrix} \check{\alpha}_i - \hat{\alpha}_i \\ \check{\psi}_i - \hat{\psi}_i \end{bmatrix}$$
 (5.56)

In this equation, $\check{\alpha}_i$, $\check{\psi}_i$ are specified by (5.36)-(5.37) and $\hat{\alpha}_i$, $\hat{\psi}_i$ are obtained similarly, as follows

$$\hat{\alpha}_i = \tan^{-1} \left(\frac{\hat{l}_y}{\hat{l}_x} \right), \tag{5.57}$$

$$\hat{\psi}_i = \sin^{-1}\left(\hat{l}_z\right). \tag{5.58}$$

The estimated line-of-sight vector $\hat{\mathbf{l}}_i = [\hat{l}_x, \, \hat{l}_y, \, \hat{l}_z]^T$ is given by

$$\hat{\mathbf{l}}_i = \frac{\hat{\boldsymbol{\rho}}_i}{\|\hat{\boldsymbol{\rho}}_i\|},\tag{5.59}$$

where the estimated relative range vector $\hat{\rho}_i$ can be expressed in terms of the filter state as

$$\hat{\boldsymbol{\rho}}_i = \hat{\mathbf{R}}_{IB} \left[\hat{\mathbf{r}}_T + \hat{\mathbf{R}}_{IT}^T \mathbf{r}_i - (\hat{\mathbf{r}} + \hat{\mathbf{R}}_{IB}^T \mathbf{r}_c) \right], \tag{5.60}$$

according to (5.40). Notice that, by (5.38)-(5.39),

$$\hat{\boldsymbol{\rho}}_{i} = \|\hat{\boldsymbol{\rho}}_{i}\|\hat{\mathbf{l}}_{i} = \|\hat{\boldsymbol{\rho}}_{i}\| \begin{bmatrix} \cos(\hat{\psi}_{i})\cos(\hat{\alpha}_{i}) \\ \cos(\hat{\psi}_{i})\sin(\hat{\alpha}_{i}) \\ \sin(\hat{\psi}_{i}) \end{bmatrix}. \tag{5.61}$$

The observation matrix for the *i*-th feature is defined as

$$\mathbf{S}_{i} = \begin{bmatrix} \partial \hat{\alpha}_{i} / \partial \hat{\mathbf{y}} \\ \partial \hat{\psi}_{i} / \partial \hat{\mathbf{y}} \end{bmatrix}, \tag{5.62}$$

where $\hat{\mathbf{y}}$ denotes the filter state. The corresponding covariance matrix is obtained from (5.36)-(5.37) as $E\left[\mathbf{w}_{i}(t_{k})\ \mathbf{w}_{i}(t_{k'})^{T}\right] = \mathbf{N}_{i}\,\delta_{kk'}$, where $\mathbf{w}_{i} = \left[w_{\alpha},\ w_{\psi}\right]^{T}$.

In order to derive the expressions for the partial derivatives in (5.62) observe that, by using the chain rule

$$\frac{\partial \hat{\boldsymbol{\rho}}_{i}}{\partial \hat{\mathbf{y}}} = \frac{\partial \hat{\boldsymbol{\rho}}_{i}}{\partial \hat{\alpha}_{i}} \frac{\partial \hat{\alpha}_{i}}{\partial \hat{\mathbf{y}}} + \frac{\partial \hat{\boldsymbol{\rho}}_{i}}{\partial \hat{\psi}_{i}} \frac{\partial \hat{\psi}_{i}}{\partial \hat{\mathbf{y}}} = \|\hat{\boldsymbol{\rho}}_{i}\| \frac{\partial \hat{\boldsymbol{l}}_{i}}{\partial \hat{\alpha}_{i}} \frac{\partial \hat{\alpha}_{i}}{\partial \hat{\mathbf{y}}} + \|\hat{\boldsymbol{\rho}}_{i}\| \frac{\partial \hat{\boldsymbol{l}}_{i}}{\partial \hat{\psi}_{i}} \frac{\partial \hat{\psi}_{i}}{\partial \hat{\mathbf{y}}}.$$
 (5.63)

The vectors $\partial \hat{l}_i/\partial \hat{\alpha}_i$ and $\partial \hat{l}_i/\partial \hat{\psi}_i$, given by

$$\partial \hat{\boldsymbol{l}}_i/\partial \hat{\alpha}_i = \begin{bmatrix} -\cos(\hat{\psi}_i)\sin(\hat{\alpha}_i) \\ \cos(\hat{\psi}_i)\cos(\hat{\alpha}_i) \\ 0 \end{bmatrix}, \quad \partial \hat{\boldsymbol{l}}_i/\partial \hat{\psi}_i = \begin{bmatrix} -\sin(\hat{\psi}_i)\cos(\hat{\alpha}_i) \\ -\sin(\hat{\psi}_i)\sin(\hat{\alpha}_i) \\ \cos(\hat{\psi}_i) \end{bmatrix}, \quad (5.64)$$

turn out to be orthogonal to each other. Then, by multiplying (5.63) by $\partial \hat{l}_i/\partial \hat{\alpha}_i$ and by $\partial \hat{l}_i/\partial \hat{\psi}_i$, and solving for $\partial \hat{\alpha}_i/\partial \hat{\mathbf{y}}$ and $\partial \hat{\psi}_i/\partial \hat{\mathbf{y}}$, one gets

$$\frac{\partial \hat{\alpha}_i}{\partial \hat{\mathbf{y}}} = \frac{\left(\partial \hat{\mathbf{l}}_i / \partial \hat{\alpha}_i\right)^T}{\|\hat{\boldsymbol{\rho}}_i\| \cos^2(\hat{\psi}_i)} \frac{\partial \hat{\boldsymbol{\rho}}_i}{\partial \hat{\mathbf{y}}},\tag{5.65}$$

$$\frac{\partial \hat{\psi}_i}{\partial \hat{\mathbf{y}}} = \frac{\left(\partial \hat{\mathbf{l}}_i / \partial \hat{\psi}_i\right)^T}{\|\hat{\boldsymbol{\rho}}_i\|} \frac{\partial \hat{\boldsymbol{\rho}}_i}{\partial \hat{\mathbf{y}}}.$$
 (5.66)

From (5.60), it follows that

$$\frac{\partial \hat{\boldsymbol{\rho}}_{i}}{\partial \hat{\mathbf{y}}} = \begin{bmatrix} \hat{\mathbf{R}}_{IB} & \mathbf{0} & -\hat{\mathbf{R}}_{TB} \mathbf{r}_{i}^{\times} & \mathbf{0} & -\hat{\mathbf{R}}_{IB} & \mathbf{0} & (\hat{\mathbf{R}}_{IB}\mathbf{r}_{T} + \hat{\mathbf{R}}_{TB}\mathbf{r}_{i} - \hat{\mathbf{R}}_{IB}\hat{\mathbf{r}})^{\times} & \mathbf{0} \end{bmatrix}, \quad (5.67)$$

where $\hat{\mathbf{R}}_{TB} = \hat{\mathbf{R}}_{IB}\hat{\mathbf{R}}_{IT}^T$. Hence, the observation matrix (5.62) can be computed by substituting (5.58)-(5.60),(5.64) and (5.67) in (5.65)-(5.66).

The procedure is repeated for each observed feature (i = 1,...,n) of the target spacecraft, with the final form of the residual $\tilde{\mathbf{z}}_o$ and the matrices \mathbf{S}_o , \mathbf{N}_o in (5.53)-(5.55) given by

$$\tilde{\mathbf{z}}_{o} = \begin{bmatrix} \tilde{\mathbf{z}}_{1} \\ \vdots \\ \tilde{\mathbf{z}}_{n} \end{bmatrix}, \qquad \mathbf{S}_{o} = \begin{bmatrix} \mathbf{S}_{1} \\ \vdots \\ \mathbf{S}_{n} \end{bmatrix}, \qquad \mathbf{N}_{o} = \begin{bmatrix} \mathbf{N}_{1} & \dots & \mathbf{0} \\ \vdots & \ddots & \vdots \\ \mathbf{0} & \dots & \mathbf{N}_{n} \end{bmatrix}. \tag{5.68}$$

Numerical Simulations

In this section, the results of numerical simulations are reported and analyzed to evaluate the performance of the proposed control techniques and the feasibility of EP systems for orbit and attitude control. The developed software includes an accurate simulator based on the dynamic models presented in Chapter 2, the GNC module described in Chapters 3-5, and the mathematical models of different types of LEO and GEO spacecraft (sensors, actuators, vehicle layouts).

6.1 Autonomous station-keeping with electric propulsion

The objective of this section is to demonstrate the applicability of the orbit control scheme developed in Section 3.2, together with the navigation system presented in Section 5.1, for autonomous station-keeping of a small LEO satellite with Hall-effect and resistojet thrusters.

6.1.1 Reference mission

In the following, details of the mission, navigation requirements, and spacecraft configuration, are provided. The reference mission orbit is a specialized sun-synchronous, repeat ground-track and frozen orbit, which is a common design for LEO satellites [13]. The orbit is nearly circular, with an altitude of around 228 km, which corresponds to a 5 day ground-track repeat period. The initial orbital elements are derived by using a simplified J2 and J3 zonal harmonics analysis and refined through numerical simulations, ignoring all the periodic orbital perturbations [131]. Table 6.1 shows the initial nominal values of the orbital elements for the chosen reference mission.

Table 6.1: Orbital elements (initial nominal values)

Semi-major axis	a	6591.338 km
Inclination	i	96.3862°
Eccentricity vector x-component	$e_x = e \cos \omega$	0
Eccentricity vector y-component	$e_y = e \sin \omega$	0.0011
Right ascension of the ascending node	Ω	10°

The reference orbit is defined in such a way that gravitational perturbations, which cause the sun synchronous secular motion of $\dot{\Omega}=360^{\circ}/\text{year}$, do not need to be counteracted. As

a consequence, the propulsion system is activated only to compensate for non gravitational disturbances, by means the orbital element control scheme discussed in Section 3.2.2. The dominant non gravitational perturbing forces on the reference orbit are due to atmospheric drag and resonance effects induced by the Sun. The most significant effects of these perturbations on the orbital elements are a constant decay in the semi-major axis, in the order of 300 m per revolution, and a small secular drift of the inclination.

The spacecraft is nominally aligned with the LVLH frame along the orbit. On-board sensors and actuators are selected in order to meet the navigation and control accuracy requirements, considering the constraints imposed by the spacecraft size. The driving requirement for orbit control is to keep the satellite orbit within a distance of about 500 m from the reference orbit. Based on this limitation, a preliminary estimate of the required navigation system accuracy of about 50 m may be considered. Hence, for absolute position determination purposes, it is sufficient to consider a GPS navigation solution in a loosely-coupled GPS/INS integration scheme, capable of providing positioning accuracy of about 20 m [7].

The satellite is equipped with the propulsion system shown in Table 6.2. A 100 W class Hall effect thruster [86, 108] is employed to compensate the secular variation in the orbit semi-major axis, caused by the along-track component of atmospheric drag. The acceleration \mathbf{a}_I provided by the Hall effect thruster, expressed in the inertial reference frame, is given by

$$\mathbf{a}_{I} = \mathbf{R}_{IL}^{T} (\mathbf{I} - \boldsymbol{\epsilon}^{\times}) \left(\mathbf{a} + \begin{bmatrix} w_{p}, & 0, & 0 \end{bmatrix}^{T} / m \right), \tag{6.1}$$

where a is the commanded acceleration in (3.5), w_p indicates the actuator noise, m is the spacecraft mass, and ϵ expresses the thrust alignment error. The covariance of the thruster noise is

$$E[w_p(t) w_p(t')] = \sigma_p^2 \delta(t - t').$$
 (6.2)

The alignment error ϵ is included in (6.1) to account for attitude deviations from the reference LVLH attitude. It is modeled as a white noise process, with covariance given by

$$E\left[\epsilon\left(t\right)\epsilon\left(t'\right)\right] = \mathbf{I}\,\sigma_{\epsilon}^{2}\,\delta(t - t')\,. \tag{6.3}$$

For the reference mission scenario, simulation results indicate that the thrust needed to continuously counteract the drag acceleration \mathbf{a}_d in (2.11), is in the throttling range of considered Hall thruster, and comparable to that required in similar missions, like GOCE (see, e.g., [21]).

A 30 W xenon resistojet [102] provides out of plane impulsive burns to compensate for the cross-track component of drag, which is due to the co-rotation of the atmosphere with the Earth, and the sun-synchronous resonance effects on the orbit inclination and right ascension of the ascending node. The impulsive velocity change $\Delta \mathbf{v}_I$ provided by the resistojet, expressed in the inertial frame, is modeled as

$$\Delta \mathbf{v}_{I} = \mathbf{R}_{IL}^{T} (\mathbf{I} - \boldsymbol{\epsilon}^{\times}) \left(\Delta \mathbf{v} + \begin{bmatrix} 0, w_{v}, 0 \end{bmatrix}^{T} \right), \tag{6.4}$$

where $\Delta \mathbf{v}$ is the commanded velocity change in (3.20) and w_v indicates the additive noise on the velocity change. The covariance of w_v is

$$E[w_v(t_k) w_v(t_{k'})] = \sigma_v^2 \delta_{k k'}.$$
(6.5)

This considered design is basically a trade-off between the thrust efficiency and the limitations imposed by the satellite payload and available power. In fact, we can take advantage of the Hall thruster high specific impulse to reduce the propellant consumption required by drag compensation, which is the dominant factor in the mission delta-v budget, while using a higher thrust, low-power resistojet to counteract smaller cross-track perturbations, at the price of a low specific impulse. Moreover, a single propellant tank containing xenon gas will be shared between the Hall effect thruster and the resistojet, resulting in a simplified satellite internal layout.

Table 6.2: Spacecraft propulsion system

The specifications of sensors and actuators are summarized in Table 6.3, where σ_p , σ_ϵ and σ_v are defined in (6.2),(6.3) and (6.5), and σ_G is defined by (5.15), with $N = I\sigma_G^2$. In order to assess the feasibility of the proposed propulsion scheme, within the considered mission, a sketch of the spacecraft size, mass and power system is provided next.

Device	Noise (σ)	Alignment error	Update frequency
Gps	$\sigma_G = 30 \text{ m}$	-	0.1 Hz
Hall thruster	$\sigma_p = 0.3 \text{ mN } \sqrt{\text{s}}$	$\sigma_{\epsilon} = 4 \text{ mrad}$	0.1 Hz modulation
Resistojet	$\sigma_v = 1 \text{ mm/s}$	$\sigma_{\epsilon}=4~\mathrm{mrad}$	Impulsive

Table 6.3: Sensor and actuator specifications

6.1.2 Spacecraft and power system

The external layout of the spacecraft is modeled as a rectangular box, with a square cross-section of $A=0.5\times0.5~\mathrm{m^2}$ and a length of 1 m, similar to the elongated shape of the GOCE spacecraft. The assumed aerodynamic drag coefficient is $C_D=2.5$. The total mass of the spacecraft is assumed to be $m=100~\mathrm{kg}$, including 30 kg of propellant mass. The Hall thruster, the cathode and the power conditioning unit (PCU) have a mass of less than 3 kg. The parameters A, m, and C_D are employed in the simulation model, to evaluate the

disturbance accelerations acting on the spacecraft. The mass of the xenon resistojet plus its power regulator can be estimated in 1 kg. The tank storing up to 30 liters of xenon and all the valves, tubing, harness can be limited to additional 6 kg. Therefore, the propulsion system has a dry mass of less than 9 kg. Including the propellant, the whole propulsion system mass will not exceed 40 kg, i.e. about 40% of the total spacecraft mass.

Power is supplied by triple junction solar cells with an efficiency of about 28%, a packing factor of 0.85, and a 3% power degradation over the expected mission life. Given these figures, it is possible to consider solar arrays with a surface area of less than $0.4~\rm m^2$ and a mass of about 2 kg, able to provide at least 100 W power at end of life. Moreover, the external layout of the spacecraft can host a solar array installation of at least 1 $\rm m^2$, whose total supplied power is largely sufficient for the proposed payload and propulsion needs. A battery system of 150 Wh/kg based on Li-ion cells is feasible for the proposed design.

The Hall thruster system is operated so that the supplied thrust can be changed about every 10 seconds. Several approaches have been proposed in literature in order to provide fast response times for this class of thrusters. Fast flow control valves (e.g. piezoelectric valves or digital MEMS actuators) can be used to quickly change the propellant flow, which in turn provides changes in the thrust (for fixed anode voltage). As an alternative, a high frequency variation (more than 10 Hz), can be obtained by pulse width modulation [65, 116]. Thrust variation can also be obtained by operating on the anode voltage through the PCU, at fixed propellant flow rate. This is the approach we refer to in this section and is feasible for the required $f_h=0.1$ Hz variation rate. Indeed, for the thrust range reported in Table 6.2, given the Hall thruster technology characteristic, a minimum thrust of 2.5 mN can be obtained with about 40 W power (e.g., 200 V and 0.2 A). A 200 V applied voltage provides a specific impulse of more than 1000 s, as expected. For a 6 mN thrust, one can increase the applied voltage to about 500 V, keeping constant the propellant flow rate, and therefore the current. Then, the specific impulse will significantly increase over the assumed 1000 s.

6.1.3 GNC system analysis

The reference mission is simulated by taking into account a realistic truth model, sensors, actuators and GNC flight algorithms. The truth model, which combines (2.7),(2.16), with (2.18)-(2.21), is given by

$$\begin{split} \dot{\mathbf{r}} &= \mathbf{v} \\ \dot{\mathbf{v}} &= -\frac{\mu}{r^3} \, \mathbf{r} + \mathbf{a}_e + \mathbf{a}_I \\ \mathbf{v}^\uparrow &= \mathbf{v}^\downarrow + \Delta \mathbf{v}_I \\ \dot{m} &= -\frac{\|m \, \mathbf{a}_I\|}{g_0 \, I_{sp}^h}. \\ m^\uparrow &= m^\downarrow \exp\left(-\frac{\|\Delta \mathbf{v}_I\|}{g_0 I_{sp}^r}\right), \end{split}$$

where \mathbf{a}_I and \mathbf{v}_I are given by (6.1) and (6.4), respectively, and I^h_{sp} , I^r_{sp} are specified in Table 6.2. The block diagram representation of the closed-loop system is reported in Figure 6.1. A worst-case scenario, featuring a high solar and geomagnetic activity, is considered, in order to validate the proposed GNC solution and to evaluate the performance of the propulsion system. The truth model, navigation state and reference dynamics are propagated for 20 days using a fourth-order Runge-Kutta integration method.

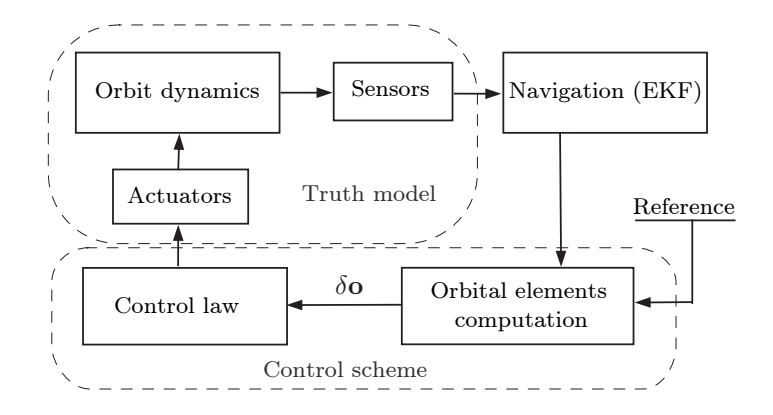


Figure 6.1: Block diagram representation of the closed-loop system.

The tuning parameters of the orbit control law are reported in Table 6.4. The control gains for (3.16) and (3.18) are selected in order to satisfy the Hall thruster output limitations. A sequence of impulsive burns at $\nu_l=0$ or $\nu_l=\pi/2$ is commanded according to (3.20), instead of directly applying (3.19), which ensures the compatibility with the resistojet specifications reported in Table 6.2. The update frequency of the control scheme is taken equal to the modulation frequency f_h of the Hall thruster command (see Section 6.1.2). The resistojet is operated such as to provide impulsive velocity changes of fixed magnitude $\Delta v_n=10$ mm/s, which correspond to 20 s firings at a thrust level of 50 mN.

Table 6.4: Orbit control law parameters

δa gain	$K_a = 10^{-10}$
$\delta e_x,\delta e_y$ gain	$K_{ex}, K_{ey} = 10^3$ $K_{\nu} = 10^{-12}$
δu_l gain	$K_{\nu} = 10^{-12}$
Integral gain	$K_I = 10^{-7}$
δi control window	$-i_L = i_U = 3.5 \cdot 10^{-5} \text{ rad}$
$\delta\Omega$ control window	$\Omega_L = 0, \; \Omega_U = 3.5 \cdot 10^{-5} \; \mathrm{rad}$
Resistojet delta-v	$\Delta v_n = 10 \text{ mm/s}$
Control update frequency	$f_h = 0.1 \; \mathrm{Hz}$

The performance of the Kalman filtering scheme (see Section 5.1) is evaluated in terms of the inertial position determination error, shown together with its 3σ confidence intervals

in Figure 6.2. The filter state is initialized with the first position measurements. After a short transient phase, each component of the 3σ ECI position vector error drops to a steady state value of approximately 20 m. Notice that the error has approximately zero mean and remains within the confidence intervals most of the time.

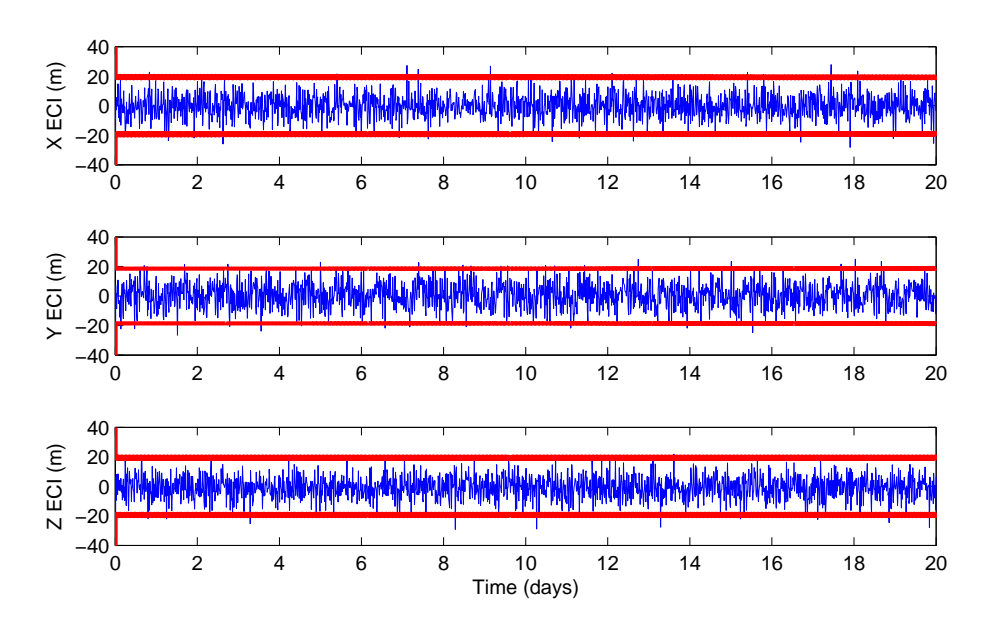


Figure 6.2: Inertial position estimation error and 3σ confidence intervals.

The control system performance is presented in Figure 6.3, in terms of position tracking error, although the control scheme is developed in the orbital element space. This is consistent with the reference trajectory generation model (3.1)-(3.2), which is propagated onboard the spacecraft. The normal component is controlled with an accuracy of less than 50 m, reflecting the effectiveness of the control law (3.18) in controlling semi-major axis error δa . The cross-track component is dependent on the inclination and right ascension of the ascending node errors δi and $\delta \Omega$: the achieved 250 m accuracy is a function of the impulsive control window size in (3.20) . The in-track component of the error, which is proportional to the mean argument of latitude error $\delta \nu_l$, has the major impact on the satellite distance from the reference orbit. It can be observed that the error is kept within 500 m after an initial transient, by using (3.18) in combination with (3.22). Figure 6.4 shows the satellite distance from the reference orbit, whose mean value is 220 m (neglecting the transient phase). These results show that the control requirements are satisfied.

The performance of the propulsion system is depicted in Figure 6.5, in terms of the Hall thruster and resistojet outputs and the Xenon propellant mass consumption. A continuous thrust with mean value of approximately 4 mN and delta-v impulses of about 10 mm/s magnitude are delivered for orbital station-keeping. In the second plot of Figure 6.5, each burn is represented by a bullet. An increased density of bullets in the plot indicates that

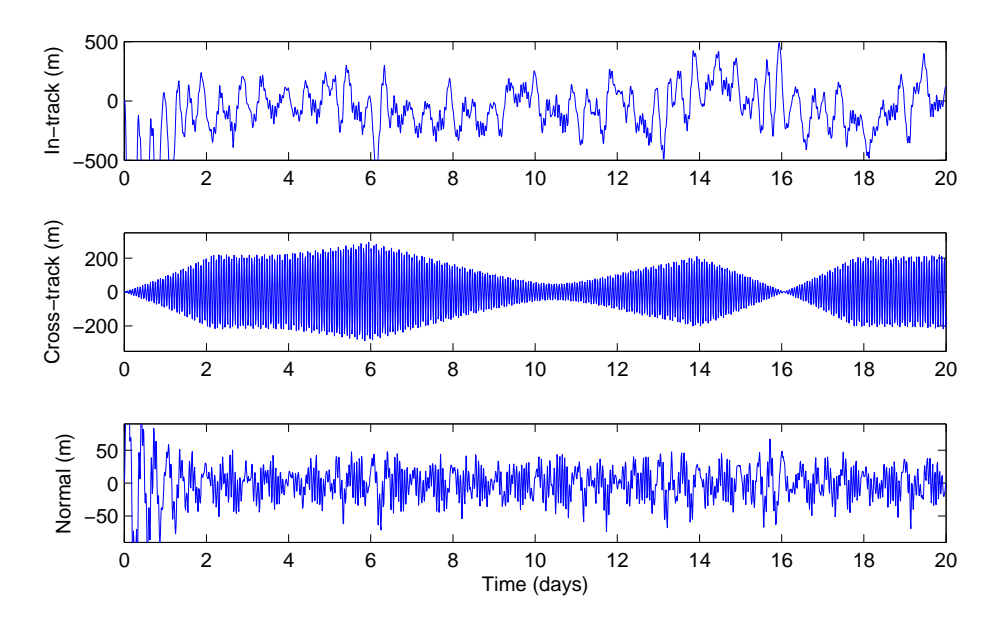


Figure 6.3: Position tracking error.

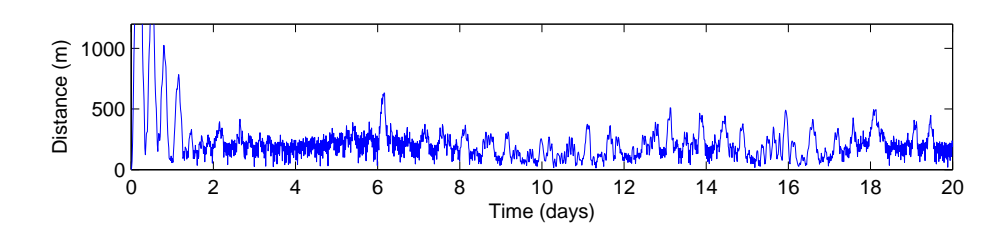


Figure 6.4: Distance from the reference orbit.

the resistojet is firing twice per orbit (at $\nu_l=0$ and $\pi/2$) rather than once (at $\nu_l=0$ or $\pi/2$), while the thruster is not firing in correspondence of empty spaces. Notice that the commanded thrust is always directed in the opposite direction of the disturbing forces. Thus, the proposed GNC system provides an efficient propellant utilization.

The power requirements for simultaneous use of the resistojet and the Hall thruster is about 140 W, which is fully compatible with the power system described in Section 6.1.2. The total propellant consumption is 1.19 kg, including 0.64 kg for continuous thrust and 0.55 kg for impulsive maneuvers. Given a 30 kg propellant tank, the expected lifetime of the satellite is approximately 500 days. As a comparison, observe that an uncontrolled satellite at the considered altitude would burn into the lower atmosphere in few days.

Finally, it is worth remarking that the result presented in this section are obtained by using conservative specifications for the GNC system, and considering a worst-case mission scenario. The fact that the control accuracy requirements can be met under such circum-

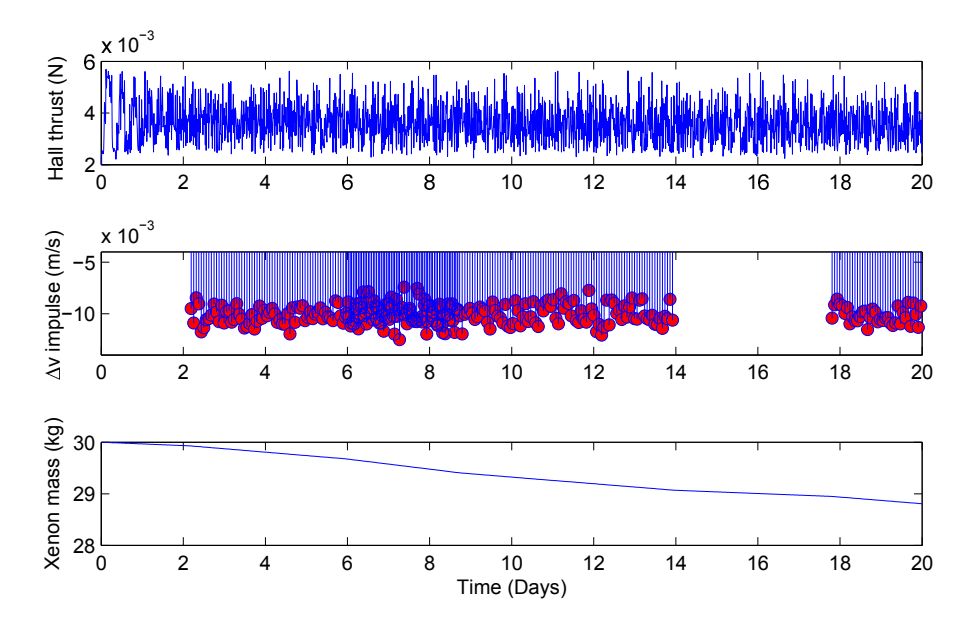


Figure 6.5: Propulsion system performance.

stances suggests the applicability of the proposed control scheme to a broad class of commercial LEO missions, which would strongly benefit from the adoption of an autonomous orbit control system based on EP. In particular, the estimated lifetime of 500 days is feasible for spacecraft orbiting at the considered altitude, and has to be interpreted as a lower bound on the mission duration, due to the assumption of a high solar activity. In this regard, consider that the expected lifetime for GOCE was of about 500 days, in the presence of a low solar activity [37], and hence of a relatively small amount of atmospheric drag to be counteracted. Moreover, despite this expectation, the mission lasted almost 5 years.

6.2 Low-thrust rendezvous and docking

In this section, the performance of the LMPC design developed in Section 3.3 is demonstrated on a small satellite rendezvous and docking mission, in comparison to MPC and LQR techniques. Moreover, the applicability of the proposed design in combination with a set of PPT specifically developed for cubesat size spacecraft is investigated.

6.2.1 Reference mission

A possible scenario for the application of the LMPC design developed in Section 3.3 is a LEO formation flying mission performed by two cubesat size spacecraft, where the relative dynamics are controlled by means of a miniaturized electric propulsion system. A schematic view of the formation is depicted in Fig. 6.6. At the beginning of the operative phase, the spacecraft are flying in a near circular polar orbit, at an altitude of approximately 450 km.

Based on relative position and velocity data, the chaser spacecraft is required to approach the target whilst satisfying LoS and thrust magnitude constraints. It is assumed that the attitude of both spacecraft is kept aligned with the LVLH frame and that the docking port is located behind the target.

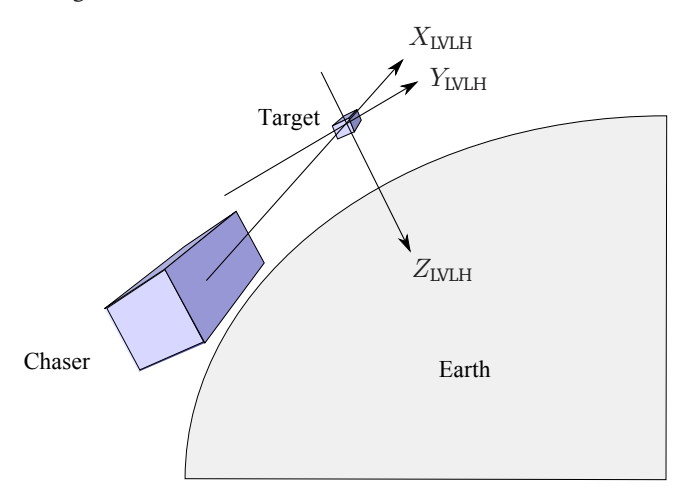


Figure 6.6: Cubesat formation.

The chaser and target spacecraft have identical physical parameters: the total mass of each of them is $3 \, \text{kg}$, the bus size is $30 \times 10 \times 10 \, \text{cm}^3$ and the cross-sectional area is $10 \times 10 \, \text{cm}^2$. The electric propulsion system installed on the chaser consists of a set of PPTs specifically designed for application to cubesats, as described in [24]. Two pairs of opposite PPTs aligned with the along-track and cross-track directions of the LVLH frame are considered. Table 6.5 gives the characteristics of the PPT model.

An integral pulse frequency modulator is used to convert the continuous control signal from the control algorithm into discrete pulses of fixed magnitude, as required by PPT operation. The modulator delivers a pulse p_j , on input channel j, whenever the integral of the commanded thrust $U_j(t)$ is greater than or equal to the impulse bit U_M of the thrusters. For each component of the input \mathbf{u} , one has

$$p_j(t_k) = \begin{cases} U_M \operatorname{sgn}(U_j(t_k)) & \text{if} \quad |U_j(t_k)| \ge U_M \\ 0 & \text{if} \quad |U_j(t_k)| < U_M, \end{cases}$$

$$(6.6)$$

where

$$U_j(t_k) = U_j(t_{k-1}) + \frac{u_j(t_{k-1}) + u_j(t_k)}{2} \Delta t - p_j(t_{k-1}),$$
(6.7)

 $\Delta t = t_k - t_{k-1} \text{ and } j = 1, 2.$

The step size of the modulator is taken as $\Delta t=1$ s, according to the thruster specifications in Table 6.5. Under the assumption that the body frame of the spacecraft is nominally aligned with the LVLH frame, the velocity change imparted by the PPT system can be expressed as

$$\Delta \mathbf{v} = (\mathbf{I} - \boldsymbol{\epsilon}^{\times}) \frac{\mathbf{p} + \mathbf{w}}{m},\tag{6.8}$$

where $\mathbf{p} = [p_1, p_2, 0]^T$, $\boldsymbol{\epsilon}$ denotes the spacecraft alignment error and $\mathbf{w} = [w_1, w_2, 0]^T$ represents the thruster noise. The covariances of the errors are given by $E[\epsilon(t_k) \ \epsilon(t_k')] =$ $\mathbf{I}\sigma_{\epsilon}^2 \, \delta_{k\,k'}$ and $E\left[\mathbf{w}(t_k) \, \mathbf{w}(t_k')\right] = \mathbf{I}\sigma_w^2 \, \delta_{k\,k'}$.

Table 6.5: PPT specifications			
Mass	180 g (wet mass) + 90 g (electronics)		
Dimensions	90.17 x 95.89 x 31 mm		
Power	0.3-4W		
Total Impulse	42 Ns $U_M = 40 \ \mu \text{Ns}$ $\leq 1 \text{ Hz}$		
Impulse Bit			
Pulse frequency			
Specific Impulse	$I_{sp} = 608 \text{ s}$		
Misalignment	$\sigma_{\epsilon}=20~\mathrm{mrad}$		
Noise	$\sigma_w=2~\mu { m Ns}$		

Relative navigation is based on differential GPS measurements during the initial phase of the rendezvous maneuver and on the Kalman filtering algorithm described in Section 5.3, which processes measurement from an optical sensor, during the final approach prior to docking. The standard deviation of differential GPS measurements is set equal to 0.2 m [20], whereas the field of view of the optical sensor is $\theta = 30^{\circ}$. Notice that θ also specifies the size of the docking cone in (3.25). The relative position estimation accuracy is depicted, as a function of the along-track separation between the two spacecraft, in Fig. 6.7.

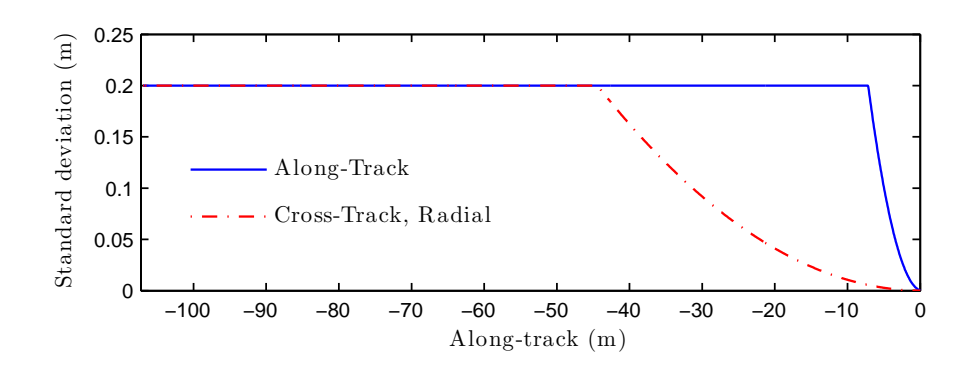


Figure 6.7: Relative position estimation accuracy.

6.2.2 LMPC performance

A high-accuracy, nonlinear simulation model is employed to validate the proposed LMPC design in a realistic scenario. The state vector of the model includes the position and velocity vectors of chaser $(\mathbf{r}, \mathbf{v} = \dot{\mathbf{r}})$ in (2.7) and those of the target $(\mathbf{r}_T = \bar{\mathbf{r}}, \mathbf{v}_T = \dot{\bar{\mathbf{r}}})$ in (3.1). The equations which describe the evolution of the state vector in the ECI frame are

$$\begin{split} \dot{\mathbf{r}}_T &= \mathbf{v}_T \\ \dot{\mathbf{v}}_T &= -\frac{\mu}{r_T^3} \, \mathbf{r}_T + \bar{\mathbf{a}}_e \\ \dot{\mathbf{r}} &= \mathbf{v} \\ \dot{\mathbf{v}} &= -\frac{\mu}{r^3} \, \mathbf{r} + \mathbf{a}_e \,, \\ \mathbf{v}^\uparrow &= \mathbf{v}^\downarrow + \mathbf{R}_{IL}^T \Delta \mathbf{v}, \\ m^\uparrow &= m^\downarrow \exp\left(-\frac{\|\Delta \mathbf{v}\|_1}{g_0 I_{sp}}\right), \end{split}$$

where $\Delta \mathbf{v}$ is given by (6.8). The terms $\bar{\mathbf{a}}_e$ and \mathbf{a}_e account for the most significant environmental perturbations. Relative position and velocity are obtained from the inertial states according to (3.24).

The LMPC control law is tuned to provide a trade-off between the maneuver time and the fuel consumption. Even if these quantities do not explicitly appear in the approximation (3.36) of the cost function (3.27), the relative dynamics are controllable to zero with vanishing input energy, from which it follows that, for a sufficiently long prediction horizon and a relatively small state penalty compared to the input penalty, the minimum energy solution approaches the minimum fuel solution [5, 124]. The elimination of radial thrust, which is an underlying assumption in the proposed design, has proven to be effective in improving the fuel efficiency of control laws based on a quadratic performance index [128]. Since the cross-track motion is a simple undamped oscillatory motion which is decoupled from the rest of the system, pure derivative control can be applied on this axis to provide adequate damping [142]. Hence, the cross-track position weighting can be set to zero. Table 6.6 gives the tuning parameters used in the simulations. Notice that the prediction horizon has been set to a value compatible with the settling time of the maneuver $(N_p T_s = 10^4 \text{ s},$ see Fig. 6.8). Moreover, the number of coefficients N_1 , N_2 of the Laguerre network is kept small to retain a sufficiently low computational complexity. The sampling time T_s is set to a small fraction of the error dynamics timescale, which happens to be very long due extremely weak thrust level generated by the PPT sytem. The remaining parameters have been tuned through numerical simulations.

An explicit solution to the LMPC problem is computed off-line by using the parameters defined in Table 6.7 in (3.65),(3.69), and solving Problem 3.3.3 with the Multi-Parametric Toolbox [64]. The solution is a piecewise affine control law defined over 946 regions of the parameter space $\bar{\mathbb{X}}_C \subset \mathbb{R}^8$, given by (3.70). The online computation of the control sequence boils down to a set-membership evaluation.

The performance of the LMPC scheme is compared to that of an LQR and a standard MPC scheme (i.e. without Laguerre parametrization, see (3.46)). In this comparison, the standard MPC formulation is recovered from the LMPC scheme by setting the scaling factors a_1 , a_2 of the Laguerre function network to zero in (3.44)-(3.45). Moreover, the same tuning parameters are used for the three control laws. Figure 6.8 gives the results for the three

Position weight	$\mathbf{W}_f = \mathbf{W} = \text{diag}(1, 0, 1, 10^5, 5 \cdot 10^5, 10^5)$
Input weight	$\mathbf{K} = \mathbf{I} \cdot 2 \cdot 10^{10}$
Slack weight	$\mathbf{R}_s = \text{diag}(2 \cdot 10^{14}, 3 \cdot 10^6)$
Sampling time	$T_s = 10 \text{ sec}$
Prediction horizon	$N_p = 1000$
Laguerre terms	$N_1 = N_2 = 4$
Scaling factor	$a_1 = a_2 = 0.67$
Thrust constraint	$u_M = 40 \ \mu \text{N}, \ \mathbb{M}_u = \{0\}$
LoS constraint	$\theta = 30^{\circ}, x_d = 2 \text{ cm}, \ \mathbb{M}_x = \{1, 50\}$

Table 6.6: *LMPC tuning parameters*

Table 6.7: Parameters of explicit LMPC

Max. feasible separation	$x_M = 350 \text{ m}$
Additional LoS region	$\mathbf{d}_s = [0.1, 10, 10, 10, 10]^T \mathbf{m}$
Velocity slopes	$k_2 = 0.002$
Velocity tolerance	$\varepsilon = 0.5 \ \mathrm{mm/s}$

controllers in terms of the magnitude of the tracking error for a sample rendezvous and docking maneuver. As expected, the fastest convergence is achieved by the LQR controller, which does not enforce input and output constraints, while the LMPC scheme shows a much better transient response than the MPC scheme. In particular, the oscillatory behavior of closed-loop trajectory is avoided. The horizontal-plane and the in-plane motions are shown in Fig. 6.9, together with the sections of the pyramid that approximate the LoS cone. It can be observed that the LQR controller is unable to keep the radial tracking error within the LoS constraints, as opposed to the LMPC and MPC schemes.

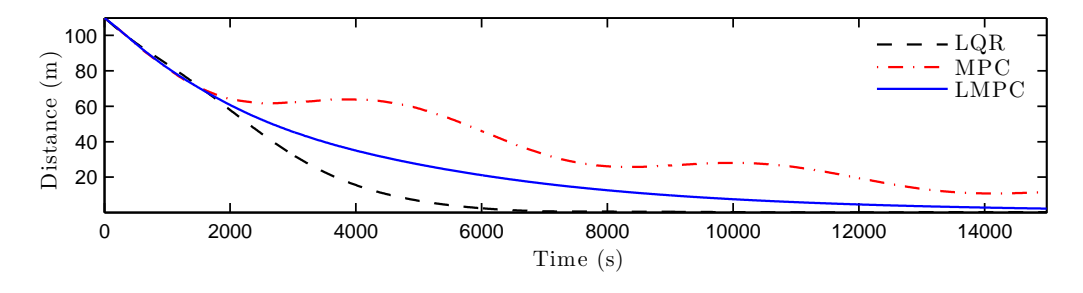


Figure 6.8: Tracking performance.

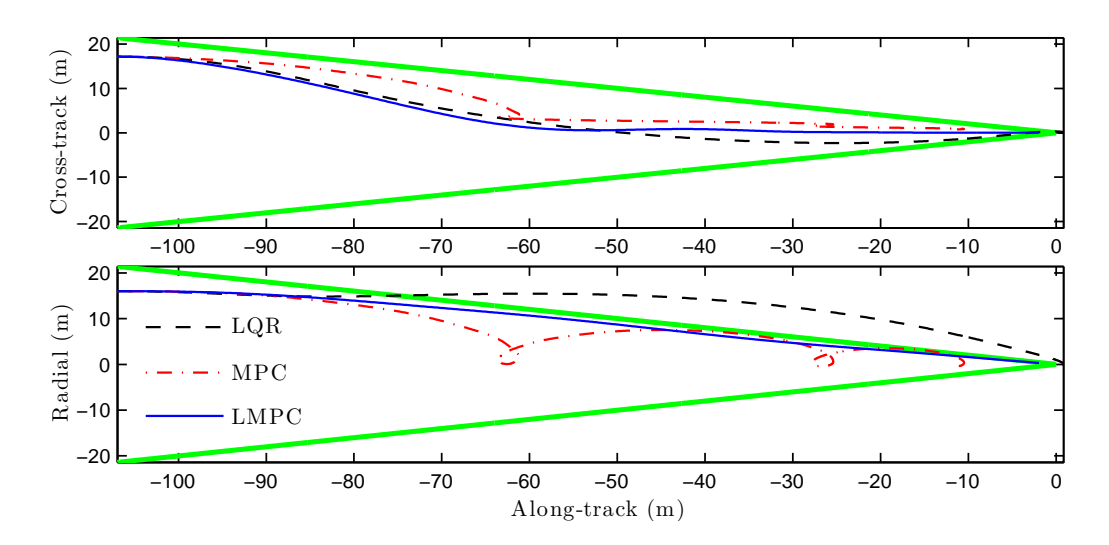


Figure 6.9: LoS constraints (shown in green) and relative trajectories.

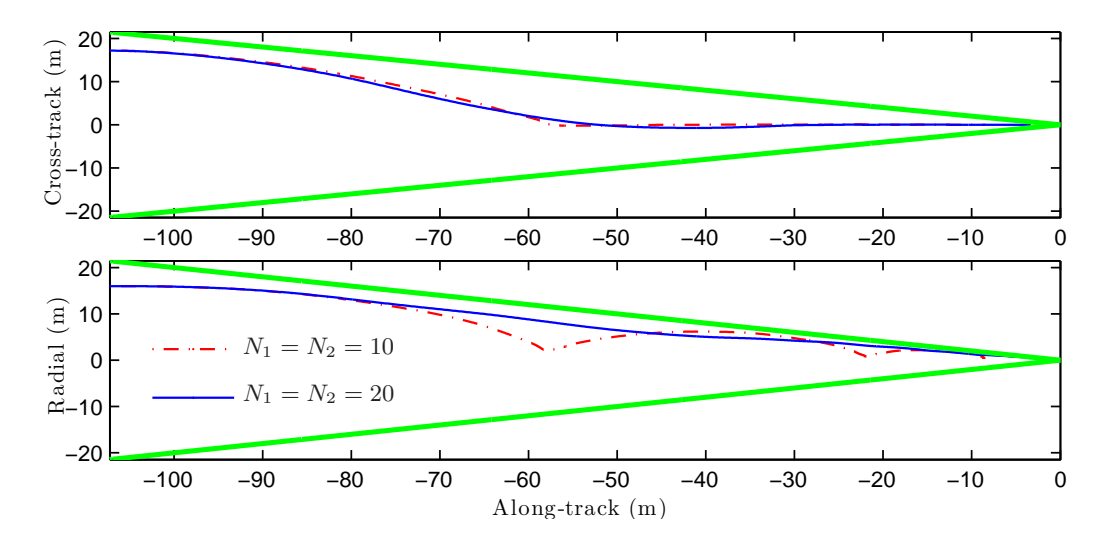


Figure 6.10: Tracking performance of MPC with different control horizons.

The explicit solution to the MPC problem requires 1015 state-space regions, which is comparable with the 946 regions over which the LMPC control law is defined. On the other hand, the modest performance of the MPC controller turns out to be due to the insufficient length $N_1=N_2=4$ of the control sequence. To illustrate this point, the tracking errors obtained with a longer control horizon are reported in Fig. 6.10. For $N_1=N_2=10$, a small performance improvement can be noticed, but the system response is still oscillatory, whereas for $N_1=N_2=20$ the closed-loop trajectories become similar to that resulting from the application of the LMPC scheme, shown in Fig. (6.9). However, we have not been able to

solve the MPC problem explicitly in the above two cases, due to the complexity introduced by the additional optimization variables. The LMPC design is not affected by this issue, thanks to the flexibility provided by the additional tuning parameters a_1 , a_2 , which specify the poles of the Laguerre functions and hence the time scale of the control sequence. For this reason, the proposed approach allows a trade-off between feasibility and performance to be made, by using only $N_1=N_2=4$ coefficients in the polynomial expansion and deriving an explicit controller.

Figure 6.11 gives the thrust profiles calculated by each control law, from uncertain observations (see Fig. 6.7). During the initial phase of the maneuver, the along-track LQR command exceeds the maximum thrust which can be delivered by the propulsion system. Since the magnitude of the input is hard-constrained in the model predictive framework, both the MPC and the LMPC commands do not exceed the operating range of the actuators.

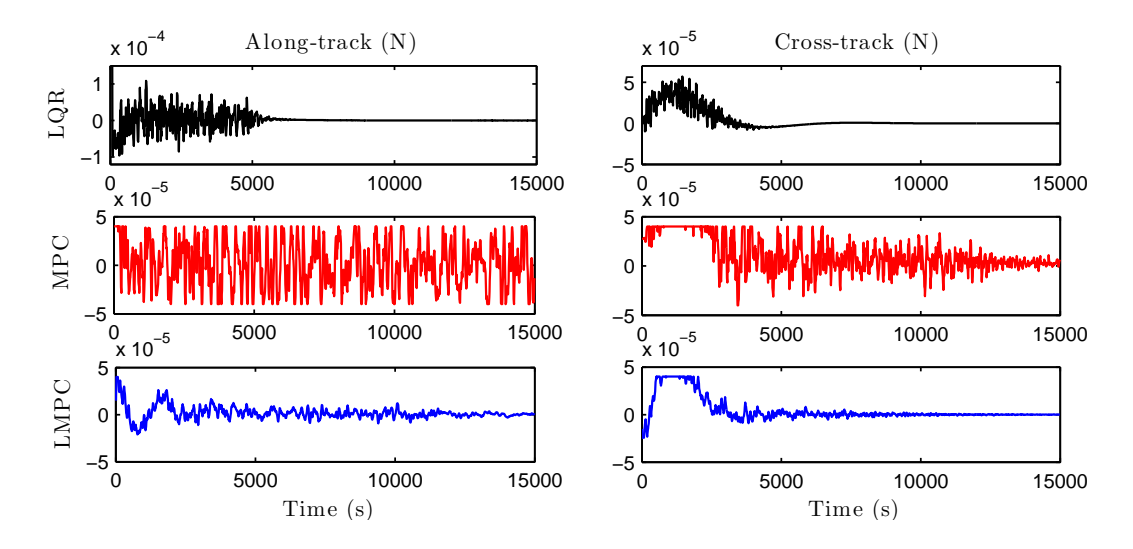


Figure 6.11: Thrust profiles from uncertain observations.

Comparing these results to the thrust profiles obtained with perfect state information, shown in Fig. 6.12, it can be seen that the use of Laguerre functions in combination with an appropriate weight on input variation provides the lowest sensitivity to observation uncertainty. This is confirmed by Table 6.8, which reports the overall impulse (i.e the integral of $\|\mathbf{u}\|_1$) required by the maneuver. The performance degradation is approximately 60% for both the LQR and the standard MPC schemes, but 46% for the LMPC design, which is especially relevant since the overall impulse is proportional to the fuel consumption of the orbit control system. The applicability of the LMPC scheme, in combination with the considered PPT system, is discussed next.

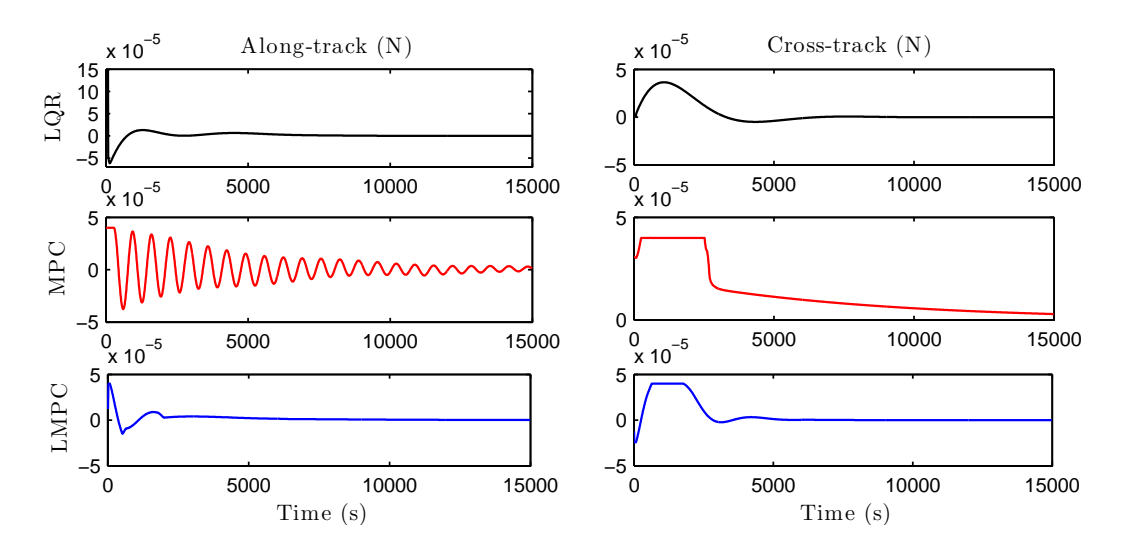


Figure 6.12: Thrust profiles

 Table 6.8: Total impulse sensitivity to observation uncertainty

Туре	LQR	MPC	LMPC
Without noise	0.146 Ns	0.330 Ns	0.109 Ns
With noise	0.241 Ns	0.534 Ns	0.159 Ns
	+65%	+62%	+46%

6.2.3 Rendezvous and docking maneuver analysis

A number of docking maneuvers have been simulated by using the LMPC control law in combination with the PPT system. The set of initial conditions for which the relative motion lies near the edge of the LoS region has been identified as the worst-case scenario for the simulation. Two representative simulation cases are reported, with equal along-track initial separation and opposite initial conditions for the cross-track and radial components of the relative position vector. The initial conditions of Case 1 are the same as those used in the previous simulations. The simulation time is set longer than the one previously used, in order to evaluate the steady state behaviour of the system.

Figures 6.13 and 6.14 show that the LMPC control law is able to drive the follower spacecraft to the docking position while satisfying the LoS constraints, in both cases. The magnitude of the relative position vector at the end of the simulation is equal to 9 mm for Case 1 and 4 cm for Case 2.

The PPT pulse profile is reported in Fig. 6.15, together with the LMPC command, for Case 1 (similar results are obtained for Case 2), where the pulse profile is obtained by modulating the commanded thrust with a step size $\Delta t = 1$ s and adding noise, according to (6.6)-(6.8). These results show that almost no impulses are commanded in the negative

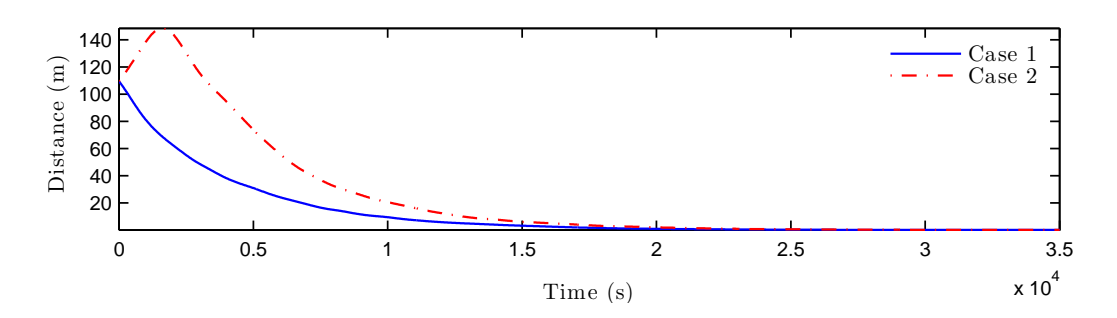


Figure 6.13: LMPC tracking performance.

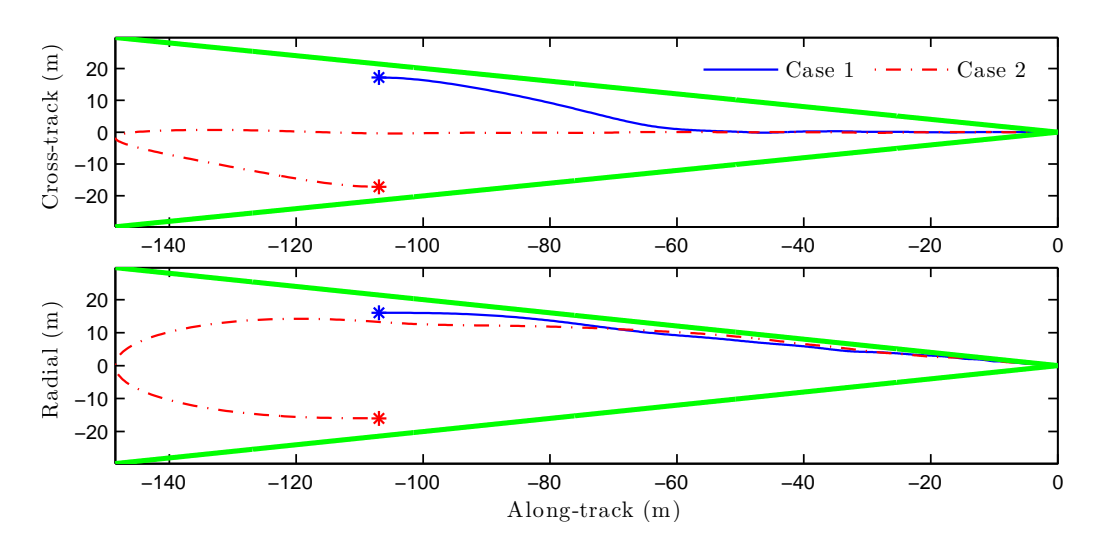


Figure 6.14: LoS constraints (shown in green) and LMPC trajectory.

along-track direction during the final phase of the approach, which indicates that plume impingement is avoided according to (3.28) (the few pulses commanded are required to brake the chaser vehicle upon reaching the target). Moreover, observe that, because the magnitude of the control inputs is constrained to be less or equal to $u_M=40~\mu{\rm N}$, integral windup in (6.7) is prevented.

As a final comparison, the results presented in this section are evaluated against the open-loop (OL) solution to Problem 3.3.1. To enable this comparison, the boundary value problem (3.30) is solved using the commercial package DIDO, which implements pseudospectral methods [115]. A value of $\alpha=1$ and $\beta=0$ is set in the cost function (3.27), which is then proportional to the fuel consumption. Instead of considering a free final time, t_f in (3.30) is set equal to the time required by the LMPC scheme to reach the steady-state, i.e. the length of the simulations presented in this section (35000 s). Moreover, the nonlinear dynamic model (2.7),(2.16),(3.1),(3.3),(3.24) is replaced by the linearized model (3.31). A good approximation of the fuel-optimal control policy is obtained by using 30 quadrature

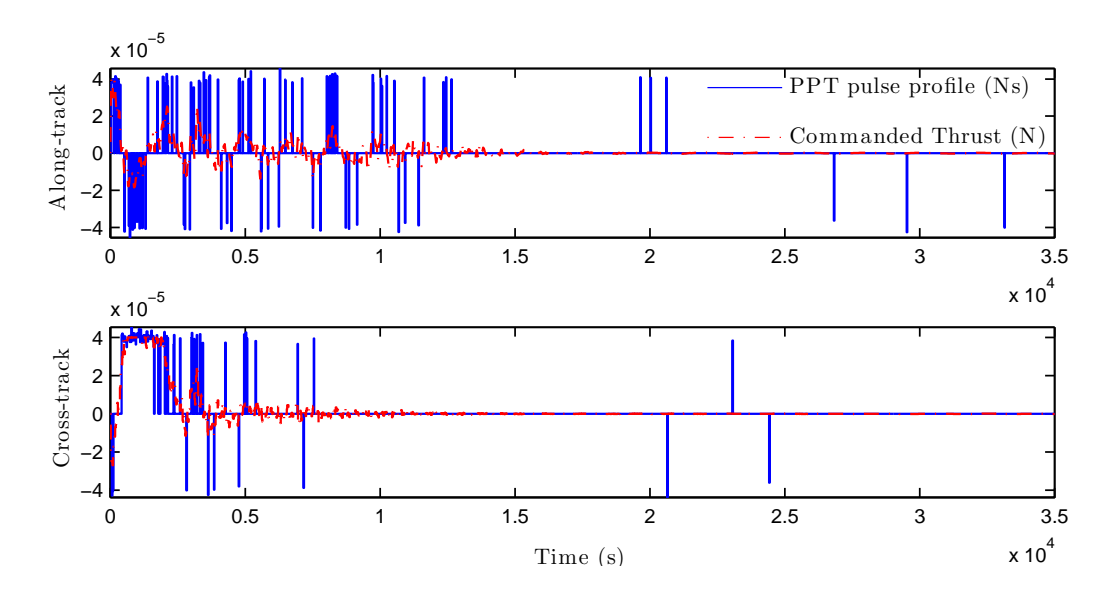


Figure 6.15: PPT pulse profile and commanded thrust for Case 1.

nodes for the pseudospectral solution.

The open-loop (OL) and feedback (LMPC) control strategies are compared in Table 6.9, in terms of the overall impulse required by the maneuver and the evaluation time of the control sequence on a 2 Ghz single-core CPU. Note that the overall impulse obtained with the LMPC scheme can be more than twice the one corresponding to the fuel-optimal OL solution. According to Table 6.8, a significant part of this mismatch is due to uncertain observations, while the rest arises from the approximations made in the design of the LMPC scheme to retain a sufficiently low computational complexity. In fact, the explicit LMPC solution is evaluated approximately 400 times faster than the OL solution.

	Type Case 1 Impulse OL 0.09 Ns		Case 2 Impulse	Running time	
			0.11 Ns	$\sim 20~\text{s}$	
	LMPC	0.16 Ns	0.25 Ns	\sim 0.05 s	
		+77%	+127%	1/400	

Table 6.9: Open-loop (OL) and feedback solution (LMPC)

Given the relatively high specific impulse of PPTs compared to traditional microthrusters, and the fact that the overall impulse commanded by the LMPC scheme is only a small fraction of the total impulse which can be delivered by the thrusters (see Table 6.5), it can be concluded that the proposed combination of technologies may represent a viable and cost-effective solution for a wide range of small spacecraft rendezvous and docking applications.

6.3 Precise attitude control of all-electric spacecraft

The objective of this section is to demonstrate the effectiveness of the MPC-based attitude control scheme developed in Section 4.5. To this purpose, the control law is applied to an all-electric GEO mission in combination with the attitude determination filter presented in Section 5.2. The suitability of a reaction control system based on emerging xenon microthruster technologies is also discussed.

6.3.1 Reference mission

In order to demonstrate the feasibility of the MPC design based on the solution to Problem 4.5.1, a sample all-electric GEO mission is numerically simulated. The orbit parameters are reported in Table 6.10. The spacecraft has the typical layout of a small two tons GEO platform, see e.g. [121]. The size of the main body is $2 \, \text{m} \times 2 \, \text{m} \times 2.5 \, \text{m}$ and two solar panels of dimensions $5 \, \text{m} \times 2 \, \text{m}$ are attached to the north and south faces of the bus, providing 4.5 kW of average power.

Table 6.10: GEO reference orbit

Semi-major axis	a	= 42165 (km)
Inclination	i	$\in [0, 0.05]$ (deg)
Longitude	λ	$\in [75.05, 75.15]$ (deg)
Eccentricity	e	$\simeq 0$

The considered propulsion system is illustrated in Fig. 6.16. Four SPT-100 Hall effect thruster (HET) modules (EP1, EP2, EP3, EP4) symmetrically oriented around the nadir vector, with an angle of 45° between the North/South axis and the thrust direction, are used for SK maneuvers. Such kind of layout is similar to the one adopted for the Small-GEO platform [32]. Nominally, the EP thrust vectors are aligned with the center of mass of the spacecraft.

Eight on/off xenon microthruster modules that can be operated either as cold gas thrusters (CGT) or high temperature electrothermal thrusters (HTET) are used for real-time attitude control. Operation in HTET mode is achieved by heating the propellant via a resistance element (ohmic heating), which allows for an increased specific impulse. Four thrusters (AT1, AT2, AT3, AT4) are mounted on the anti-nadir face, with an angle of 48.5° between the diagonal of the face and the thrust direction, to maximize the lever arm and hence the torque about both the roll and pitch axes. The remaining four thruster (AT5a, AT5b, AT6a, AT6b) are symmetrically oriented around the nadir vector, with an angle of 135° between the North/South axis and the thrust direction, and fired in pairs to provide pure torques around the yaw axis. Notice that thrusters AT1-AT4 produce coupled control torques about the roll and pitch axes. In general, such kind of design may be due to structural and operational constraints imposed by the overall configuration of the spacecraft, or beneficial to the performance of the ACS. In the considered application, it ensures full compatibility with thruster

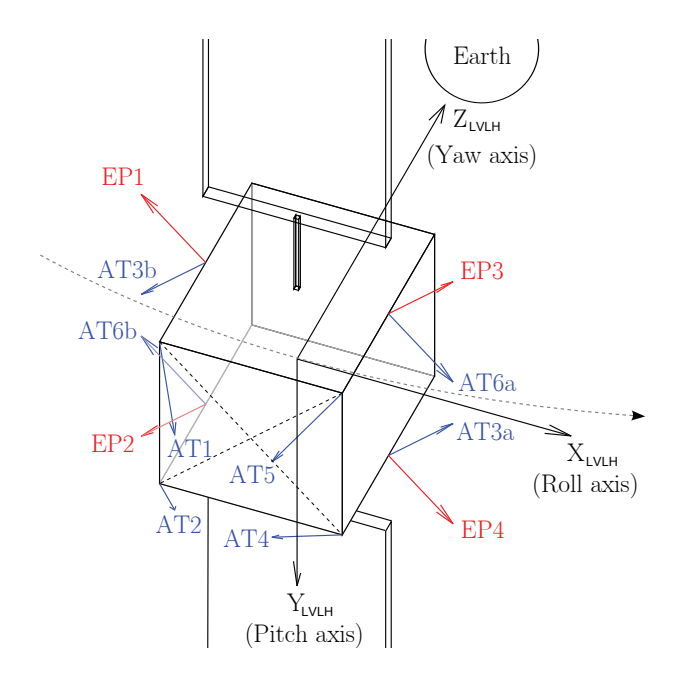


Figure 6.16: Thrusters layout.

plume direction, torque level and power requirements of the mission. The basic specifications of the propulsion system are summarized in Table 6.11, where the specific impulse for HTET opertation is taken compatible with that expected for high temperature resistojet and hollow cathode thruster technologies fed by xenon [47]. To avoid control torques summing up to zero, the simultaneous use of thrusters AT1-AT4, AT2-AT3 and AT5-AT6 is prevented by setting the constraint matrix M in (4.98) to

$$\mathbf{M} = \begin{bmatrix} 1 & 0 & 0 & 1 & 0 & 0 \\ 0 & 1 & 0 & 0 & 1 & 0 \\ 0 & 0 & 1 & 0 & 0 & 1 \end{bmatrix} . \tag{6.9}$$

Table 6.11: Propulsion system specifications

Туре	Thrust	I_{sp}	Power	Mass
HET	75 mN	1500 s	1350 W	3.5 kg
CGT/HTET	0.5/1.5 mN	30/90 s	< 60 W	< 0.3 kg

A detailed analysis of the disturbance torques τ_e in (4.10) is performed. The drag torque τ_d is not present, because there is not atmosphere at the considered altitude. The gravity gradient torque τ_g and magnetic torque torque τ_m are usually negligible in GEO, since they decrease with the inverse cubic power of the distance from the Earth [137]. The solar ra-

diation pressure torque τ_r depends on the orientation of the solar panels. Since the solar panels rotate at a rate of one rotation per day to track the sun, the resulting disturbance is characterized by daily quasi-periodic oscillations with an amplitude that depends on the offset between the center of mass of the spacecraft and the center of solar pressure. Moreover, this disturbance vanishes during eclipses. The disturbance torque τ_0 , arising from stationkeeping operations, depends on both the offset $\Delta \mathbf{c}_m$ of the center of mass with respect to the nominal position and the misalignment β_t of the EP thrust vector from the nominal direction. The geometry of a North/South station-keeping (NSSK) maneuver is depicted in Figure 6.17, where the EP thrusters are fired in correspondence of circular arcs around the orbit nodes. During most of the orbital period, the spacecraft is allowed to drift with respect to the nominal orbit and experiences environmental torques only, while an additional persistent torque is generated during orbit correction maneuvers. By simulating a weekly NSSK cycle, with one day devoted to orbit determination followed by six days of pre-planned maneuvers (see e.g. [9]), it turns out that the maximum magnitude of the SK disturbance torques is much greater than that of the environmental torques. This is clearly visible in Figure 6.18 which shows the disturbance torques acting on the spacecraft, for a typical worst-case simulation with respect to the thruster alignment and center of mass offset (notice the different magnitudes of the torques).

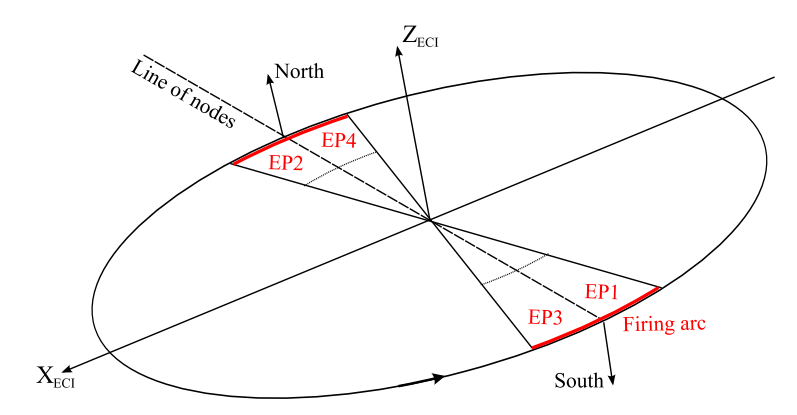


Figure 6.17: *North/South station-keeping maneuver.*

Being the maximum magnitude of the SK disturbance torques much greater than that of the environmental torques, the thruster layout is designed to efficiently reject such a disturbance. If the EP thrust vector misalignment with respect to the spacecraft center of mass is reasonably low, the pitch and roll components of the SK disturbance torque are coupled and have approximately the same magnitude, while the yaw component, with a larger worst-case magnitude, is almost decoupled. For this reason, coupled control torques of equal magnitude are produced around the roll and pitch axes by thrusters AT1-AT4, while a decoupled control torque is generated by the AT5 and AT6 pairs of thrusters around the yaw axis. The acceleration \mathbf{a}_a in (2.16), generated by the AT1-AT6 thrusters, represents a minor orbit perturbation, so that an eventual long-term contribution is easily compensated by sporadic EP maneuvers. Thrusters AT5a and AT5b, as well as thrusters AT6a and AT6b

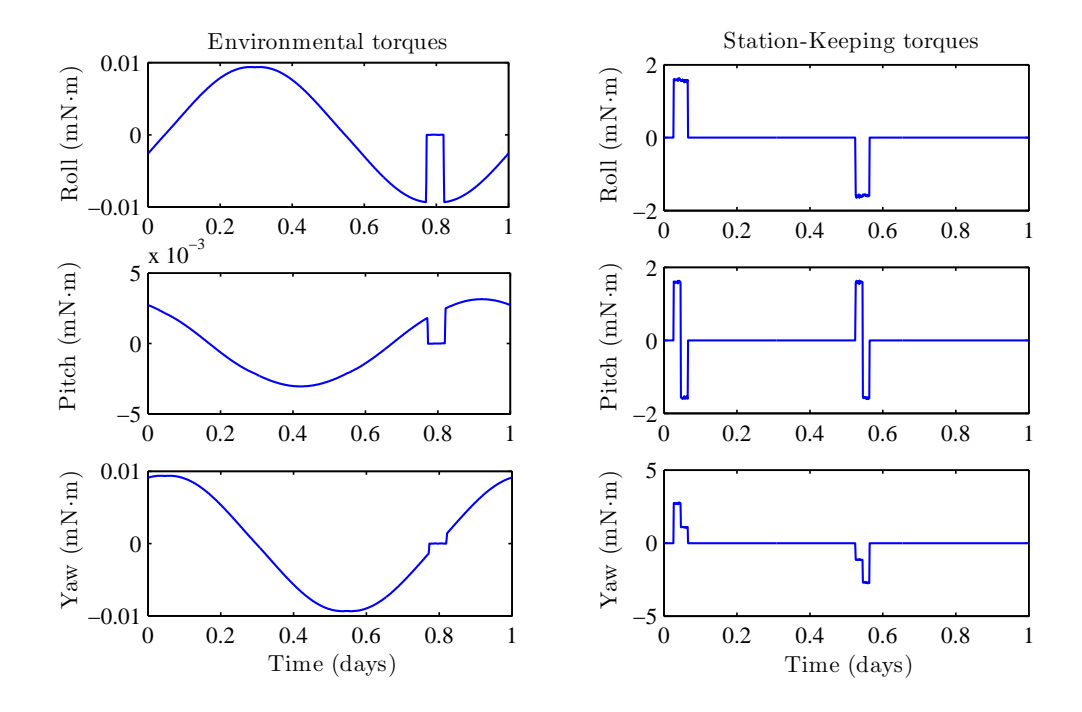


Figure 6.18: Disturbance torques.

(see Fig. 6.16), are fired simultaneously. Hence, the thruster activation command in (4.11) is denoted by $\boldsymbol{\mu} = [\mu_1, \dots \mu_6]^T$, where μ_1, \dots, μ_4 are the command variables of thrusters AT1-AT4, while μ_5 and μ_6 control the AT5 and AT6 pairs of thrusters. Given the thruster alignments, the matrix \mathbf{G} in (4.11) has the following structure

$$\mathbf{G} = \begin{bmatrix} \widetilde{\mathbf{G}}, -\widetilde{\mathbf{G}} \end{bmatrix} = \bar{p} \begin{bmatrix} -d_{xy} & d_{xy} & 0 & d_{xy} & -d_{xy} & 0 \\ d_{xy} & d_{xy} & 0 & -d_{xy} & -d_{xy} & 0 \\ 0 & 0 & 2d_z & 0 & 0 & -2d_z \end{bmatrix},$$
(6.10)

where \bar{p} is the nominal thrust level and d_{xy} , d_z are constant lever arms. Thrusters are designed to be possibly operated in HTET mode, by ohmic heating of a resistance element. To retain an acceptable number of thermal cycles, the following operation regime is considered: (i) CGT mode operation of AT thrusters for attitude control during free orbit drift, when a low delta-v is required to counteract the environmental torques; (ii) HTET mode operation of AT thrusters for attitude control during SK maneuvers, providing increased thrust and I_{sp} for efficient compensation of additional EP-induced torques. A unique thermal cycle is performed for each SK maneuver.

The attitude control accuracy specifications (4.95) are summarized in Table 6.12, according to the typical requirements of a multi-mission platform with Ka/Ku-band communication and Earth imaging payloads (see, e.g., [71]). Therein, the time interval in which SK maneuvers are not performed is referred as free orbit drift. Notice that pointing rate accuracy

ACS requirements	Free orbit drift		Station-Keeping	
ACS requirements	Roll, Pitch	Yaw	Roll, Pitch	Yaw
Pointing accuracy	0.5 mrad	1 mrad	0.5 mrad	1 mrad
Rate accuracy	1.5 μ rad/s	$3~\mu \mathrm{rad/s}$	10 μ rad/s	20 μ rad/s

Table 6.12: Attitude control requirements

requirements are relaxed for SK maneuvers, since Earth imaging is not performed during such operations. Also, observe that control accuracy requirements for the yaw axis are less stringent than those for the roll and pitch axes, because the yaw pointing error does not directly affect the quality of communications and observations. The constraint matrix **W** in (4.95) is set according to the bounds reported in Table 6.12. The tuning of the control law (4.99) is addressed next.

6.3.2 MPC tuning strategy

A high-fidelity simulator has been developed, combining a realistic truth model, sensors, actuators and the EKF in Section 5.2, to tune the control law and evaluate the performance of the ACS. The truth model is obtained from (2.26),(2.31),(4.10), as follows

$$\dot{\mathbf{q}}_{IB} = \frac{1}{2} \begin{bmatrix} 0 \\ \omega \end{bmatrix} \circ \mathbf{q}_{IB}. \tag{6.11}$$

$$\dot{\boldsymbol{\omega}} = \mathbf{I}_{M}^{-1} \left(\boldsymbol{\tau}_{e} + \boldsymbol{\tau}_{u} - \boldsymbol{\omega} \times \mathbf{I}_{M} \ \boldsymbol{\omega} - \dot{\mathbf{I}}_{M} \ \boldsymbol{\omega} \right). \tag{6.12}$$

$$\dot{m} = -\frac{\bar{p} \parallel \mathbf{\Lambda} \boldsymbol{\mu} \parallel_1}{g I_{sp}}, \tag{6.13}$$

where $\Lambda=\mathrm{diag}(1,1,1,1,2,2)$ accounts for the specific thruster layout. The torque τ_u in (6.12) is modeled as the commanded torque $G\mu$ plus actuator noise \mathbf{w}_a and thruster misalignment $\boldsymbol{\beta}_a$

$$\boldsymbol{\tau}_{u} = (\mathbf{I} - \boldsymbol{\beta}_{a}^{\times}) \mathbf{G} (\boldsymbol{\mu} + \mathbf{w}_{a}), \tag{6.14}$$

where $E\left[\mathbf{w}_a(t)\ \mathbf{w}_a(t')^T\right] = \mathbf{I}\,\sigma_a^2\,\delta(t-t')$ and $\boldsymbol{\beta}_a$ is fixed. The term $\boldsymbol{\tau}_e$ in (6.12) includes the most relevant torques, whose profile is depicted in Fig. 6.18. The block diagram representation of the closed-loop system is depicted in Fig. 6.19. Table 6.13 summarizes the main simulation parameters, where σ_θ and σ_ω are given by (5.34) and (5.35), with $\mathbf{N}_\theta = \mathbf{I}\sigma_\theta^2$ and $\mathbf{N}_\omega = \mathbf{I}\sigma_\omega^2$.

The tuning parameters of the controller are $\Delta t_s N_u$, N, \mathbf{K}_s , \mathbf{K}_y and α in (4.99). A sampling time $\Delta t_s = 0.5$ s is chosen. Such a value is adequate for discretizing the spacecraft dynamic model and is well within the constraints on the minimum firing time imposed by the thruster technology. The control horizon N_u , which is proportional to the

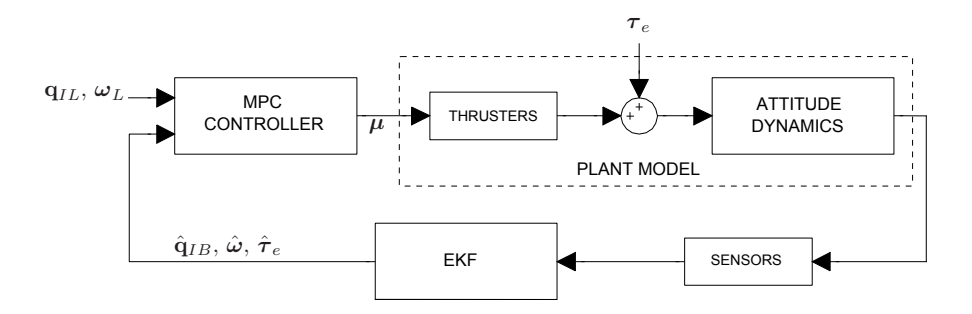


Figure 6.19: Closed-loop system

Table 6.13: Simulation parameters

Parameter	Value	
Center of solar pressure offset	5 cm along the pitch axis	
Center of mass offset	$\Delta \mathbf{c}_m = 1.5$ cm per axis	
EP thrust vector misalignment	$\boldsymbol{\beta}_t = 0.6$ deg per axis	
AT thrust vector misalignment	$\boldsymbol{\beta}_a = 0.1$ deg per axis	
AT thrust noise (normalized)	$\sigma_a = 0.01$	
Star-tracker measurement noise	$\sigma_{\theta} = 0.05 \text{ mrad}$	
Gyro measurement noise	$\sigma_{\omega} = 1 \; \mu \text{rad/s}$	

number of binary variables in the optimization problem, has the major impact on the computational burden of the real-time control system. Since the amount of computational resources available on-board a spacecraft is typically limited, $N_u = 3$ is chosen. A prediction horizon three times longer than the control horizon is selected, by setting N=9. The penalty term K_s , which affects the constraint violations, is chosen as a block diagonal matrix $\mathbf{K}_s = \text{blockdiag}(10^2 \, \mathbf{I}, \ 10 \, \mathbf{I}), \text{ while the terminal weight is set to } \mathbf{K}_u = \text{blockdiag}(\mathbf{I}, \ 0.1 \, \mathbf{I}) \mathbf{W}$ (see (4.99)). Finally, the parameter α determines the relative weight of the fuel consumption and the number of thruster firings in the cost function of the optimization problem. In order to find a suitable value of α , the ACS is simulated with values of α ranging from zero to one. Since different control modes are defined according to the mission requirements, free orbit periods lasting one day and NSSK maneuvers of 55 minutes have been simulated separately. A worst-case scenario is considered, by assuming the maximum disturbance torque compatible with the uncertainty on the center of mass, center of solar pressure and thruster misalignment. In both cases, the attitude, angular rate and disturbance torque are estimated by the EKF. The results are depicted in Fig. 6.20, where the fuel consumption and the number of thruster firings are reported for SK and free orbit drift periods. As expected, the parameter α allows one to trade-off between two objectives. It can be noticed that for both SK and free orbit drift the fuel consumption is approximately constant as long as α is smaller than 0.8, while it rapidly grows as α approaches 1. Conversely, an acceptable number of firings is achieved only if α is larger than 0.7. From these observations, $\alpha=0.78$ is selected. Fig. 6.20 also confirms that the major contribution to the attitude control delta-v budget is due to SK operations. Even if the microthrusters efficiency is increased by HTET mode operation, the fuel required for disturbance rejection on a single NSSK maneuver is still considerably higher than the fuel needed to compensate for one day of environmental torques by using thrusters in CGT mode. The proposed combination of tuning parameters provides an average computational time of the control law in the 25 millisecond range on a 2 GHz single-core CPU, by using the IBM ILOG CPLEX mixed-integer programming solver [66], based on a branch and bound algorithm.

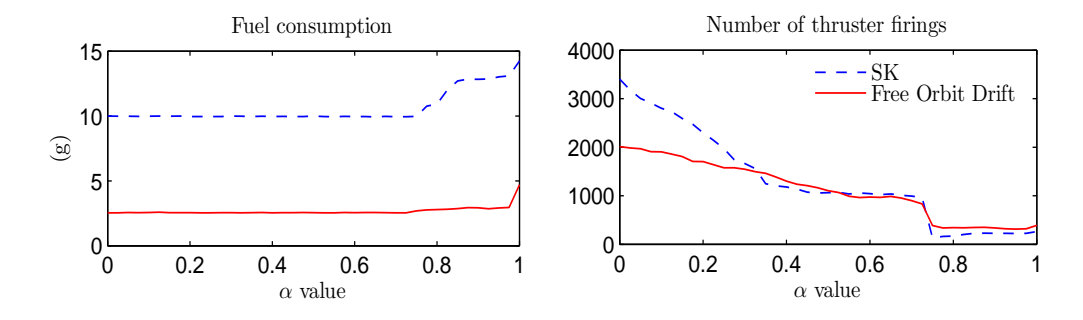


Figure 6.20: Tuning of parameter α .

The performance of the control law with the set of tuning parameters described above is compared to a LQR+PWPF scheme [1], consisting of the cascade of a LQR controller and a PWPF modulator, for SK disturbance rejection. The SK maneuver consists of firing a pair of thrusters in sequence around an orbit node. Therefore, the resulting disturbance torque, depending on the displacement of the thrust vectors with respect to the spacecraft center of mass, is piecewise constant, as illustrated in Fig. 6.18. In Fig. 6.21, it can be observed that both controllers succeed in keeping the errors within the maximum allowed deviation, for all axes (although the LQR law fails to keep the pitch and yaw rate transient within the bounds due to an impulsive variation of the disturbance torque at time t=1683 s). Clearly, an advantage of the MPC approach is that the error bounds are enforced directly as constraints in the optimization problem (4.99), while a trial-and-error procedure has been necessary to suitably tune the parameters of the LQR+PWPF controller.

The fuel consumption and number of thruster firings of the two control schemes are reported in Fig. 6.22. The MPC scheme requires about 5% less fuel and 25% less thruster firings with respect to the LQR+PWPF one, mainly due to a more efficient management of the firing cycles for the cross-coupled axes (roll and pitch).

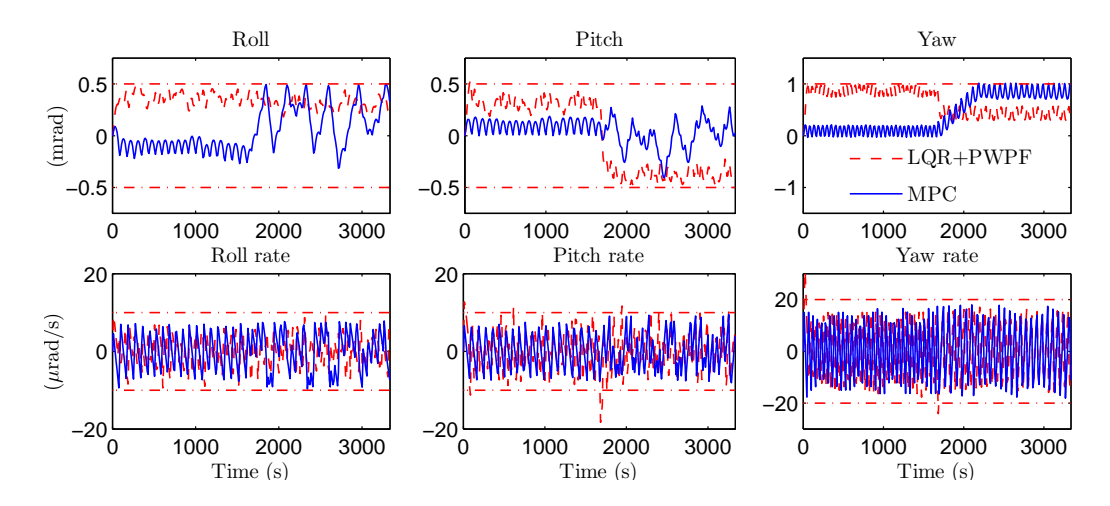


Figure 6.21: Tracking errors for a sample SK maneuver.

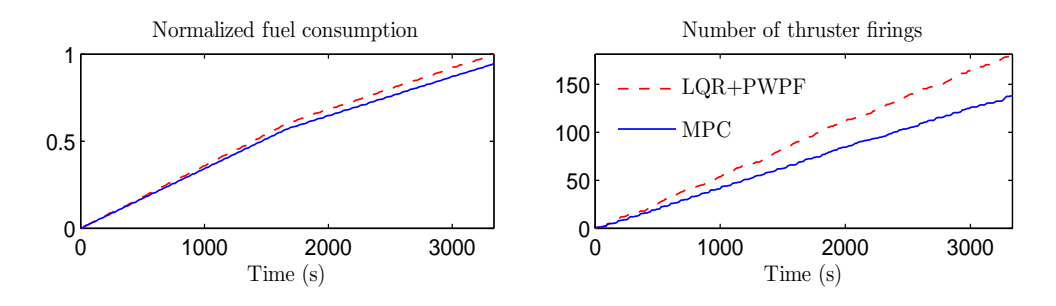


Figure 6.22: Fuel consumption and number of firings in comparison.

6.3.3 Attitude control system analysis

The reference mission is simulated in order to validate the proposed MPC design and to evaluate the performance of the attitude control system. The simulation model is propagated for a time interval of one week using a fourth-order Runge-Kutta integration method. The steady state behaviour of the ACS is reported in Fig. 6.23. The attitude tracking error remains always well enclosed within the bounds (dash-dotted lines) specified by the pointing accuracy requirements, and shows an oscillating trend that corresponds to the disturbance torque profile, except from periodic spikes due thruster operation within solar eclipses, when the environmental torques vanish resulting in closed-loop oscillations with the same amplitude of the deadband (due to the minimum impulse bit of the thrusters, see e.g. Fig. 4.4). Such kind of behaviour is typical for pulse-modulated thruster control systems. Similarly to what observed for the attitude error, the angular rate tracking error does not exceed the pointing rate accuracy bounds, as illustrated in Fig. 6.24. The performance of the microthruster reaction system is reported in Fig. 6.25, in terms of fuel consumption (left) and number of firings cyles per thruster (right, where each line represents a single

thruster). The microthrusters are operated in CGT mode during free orbit drift and in HTET mode during SK maneuvers.

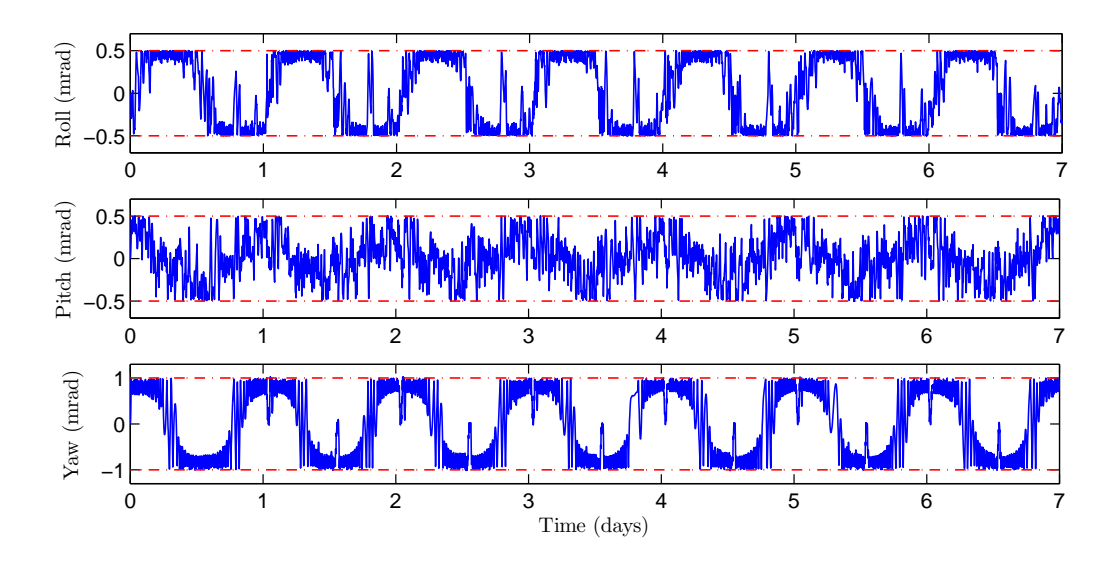


Figure 6.23: Pointing error.

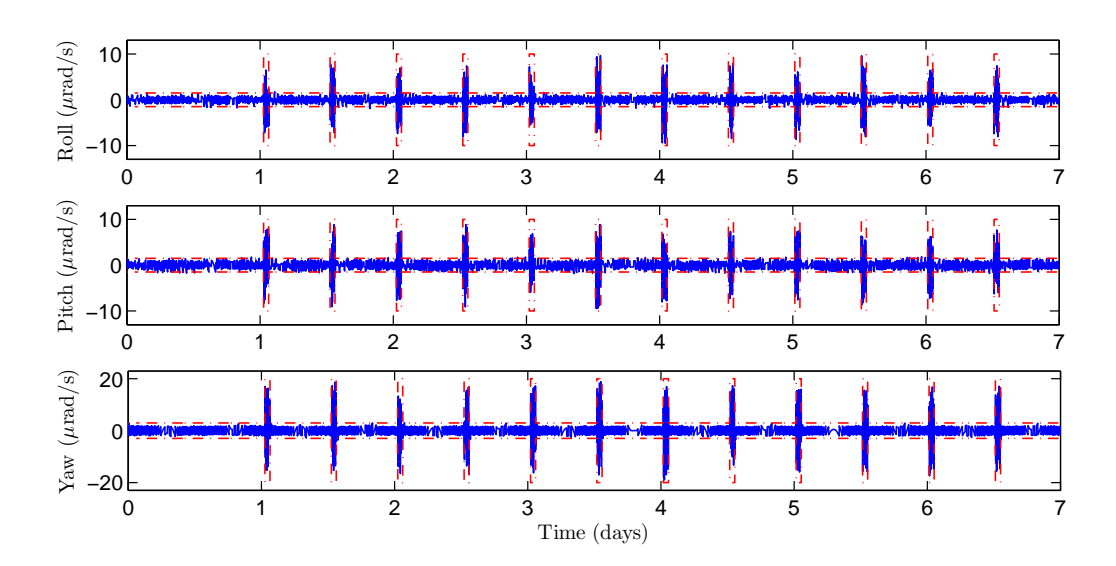


Figure 6.24: Pointing rate error.

The stair-step profile of the expelled fuel clearly indicates that the major contribution to the propellant budget is due to SK disturbance rejection, as expected. The overall xenon mass required for precise attitude control is approximately 0.135 kg: 0.019 kg to counteract

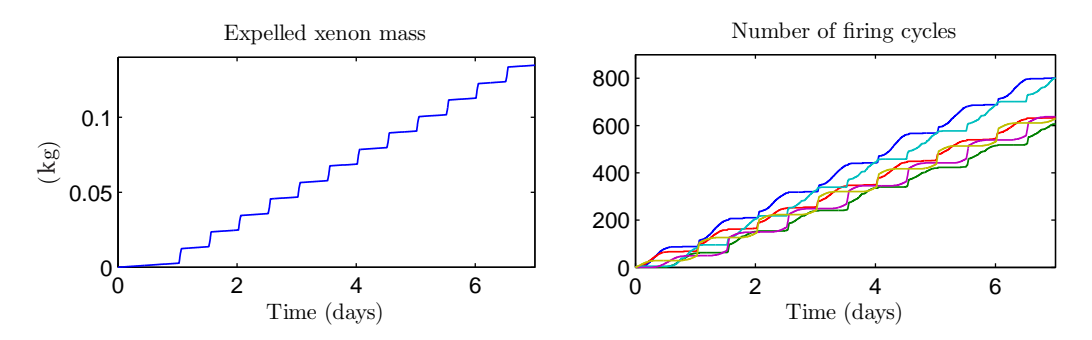


Figure 6.25: Microthruster reaction system performance.

environmental disturbances and 0.116 kg to compensate for SK disturbance torques. The amount of firing cycles is fairly distributed among free orbit drift and SK periods, and grows regularly for each thruster. At the end of the simulation, about 800 on/off cycles are accumulated by thrusters AT1 and AT4, while a number of cycles between 600 and 650 is observed for the remaining thrusters. The overall firing time per thruster varies between 2.5 hr and 2.9 hr, about 85% of which being spent for SK disturbance rejection. Based on these results, Table 6.14 summarizes the performance of the reaction control system for a mission duration of 15 years. The total amount of xenon needed for microthruster operation represents a significant addition to the fuel budget of the mission, being the propellant mass required for 15 years of NSSK in the order of 150 kg for the HET thrusters considered in Table 6.11. However, considering that the typical mass of momentum-exchange devices, such as reaction wheels or control moment gyros, together with the xenon mass required for wheel desaturation, can easily exceed 50 kg, and that such systems are replaced by lightweight microthrusters, the overall penalty on the spacecraft mass is predicted in the 60 kg range. It is believed that this is a reasonable trade-off as it allows one to remove moving and vibrating parts from the attitude control system, as well as to reduce its complexity and cost. Moreover, the results presented so far are obtained by using conservative propulsion system specifications, which ensure compatibility with different models of EP and HTET thrusters. In specific cases, where a better alignment of the EP thrust vector and/or an increased I_{sp} of the reaction thrusters can be guaranteed, a significant reduction of the propellant consumption is expected, since the amount of xenon required for EP torques compensation scales approximately linearly with these quantities. For instance, the performance reported in Table 6.15 is obtained for an EP thrust vector misalignment of 0.1 deg, as in [9, 70], and an I_{sp} of 200 s, which is the target value for the development of the hollow cathode technology [53]. Such a performance makes the proposed ACS a competitive alternative to systems based on momentum exchange devices.

Finally, it must be observed that the firing time and the number of on/off and thermal cycles per thruster, given in Tables 6.14 and 6.15, are compatible with the considered CGT/HTET technology. In particular, the difference between the number of on/off and thermal cycles for HTET is due to the fact that for each SK maneuver a single thermal cycle is performed, while several valve switchings are required to meet the desired control accuracy.

Type	Xenon mass	On/off cycles	Firing time	Thermal cycles
CGT	15 kg	350000	300 hr	-
HTET	91 kg	300000	2000 hr	10000
Total	106 kg	650000	2300 hr	10000

Table 6.14: Propulsion system performance: EP misalignment 0.6° , HTET $I_{sp} = 90 \text{ s}$

Table 6.15: Propulsion system performance: EP misalignment 0.1° , HTET $I_{sp} = 200 \text{ s}$

Type	Xenon mass	On/off cycles	Firing time	Thermal cycles
CGT	15 kg	350000	300 hr	-
HTET	22.5 kg	380000	1100 hr	10000
Total	37.5 kg	730000	1400 hr	10000

6.4 Performance evaluation of attitude control laws

As discussed in Chapter 4, an efficient attitude control scheme must focus on simultaneously minimizing the fuel consumption and the number of thruster firings of the reaction control system, while at the same time enforcing the attitude control accuracy requirements. To this aim, two suboptimal solutions have been derived for the coupled double integrator model (4.9), which guarantee an upper bound on the minimum actuator switching frequency and a predefined pointing accuracy. For the more general linearized attitude error dynamics (4.91), an MPC scheme, based on the numerical solution of a mixed-integer linear program, has been also developed. This control scheme has been found to yield a good tracking accuracy when applied to the all-electric GEO mission in the Section 6.3, but suffers from a finite-horizon approximation of the fuel and switching costs, which may limit its applicability within other types of mission. It is therefore of interest to asses the performance of the proposed solutions and see how they compare on different scenarios.

In order to evaluate the performance of minimum switching (MS) control laws (4.74) and (4.76), versus the one of the MPC scheme, two aspects should be noticed. The first is that the MPC formulation in Problem 4.5.1 can explicitly account for angular rate constraints, while for the MS strategies such constraints are implicitly defined by the disturbance torque size and by the amplitude of the attitude error oscillations on each axis of the transformed system (4.18), see e.g. Fig. 4.7. The second is that the MPC scheme is able to handle arbitrary thrusters configurations in (4.11), while the provided MS solution is limited to symmetric thruster configurations of the form defined by (4.12), with one input per axis. In practice, however, one can always enforce a set of suitable attitude error bounds which enable to meet the desired pointing rate accuracy, thus allowing one to apply the control laws (4.74) and (4.76) also in the presence of angular rate constraints. Moreover, in many cases the spacecraft architecture is such that the thruster configuration is minimal

(but redundant) and symmetric, as in (6.10) (see for example Fig. 6.16).

6.4.1 GEO scenario

In the following, the proposed solutions are compared on the GEO mission scenario described in Section 6.3, in terms of effectiveness in rejecting persistent SK disturbances. In this scenario, the pointing rate accuracy requirements do not allow the attitude error to span the entire size of the attitude error deadband, as clearly visible in Fig. 6.21 (loosely speaking, the pointing rate constraints are more stringent than the attitude error ones). This is in conflict with the solutions provided by Theorems 4.3.1 and 4.3.2, which aim at maximizing the attitude error excursion within the feasible set, as can be seen, for instance, in Fig. 4.11. Therefore, the size of the feasible set used by these results must be scaled, to ensure that the required pointing rate accuracy can also be met. This amounts to consider

$$\mathbf{W}_{\theta} = \operatorname{diag}(\kappa \, 0.5 \cdot 10^{-3}, \kappa \, 0.5 \cdot 10^{-3}, \kappa \, 10^{-3})^{-1} \tag{6.15}$$

in (4.14), where the SK pointing accuracy requirements from Table 6.12 are scaled by the scalar term κ . Based on a trial and error procedure, κ has been set to 0.14 for the considered scenario (this low value confirms that, in this scenario, the bottleneck in the limit of performance is determined by the angular rate constraints).

The SK maneuver has a duration of about 3300 sec, and the disturbance acting on the spacecraft is piecewise constant: $\boldsymbol{\tau}_o = [1.6, \ 1.7, \ 2.7]^T$ mN·m during the first half of the maneuver and $\boldsymbol{\tau}_o = [1.7, -1.6, \ 1.1]^T$ mN·m during the second half. The periodic trajectories returned by Theorems 4.3.1 and 4.3.2, for the first half of the SK maneuver, are reported in Fig. 6.26 (a similar solution is obtained for the second half). Notice that the solution provided by Theorem 4.3.2 has no visible advantages over that provided by Theorem 4.3.1, due to the particular structure of the problem. Therefore, we expect a similar performance for the control law (4.74), with the set of parameters prescribed by Corollary 4.4.1 (hereafter, referred as MS+C1), and the control law (4.76), with that specified by Corollary 4.4.2 (MS+C2).

The MPC scheme (4.99) is compared to the MS control strategies on the considered SK maneuver. Because the SK disturbance can take two different values, to be estimated by the EKF, the parameters provided by (4.66) and (4.70)-(4.71) are computed in real-time. In particular, (4.70)-(4.71) is evaluated by numerical search over a 10×10 grid on the parameters (ϕ_2 , ϕ_3). The evaluation takes approximately 10 ms on a 2Ghz single-core CPU, which of the same order of the time required to solve the MPC problem.

The tracking errors obtained with the three control laws are reported in Fig. 6.27. It can be seen that the pointing and pointing rate accuracy requirements are satisfied by the three solutions. Moreover, notice that the roll and pitch angular errors from the application of the MS laws are constrained to lie in a smaller region near the origin with respect to those of the MPC law, because the size of the feasible set in Fig 6.26 (i.e. the outer parallelotope) has been scaled to meet the desired pointing rate accuracy, according to (6.15).

The average fuel consumption $J_f(T)$ and switching frequency $J_s(T)$, resulting from the application of the two control laws, are reported in Fig. 6.28, as a function of the simu-

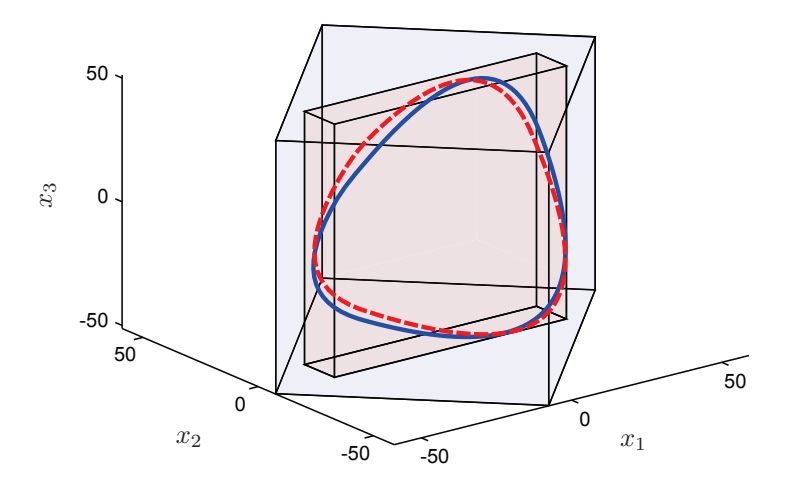


Figure 6.26: Trajectories corresponding to the solution to (4.65) (dashed) and (4.69) (solid), together with state constraints (4.20) (outer parallelotope) and $|x_i| \le a_i^*$ (inner box).

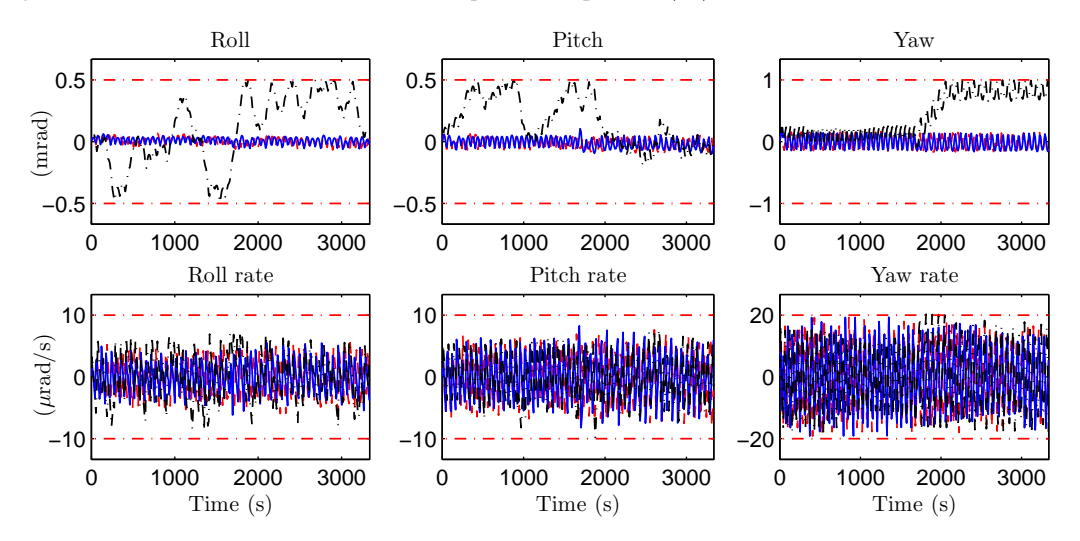


Figure 6.27: Tracking error for a sample SK maneuver: MS+C1 (red, dashed), MS+C2 (blue, solid) and MPC (black, dash-dotted).

lation time T. These cost functions are obtained from (4.15) and (4.48), respectively, by removing the limit operation. It can be seen that the fuel consumption is approximately the same for the three solutions, while the MS+C1 law provides a smaller actuator switching frequency, (in the order of 5%) with respect to the MS+C2 and MPC laws. In particular, the performance gap between the MS+C1 and MS+C2 schemes is due to the additional input transitions required by the MS+C2 scheme to reject the effect of noise on the relative phases (despite the fact that tracking a desired phase does not give any theoretical advantage in this scenario, according to the structure of the solutions in Fig. 6.26).

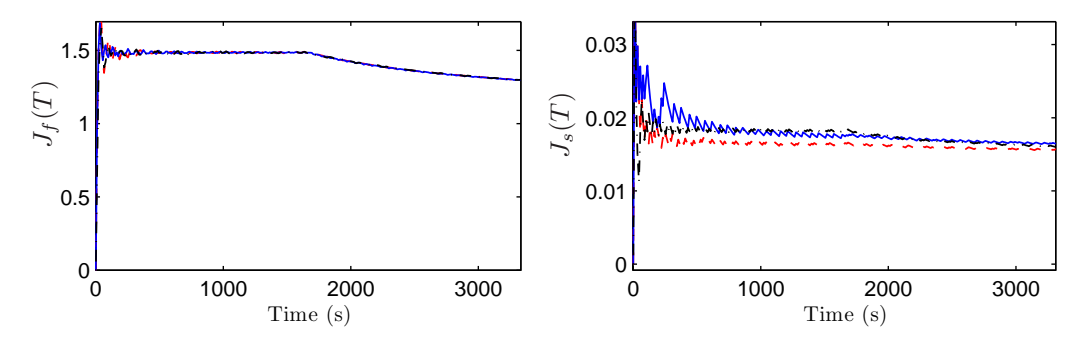


Figure 6.28: Average fuel consumption and switching frequency: MS+C1 (red, dashed), MS+C2 (blue, solid) and MPC (black, dash-dotted).

Clearly, an advantage of the MPC approach in the considered application is that the rate error bounds are enforced directly as constraints in the optimization problem (4.99), while an heuristic procedure has been necessary to suitably tune the parameter κ in (6.15). In this respect, the solution to the minimum switching Problem 4.3.1, in the presence of angular rate constraints, represents one interesting subject for future investigations.

6.4.2 LEO scenario

In the following, the proposed control laws are compared on a LEO mission scenario with the following features:

- The required pointing accuracy is 0.5 mrad per axis, while no angular rate constraints are specified;
- A persistent disturbance torque $\tau_d = [0, 0.5, 0.2]^T$ mN·m, due to drag, is the main disturbance acting on the system;
- A 500 kg class spacecraft is considered, whose design is the same reported in Fig. 6.16, except for a scaling and the fact that solar appendages are not present (panels are mounted on the external body surfaces).

Notice that the magnitude of the LVLH rate ω_L in (4.2) and (4.8), for this scenario, is about 15 times higher than that considered in the previous simulations. Moreover, the parameters of the navigation system are left unchanged. The matrix \mathbf{W}_{θ} in (4.14) is set to $\mathbf{W}_{\theta} = (\kappa \, 0.5 \cdot 10^{-3})^{-1} \mathbf{I}$, where $\kappa = 0.9$ introduces a 10% safety margin with respect the pointing accuracy requirements, to account for discretisation and measurement errors.

The periodic trajectories specified by Theorems 4.3.1 and 4.3.2 are reported in Fig. 6.29. The solution returned by Theorem 4.3.2 provides a 18% reduction of the actuator switching frequency with respect to that of Theorem 4.3.1. Therefore, we expect a similar advantage for the MS+C2 law over the MS+C1 law.

The tracking error profiles from the application of the MS+C1 and MS+C2 schemes are reported in Fig. 6.30. It can be seen that, with the exception of a short initial transient,

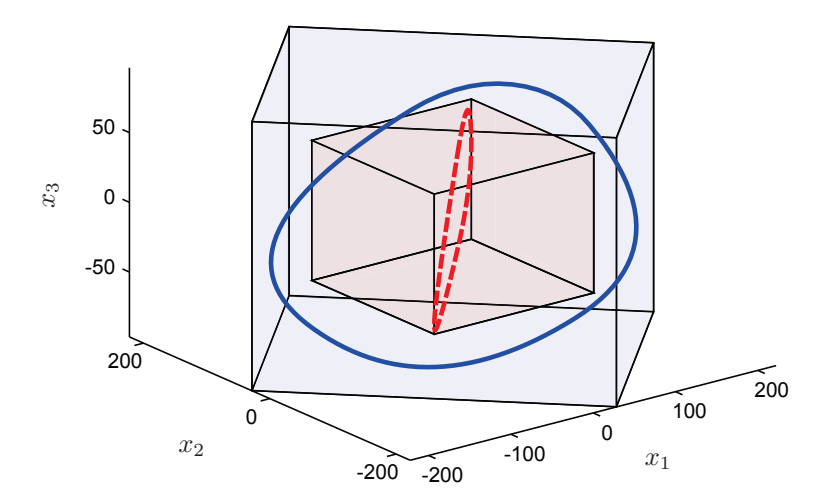


Figure 6.29: Trajectories corresponding to the solution to (4.65) (dashed) and (4.69) (solid), together with state constraints (4.20) (outer parallelotope) and $|x_i| \le a_i^*$ (inner box).

during which the MS+C2 controller has to track the desired phases (see the pitch error profile), the pointing accuracy requirements are satisfied by both solutions. This confirms that the double integrator model (4.9), which is obtained by neglecting the cross coupling terms depending on ω_L in (4.8), provides reasonable approximation of the attitude error dynamics for the considered control problem.

Observe from Fig. 6.30 that the growing amplitude of the oscillations about the roll axis for the MS+C1 law is due to a phase shift effect, arising from measurement and discretisation errors (the amplitude of the oscillations about the pitch axis is decreasing, although not clearly visible in Fig. 6.30). This phenomenon is better understood by observing the closed-loop trajectories in the transformed space (x_1, x_2, x_3) , shown in Fig. 6.31. It can be seen that, although the trajectory resulting from the application of the MS+C1 scheme (red, dashed) does not follow the path obtained for $\phi_1 = \phi_2 = \phi_3 = 0$ in Fig. 6.29, it is maintained within the box $|x_i| \le a_i^*$ specified by Theorem 4.3.1, with few constraint violations

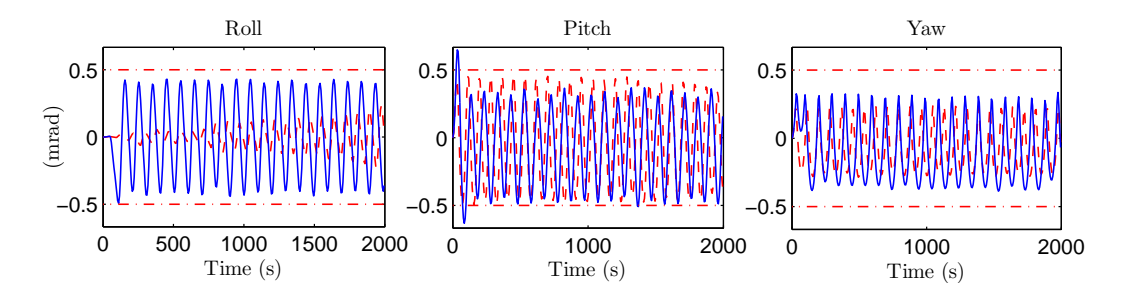


Figure 6.30: Tracking error profile: MS+C1 (red, dashed) and MS+C2 (blue, solid).

due to noise. In fact, the result provided by this theorem does not depend on the relative phases of the oscillations. Conversely, the oscillations resulting from the application of the MS+C2 scheme (blue, solid) closely follows the path depicted in Fig. 6.29, because in this case the relative phases are controlled.

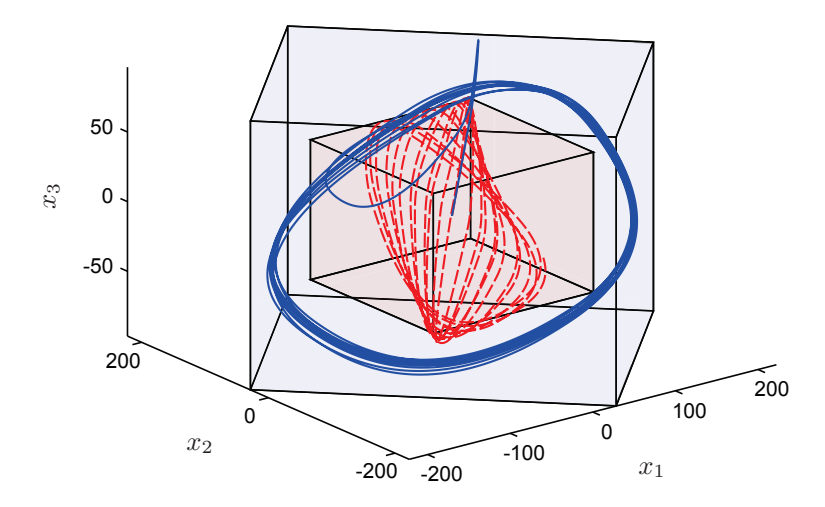


Figure 6.31: Trajectories from the application of the MS+C1 (red, dashed) and MS+C2 (blue, solid) schemes, together with state constraints (4.20) (outer parallelotope) and $|x_i| \le a_i^*$ (inner box).

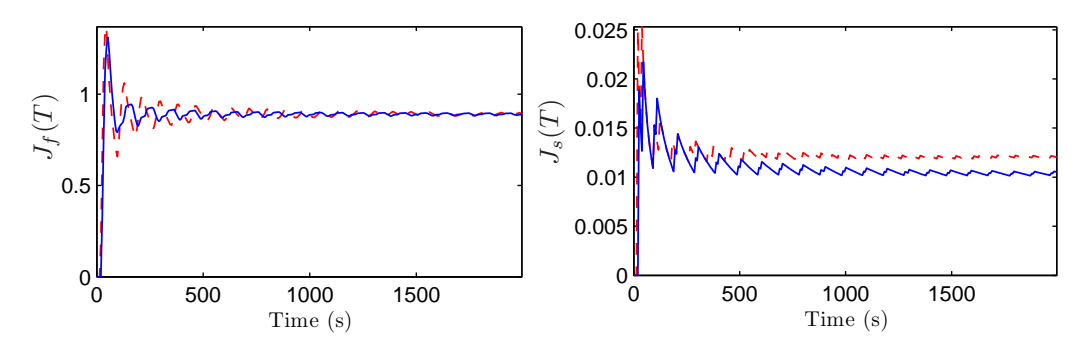


Figure 6.32: Average fuel consumption and switching frequency: MS+C1 (red, dashed) and MS+C2 (blue, solid).

The average fuel consumption $J_f(T)$ and switching frequency $J_s(T)$, obtained with the two control schemes, are reported in Fig. 6.32. As expected, the MS+C2 scheme performs better than the MS+C1 scheme in terms of switching frequency. In particular, it provides a 14% reduction of the switching cost $J_s(T)$ at the end of the simulation (the expected 18% reduction, found by comparing the optimal costs of Theorems 4.3.1 and 4.3.2, is matched for longer simulations, as the effect of the initial transient is averaged out).

The MPC controller is tuned by using $\mathbf{K}_y = 10^4 \operatorname{diag}(0.2, 0.2, 0.2, 4, 4, 2)$ and $\mathbf{K}_s = 10^2 \mathbf{I}$ in (4.99) (where angular rate constraints are not enforced), while the parameters Δt_s , N_u

and N are set as in Section 6.3.2. Figures 6.33 and 6.34 show the performance obtained for $\alpha=0.7$ and $\alpha=0.8$ in (4.99). For $\alpha=0.7$, the fuel consumption is the same as that obtained with MS laws, reported in Fig. 6.32, but the switching frequency is about 10 times higher. For $\alpha=0.8$, a reduction of the switching frequency can be noticed, but the fuel consumption is increased by approximately 10%. Moreover, the switching cost is still considerably higher than that of the MS schemes, and the controller is not able to keep the roll error in Fig. 6.33 within the bounds.

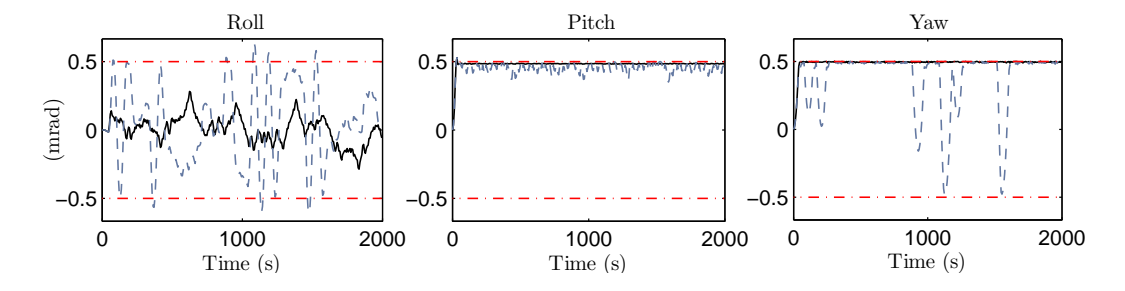


Figure 6.33: Tracking error profile of MPC: $\alpha = 0.7$ (black, solid) and $\alpha = 0.8$ (blue, dashed).

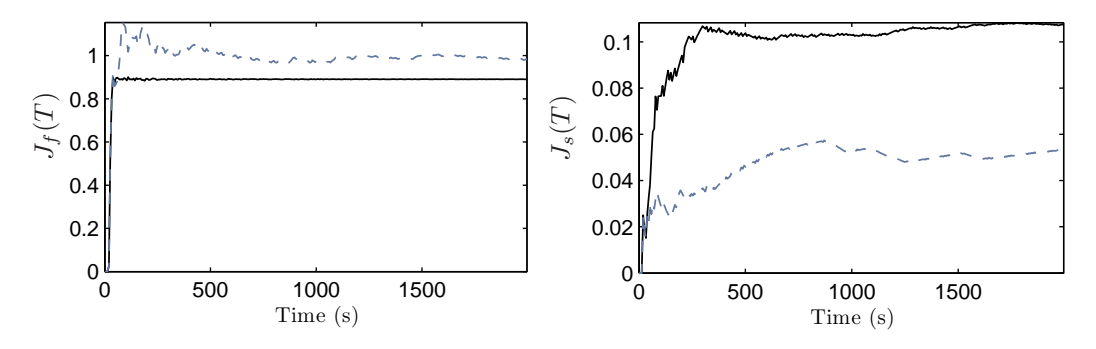


Figure 6.34: Average fuel consumption and switching frequency of MPC: $\alpha = 0.7$ (black, solid) and $\alpha = 0.8$ (blue, dashed).

The poor performance of the MPC scheme in this scenario appears to be related to the prediction horizon N=9 and control horizon $N_u=3$ used by the controller. In particular, the violation of the roll error bounds in Fig. 6.33 indicates a lack of anticipative action, due to a too short prediction horizon. Moreover, the fact that the period of the MS trajectories in Fig. 6.30, and therefore of the underlying control sequence, is of about 100 s, suggests that the control horizon of the MPC scheme should be set to a similar length. Unfortunately, the computational time necessary to solve the MILP problem (4.100), scales badly with the length of the control horizon, as illustrated in Table 6.16 for different values of N_u and N. In fact, despite the efforts to tune the parameters of the controller, it has not been possible to increase the performance of the MPC scheme significantly, without compromising the feasibility of its online implementation.

Parameter	$N_u = 3, N = 9$	$N_u = 6, N = 9$	$N_u = N = 25$
Running time	25 ms	0.5 s	minutes

Table 6.16: Computational time required by MPC for different prediction and control horizons

6.4.3 Time-varying torques

In the following, the case in which an additional time-varying disturbance τ_m acts on the system, due to a large residual magnetic dipole of the spacecraft, is addressed within the LEO mission scenario considered in Section 6.4.2. The profile of the overall disturbance $\tau_e \approx \tau_a + \tau_m$ is depicted in Fig. 6.35.

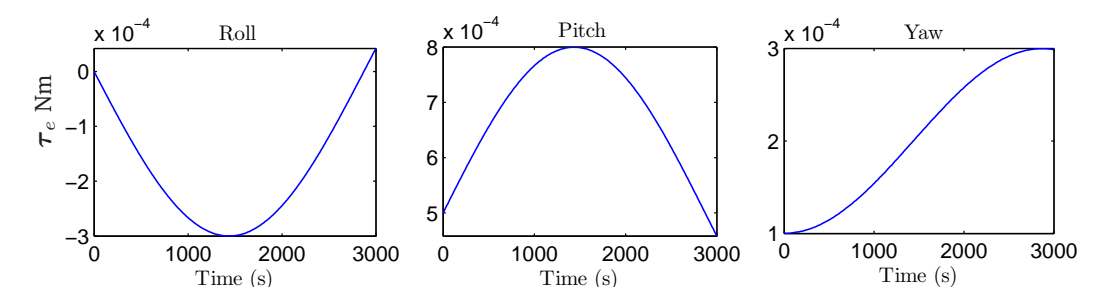


Figure 6.35: Disturbance torque profile.

Notice that the frequency of the disturbance is equal to the IVLH rate ω_L , and hence its period is equal to the orbital period. Because of the slow variation of the attitude disturbance, with respect to the error dynamics timescale, it is still possible to apply the MS+C1 and MS+C2 schemes. To this purpose, (4.66) and (4.70)-(4.71) are evaluated in real-time, as outlined in Section 6.4.1.

The system is simulated for 3000 s. The attitude error profile resulting from the application of the MS+C1 and MS+C2 schemes is reported in Fig. 6.36. It can be seen that the MS+C1 scheme is able to keep the attitude error within the pointing accuracy bounds for the entire simulation period, as opposed to the MS+C2 scheme. This is due to the requirement for the MS+C2 scheme to track a time-varying phase, as confirmed by the profile of the phase tracking errors $\widetilde{\phi}$ in (4.84), depicted in Fig. 6.37. Observe that the reference phase signal from the online solution to (4.71) can change abruptly as the disturbance torque varies (which is likely due to the fact that, in the presence of noise, different local minima are found by solving (4.71) at different sampling times). In order to track this signal, frequent adjustments of the amplitude (and hence the period) of the oscillations have to be performed, according to (4.83), which turns out to be the main reason for state constraint violations. On the other hand, one cannot blame the MS+C2 scheme for such type of behaviour, as it is designed to reject a constant disturbance torque.

The fuel consumption and switching frequency resulting from the application of the two control schemes is reported in Fig. 6.38. The fuel consumption is the same for both solutions,

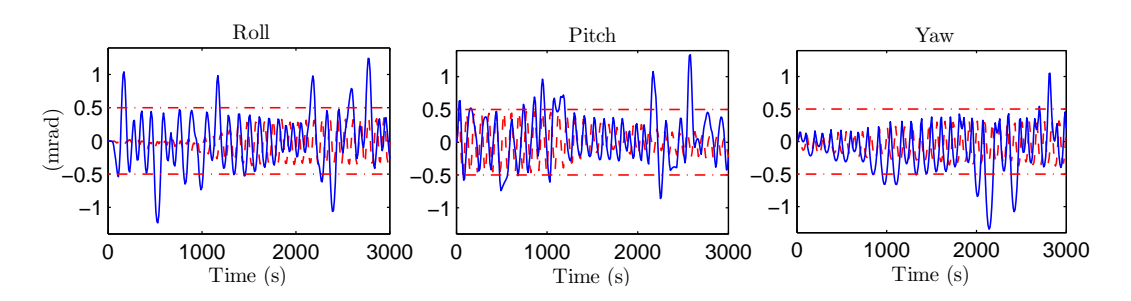


Figure 6.36: Tracking error profile: MS+C1 (red, dashed) and MS+C2 (blue, solid).

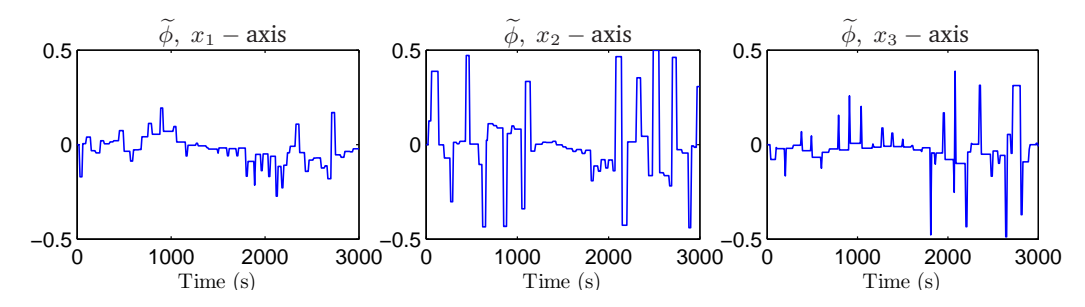


Figure 6.37: Phase tracking errors.

while the MS+C2 scheme performs better than the MS+C1 scheme in terms of switching frequency. This advantage, however, comes at the price of a lower tracking accuracy.

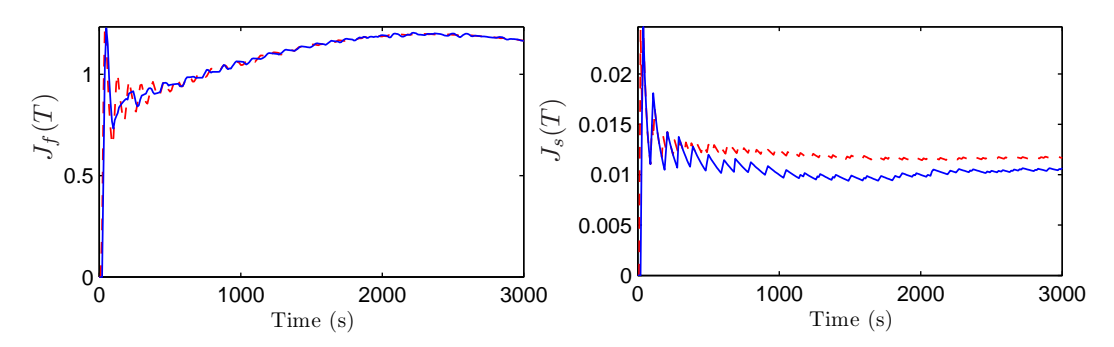


Figure 6.38: Average fuel consumption and switching frequency: MS+C1 (red, dashed) and MS+C2 (blue, solid).

Finally, it is worth remarking that, by focusing the analysis on a LEO orbit, a quite high value of the frequency ω_L of the disturbance has been considered. For disturbances with a very low frequency, e.g. solar radiation pressure torques in GEO, a better tracking accuracy of the MS+C2 scheme can be expected. Nevertheless, the extension of this control scheme to the case of time-varying disturbances is an important topic that remains to be addressed.

Conclusions and Future Work

This final chapter contains a summary of the thesis contributions and a discussion of the achieved results and of future research directions.

7.1 Summary of contributions

The contributions of this thesis can be divided into three categories: *orbit control techniques*, *attitude control techniques*, *validation of the proposed techniques on EP-based missions*.

Orbit control techniques

An orbital element control scheme has been derived for autonomous station-keeping of low Earth orbiting spacecraft. The proposed design relies on a continuous thrust control strategy, providing asymptotic tracking of the desired in-plane motion, by means of an efficient rejection of atmospheric drag, and an impulsive control scheme, which compensates for minor cross-track perturbations, by using small velocity increments of fixed magnitude.

An LMPC scheme has been developed for the autonomous rendezvous and docking problem. The proposed design is general enough to handle path constraints, as well as thrust magnitude and rate constraints. By exploiting the use of Laguerre functions, in combination with multi-parametric programming techniques, the optimal control problem is solved explicitly, which allows for the implementation of the control law on simple hardware.

Attitude control techniques

The minimum fuel and minimum switching control problem has been addressed for systems of coupled double integrators, in the context of precise attitude control with on/off actuators. Two suboptimal control strategies have been derived, providing upper bounds on the minimum switching frequency required to satisfy given state constraints, while rejecting a persistent disturbance with the minimum propellant consumption.

An MPC scheme, based on the linearized model of the attitude error dynamics, has been derived. The proposed methodology allows the designer to explicitly take into account both the fuel consumption and the number of actuator switching cycles, providing a suitable way to trade-off these objectives by means of a scalar parameter. The approach is general enough

to be applied also in the case of nonsymmetric thruster configurations, and in the presence of angular rate constraints.

Validation of the proposed techniques on EP-based missions

A simulation software has been implemented in MATLAB, including an accurate dynamic model of the spacecraft, as well as a GNC module based on the proposed control techniques and the developed EKF schemes. The simulation software can be used to design and analyze the principal classes of Earth orbit missions with electric propulsion.

The proposed control techniques have been validated on different mission scenarios. A LEO mission has been simulated to demonstrate the effectiveness of the orbital element control system. The performance of the LMPC design has been compared to standard MPC and LQR techniques on a formation flying mission, in terms of propellant consumption, maneuver completion time and safety of operation. The performance of the attitude control laws has been evaluated on GEO and LEO scenarios, in terms of fuel consumption and thruster switching frequency.

7.2 Discussion of the results

The autonomous station-keeping problem has been addressed for spacecraft with electric propulsion. By using the proposed control scheme in combination with an Hall effect thruster, it has been shown that the effect of atmospheric drag on spacecraft flying at very low altitudes can be compensated for sufficiently long mission lifetimes. The control scheme permits to compensate also the cross-track perturbations, by using a low power resistojet which is fed by the same xenon tank used by the Hall thruster. This provides a suitable trade-off between thrust efficiency and power requirements of the propulsion subsystem. The results from a case study of a small satellite LEO mission demonstrate the viability of the proposed solution, in terms of control accuracy and performance of the propulsion system. It is believed that this technology will play a key role in a number of future low-cost missions for remote sensing and Earth observation.

Concerning the autonomous rendezvous and docking problem, it has been shown that the use of Laguerre functions can be effective in improving the computational efficiency of model predictive control. The proposed controller accounts for the low thrust level delivered by the EP technology, while guaranteeing safe proximity operations. Moreover, it does not require a dedicated solver onboard the spacecraft thanks to the explicit formulation, whose implementation boils down to the evaluation of a piecewise affine state feedback control law. The results from the simulation case study of a cubesat formation flying mission indicate that the achievable performance, in terms of control accuracy and propellant usage, is compatible with the specifications of a PPT system that is close to flight qualification. Moreover, the required computations are found to be feasible on low-power hardware, within the sampling interval of the control system.

The attitude control problem has been studied for spacecraft equipped with on/off reaction control systems. The proposed control techniques allow one to confine the attitude tracking errors within prescribed bounds, while at the same time satisfying the constraints imposed by the technological limitations of the actuators, and are general enough to be employed in the presence of coupled dynamics. This is the case, for instance, whenever non-orthogonal thruster configurations are adopted for maximizing the generated torque or satisfying constraints coming from the spacecraft layout. The results from a simulation case study of an all-electric mission show that the additional propellant mass required by the considered attitude control system, based on small EP thrusters, is balanced by the benefits of removing momentum/reaction wheels from the ACS design, in terms of enhanced reliability and pointing stability.

From the comparison of the control laws (see Section 6.4), it can be concluded that, at the current status of the design, both the minimum switching schemes (MS+C1 and MS+C2) are well-suited for applications in which the disturbance torque is approximately constant or varies very slowly. However, the MS+C2 scheme is affected by a degradation of the tracking performance in the case of time-varying torques. In this case, the presence of many local minima in the objective function that is optimized, at each time step, in order to compute the reference phase signals, renders the control scheme highly sensitive to noise. In fact, the MS+C1 law, which does not rely on the optimization of the relative phases, is not affected by this problem. Moreover, the parameters of both the MS+C1 and MS+C2 schemes have to be scaled in order to cope with angular rate constraints. Alternatively, the proposed MPC design allows one to optimize the fuel consumption and the number of actuator switching cycles, while accounting in a systematic way for attitude and angular rate constraints, as well as for arbitrary thruster configurations. However, it is worth remarking that the mixed integer optimization problem involved in the computation of the MPC law is quite challenging. The computational burden is heavily affected by the length of the control horizon. The latter, in turns, depends on the pointing requirements and has an impact on the control performance. For the considered GEO mission, it turns out that the required processing power is compatible with state-of-the-art flight qualified CPUs. On the other hand, for more general cases (e.g. the LEO scenario in Section 6.4.2), it has not been possible to obtain a satisfactory performance of the MPC scheme, without compromising the feasibility of its online implementation.

7.3 Future research directions

The results obtained are by no means exhaustive and there are many aspects of the considered problems that still remain to be investigated.

A continuous/impulsive control scheme has been developed in Section 3.2 for the station-keeping problem. Although the stability of the closed-loop system has been shown under simplifying assumptions on the system structure, the provided results do not extend to the fully interconnected dynamical system. Therefore, a formal stability proof of the overall design wold be a valuable add-on to the theoretical analysis presented in this thesis. In this

respect, the application of backstepping techniques can be envisaged.

An explicit LMPC design has been developed in Section 3.3, for the rendezvous and docking problem. An underlying assumption in the derivation is that the attitude of the target spacecraft is aligned to the LVLH frame orientation and that the spacecraft have similar physical properties. However, this is only true for spacecraft formations which are specifically designed to satisfy these requirements. In the case of rendezvous and docking with a tumbling, noncooperative target, e.g. repairing and refueling of defunct satellites, or space debris removal, the applicability of the explicit controller might be limited, due to the presence of time-varying constraints. From a theoretical viewpoint, it will be interesting to see how the MPC and LMPC schemes compare under a dual-mode formulation of the corresponding control problems.

Concerning the attitude control problem, in Chapter 4, it is worth remarking that the optimization of the relative phases of the attitude error oscillations gives a conservative upper bound on the minimum actuator switching frequency. In fact, we have found empirically that periodic trajectories with a lower switching cost do indeed exist. Moreover, it is still not clear how to tackle the minimum switching problem without enforcing the constraint that the periodic solution of each state variable must take the same form as the optimal solution for the single-axis case. For instance, one could consider periodic trajectories having asymmetric amplitudes or different periods along different state components. Another important aspect for future investigations is the possibility to extend the obtained results to the case of time varying torques and angular rate constraints, as well as for other classes of multivariable linear dynamic systems. In this respect, developing methods for improving the computational efficiency of the mixed-integer MPC algorithm may play a significant role.

Appendix A

Appendix

For completeness, the proofs of Propositions 3.2.1, 3.2.2, 3.2.4 and 3.3.2 are reported next.

Proof of Proposition 3.2.1

Proof. For system (3.15)-(3.16), a candidate Lyapunov function is

$$V = \frac{1}{2} \delta \mathbf{o}_1^T \mathbf{K}_1 \delta \mathbf{o}_1, \tag{A.1}$$

which is positive definite. The time derivative of (A.1) is

$$\dot{V} = \delta \mathbf{o}_1^T \mathbf{K}_1 \delta \dot{\mathbf{o}}_1 = -\delta \mathbf{o}_1^T \mathbf{K}_1 \mathbf{b}_1 \mathbf{b}_1^T \mathbf{K}_1 \delta \mathbf{o}_1$$
(A.2)

which is negative semidefinite. Consequently, $\delta \mathbf{o}_1$, $a = \bar{a} + \delta a$, and hence \mathbf{b}_1 from (3.17) are bounded. To prove asymptotic stability, we use Barbalat's lemma. Let $\mathbf{x} = \mathbf{K}_1 \delta \mathbf{o}_1$. Then $\dot{V} = -\mathbf{x}^T \mathbf{b}_1 \mathbf{b}_1^T \mathbf{x}$ and its time derivative is given by

$$\ddot{V} = -2\mathbf{x}^T \dot{\mathbf{b}}_1 \mathbf{b}_1^T \mathbf{x} - 2\mathbf{x}^T \mathbf{b}_1 \mathbf{b}_1^T \dot{\mathbf{x}}, \tag{A.3}$$

which is bounded because $\mathbf{x} = \mathbf{K}_1 \delta \mathbf{o}_1$ and $\dot{\mathbf{x}} = -\mathbf{K}_1^2 \mathbf{b}_1 \delta \mathbf{o}_1$ are bounded, and $\dot{\mathbf{b}}_1$ is bounded for a > 0. Then,

$$\lim_{t \to \infty} \dot{V}(t) = 0.$$

Notice that $\mathbf{b}_1^T \mathbf{K}_1 \delta \mathbf{o}_1 = 0$ in (A.2) implies u = 0 in (3.16) and therefore $\delta \dot{\mathbf{o}}_1 = \mathbf{0}$ in (3.15). Combining this observation with the fact that, due to the presence of the time-varying term $\nu_l(t)$ in (3.17), the vector $\mathbf{b}_1(t)$ spans the whole \mathbb{R}^3 space over time, one has that $\lim_{t \to \infty} \dot{V}(t) = 0$ implies $\lim_{t \to \infty} \mathbf{x}(t) = \mathbf{0}$. Hence, $\lim_{t \to \infty} \delta \mathbf{o}_1(t) = \mathbf{0}$, which concludes the proof. \square

Proof of Proposition 3.2.2

Proof. Define $\tilde{z} = (K_I z + d)$. System (3.12), with the control law (3.18), can be rewritten as

$$\delta \dot{\mathbf{o}}_{1} = -\mathbf{b}_{1} \mathbf{b}_{1}^{T} \mathbf{K}_{1} \delta \mathbf{o}_{1} + \mathbf{b}_{1} \widetilde{z}$$

$$\dot{\widetilde{z}} = -K_{I}^{2} \mathbf{b}_{1}^{T} \delta \mathbf{o}_{1}.$$
(A.4)

For system (A.4), a candidate Lyapunov function is

$$V = \frac{1}{2}\delta \mathbf{o}_1^T \mathbf{K}_1 \delta \mathbf{o}_1 + \frac{1}{2K_I^2} \widetilde{z}^2, \tag{A.5}$$

134 A. Appendix

which is positive definite. The time derivative of (A.5) is

$$\dot{V} = \delta \mathbf{o}_1^T \mathbf{K}_1 \delta \dot{\mathbf{o}}_1 + \frac{1}{K_I^2} \tilde{z} \dot{\tilde{z}} = -\delta \mathbf{o}_1^T \mathbf{K}_1 \mathbf{b}_1 \mathbf{b}_1^T \mathbf{K}_1 \delta \mathbf{o}_1 = -\mathbf{x}^T \mathbf{b}_1 \mathbf{b}_1^T \mathbf{x}, \tag{A.6}$$

which is negative semidefinite. By using the same arguments as in the proof of Theorem 3.2.1, one has that

$$\lim_{t \to \infty} \dot{V}(t) = 0,\tag{A.7}$$

which implies that, for $t \to \infty$,

$$\begin{array}{rcl}
\delta \dot{\mathbf{o}}_1 & \rightarrow & \mathbf{b}_1 \widetilde{z} \\
\dot{\widetilde{z}} & \rightarrow & 0.
\end{array} \tag{A.8}$$

Notice that, with the same reasoning as in Theorem 3.2.1, the only solution to (A.4) satisfying (A.8) is the trivial one $(\delta \mathbf{o}_1, \widetilde{z}) = (\mathbf{0}, 0)$. Then, $\lim_{t \to \infty} \delta \mathbf{o}_1(t) = \mathbf{0}$, which concludes the proof.

Proof of Proposition 3.2.4

Proof. By substituting (3.21) in (3.14), one gets

$$\delta \dot{\nu}_l = \left| -\sqrt{\mu} K_{\nu} \, \delta \nu_l + \sqrt{\frac{\mu}{\bar{a}^3}} \right| - \sqrt{\frac{\mu}{\bar{a}^3}},$$

where $\delta \nu_l \in (-\pi, \pi]$. Then, for $0 < K_{\nu} \le \frac{1}{\pi \bar{a}^{\frac{3}{2}}}$,

$$\delta \dot{\nu}_l = -\sqrt{\mu} K_{\nu} \, \delta \nu_l,$$

and therefore $\lim_{t\to\infty} \delta\nu_l = 0$, which concludes the proof.

Proof of Proposition 3.3.2

Proof. Under the assumptions of Proposition 3.3.2, (3.59) boils down to

$$\min_{\boldsymbol{\eta}} \quad J = \boldsymbol{\eta}^T \boldsymbol{\Omega} \, \boldsymbol{\eta} + 2 \, \mathbf{x}^T(k) \boldsymbol{\Psi} \boldsymbol{\eta}$$
s.t. (3.58), $s_2 = 0$, $\mathbf{x}(k + N_p | k) = 0$. (A.9)

Let $J^*(k)$ and $J^*(k+1)$ denote the optimal value functions for problem (A.9) at sampling times k and k+1. Moreover, denote by

$$\mathbf{U}^*(k) = {\mathbf{L}(0)\boldsymbol{\eta}^*(k), \dots, \mathbf{L}(N_n - 1)\boldsymbol{\eta}^*(k)}$$

the optimal input sequence at time k. Because the problem is feasible at each time sample, a feasible input sequence a time k+1, starting from $\mathbf{x}(k+1) = \mathbf{x}(k+1|k)$, is

$$\mathbf{U}(k+1) = {\mathbf{L}(1)\boldsymbol{\eta}^*(k), \dots, \mathbf{L}(N_p-2)\boldsymbol{\eta}^*(k), 0},$$

corresponding to the cost J(k+1). By definition, one has that $J^*(k+1) \leq J(k+1)$ and therefore

$$J^*(k+1) - J^*(k) \le J(k+1) - J^*(k). \tag{A.10}$$

Because J(k+1) and $J^*(k)$ share the same control and state sequences for the set of samples $k+1,\ldots,k+N_p-1$, and $\mathbf{x}(k+N_p|k)=0$, it can be verified that

$$J(k+1) - J^*(k) = -\mathbf{x}(k+1)^T \mathbf{Q}_d \mathbf{x}(k+1) - \mathbf{u}(k)^T \mathbf{R}_d \mathbf{u}(k). \tag{A.11}$$

where the matrices $\mathbf{Q}_d = T_s \mathbf{Q}_c^T \mathbf{Q}_c$ and $\mathbf{R}_d = T_s \mathbf{R}_c^T \mathbf{R}_c$ are assumed positive definite. By using (A.11) in (A.10), it follows that

$$J^*(k+1) - J^*(k) < 0,$$

for $\mathbf{x} \neq \mathbf{0}$, $\mathbf{u} \neq \mathbf{0}$, which concludes the proof.

Bibliography

- [1] B. Agrawal, R. Mcclelland, and G. Song, "Attitude control of flexible spacecraft using pulsewidth pulse-frequency modulated thrusters," *Space Technology*, vol. 17, no. 1, pp. 15–34, 1997.
- [2] B. N. Agrawal, Design of Geosynchronous Spacecraft. Prentice-Hall, 1986.
- [3] M. Andraschko, J. Antol, S. Baize, R. and Horan, D. Neil, P. Rinsland, and R. Zaiceva, "The potential for hosted payloads at NASA," in *IEEE Aerospace Conference*, 2012.
- [4] M. Athans and P. L. Falb, *Optimal Control: An Introduction to the Theory and its Applications*. Courier Dover Publications, 2006.
- [5] M. Bando and A. Ichikawa, "In-plane motion control of Hill-Clohessy-Wiltshire equations by single input," *Journal of Guidance, Control, and Dynamics*, vol. 36, no. 5, pp. 1–10, 2013.
- [6] C. Barton, "International Geomagnetic Reference Field: The seventh generation." *Journal of Geomagnetism and Geoelectricity*, vol. 49, pp. 123–148, 1997.
- [7] F. H. Bauer, K. Hartman, and E. G. Lightsey, "Spaceborne GPS current status and future visions," in *IEEE Aerospace Conference*, vol. 3, 1998, pp. 195–208.
- [8] A. Bemporad, M. Morari, V. Dua, and E. N. Pistikopoulos, "The explicit linear quadratic regulator for constrained systems," *Automatica*, vol. 38, no. 1, pp. 3–20, 2002.
- [9] S. Berge, A. Edfors, T. Olsson, G. Pionnier, M. Björk, C. Chasset, T. Nordebäck, M. Rieschel, B. Lübke-Ossenbeck, and P. Zentgraf, "Advanced AOCS design on the first Small GEO telecom satellite," in 60th International Astronautical Congress, 2009.
- [10] J. T. Betts, "Survey of numerical methods for trajectory optimization," *Journal of Guidance, Control, and Dynamics*, vol. 21, no. 2, pp. 193–207, 1998.
- [11] R. Bevilacqua, M. Romano, and O. Yakimenko, "Online generation of quasi-optimal spacecraft rendezvous trajectories," *Acta Astronautica*, vol. 64, no. 2, pp. 345–358, 2009.
- [12] J. Blandino, P. Marchetti, and M. Demetriou, "Electric propulsion and controller design for drag-free spacecraft operation," *Journal of Spacecraft and Rockets*, vol. 45, no. 6, pp. 1303–1315, 2008.

[13] R. J. Boain, "A-B-Cs of sun-synchronous orbit mission design," in *Spaceflight Mechanics 2004*, ser. Advances in the Astronautical Sciences Series. Univelt, Incorporated, 2005, vol. 119, pp. 85–104.

- [14] M. Boccadoro, Y. Wardi, M. Egerstedt, and E. Verriest, "Optimal control of switching surfaces in hybrid dynamical systems," *Discrete Event Dynamic Systems*, vol. 15, no. 4, pp. 433–448, 2005.
- [15] S. Boyd, "Multitone signals with low crest factor," *IEEE Transactions on Circuits and Systems*, vol. 33, no. 10, pp. 1018–1022, 1986.
- [16] L. Breger, J. How, and A. Richards, "Model predictive control of spacecraft formations with sensing noise," in *Proceedings of the American Control Conference*, 2005, pp. 2385–2390.
- [17] L. S. Breger and J. P. How, "Safe trajectories for autonomous rendezvous of spacecraft," *Journal of Guidance, Control, and Dynamics*, vol. 31, no. 5, pp. 1478–1489, 2008.
- [18] D. Brouwer, "Solution of the problem of artificial satellite theory without drag," *Journal of Guidance, Control, and Dynamics*, vol. 64, no. 1274, pp. 378–397, 1959.
- [19] T. Brown, "In-flight tuning of the Cassini RCS attitude controller," in AIAA Guidance, Navigation, and Control Conference, Portland, OR, August 2011.
- [20] F. D. Busse, J. P. How, and J. Simpson, "Demonstration of adaptive extended kalman filter for low Earth orbit formation estimation using CDGPS," *Journal of the Institute of Navigation*, vol. 50, pp. 79–94, 2003.
- [21] E. Canuto and L. Massotti, "All-propulsion design of the drag-free and attitude control of the european satellite GOCE," *Acta Astronautica*, vol. 64, no. 2-3, pp. 325–344, 2009.
- [22] W. H. Clohessy and R. S. Wiltshire, "Terminal guidance system for satellite rendezvous," *Journal of the Aerospace Sciences*, vol. 27, no. 9, pp. 653–658, 1960.
- [23] M. Coletti, A. Grubisic, C. Collingwood, and S. Gabriel, "Solar electric propulsion subsystem architecture for an all-electric spacecraft," in *Advances in Spacecraft Technologies*, J. Hall, Ed. InTech, 2011, pp. 123–138.
- [24] M. Coletti, F. Guarducci, and S. Gabriel, "A micro PPT for cubesat application: Design and preliminary experimental results," *Acta Astronautica*, vol. 69, no. 3, pp. 200–208, 2011.
- [25] S. Cornara, F. Pirondini, A. Caramagno, M. Price, J. G. Del Amo, and B. Carnicero-Domínguez, "Analyses of remote sensing mission scenarios with electric propulsion," in *56th International Astronautical Congress*, 2005.
- [26] V. Coverstone-Carroll, J. Hartmann, and W. Mason, "Optimal multi-objective low-thrust space-craft trajectories," Computer Methods in Applied Mechanics and Engineering, vol. 186, no. 2, pp. 387–402, 2000.
- [27] J. L. Crassidis and J. L. Junkins, *Optimal Estimation of Dynamic Systems*. Boca Raton, Florida: Chapman & Hall/CRC press, 2004, chap. 5.
- [28] R. Crisp and D. W. Keene, *Apollo Command and Service Module Reaction Control by the Digital Autopilot*. MIT Instrumentation Laboratory, 1966.

[29] S. De Florio, S. D'Amico, and G. Radice, "Virtual formation method for precise autonomous absolute orbit control," *Journal of Guidance, Control, and Dynamics*, vol. 37, no. 2, pp. 425–438, 2014.

- [30] S. De Florio and S. D'Amico, "Optimal autonomous orbit control of a remote sensing spacecraft," in *Spaceflight Mechanics*. Univelt, Incorporated, 2009, vol. 134, pp. 949–968.
- [31] S. De Florio, S. D'Amico, and G. Radice, "Flight results of precise autonomous orbit keeping experiment on PRISMA mission," *Journal of Spacecraft and Rockets*, vol. 50, no. 3, pp. 662–674, 2013.
- [32] M. De Tata, P. Frigot, S. Beekmans, H. Lübberstedt, D. Birreck, A. Demairé, and P. Rathsman, "SGEO development status and opportunities for the EP-based small european telecommunication platform," in *32nd International Electric Propulsion Conference*, 2011.
- [33] S. Di Cairano, H. Park, and I. Kolmanovsky, "Model predictive control approach for guidance of spacecraft rendezvous and proximity maneuvering," *International Journal of Robust and Nonlinear Control*, vol. 22, no. 12, pp. 1398–1427, 2012.
- [34] S. Dodds, "Adaptive, high precision, satellite attitude control for microprocessor implementation," *Automatica*, vol. 17, no. 4, pp. 563–573, 1981.
- [35] S. Dodds and S. Williamson, "A signed switching time bang-bang attitude control law for fine pointing of flexible spacecraft," *International Journal of Control*, vol. 40, no. 4, pp. 795–811, 1984.
- [36] D. B. Doman, B. J. Gamble, and A. D. Ngo, "Quantized control allocation of reaction control jets and aerodynamic control surfaces," *Journal of Guidance, Control and Dynamics*, vol. 32, no. 1, pp. 13–24, 2009.
- [37] M. Drinkwater, R. Floberghagen, R. Haagmans, D. Muzi, and A. Popescu, "GOCE: ESA's first Earth explorer core mission," in *Earth Gravity Field from Spacefrom Sensors to Earth Sciences*. Springer, 2003, pp. 419–432.
- [38] S. Dunn and R. Edelmann, "Minimum power spacecraft attitude control laws for small constant disturbance torques," *IEEE Transactions on Automatic Control*, vol. 13, no. 6, pp. 691–694, 1968.
- [39] J. W. Dunning, S. Benson, and S. Oleson, "NASA's electric propulsion program," in 27th International Electric Propulsion Conference, 2001.
- [40] R. Epenoy, "Fuel optimization for continuous-thrust orbital rendezvous with collision avoidance constraint," *Journal of Guidance, Control, and Dynamics*, vol. 34, no. 2, pp. 493–503, 2011.
- [41] European Cooperation for Space Standardization, *Space engineering*, 2200 AG Noordwijk, The Netherlands, 2000.
- [42] D. Fearn, "Economical remote sensing from a low altitude with continuous drag compensation," *Acta Astronautica*, vol. 56, no. 5, pp. 555–572, 2005.
- [43] S. A. Feuerborn, D. Neary, and J. Perkins, "Finding a way: Boeing's all electric propulsion satellite," in 49th AIAA/ASME/SAE/ASEE Joint Propulsion Conference & Exhibit, 2013.

[44] M. E. Fleck and S. R. Starin, "Evaluation of a drag-free control concept for missions in low Earth orbit," in AIAA Guidance, Navigation, and Control Conference and Exhibit, 2003.

- [45] M. Fouquet and M. Sweeting, "UoSAT-12 minisatellite for high performance Earth observation at low cost," *Acta Astronautica*, vol. 41, no. 3, pp. 173–182, 1997.
- [46] C. Fridlund, "DARWIN-the infrared space interferometry mission," *ESA bulletin*, vol. 103, pp. 20–25, 2000.
- [47] D. Frollani, M. Coletti, and S. Gabriel, "A T5 hollow cathode thruster: Experimental results and modelling," in 48th AIAA/ASME/SAE/ASEE Joint Propulsion Conference & Exhibit, 2012.
- [48] S. Gabriel, E. Rogers, and M. Leomanni, "The applicability of pulsed plasma thrusters to rendezvous and docking of cubesats," in *33rd International Electric Propulsion Conference*, 2013.
- [49] H. Gao, X. Yang, and P. Shi, "Multi-objective robust control of spacecraft rendezvous," *IEEE Transactions on Control Systems Technology*, vol. 17, no. 4, pp. 794–802, 2009.
- [50] A. Garulli, A. Giannitrapani, M. Leomanni, and F. Scortecci, "Autonomous low-Earth-orbit station-keeping with electric propulsion," *Journal of Guidance Control and Dynamics*, vol. 34, no. 6, pp. 1683–1693, 2011.
- [51] A. Garulli, A. Giannitrapani, and M. Leomanni, "Autonomous LEO station-keeping with a hybrid continuous/impulsive electric propulsion system," in *32nd International Electric Propulsion Conference*, 2011.
- [52] A. Garulli, A. Giannitrapani, and M. Leomanni, "Minimum switching limit cycle oscillations for systems of coupled double integrators," in *Proceedings of 53rd IEEE Conference on Decision and Control*, 2014.
- [53] P. Gessini, M. Coletti, A. Grubisic, S. Gabriel, N. Wallace, and D. Fearn, "Hollow cathode thruster for all-electric spacecraft," in 43rd AIAA/ASME/SAE/ASEE Joint Propulsion Conference & Exhibit, 2007.
- [54] E. Gill, O. Montenbruck, and S. D'Amico, "Autonomous formation flying for the PRISMA mission," *Journal of Spacecraft and Rockets*, vol. 44, no. 3, pp. 671–681, 2007.
- [55] J. Gonzalez and G. Saccoccia, "ESA electric propulsion activities," in *32nd International Electric Propulsion Conference*, 2011.
- [56] M. D. Griffin and J. R. French, *Space Veichle Design*, 1st ed. American Institute of Aeronautics and Astronautics, Inc., 1991.
- [57] M. Guelman and M. Aleshin, "Optimal bounded low-thrust rendezvous with fixed terminal-approach direction," *Journal of Guidance, Control, and Dynamics*, vol. 24, no. 2, pp. 378–385, 2001.
- [58] P. Gurfil, "Control-theoretic analysis of low-thrust orbital transfer using orbital elements," *Journal of Guidance, Control, and Dynamics*, vol. 26, no. 6, pp. 979–983, 2003.
- [59] T. Haberkorn, P. Martinon, and J. Gergaud, "Low thrust minimum-fuel orbital transfer: A homotopic approach," *Journal of Guidance, Control, and Dynamics*, vol. 27, no. 6, pp. 1046–1060, 2004.

[60] Y. Hanawa, "Fuel efficient attitude control of spacecraft," Ph.D. dissertation, Massachusetts Institute of Technology, 1979.

- [61] C. R. Hargraves and S. W. Paris, "Direct trajectory optimization using nonlinear programming and collocation," *Journal of Guidance, Control, and Dynamics*, vol. 10, no. 4, pp. 338–342, 1987.
- [62] E. N. Hartley, P. A. Trodden, A. G. Richards, and J. M. Maciejowski, "Model predictive control system design and implementation for spacecraft rendezvous," *Control Engineering Practice*, vol. 20, no. 7, pp. 695–713, 2012.
- [63] Ø. Hegrenæs, J. Gravdahl, and P. Tøndel, "Spacecraft attitude control using explicit model predictive control," *Automatica*, vol. 41, no. 12, pp. 2107–2114, 2005.
- [64] M. Herceg, M. Kvasnica, C. Jones, and M. Morari, "Multi-Parametric Toolbox 3.0," in *Proceedings of the European Control Conference*, 2013, pp. 502–510.
- [65] V. Hruby, B. Pote, M. Gamero-Castao, G. Kolencik, L. Byrne, R. Tedrake, and M. Delichatsios, "Hall thrusters operating in pulsed mode," in *27th International Electric Propulsion Conference*, 2001.
- [66] IBM, CPLEX, ILOG 11.0 User's Manual. ILOG CPLEX Division. Incline Village, NV, 2007.
- [67] L. G. Jacchia, "Revised static models of the thermosphere and exosphere with empirical temperature profiles," Smithsonian Astrophysical Observatory, Tech. Rep. 332, 1971.
- [68] C. Kaiser, F. Sjöberg, J. M. Delcura, and B. Eilertsen, "SMART-OLEV—an orbital life extension vehicle for servicing commercial spacecrafts in geo," *Acta Astronautica*, vol. 63, no. 1, pp. 400–410, 2008.
- [69] M. H. Kaplan, *Modern Spacecraft Dynamics and Control*. New York: John Wiley and Sons, 1976.
- [70] M. H. Kaplan, "All-electric thruster control of a geostationary communications satellite," *Journal of Spacecraft and Rockets*, vol. 10, no. 2, pp. 119–125, 1973.
- [71] H.-D. Kim et al., "COMS, the new eyes in the sky for geostationary remote sensing," *Remote Sensing–Advanced Techniques and Platforms*, pp. 235–268, 2012.
- [72] D. King-Hele, Satellite Orbits in an Atmosphere: Theory and Applications. London, United Kingdom: Blackie and Son Ltd, 1987.
- [73] H. J. Königsmann, J. T. Collins, S. Dawson, and J. R. Wertz, "Autonomous orbit maintenance system," *Acta Astronautica*, vol. 39, no. 9, pp. 977–985, 1996.
- [74] A. Krimchansky, D. Machi, S. Cauffman, and M. Davis, "Next-generation geostationary operational environmental satellite (GOES-R series): A space segment overview," in *Remote Sensing*. International Society for Optics and Photonics, 2004, pp. 155–164.
- [75] R. Kristiansen and P. J. Nicklasson, "Spacecraft formation flying: A review and new results on state feedback control," *Acta Astronautica*, vol. 65, no. 11, pp. 1537–1552, 2009.
- [76] T. Krovel, "Optimal tuning of PWPF modulator for attitude control," Ph.D. dissertation, Norwegian University of Science and Technology, 2009.

[77] T. Krøvel, F. Dörfler, M. Berger, and J. Rieber, "High-precision spacecraft attitude and manoeuvre control using electric propulsion," in *60th International Austronautical Congress*, 2009.

- [78] A. Lamy, M.-C. Charmeau, and D. Laurichesse, "Experiment of autonomous orbit control on DEMETER: In-flight results and perspectives," in *AIAA Astrodynamics Specialist Conference*, 2006, pp. 21–24.
- [79] G. Lantoine and R. Epenoy, "Quadratically constrained linear-quadratic regulator approach for finite-thrust orbital rendezvous," *Journal of Guidance, Control, and Dynamics*, vol. 35, no. 6, pp. 1787–1797, 2012.
- [80] M. Leomanni, A. Garulli, A. Giannitrapani, and F. Scortecci, "Precise attitude control of allelectric GEO spacecraft using xenon microthrusters," in *33rd International Electric Propulsion Conference*, 2013.
- [81] M. Leomanni, A. Garulli, A. Giannitrapani, and F. Scortecci, "An MPC-based attitude control system for all-electric spacecraft with on/off actuators," in *Proceedings of 52nd IEEE Conference on Decision and Control*, 2013.
- [82] M. Leomanni, A. Garulli, A. Giannitrapani, and F. Scortecci, "All-electric spacecraft precision pointing using model predictive control," *Journal of Guidance, Control, and Dynamics*, vol. 38, no. 1, pp. 161–168, 2015.
- [83] M. Leomanni, E. Rogers, and S. B. Gabriel, "Explicit model predictive control approach for low-thrust spacecraft proximity operations," *Journal of Guidance, Control and Dynamics*, vol. 37, no. 6, pp. 1780–1790, 2014.
- [84] W. S. Levine, The Control Handbook. CRC press, 1996.
- [85] H. Liu, J. Li, and B. Hexi, "Sliding mode control for low-thrust Earth-orbiting spacecraft formation maneuvering," *Aerospace Science and Technology*, vol. 10, no. 7, pp. 636–643, 2006.
- [86] A. V. Loyan and T. A. Maksymenko, "Performance investigation of SPT-20M low power Hall effect thruster," *Journal of Technical Physics*, vol. 49, no. 3–4, pp. 283–302, 2008.
- [87] W. Luo, Y.-C. Chu, and K.-V. Ling, "Inverse optimal adaptive control for attitude tracking of spacecraft," *IEEE Transactions on Automatic Control*, vol. 50, no. 11, pp. 1639–1654, 2005.
- [88] Y.-Z. Luo, G.-J. Tang, and Y.-J. Lei, "Optimal multi-objective linearized impulsive rendezvous," *Journal of Guidance, Control, and Dynamics*, vol. 30, no. 2, pp. 383–389, 2007.
- [89] J. Maciejowski, *Predictive Control with Constraints*. Pearson education, 2002, pp. 1–32.
- [90] L. M. Mailhe and S. D. Heister, "Design of a hybrid chemical/electric propulsion orbital transfer vehicle," *Journal of Spacecraft and Rockets*, vol. 39, no. 1, pp. 131–139, 2002.
- [91] D. Manzella, "Low cost electric propulsion thruster for deep space robotic missions," in *NASA Science Technology Conference*, Hyattsville, Maryland, 2007.
- [92] A. D. Marinan, "From cubesats to constellations: Systems design and performance analysis," Ph.D. dissertation, Massachusetts Institute of Technology, 2013.

[93] M. Martinez-Sanchez and J. E. Pollard, "Spacecraft electric propulsion—an overview," *Journal of Propulsion and Power*, vol. 14, no. 5, pp. 688–699, 1998.

- [94] J. Mattingley, Y. Wang, and S. Boyd, "Receding horizon control," *IEEE Control Systems Magazine*, vol. 31, no. 3, pp. 52–65, 2011.
- [95] R. Mattingly, S. Hayati, and G. Udomkesmalee, "Technology development plans for the Mars sample return mission," in *Aerospace Conference*, 2005, pp. 982–995.
- [96] D. Mayne, J. Rawlings, C. Rao, and P. Scokaert, "Constrained model predictive control: Stability and optimality," *Automatica*, vol. 36, no. 6, pp. 789–814, 2000.
- [97] L. Mazal, G. Mingotti, and P. Gurfil, "Optimal on–off cooperative maneuvers for long-term satellite cluster flight," *Journal of Guidance, Control, and Dynamics*, vol. 37, no. 2, pp. 391–402, 2014.
- [98] P. Micheau, "Orbit control techniques for low Earth orbiting (LEO) satellites," in *Spaceflight Dynamics*. Cepadues Editions, 1995, vol. 1, pp. 793–902.
- [99] O. Montenbruck and E. Gill, Satellite Orbits. Springer-Verlag, Berlin, Germany, 2000.
- [100] D. Muzi and A. Allasio, "GOCE: The first core Earth explorer of ESA's Earth observation programme," *Acta Astronautica*, vol. 54, no. 3, pp. 167–175, 2004.
- [101] B. J. Naasz, "Classical element feedback control for spacecraft orbital maneuvers," Master's thesis, Department of Aerospace and Ocean Engineering, Virginia Polytechnic Institute and State University, 2002.
- [102] D. Nicolini, D. Robertson, E. Chesta, G. Saccoccia, D. Gibbon, and A. M. Baker, "Xenon resistojets as a secondary propulsion on EP spacecrafts and performance results of resistojets using xenon," in 28th International Electric Propulsion Conference, 2003.
- [103] S. R. Oleson, R. M. Myers, C. A. Kluever, J. P. Riehl, and F. M. Curran, "Advanced propulsion for geostationary orbit insertion and north-south station keeping," *Journal of Spacecraft and Rockets*, vol. 34, no. 1, pp. 22–28, 1997.
- [104] N. Oliveira and K. Kienitz, "Attitude controller design for a system using actuators with switching-time restrictions and delays," in AIAA Guidance, Navigation, and Control Conference and Exhibit, 2000.
- [105] P. Patel, D. Scheeres, and A. Gallimore, "Maximizing payload mass fractions of spacecraft for interplanetary electric propulsion missions," *Journal of Spacecraft and Rockets*, vol. 43, no. 4, pp. 822–827, 2006.
- [106] G. Personne, A. Lopez-Y-Diaz, and P. Delpy, "ATV GNC synthesis: Overall design, operations and main performances," in *Proceedings of the 6th International ESA Conference on Guidance, Navigation and Control Systems*, 2006.
- [107] M. E. Pittelkau, "Rotation vector in attitude estimation," *Journal of Guidance, Control, and Dynamics*, vol. 26, no. 6, pp. 855–860, 2003.

[108] K. A. Polzin, T. E. Markusic, B. J. Stanojev, A. DeHoyos, Y. Raitses, A. Smirnov, and N. J. Fisch, "Performance of a low-power cylindrical Hall thruster," *Journal of Propulsion and Power*, vol. 23, no. 4, pp. 886–888, 2007.

- [109] R. Pongvthithum, S. M. Veres, S. Gabriel, and E. Rogers, "Universal adaptive control of satellite formation flying," *International Journal of Control*, vol. 78, no. 1, pp. 45–52, 2005.
- [110] J. Reichbach, R. J. Sedwick, and M. Martinez-Sanchez, "Micropropulsion system selection for precision formation flying satellites," Ph.D. dissertation, Massachusetts Institute of Technology, 2001.
- [111] A. Richards and J. P. How, "Model predictive control of vehicle maneuvers with guaranteed completion time and robust feasibility," in *Proceedings of the American Control Conference*, 2003, pp. 4034–4040.
- [112] A. Richards, T. Schouwenaars, J. P. How, and E. Feron, "Spacecraft trajectory planning with avoidance constraints using mixed-integer linear programming," *Journal of Guidance, Control, and Dynamics*, vol. 25, no. 4, pp. 755–764, 2002.
- [113] P. Riedinger, I.-C. Morarescu *et al.*, "A numerical framework for optimal control of switched affine systems with state constraint," in 4th IFAC Conference on Analysis and Design of Hybrid Systems, 2011.
- [114] P. Romero, J. M. Gambi, E. Patio, and R. Antolin, "Optimal station keeping for geostationary satellites with electric propulsion systems under eclipse constraints," in *Progress in Industrial Mathematics at ECMI 2006*. Springer-Verlag, 2008, vol. 12, pp. 260–264.
- [115] I. M. Ross and F. Fahroo, "Pseudospectral knotting methods for solving nonsmooth optimal control problems," *Journal of Guidance, Control, and Dynamics*, vol. 27, no. 3, pp. 397–405, 2004.
- [116] P. Rossetti and D. Valentian, "Analysis of Hall-effect thrusters application to formation flying and drag compensation," in *30th International Electric Propulsion Conference*, 2007.
- [117] M. Rubagotti, S. Trimboli, and A. Bemporad, "Stability and invariance analysis of uncertain discrete-time piecewise affine systems," *IEEE Transactions on Automatic Control*, vol. 58, no. 9, pp. 2359–2365, 2013.
- [118] L. Sauter and P. Palmer, "Analytic model predictive controller for collision-free relative motion reconfiguration," *Journal of Guidance, Control, and Dynamics*, vol. 35, no. 4, pp. 1069–1079, 2012.
- [119] H. Schaub and K. T. Alfriend, "Impulsive feedback control to establish specific mean orbit elements of spacecraft formations," *Journal of Guidance, Control, and Dynamics*, vol. 24, no. 4, pp. 739–745, 2001.
- [120] H. Schaub, S. R. Vadali, J. L. Junkins, and K. T. Alfriend, "Spacecraft formation flying control using mean orbit elements," *Journal of the Astronautical Sciences*, vol. 48, no. 1, pp. 69–87, 2000.
- [121] A. Schneider, W. Sun, and H. Schuff, "The european platform LUXOR for small communications satellites," in *26th International Communications Satellite Systems Conference*, 2008.

[122] S. A. Schweighart and R. J. Sedwick, "High-fidelity linearized J2 model for satellite formation flight," *Journal of Guidance, Control, and Dynamics*, vol. 25, no. 6, pp. 1073–1080, 2002.

- [123] C. Seatzu, D. Corona, A. Giua, and A. Bemporad, "Optimal control of continuous-time switched affine systems," *IEEE Transactions on Automatic Control*, vol. 51, no. 5, pp. 726–741, 2006.
- [124] M. Shibata and A. Ichikawa, "Orbital rendezvous and flyaround based on null controllability with vanishing energy," *Journal of Guidance, Control, and Dynamics*, vol. 30, no. 4, pp. 934–945, 2007.
- [125] J. Shim, "Korea geostationary satellite program: Communication, ocean, and meteorological satellite (COMS)," in *The 2006 EUMETSAT Meteorological Satellite Conference*, 2006.
- [126] P. Singla, K. Subbarao, and J. L. Junkins, "Adaptive output feedback control for spacecraft rendezvous and docking under measurement uncertainty," *Journal of guidance, control, and dynamics*, vol. 29, no. 4, pp. 892–902, 2006.
- [127] F. Sjoberg, A. Karlsson, and B. Jakobsson, "PROBA-3: A formation flying demonstration mission on the verge to be realised," in *Proceedings of the 3rd International Symposium on Formation Flying, Missions and Technologies*, 2008.
- [128] S. R. Starin, R. Yedavalli, and A. G. Sparks, "Spacecraft formation flying maneuvers using linear quadratic regulation with no radial axis inputs," in *AIAA Guidance, Navigation, and Control Conference and Exhibit*, 2001, pp. 6–9.
- [129] J. Tschauner, "Elliptic orbit rendezvous," AIAA journal, vol. 5, no. 6, pp. 1110-1113, 1967.
- [130] G. Valencia-Palomo and J. Rossiter, "Using Laguerre functions to improve efficiency of multiparametric predictive control," in *Proceedings of the American Control Conference*, 2010, pp. 4731–4736.
- [131] D. A. Vallado, *Fundamental of Astrodynamics and Applications*, 2nd ed. El Segundo, California: Microcosm Press, 2001.
- [132] M. Vieira, R. Galvao, and K. Kienitz, "Attitude stabilization with actuators subject to switching-time constraints using explicit MPC," in *IEEE Aerospace Conference*, 2011.
- [133] L. Wang, "Discrete model predictive controller design using Laguerre functions," *Journal of Process Control*, vol. 14, no. 2, pp. 131–142, 2004.
- [134] Y. Wang and S. Boyd, "Fast model predictive control using online optimization," *IEEE Transactions on Control Systems Technology*, vol. 18, no. 2, pp. 267–278, 2010.
- [135] J. R. Wertz and R. Bell, "Autonomous rendezvous and docking technologies: Status and prospects," in *Proceedings of the SPIE AeroSense Symposium*, 2003, pp. 20–30.
- [136] J. R. Wertz, J. T. Collins, S. Dawson, H. J. Koenigsmann, and C. W. Potterveld, "Autonomous constellation maintenance," in *Mission Design & Implementation of Satellite Constellations*. Springer, 1998, pp. 263–273.
- [137] J. Wertz, Spacecraft Attitude Determination and Control. Reidel Publishing Company, 1978.

[138] B. Wie, "Solar sail attitude control and dynamics, part 2," *Journal of Guidance Control and Dynamics*, vol. 27, no. 4, pp. 536–544, 2004.

- [139] D. C. Woffinden and D. K. Geller, "Relative angles-only navigation and pose estimation for autonomous orbital rendezvous," *Journal of Guidance, Control, and Dynamics*, vol. 30, no. 5, pp. 1455–1469, 2007.
- [140] D. C. Woffinden and D. K. Geller, "Navigating the road to autonomous orbital rendezvous," *Journal of Spacecraft and Rockets*, vol. 44, no. 4, pp. 898–909, 2007.
- [141] X. Xu and P. J. Antsaklis, "Optimal control of switched systems based on parameterization of the switching instants," *IEEE Transactions on Automatic Control*, vol. 49, no. 1, pp. 2–16, 2004.
- [142] H. Yoon and B. N. Agrawal, "Novel expressions of equations of relative motion and control in keplerian orbits," *Journal of Guidance, Control, and Dynamics*, vol. 32, no. 2, pp. 664–669, 2009.
- [143] C. Zakrzwski, S. Benson, P. Sanneman, and A. Hoskins, "On-orbit testing of the EO-1 pulsed plasma thruster," in 38th AIAA/ASME/SAE/ASEE Joint Propulsion Conference & Exhibit, 2002.
- [144] O. Zeiler, A. Schubert, B. Häusler, and J. Puls, "Autonomous orbit control for Earth-observation satellites," in 4th ESA International Conference on Spacecraft Guidance, Navigation and Control Systems, 1999, pp. 189–194.

Cover

GOCE Satellite

Image Credit: ESA/AOES Medialab

Abstract of the thesis:

Electric propulsion represents nowadays a solid established technology which can provide benefits over a large number of space missions and enable new challenging applications, as it allows for significant propellant mass savings and hence for reduced satellite launch costs. However, the application of this technology cannot rely on the impulsive control strategies established for the traditional chemical propulsion, calling for a re-design of the spacecraft control system. This thesis tackles the design problem by developing low-thrust attitude and orbit control techniques, tailored to station-keeping, formation flying and precision pointing of Earth orbiting spacecraft driven by electric propulsion. Numerical simulations of state-of-the-art dynamic models of the spacecraft demonstrate the effectiveness of the proposed techniques, within an autonomous guidance, navigation and control system.



The PhD School Engineering and Science of Siena school aiming at educating scholars in a number of fields of

research in the areas of Information Engineering and Mathematics. The PhD School of Information Engineering and Science is part of the Santa Chiara High School of the University of Siena. A Scientific Committee of external experts recognized PhD Schools belonging to Santa Chiara as excellent, according to their degree of internationalization, their research, and educational